Coupling Flight Mechanics and CFD

Numerical Simulation of Shipborne Rotors

by

Clément Crozon

Thesis submitted in accordance with the
requirements of the University of Liverpool for
the degree of Doctor in Philosophy by
Clément Crozon
June 2015

Declaration

I hereby declare that this dissertation is a record of work carried out in the School of Engineering at the University of Liverpool during the period from November 2011 to June 2015. The dissertation is original in content except where otherwise indicated.

8 June 2015

.....

(Clément Crozon)

Abstract

This thesis demonstrates the use of Computational Fluid Dynamics (CFD) for the simulation of manoeuvring helicopters. Results are presented for the problem of shipborne operations, for which a literature survey showed that little work has been carried out.

The CFD solver HMB2 was first validated using available experimental data for isolated ship wakes and helicopter loads at low advance ratios. A rotorcraft flight mechanics model was then developed and integrated into HMB2. The model includes a trimming method and a linearisation routine based on finite differences. The linear model of the aircraft can be used to estimate the controls applied by the pilot during a prescribed manoeuvre via the use of the SYCOS inverse-simulation method or via an LQR auto-pilot. The methods developed in the framework of this thesis include a general multi-body grid motion and an alternative formulation for earth-fixed frame of reference in the CFD.

A study of the ship/rotor wake interaction was carried out using the actuator disc method that approximated the effect of the rotor, in a steady fashion and without resolving the flow around the blades. Various positions and thrust of the rotor were tested and the flowfield obtained via coupled simulations were compared with those obtained by super-imposing isolated rotor and ship flowfields. The results show that the superposition principle is not valid and leads to flowfields that have little to do with the real flow that is dominated by the interaction of helicopter and ship airwakes. The case of a rotor hovering in close proximity to a frigate deck was reproduced with fully-resolved blades, and the results shows a significant reduction of thrust due to the flow topology behind the hangar.

The Helicopter Flight Mechanics (HFM) method was tested by simulating the aircraft response to a collective pilot input, using simplified models and coupled with CFD. Then, the coupled HFM/HMB2 method was used, in conjunction with the LQR auto-pilot, to simulate the phase of landing of a Sea King helicopter. Simulations were carried-out in free-air and above the frigate deck and the specified trajectories were followed adequately.

Results for the ship landing show that the wake of the ship alters the obtained landing trajectory and that the current method captures some of the effects of the wake interaction.

Acknowledgements

I would like to express my deepest appreciation to my supervisors Prof. George Barakos, Dr. Rene Steijl and Dr. Mark White. Without their guidance and their dedication, this thesis would not have been possible.

I would like to thank Dr. Mark Woodgate, for all the help in understanding the solver and resolving (user-related) technical problems.

I would also like to extend my gratitude to AgustaWestland for funding this project and providing the Sea King geometry data.

I have met many great people working in the CFD lab for almost four years: Mikolaj, Savio, Florent, Marina, little George, Vasilis, Amir, Gaetan, Yaxine, Cathy, Antonio, Matt, Massimo, Ghazal, Simone, Vladmir, Vincent, Jacob, Jurr and Giulia.

Most of all I would like to thank my family, for their unwavering love and support throughout this project.

The use of the POLARIS HPC cluster of N8 and the Chadwick HPC cluster of the University of Liverpool are also gratefully acknowledged.

Publications

Journal Papers

C. Crozon, R. Steijl and G. Barakos, Numerical Study of Rotors in Ship Airwake, *The American Institute of Aeronautics and Astronautics Journal of Aircraft*, Vol. 51, No. 6 (2014), pp. 1813-1832. doi: 10.2514/1.C032535
C. Crozon, R. Steijl and G. Barakos, Coupled Flight Dynamics and CFD - Demonstration for Helicopters in Shipborne Environment, *Submitted to the American Institute of Aeronautics and Astronautics Journal*.

Papers in Conference Proceedings

S. Lawson, C. Crozon, F. Dehaeze, R. Steijl, G. Barakos, Computational Fluid Dynamics Analysis of Ship Air Wakes Using Detached-Eddy Simulation, *Proceedings of the European Rotorcraft Forum, 4-7 September 2012, Amsterdam, Netherlands.*
C. Crozon, R. Steijl, G. Barakos, Numerical Study of Rotors in Ship Airwake, *Proceedings of the European Rotorcraft Forum, 3-6 September 2013, Moscow, Russia.*
G. Barakos, C. Crozon, R. Steijl and M. Woodgate, Numerical Simulation of Shipborne Rotors, *Keynote Lecture in the proceedings of the 2nd Asian Australian Rotorcraft Forum, Tianjin, China, 8 Sept. 2013*, ISSN 1552-2938
C. Crozon, R. Steijl, G. Barakos, Coupled Flight Dynamics and CFD - Demonstration for Helicopters in Shipborne Environment, *Proceedings of the European Rotorcraft Forum, 2-5 September 2014, Southampton, United Kingdom.*

Internal Reports

C. Crozon, Grid Motion for Rigid-Bodies and Rotors in HMB2, *Technical Note TN12-002, 2012*.
C. Crozon, Generation of 3D multi-block structured grids around ships and rotors with ICEM, *Technical Note TN12-005, 2012*.
C. Crozon, Version Control of HMB2 with Subversion, *Technical Note TN13-005, 2013*.
C. Crozon, Running Forward Flight Cases with HMB2, *Technical Note TN13-006, 2013*.
C. Crozon, Flight Mechanics Model for Coupled CFD Calculations with HMB2, *Technical Note TN13-011, 2013*.

Contents

List of Figures

List of Tables

Nomenclature

Acronyms	Definition
BEM	Blade Element Modeling
CFD	Computational Fluid Dynamics
CPF	Canadian Patrol Frigate
CPU	Central Processing Unit
DES	Detached Eddy Simulation
DI	Dynamic Interface
FOCFT	First-Of-Class Flight Trial
GE	Ground Effect
HFM	Helicopter Flight Mechanics
*HMB*2	Helicopter Multi-Block CFD solver
IGE/*OGE*	In/Out of Ground Effect
LES	Large Eddy Simulation
LHA	Landing Helicopter Assault - Simplified aircraft carrier model
NRC	National Research Council of Canada
PIV	Particle Imaging Velocimetry
SFS	Simple Frigate Shape
*SFS*2	Modified Simple Frigate Shape
SHOL	Ship-Helicopter Operating Limitations
*T*23	Type 23 frigate
TTCP	The Technical Cooperation Program
V/*STOL*	Vertical/Short Take-Off and Landing
VTOL	Vertical Take-Off and Landing
WOD	Wind Over Deck
WT	Wind tunnel

Greek Symbols	Definition
β_0	Cone angle [degrees]
β_{1c} , β_{1s}	First harmonic flapping coefficients [degrees]
δ_0	Rotor prescribed lead-lag [degrees]
δ_3	Pitch/Flap coupling angle
δ_{1c} , δ_{1s}	First harmonic lead-lag coefficients [degrees]
γ	Lock number, $\gamma = \frac{\rho acR^4}{I}$
λ	Inflow factor, $\lambda = \frac{v_i}{V_{\text{tip}}}$
μ	Rotor advance ratio, $\mu = \frac{M_\infty}{M_{\text{tip}}}$
Ω	Rotor rotation rate $[rad.s^{-1}]$
$\Omega_{magnitude}$	Vorticity magnitude
Φ, θ, Ψ	Euler orientation angles [degrees]
Φ_{wind}	Wind pitch angle [degrees]
ψ	Blade azimuth (zero degrees at the rear of the rotor disc) [degrees]
Ψ_{wind}	Wind yaw angle [degrees]
ρ_∞	Freestream density $[kg.m^{-3}]$
σ	Rotor solidity, $\sigma = \frac{N_{\text{blades}}c}{\pi R}$
θ_0	Rotor collective [degrees]
Θ_{S}	Shaft angle [degrees]
θ_{1c} , θ_{1s}	First harmonic pitching coefficients [degrees]
θ_{tw}	Rotor twist [degrees]

Roman Symbols	Definition
$\dot{m}$	Mass flow rate $[kg.s^{-1}]$
Γ	Lapse rate
L	Ship length [m]
W	Ship beam width [m]
$\tilde{u}$	Velocity perturbation $[m.s^{-1}]$
u	Control vector (group of control variables)
$\underline{u}$	Velocity vector $\underline{u} = [u, v, w]^{\text{T}}$
x	State vector (group of state variables)
y	Reduced state vector
A	Rotor disc area, $A = \pi R^2$ $[m^2]$

a_∞	Freestream speed of sound $[m.s^{-1}]$
b	Ship beam length
c	Rotor chord [m]
C_D	Airfoil drag coefficient
C_L	Airfoil lift coefficient
C_T	Rotor thrust coefficient, $C_\mathrm{T} = \frac{T}{\rho_\infty A(\Omega R)^2}$
C_T^UK	Rotor UK thrust coefficient, $C_\mathrm{T}^\mathrm{UK} = \frac{T}{\frac{1}{2}\rho_\infty A(\Omega R)^2}$
M_tip	Mach number at blade tip $M_\mathrm{tip} = \frac{\Omega R}{a_\infty}$
$M_{0.75}$	Mach number at $\frac{r}{R} = 0.75$, $M_{0.75} = 0.75 \cdot M_\mathrm{tip}$
M_∞	Freestream Mach number
N_blades	Number of rotor blades
P^*	Dimensionless pressure
P_QNH	Pressure at sea level [hPa]
p_∞	Freestream pressure $[Pa]$
q_∞	Freestream dynamic pressure, $\frac{1}{2}\rho_\infty U_\infty^2$,$[Pa]$
R	Rotor radius [m]
r	Coordinate along the blade span $[m]$
T	Rotor thrust $[N]$
T_QNH	Temperature at sea level $[^\circ C]$
T_h	Temperature at the altitude h $T_h = T_\mathrm{QNH} + \Gamma h$
U	Mean value of flow velocity $[m.s^{-1}]$
U_P	Out-of-plane component velocity at blade section $[m.s^{-1}]$
U_R	Radial component velocity at blade section $[m.s^{-1}]$
U_tip	Rotor blade tip speed $[m.s^{-1}]$
U_tip	Rotor blade tip speed
U_T	In-plane component velocity at blade section $[m.s^{-1}]$
U_S	Velocity correction $[m.s^{-1}]$
U_{10}	Wind velocity at 10 meters above the sea $[m.s^{-1}]$
U_∞	Freestream velocity $[m.s^{-1}]$
v_i	Rotor induced velocity $[m.s^{-1}]$
z_0	Roughness coefficient [m]

Subscripts	**Definition**

0	Main term of the fourier decomposition
$1c$	Cosinus term of the first harmonic of the fourier decomposition
$1s$	Sinus term of the first harmonic of the fourier decomposition
∞	Value at “infinity” or farfield boundary
ref	Reference value
tip	Reference value taken at the blade tip
X	X-direction component
Y	Y-direction component
Z	Z-direction component

Superscripts	**Definition**
T	Matrix transpose operation
ext	External
Fus	Fuselage
M	Main rotor
T	Tail rotor

Chapter 1

Introduction

1.1 Project Motivation

Helicopters are versatile, manoeuvrable aircraft and a key element of a variety of ship-based operations: search and rescue missions, counter-piracy, transport of freight and crew, reconnaissance and target identification, etc. Operating helicopters in a maritime environment is challenging as the pilot is required to manoeuvre in close proximity to the ship superstructure. The size of the deck, the ship motion, the wake unsteadiness, the weather and lighting conditions are some of the factors that contribute to increasing the pilot workload. As a result, take-off and recovery operations may be impossible to complete without over-stressing the aircraft structure and decreasing the safety [3].

To assess the level of hazard of take-off and recovery operations, every ship/aircraft configuration is tested through a campaign of First-Of-Class Flight Trials (FOCFT) during which a series of take-off and landings are performed by a test pilot for different conditions of wind strength and direction. A subjective feedback is given by the pilot using the Bedford rating scale shown in figure 1.1 (a) to estimate the difficulty to complete a given task. Results are gathered in the form of a Ship/Helicopter Operational Limitations diagram (SHOL), as shown in figure 1.1 (b), and gives future pilots an estimate of the hazard of the manoeuvre for specific wind conditions.

Military aircraft and helicopter carriers operate as sea-going air-bases and offer a large deck area to accommodate a wide range of Vertical or Short Take-Off and Landing (VSTOL) aircraft. Frigates, tankers, ferries and other "non-aviation" ships are often fitted with a deck or landing platform located at the stern to offer the possibility for helicopter operations, as shown in figure 1.2.

The turbulent wake that develops behind the ship as a result of the wind and the ship forward motion has a complex flow structure with flow separation due to sharp

Ship Airwake	**Aircraft Aerodynamics**
Complex Geometry	Complex Geometry
Large Turbulence Length Scale	Smaller Turbulence Length Scales
Low Velocity Wind Over Deck	High Velocity Jet/Rotor Wake
Incompressible Flow	Compressible Flow
Unsteady	Steady/Unsteady

Table 1.1: Main concerns on coupled Ship/Aircraft CFD simulations (from Polsky [6])

edges, strong unsteady vortices and high levels of turbulence. In return, the helicopter downwash changes the global wake, creating a coupled aerodynamic problem [4]. The proximity of the superstructure (deck, hangar, instruments and weaponry) leads to complex interactions and the helicopter can be considered as in "partial ground effect" [5] with addition of recirculation effects.

This complex interaction usually leads to reduced manoeuvrability and safety margins, and increased pilot workload during the critical phases of take-off and landing. The simulation of the aerodynamic interference between the ship and rotorcraft wakes, or Dynamic Interface (DI), has been an important subject of research, mainly as a way to improve the realism of flight simulation environments used for pilot training.

The development of Computational Fluid Dynamics (CFD) methods and high-performance flight simulation techniques permit to foresee the use of fully-simulated trials to broaden the range of conditions investigated during SHOL campaigns while reducing their cost and dangerousness.

Table 1.1 was reproduced from Polsky [6] and gives an overview of the main numerical difficulties to simulate coupled ship/aircraft operations using CFD. The wide range of flow conditions requires advanced, high-fidelity computational tools that must be validated for such cases.

To date, CFD cannot support real-time flight simulations and is used mainly to enhance the realism of flight simulations that are used for flight tests and as training tools. However, simulations have not advanced to the point where they can replace part of the at-sea trials [3]. The outcomes of advanced Dynamic Interface simulations are various: improving flight simulations for training and definition of the SHOL, contribution to ship and aircraft design, flight control design, ship-based aircraft control system design [7].

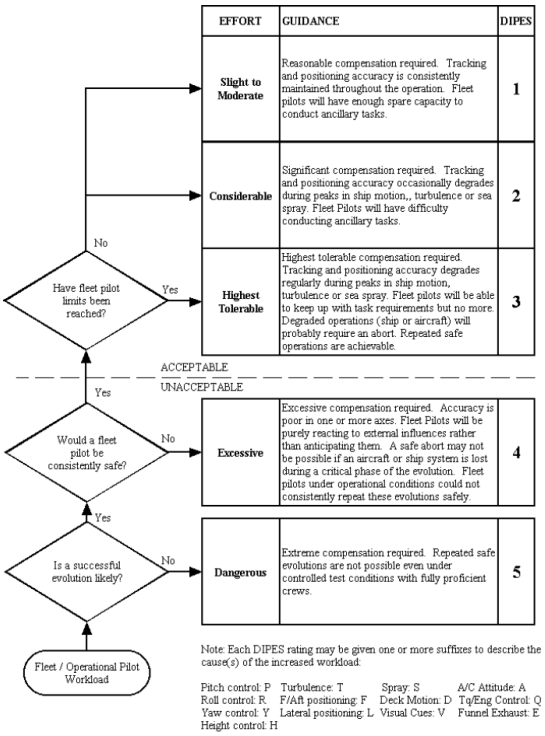

Figure 1.1: (a) Bedford workload rating scale and (b) SHOL chart for the Liverpool generic helicopter model / Simple Frigate Shape 2 (from Roper [8])

Figure 1.2: Westland Wildcat landing on the Type-23 frigate HMS Lancaster (from *https://navynews.co.uk*)

1.2 Literature Survey on SHOL Simulations

A literature survey is conducted, focusing on the past 20 years of progress in modelling ship and rotorcraft airwakes and the problem of the dynamic interface. Studies on the simulation of helicopter flight, specification of Ship/Helicopter Operational Limitations, aircraft-obstacle and aircraft-aircraft interference are of interest for the present work. Related studies including blade aero-elasticity using coupled CFD/CSD (Computational Structural Dynamics) methods, blade sailing and engagement/disengagement, rotors in ground effect are also mentioned. The Scopus, NASA Technical Report Server (NTRS), Web of Knowledge (WoK) and Compendex databases were surveyed using relevant keyword searches. It appears that most of the experimental and numerical studies in this domain use simplified ship models such as the Simple Frigate Shape (SFS) and its derivative, the SFS2. However, they are deemed too simple for such applications and more realistic ship models are available such as the Canadian Patrol Frigates (CPF), the Landing Helicopter Assault (LHA) from NASA and the Type-23 frigate. Four ship geometries with increasing level of detail are shown in figure 1.3.

Table 1.2 presents the most relevant keywords along with the number of publications consequently listed.

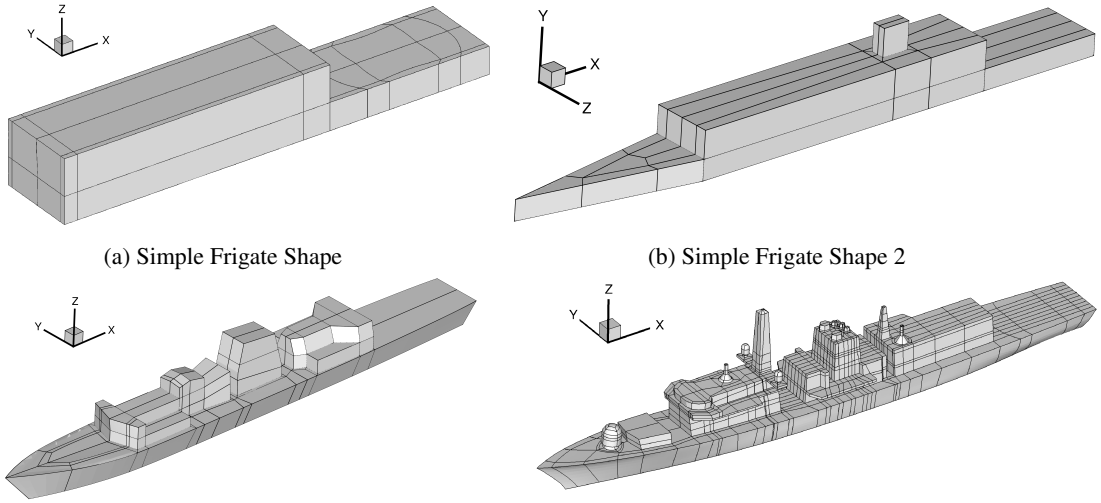

(a) Simple Frigate Shape

(b) Simple Frigate Shape 2

(c) Canadian Patrol Frigate

(d) Type-23 Frigate

Figure 1.3: Four examples of frigates shapes of different levels of realism.

1.2.1 The Problem of the Ship Airwake

The ship airwake results from the complex interaction between the relative wind and the ship superstructure. For the purpose of studying this problem, the standard, Simple

Keywords	Number of results			
	Scopus	NTRS	WoK	Compendex
Ship airwake	109	60	35	108
Ship helicopter	1138	3232	248	871
Helicopter downwash	158	1361	32	132
Ship airwake helicopter downwash	7	29	1	7
Simple frigate shape	8	76	2	8
Simple frigate shape helicopter	8	55	2	8
Canadian patrol frigate	30	17	17	26
Canadian patrol frigate helicopter	7	16	3	6
SHOL	114	646	24	127
Pilot models	441	282	44	61
Helicopter ground effect	459	6807	224	526

Table 1.2: List of database keywords and corresponding number of findings. Search realised at the beginning of the study (2012)

Frigate Shape (SFS) model was created under The Technical Co-operation Program (TTCP). The goal was to provide a simple geometry for wind tunnel testings and the validation of numerical tools. The SFS geometry and its evolution, the SFS2 are used extensively in the literature but results have shown that smaller elements such as details of the superstructure, radar and weaponry may affect the flowfield and contribute in increasing the pilot workload [9]. Many authors chose more realistic geometries to improve the realism of the wind tunnel tests and numerical simulations.

The maximum Reynolds numbers associated with the ship aerodynamics are in the region of 10^7 to 10^8, based on the ship beam. However, most ship shapes have sharp edges that lead to immediate flow separation and it is commonly admitted that the flow characteristics do not change significantly with the Reynolds number. Ship airwakes are typically unsteady, with the most energetic part corresponding to shed structures with frequencies below 2Hz. According to Zan [3], most helicopter pilots consciously respond to changes in aircraft attitude at a rate of 1.6Hz and below while higher frequencies are perceived as vibrations and do not result in a direct action of the pilot. As a result, the ship wake may have a direct effect on the aircraft motion and increase the pilot workload.

In addition to the unsteadiness of the ship airwake, the pilot has to cope with the strong differences in the flow the helicopter encounters. During a typical approach as shown figure 1.5 and depending on the wind direction, the helicopter may experience successively free-stream conditions, lateral wind, ground effect, strong rolling moment due to the vortical structure of the wake and additional downwash behind the hangar. These effects directly contribute in reducing the aircraft margin of manoeuvre and therefore its safety.

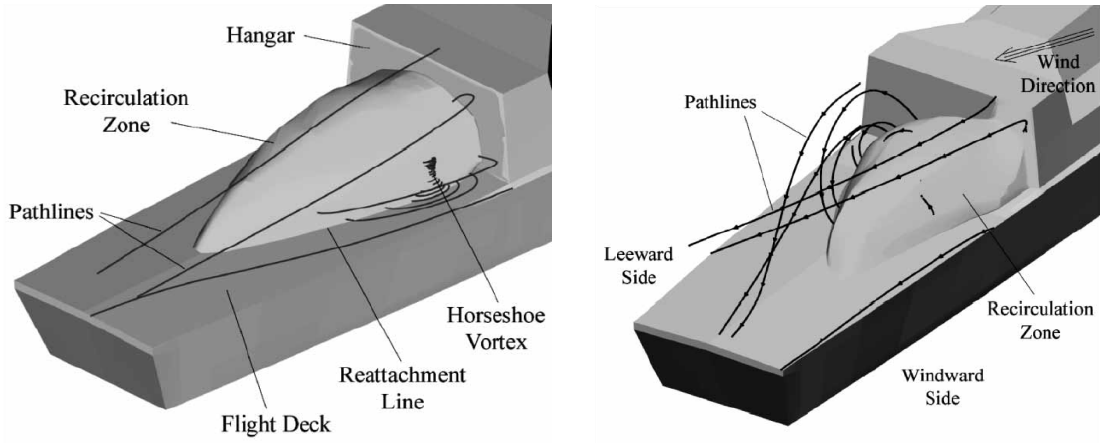

Figure 1.4: Flow topology above the deck of the Modified Canadian Patrol Frigate (from Syms [10])

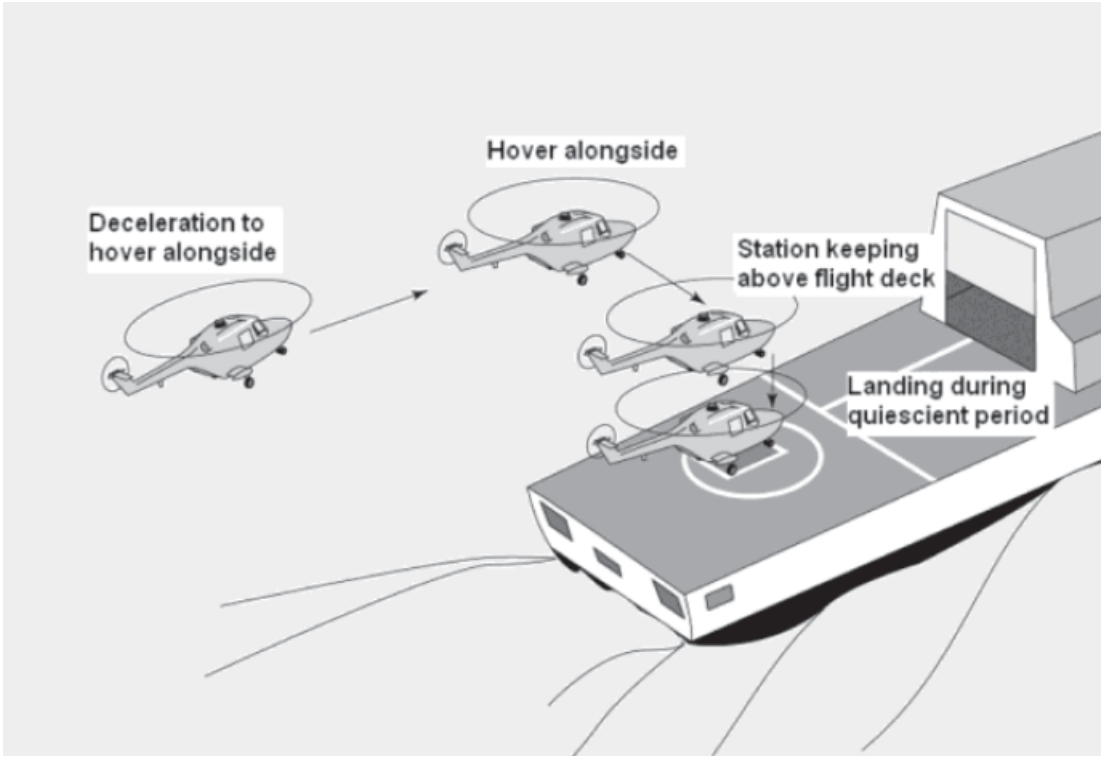

Figure 1.5: Typical frigate landing path (from Kàària *et al.* [11])

The ground and confinement effects are shown to modify helicopter performances when the distance between the obstacle and the aircraft is around or below three rotor radii. The ground effect is known to decrease quickly with the advance ratio and it becomes less important if the ship or wind speed increases. If this is the case for clear decks (aircraft carriers for example), it is less so behind the hangar of a frigate where the airflow is effectively blocked, in particular for headwind [12].

1.2.2 Helicopter Aerodynamics

"A helicopter can be defined as any flying machine using [powered] rotary wings (i.e. rotors) to provide lift, propulsion and control forces" [13]. To achieve this goal while dealing with the underlying problems, many configurations have been developed over the last century. Four configurations are used nowadays: the main/tail rotor, tandem, coaxial rotors and the synchropter configuration. One can include in this list the tilt-rotor configuration which allows the aircraft to vertically take-off and land while cruising like a regular aeroplane by tilting the rotors into a propeller configuration. Some concepts of compound helicopters also use propulsive rotors and small lifting surfaces to improve cruise performance.

The efficiency of a helicopter comes from its ability to move a large mass of air at low velocity, hence leading to large rotor diameters. As mentioned in Leishman [13], the development of modern helicopters was challenging: development of high power-to-weight ratio engines, ability to counteract the rotor-torque reaction, stability for a range of flight conditions, ability to autorotate in case of engine failure. The irreplaceable capabilities of modern helicopters (vertical take-off and landing, versatility, etc.) come at a price: vibrations and mechanical complexity leading to high maintenance costs, complex aerodynamics, risks of mechanical failure, etc.

As for any flying machine, helicopter flight is achieved through an equilibrated budget of propulsive lift, drag and weight forces. In steady hover, the rotor produces the necessary lift to counteract the weight of the aircraft. As torque is applied to maintain the rotor rotation, an opposite moment is applied on the aircraft fuselage that needs to be compensated. In the standard main/tail rotor configuration, the secondary rotor at the tail provides the counteracting force. Other configurations use two coaxial or side-by-side main rotors to alleviate this problem without addition of a tail rotor, albeit with a greater mechanical complexity. In forward flight, a fraction of the lift is used to induce forward forces and counteract the drag of the fuselage. This leads to a much more complex distribution of forces on the rotor and represent most of the operational limitations of the aircraft.

The control of the aircraft by the pilot is achieved by modifying the main rotor collective and cyclic angles as well as the tail rotor collective. The rotor hub must therefore allow the blades to rotate in every direction, leading to a complex mechanical system (Figure 1.6). The pitch of the blades is controlled via a set of rods connected at the bottom to a swash-plate. This particular assembly permits to control the collective and cyclic simultaneously and imposes a 1-per-rev sinusoidal variation of the blade pitch. In the case of a fully-articulated rotor hub, blades are controlled in pitch θ and

free to rotate in the two other directions: flapping β and lead-lagging δ (Figure 1.7). Semi-rigid rotors are simpler and use a flexible material to accommodate the flapping and lead-lag forces. Pitching, flapping and lead-lag angles are functions of the azimuth and are commonly decomposed in Fourier series (a negative convention is used here), with only the first harmonic terms:

$$\psi = \omega t \tag{1.1a}$$

$$\beta(\psi) = \beta_0 - \beta_{1c} cos(\psi) - \beta_{1s} sin(\psi) \tag{1.1b}$$

$$\delta(\psi) = \delta_0 - \delta_{1c} cos(\psi) - \delta_{1s} sin(\psi) \tag{1.1c}$$

$$\theta(\psi) = \theta_0 - \theta_{1c} cos(\psi) - \theta_{1s} sin(\psi) \tag{1.1d}$$

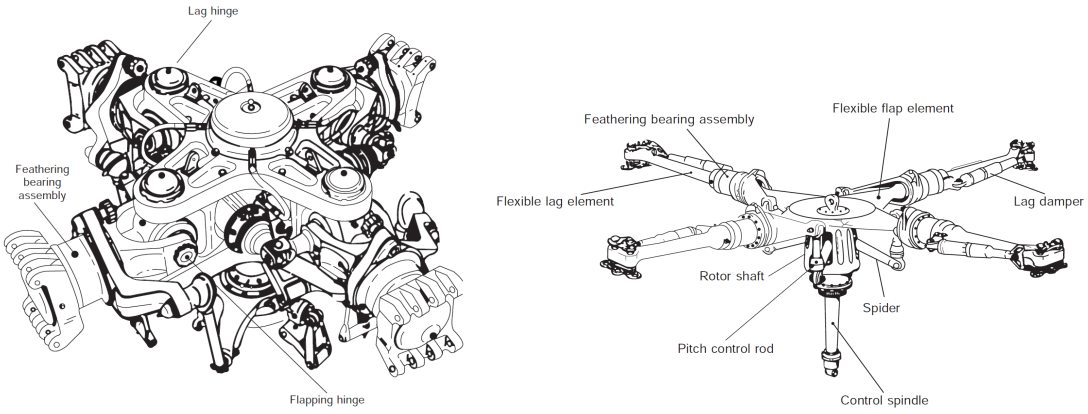

Figure 1.6: Two kinds of helicopter hubs: Fully-Articulated (Left) and Semi-Rigid (Right) (from Bramwell [1])

The momentum theory gives the simplest description of rotor characteristics. It assumes a uniform, quasi-steady, incompressible, inviscid and non-swirling flow through the rotor disc, with no variation of velocity but a jump of pressure through the disc. This theory can also provide estimates of the downwash and rotor power.

Taking the blades rotational velocity Ω and radius R as references, we can define the induced flow ratio λ_i and the thrust, power and torque coefficients (C_{T}, C_{P} and C_{Q} respectively):

The typical rotor wake geometry of a hovering rotor consists in a set of inter-digitated spiral-shaped vortices originating from each blade tip and convected downward by the local streamwise velocity, as shown in figure 1.8. A set of inner vortex sheets originates from the blades trailing edges and are convected faster due to the higher local velocity, hence dissociating from the tip vortices. The stream-tube defined by the rotor disc circumference contracts progressively below the rotor so that the section of this stream-tube is theoretically of half the rotor disc area.

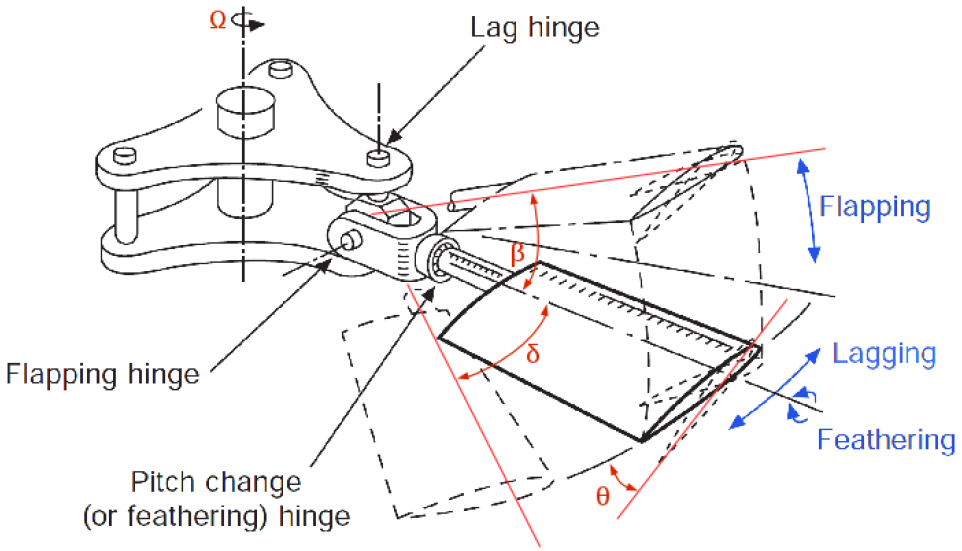

Figure 1.7: Definition of the main notations for angles (adapted from Bramwell [1])

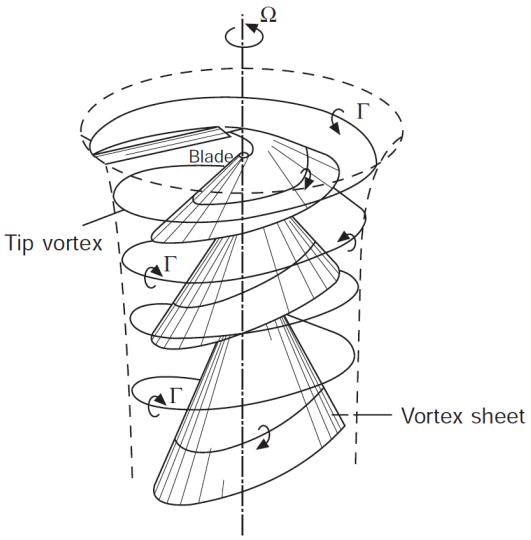

Figure 1.8: Rotor wake geometry Out of Ground Effect (OGE) (from Bramwell [1])

1.2.3 Ground Effect

When a hovering rotor operates in close proximity to the ground, the development of the wake is constrained, forcing it to expand radially as shown in figure 1.9. The Ground Effect (GE) decreases the induced flow through the rotor, increasing the angle of attack seen by the blades. The pressure rise below the rotor acts as a cushion, increasing the thrust coefficient. The wake first contracts and then is rapidly expand as it is convected away from the rotor by the mean flow. The individual blade vortices are closer to each other and their mutual interactions lead to a more complex wake geometry with vortices pairing into larger structures, as shown in figure 1.10. The

phenomenon of pairing does not necessarily preserve the azimuthal periodicity and may induce changes in trim state, handling problems, imbalance in moments and vibrations.

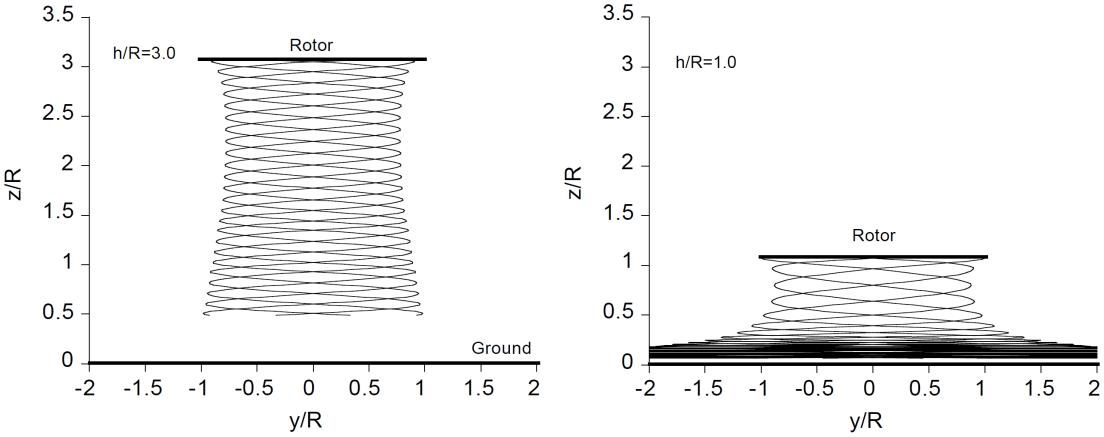

Figure 1.9: Effect of the ground on wake geometry at 3 and 1 rotor radii (from Griffiths [14])

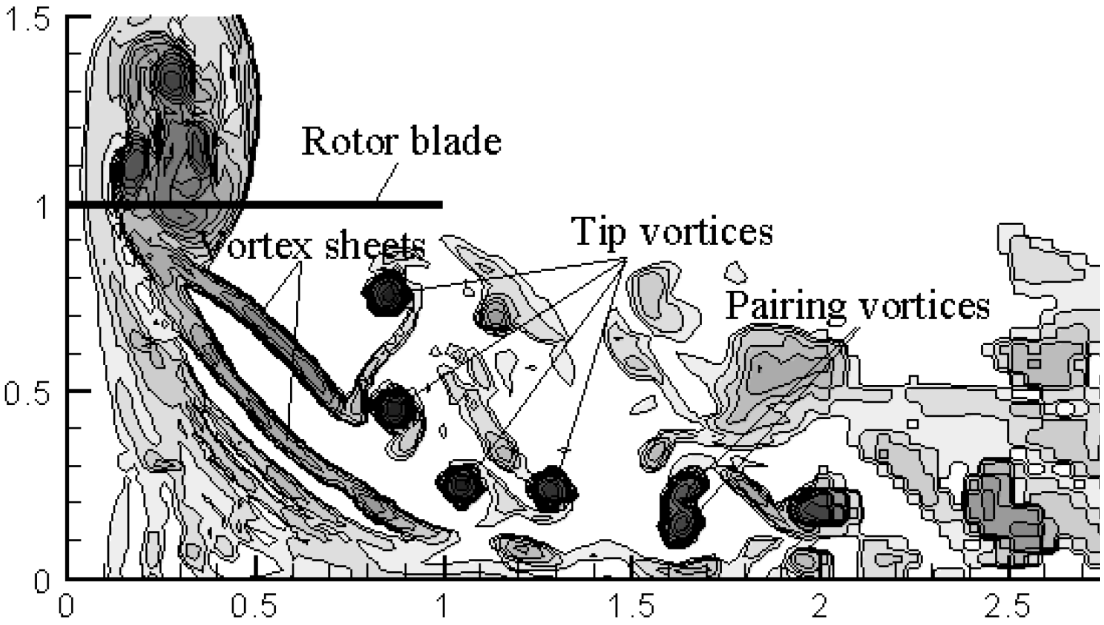

Figure 1.10: Pairing effect on the vortices in Ground Effect (from Phillips *et al.* [15])

In forward flight, the rotor disc can be approximated to a single lifting surface, with the difference of pressure below and above the rotor leading to two important recirculations on both sides of the rotor disc. These two super-vortices interact with the blade tip vortices, resulting in a complex flow geometry as shown in figure 1.11 (a). The second figure 1.11 (b) shows that the presence of the ground further distorts the wake by forcing it to expand both longitudinally and laterally.

Figure 1.12 shows the effect of the advance ratio on the wake topology in ground

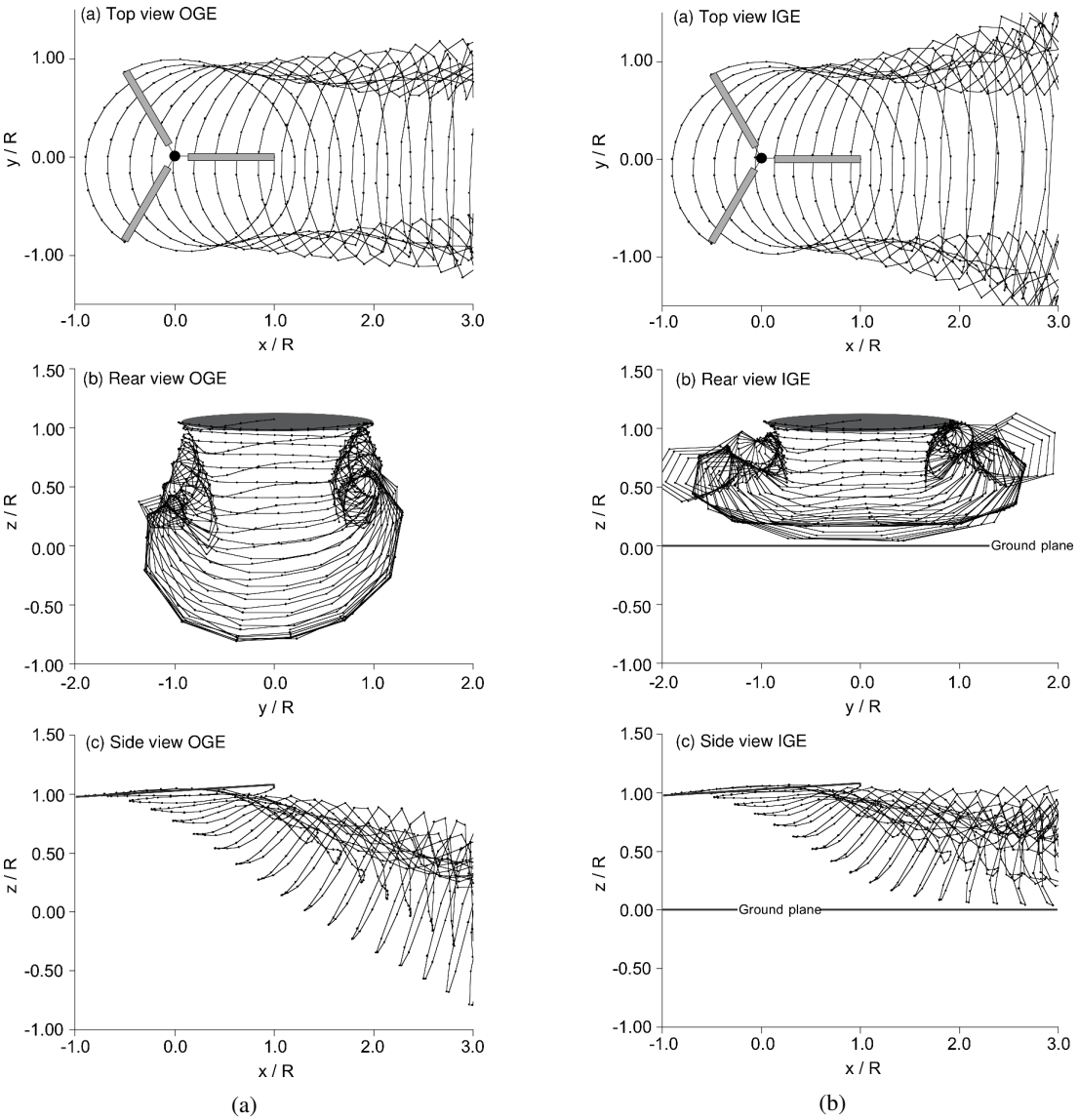

Figure 1.11: Wake geometry in forward flight Out and In Ground Effect. Rotor shaft is tilted 3° forward, advance ratio $\mu = 0.10$, $h/R = 1.0$ for the IGE case (from Griffiths [14])

effect. At very-low speed such as during taxi, a horseshoe vortex appears in front of the aircraft as a result of the blockage caused by the downwash [16] and is associated with a decrease of the required power. When transitioning to forward flight, an important recirculation appears at the leading edge of the rotor disc, associated with a rapid increase in required power. At higher advance ratios, the ground effect progressively decreases and the required power increases accordingly.

Experimental work on ground effect has been conducted to understand the underlying flow physics [17–20]. Although the ground effect is beneficial in terms of thrust coefficient, it varies depending on the rotor properties: solidity, specific loading and twist. Adverse effects such as ground resonance which causes excessive flapping

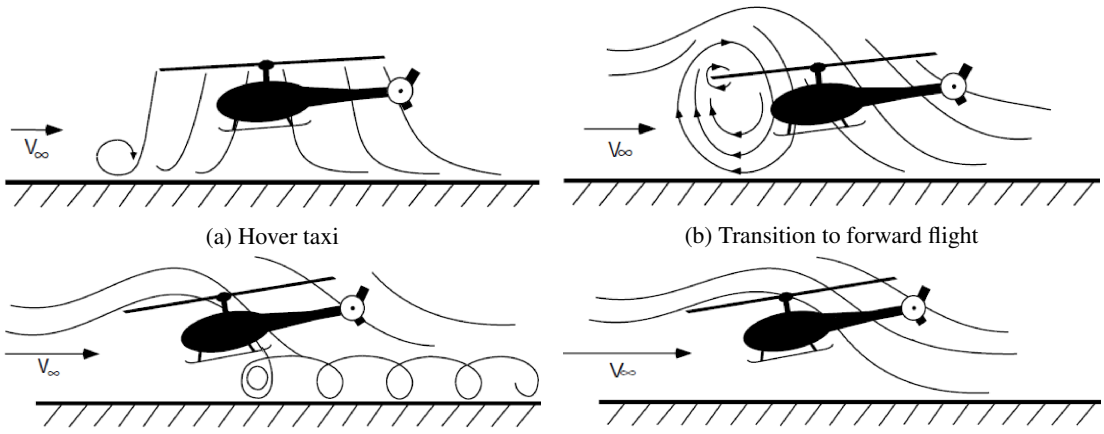

(a) Hover taxi

(b) Transition to forward flight

(c) Low-speed forward flight

(d) Higher-speed forward flight

Figure 1.12: Flow states encountered during transition to forward flight In Ground Effect (from Griffiths [14])

of the rotor blades, ultimately damaging the blades and the fuselage structure. Further confinement caused by nearby vertical surfaces such as buildings also affect the global performance of the rotor. Iboshi *et al.* [21] performed a series of experiments on a model rotor in ground effect with the presence of vertical walls. Some results showed an important increase in torque as well as variations in thrust around the azimuth while the thrust was kept constant, which reduces the lift capabilities of the aircraft and is likely to induce vibratory loads to the rest of the aircraft.

Some more details on theoretical modelling of the ground effect are given in section 2.1.3

1.2.4 Ship/Helicopter Operational Limitations

The Ship/Helicopter Operational Limitations (SHOL) define the range of conditions a helicopter can safely operate within. They are given to pilots in the form of a diagram that provides an estimate of the dangerousness of a procedure depending on the wind strength and direction. Zan [3] points out that the pilot workload, thrust and pedal margins are the three main contributors when defining the operational limitations for a given aircraft/ship configuration. The relative importance of each contributor is directly linked to the wind conditions: pedal and thrust margins are limited by the need to counteract the effects of wind gusts and maintain the position and attitude of the aircraft above the deck while the pilot workload appears to limit the operational envelope for strong winds because of the flow unsteadiness. A realistic representation of the pilot workload in simulated flights requires an accurate representation of the global flowfield and its effect on the aircraft aerodynamics.

Flight simulations have been considered as a mean to extend or partially replace at-sea trials, as well as provide training tools for future pilots. Shipborne flight simulations often use existing data for the isolated ship wake, extracted from at-sea measurements or CFD results and can be steady or unsteady. A flight mechanics model is used to calculate the helicopter position and attitude in real time and include the ship wake into the calculation via look-up tables. Since the wake is "frozen", the method takes into account only the effect of the ship wake on the rotor inflow and do not couple the two wakes [8, 22]. This simplification is dictated by the fact that no CFD simulation can be performed in real time, and the amount of CFD data required to give an estimate of the global flowfield for each position of the helicopter is very important.

1.2.5 Definition of the Coupling

The simulation of rotorcraft in ship airwakes involves the notion of coupling between the different elements of the simulation. In the following, the expression "Two-way coupling" refers to a simulation in which the ship and aircraft wakes are both dependant on each other (hence necessarily computed simultaneously). The expression "One-way coupling" refers to a simulation in which the ship airwake is computed *a priori* and is independant from the aircraft wake. The airwake is sometimes referred to as "frozen" even in case of unsteady simulations. The notion of "level of coupling" refers to the number of parameters taken into account and therefore the accuracy of the simulation.

The following figures (1.13 and 1.14) present the elements involved in one-way and two-way coupled simulation and the relation between them.

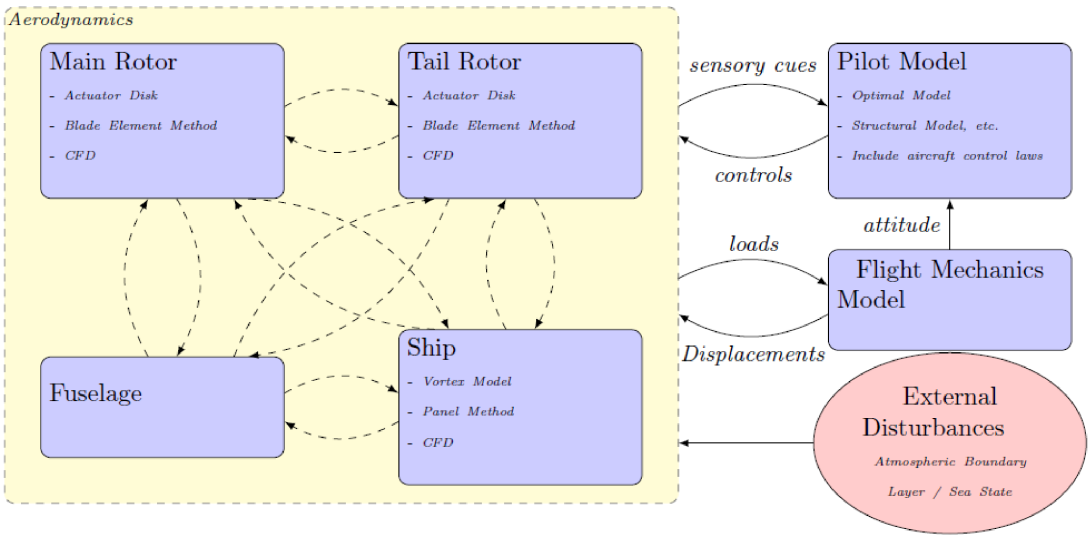

Figure 1.13: Elements of a two-way coupled ship-rotorcraft simulation. Dashed arrows denote an implicit coupling.

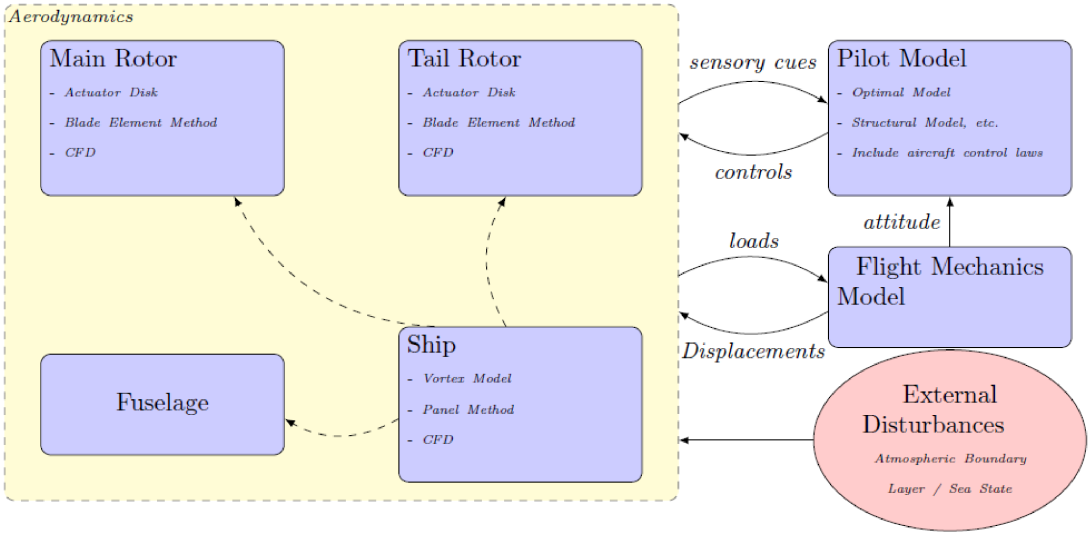

Figure 1.14: Elements of a one-way coupled ship-rotorcraft simulation. The ship wake is not modified by the presence of the aircraft (”Frozen wake”, steady or unsteady)

Aerodynamic Coupling

The level of aerodynamic coupling is directly related to the level of detail and the modelling strategies employed for the different elements of the aircraft. The main and tail rotors can be modelled in many ways, from actuator discs, resulting in a weak response of the rotor to the flowfield, to the use of CFD simulation for fully articulated and deformable blades. The different elements of the aircraft (rotors, fuselage, etc.) are implicitly coupled within the simulation, however, the fuselage and tail rotor are not always taken into account, hence reducing the level of aerodynamic coupling.

External Environment

The external environment of the coupled ship/aircraft plays a key role in the accuracy of a coupled simulation and includes the pilot (human behavioural response to the aircraft attitude), the flight mechanics (Response of the aircraft to aerodynamic conditions) and the disturbances (Atmospheric boundary layer profile and turbulence, sea state and ship motion).

Coupled Simulations

Since no CFD simulation can be performed in real time during trials in a flight simulator, the pilot’s behaviour has to be modelled. A wide variety of pilot models have been developed over the years and have to be associated with a flight mechanics model to transform the CFD-computed loads into aircraft displacements. The flight

mechanics model can also be implemented in different ways, from a simplified "flying brick" model to more complex descriptions.

Regarding the number of parameters involved in a coupled simulation, it appears impossible to rank each configuration by evaluating the level of coupling. Table 1.3 provides a comparison of different configurations that can be considered or were found in publications.

Type of coupling	Aerodynamics				External environment			References
	Main rotor	Tail rotor	Fuselage	Ship	Pilot model	Flight mechanics	Disturbances	
Type 0	Actuator disc	NO	NO	NO [1]	NO	NO	NO/ABL	
Type 1	Actuator disc	NO	NO	YES	NO	NO	NO/ABL	Wakefield [4, 23]
Type 2	Actuator disc	Actuator disc	YES	YES	Prescribed path	NO	NO/ABL	Polsky [6, 7]
Type 3	Resolved blades	NO	NO	YES	NO	NO	NO	
Type 4	Actuator disc	NO	NO	YES	Optimal model	Flying brick	NO	
Type 5	Blade Element Model	NO	NO	YES	Optimal model	Flying brick	NO	Alpman, Bridges *et al.* [24, 25]
Type 6	Resolved blades	NO	NO	YES	YES	Flying brick		
Type 7	Resolved blades	Resolved blades	YES	YES	NO	NO	NO	
Type 8	Resolved blades	Resolved blades	YES	YES	YES	Flying brick	YES	

Table 1.3: Types of coupling encountered in the literature and for this project for CFD simulations. [1] Ship wake computed separately and input as a frozen wake.

A number of simplifying assumptions are usually made when simulating the dynamic interface [24]: neglecting the time varying component of the ship airwake, assuming the ship airwake is frozen with respect to the ship and not affected by the ship motion, neglecting the effects of atmospheric turbulence and boundary layer, simplifying the representation of the effect of the ship deck on the rotor wake (simplified ground effect) and assuming some sort of one-way coupling in modelling interactions between ship/helicopter aerodynamics and dynamics.

Alpman, Bridges *et al.* [24, 25] demonstrated the importance of the coupling on the pilot workload by performing several coupled simulations, using three different strategies: uncoupled, one-way coupled and two-way coupled (Figure 1.15). Uncoupled simulations refer to separate computations with an absence of interference from one solution to the other. In the case of a one-way coupling, the effect of only one simulation is added to the other, usually the effect of the ship wake on the rotor aerodynamics. To achieve two-way coupling, both solutions must be mutually dependent. In every case, a pilot model is used to update the helicopter controls at

each time step and a blade element model combined with a pilot/flight-mechanics model provides the helicopter attitude (Configuration referenced as Type-4 in table 1.3). The information on the blades loads and position is reused by the CFD code to recompute the ship airwake. The figures clearly show the difference between a two-way coupled simulation and a one-way coupled or uncoupled simulation. However, the improvements gained through the use of the two-way coupling are difficult to assess when compared with an actual pilot response.

1.2.6 Flight Simulations

Real-time piloted flight simulations of rotorcraft operating in the vicinity of ships are of great interest, especially to support the training of future pilots and the definition of Ship/Helicopter Operational Limitations. Flight simulation environments implement a flight mechanics model to reproduce the behaviour of a given aircraft. It predicts the aircraft attitude from values of the flowfield velocity taken at defined locations on the aircraft body and blades (Figure 1.16). To take into account the presence of the ship, the airwake is usually implemented through look-up tables. These tables can be extrapolated from at-sea measurements, CFD calculations, wake models, etc. and therefore do not take into account the modifications of the flowfield due to the presence of the helicopter [8].

Several publications report the implementation of computed ship airwake into a flight simulation environment [8, 11, 22, 26–28].

1.2.7 Presence of Atmospheric Boundary Layer

Boundary conditions are of major importance for the solver as they provide the necessary information about the flow. For most external-flow cases, the outer boundary of the domain is purposely located far away from the object so that the fluid can be considered as uniform without affecting significantly the results.

For hovering-rotor flow simulations, the wake remains strong even far from the blades. In that case, the simple momentum theory provides the tools to impose the more accurate Froude boundary condition: the distribution of velocity around and downstream from the rotor is calculated depending on the rotor thrust coefficient, and includes the wake contraction. It prevents the flow from recirculating inside the domain. The far-field and upper boundary conditions are determined by modelling the rotor as a source-sink point and corrected to ensure mass conservation.

Near the walls, the boundary condition has to impose a no-flux condition in the normal direction to the wall. Depending on the case, a zero-velocity or slip condition

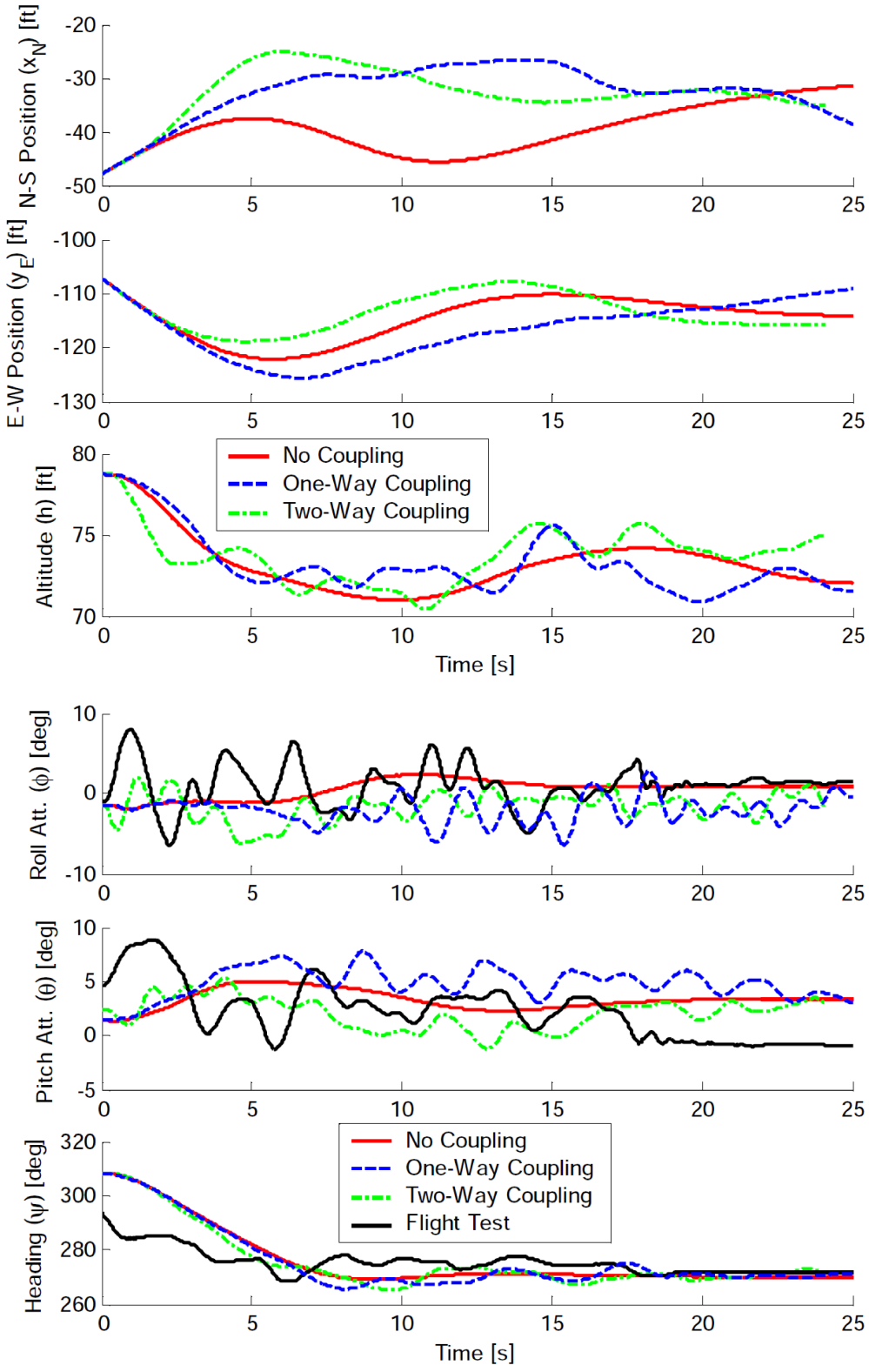

Figure 1.15: Time history of helicopter flight parameters for three different coupling. The helicopter is hovering at 50ft over the ground in a hangar airwake (from Bridges [25])

can be imposed to the tangential velocity.

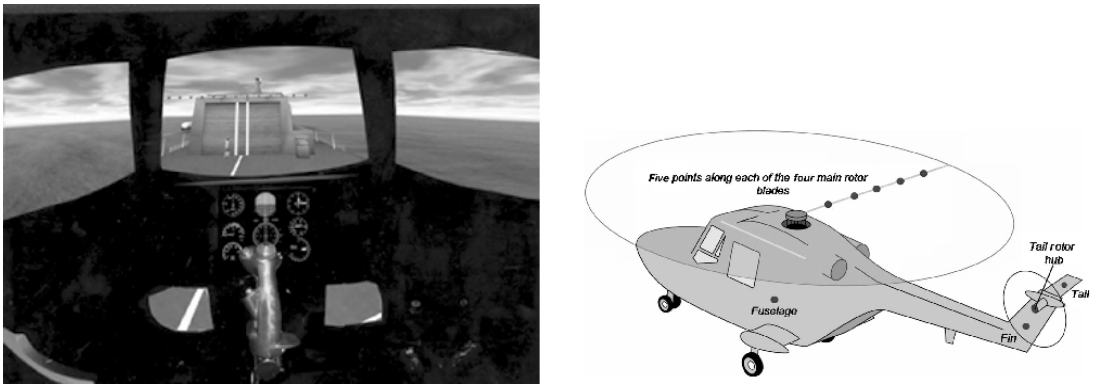

Figure 1.16: Liverpool university flight simulator and example of aircraft model air-load computation points (from Hodge [22])

The thickness of the boundary layer is a function of the distance of travel and become very thick in the case of atmospheric boundary layer over the sea The ABL has a favourable impact on the overall problem of the ship wake since it reduces the wind velocity over the flight deck. The typical boundary layer thickness is about 300m to 1km deep and at 5 meters above the water, the wind velocity is about 20% smaller than at 25 meters [29].

Some more details on modelling atmospheric boundary layer profiles are given in section 4.10.1

1.3 Experimental Works

As discussed previously, different models of ships have been considered with various levels of complexity and detail. The SFS and SFS2 models aim to give generic, easy to reproduce, geometries for the study of ship/helicopter interaction. However, Lee and Zan [9] mention that both pilot feedback and wind tunnel experiments report a higher unsteadiness behind small elements (such as weaponry, antennas and parts of the superstructure) that can affect significantly the handling qualities and it is believed that a realistic ship model is necessary to produce realistic SHOL data. The Canadian Patrol Frigate (CPF) and Landing Helicopter Assault ship (LHA) geometries are much closer to real ships, with only the smallest features removed.

Simple Frigate Shape (SFS & SFS2)

Some of the latest work on the modelling of the ship/helicopter dynamic interface had been carried out under the auspices of The Technical Co-operation Programme (TTCP) with participants in 4 countries: United Kingdom, Canada, Australia and United States

[12]. The aim of this programme is to expand the general knowledge in modelling the Dynamic Interface (DI) by conducting series of experiments and CFD computations and producing a validation database.

The development of accurate dynamic interface models could permit to conduct realistic flight simulations, for training or definition of the Ship/Helicopter Operational envelope [3]. To reach this goal, two simplified models of frigate (Simple Frigate Shape - SFS and SFS2) were created and the geometries made available (Figure 1.17). Experimental data have been produced for the SFS and its successor, the SFS2 and widely used for validation purposes.

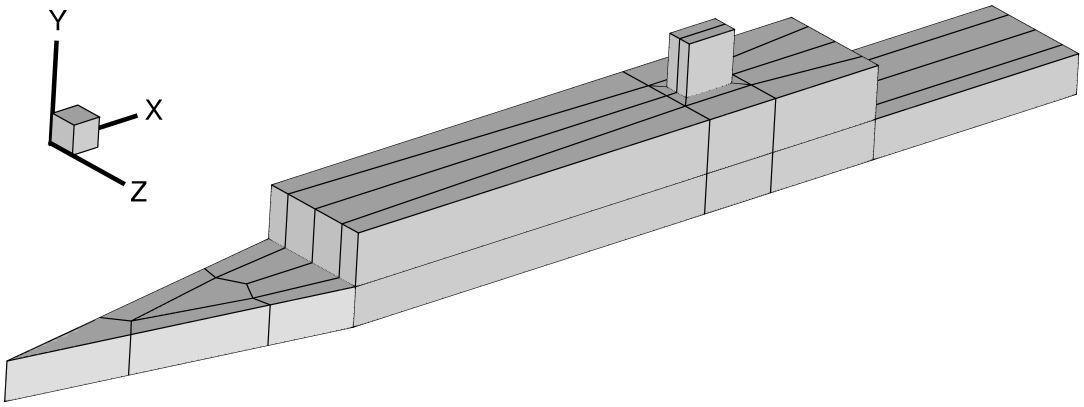

Figure 1.17: Geometry of the Modified Simple Frigate Shape (SFS2)

Most of the experimental work on the SFS and SFS2 models has been carried out in Canada by Cheney and Zan [30,31] and more recently by Landman *et al.* [32,33] at the Old Dominion University.

Cheney and Zan [30,31] performed wind tunnel tests at the National Research Council (NRC) in Canada successively on a 1:100 scaled SFS (Simple Frigate Shape) and SFS2 (Modified Simple Frigate Shape) models. Experimental data includes surface flow visualisations and hot-wire off-body velocity measurements (with mean and unsteady values), in particular over the deck. Results provided a database of experimental data for a simple geometry, useful for the validation of numerical methods. However, the geometry of the ship model was too simplified to provide a realistic ship wake topology.

More recently, Nacakli, Landman and Doane [32,33] from the Old Dominion University, re-used the SFS geometry to perform wind tunnel experiments. They extracted PIV data over the landing deck of the isolated SFS, around an isolated 4-bladed rotor and the same rotor at different positions over the flight deck (Figure 1.18).

The presence of the rotor downwash proves to have a strong impact on the size

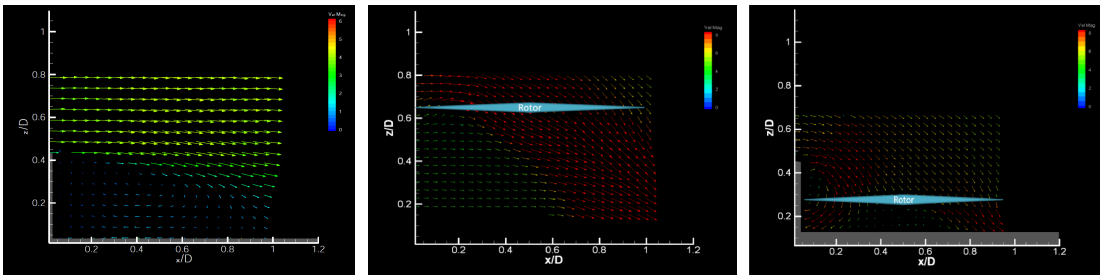

Figure 1.18: PIV fields of the flow around the isolated ship, isolated rotor, and rotor near the deck, $V_\infty = 5.14 m.s^{-1}$ (from Nacakli *et al.* [32])

of the recirculation region aft the hangar. Close to the flight deck, the proximity to the ground coupled with the re-ingestion due to the presence of the hangar door and the low streamwise flow component lead to a much higher thrust coefficient. The survey on the ship in isolation shows that the flow reattaches about half-way along the flight deck, this result is commonly admitted for the flow around this model [4,34].

Nacakli *et al.* also give a view of the flow topology around the flight deck (Figure 1.19)

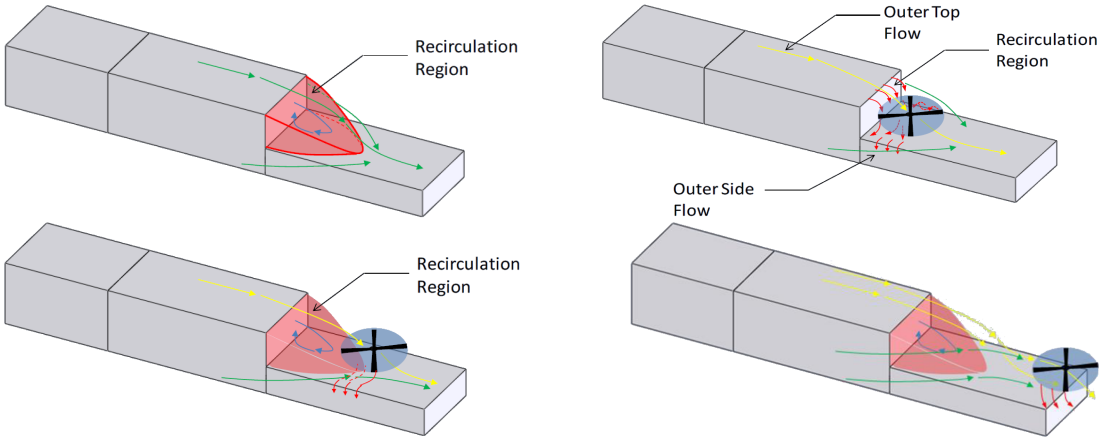

Figure 1.19: Flow topology around the flight deck of the SFS for different rotor positions (from Nacakli *et al.* [32])

Considering the size of the experimental set-up, many simplifications have been made: the rotor used is a model-scaled 4-bladed propeller and hence has fixed pitch and no flapping and lead-lagging freedom. Moreover, experiments are conducted at high-rotational speed: the thrust coefficient is realistic but the advance ratio is very low. Despite the rotational speed, the Reynolds and Mach numbers are below what is usually encountered on a real rotor blade.

Canadian Patrol Frigate (CPF)

More extended experimental data was also produced on a more realistic model of a CPF (Figure 1.20), with or without a helicopter model upon the flight deck.

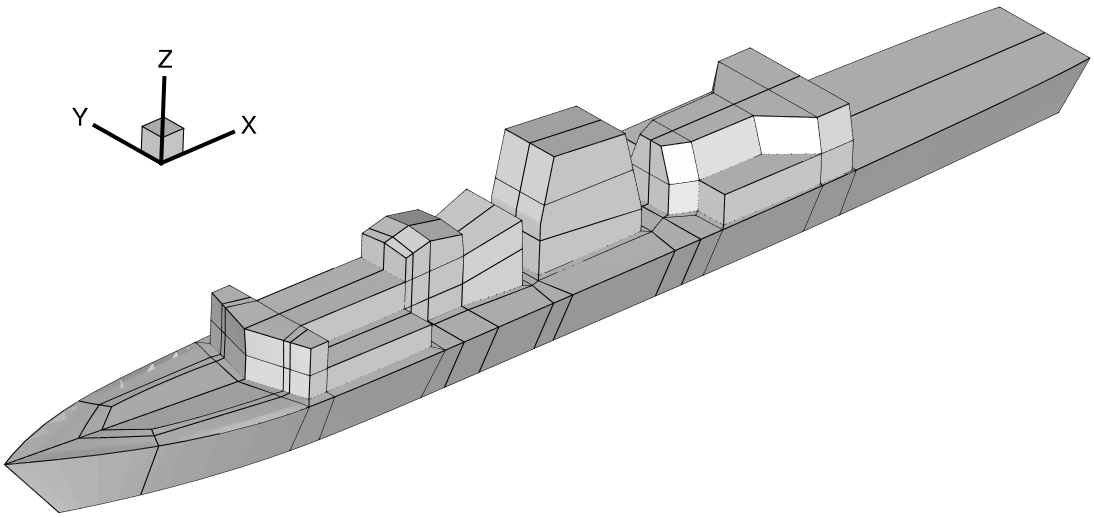

Figure 1.20: Geometry of the Canadian Patrol Frigate (CPF)

Wind tunnel experiments were conducted by Zan [35] at the Aerodynamics Laboratory of the National Research Council of Canada in 1998. The 1:50 scaled model of the Canadian Patrol Frigate was tested at two different WOD angles: 0 and 12 degrees and the flow field is mapped using hot-film anemometry in the vicinity of the ship. The atmospheric boundary layer was taken into account. The time-averaged results are compared with at-sea trials and a CFD computation using a Navier-Stokes solver that also take the atmospheric boundary layer into account.

It is shown that the turbulence intensity raises by up to 20% on the flight deck with length scale of about one rotor radius. It is reported that the blade sections of a rotor in the vicinity of the ship might therefore experience variations in the local angle of attack of up to 2.5 degrees, contributing in increasing the pilot workload and vibrations. Wind tunnel experiments show reasonable agreement with the at-sea trials and are comparable with the CFD results.

Between 2002 and 2005, Zan and Lee [9,29,36] performed a series of experiments in wind tunnel re-using the CPF. A scaled model of 4-bladed rotor as well as a CH-124 Sea King fuselage and its 5-bladed rotor were mounted on a dynamic balance in the vicinity of the ship. The atmospheric boundary layer is still taken into account and several Wind Over Deck (WOD) conditions are covered between -25 and 25 degrees. The loads are extracted for the fuselage only [9], the rotor only [29] and both [36]. The frequency analysis of the drag force, side force and yawing moment show that an

important part of the unsteadiness is comprised between 0.2 and 2 Hz (Full-scale) for a wind speed of 44 knots (Figure 1.21).

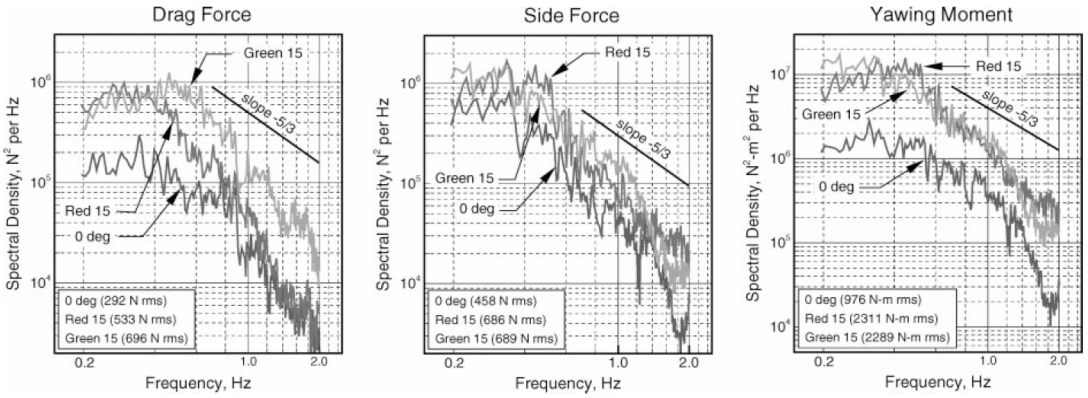

Figure 1.21: Typical full-scale spectral densities of RMS loadings for the CPF in wind tunnel (from Lee *et al.* [9])

The effects of the wind direction on RMS values of the loads clearly show that the unsteadiness of the flow increases with the WOD angle.

Thrust coefficient contours maps are available for the experiment with the rotor only. Results show that the effect of the wind direction on the thrust coefficient is significant. The partial ground effect also plays a key role as the thrust coefficient varies by about 10% during a lateral translation at 9 meters above the flight deck.

Again, due to the size of the experimental set-up and the high rotational speeds, a lot of limitations can be found: the rotors used are not articulated or based on a real geometry, the blade's Reynolds number does not match the full scale conditions, the advance ratio is irrealistically low. In case of the isolated 4-bladed rotor, the Mach number is too low as well as the thrust coefficient but this has been corrected on the 5-bladed rotor.

Landing Helicopter Assault Ship (LHA)

NASA Ames Research Center, Yamauchi *et al.* [37–41] performed series of experiments including PIV measurements on a model of Landing Helicopter Assault ship (LHA) (Figure 1.22) and different VTOL aircraft.

In 1999 during shipboard compatibility trials on the deck of a LHA-class ship, a V-22 Osprey experienced an uncommand roll in response to another aircraft landing upwind. This problem was classified as a problem to resolve before operational deployment. To investigate the problem, Yamauchi *et al.* [37–42] performed series of experiments at NASA Ames research center on a 1:48 scale models of helicopter and a LHA-class ship (Figure 1.23).

Figure 1.22: Model of the Landing Helicopter Assault ship (LHA) used at NASA Ames Research Center

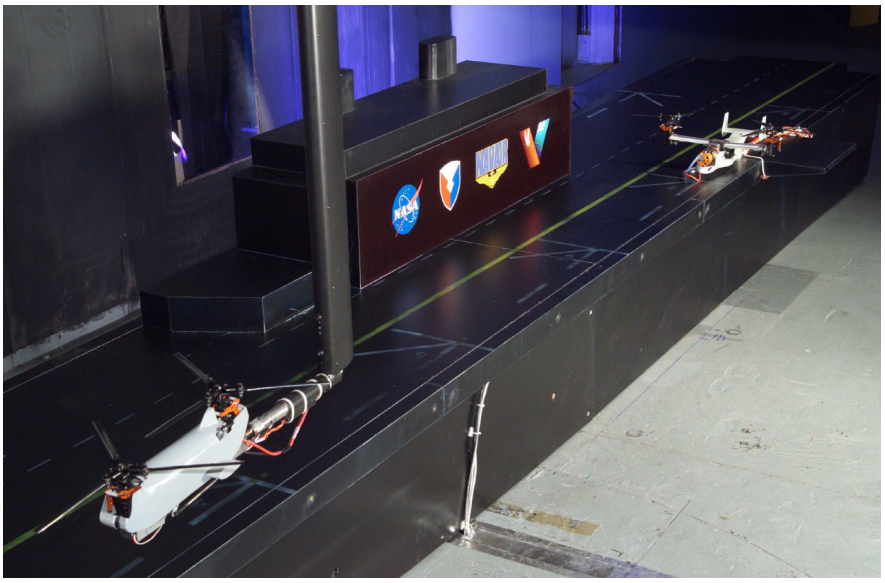

Figure 1.23: Example of experimental set-up for the study of the interaction between a tandem-rotor and a tilt-rotor on the deck of a LHA-type ship (from Rajagopalan [42])

Two scaled models of V22 Osprey tilt-rotor aircraft were first built to study their mutual interaction when flying close to each other and to a superstructure (buildings, ground) [39,41]. The models use articulated hubs that allow the modification of the collective angle. They are both mounted on a load balance and three scenarios are examined: flight level, tandem operations near the ground and single tilt rotor in winds.

The interactions between the two models show a maximum in rolling moment when the left (right) rotor of the upstream aircraft is exactly aligned with the right (left) rotor of the downstream aircraft as well as a significant reduction of the thrust coefficient when the downwind aircraft is directly behind the upwind aircraft. These

effects tend to decrease when the distance between both aircraft increases.

The results for the thrust of the upwind aircraft near the ground show that the distance to the ground has a direct impact on the thrust (ground effect) for hover and low advance ratio and this phenomenon disappears progressively with higher advance ratios (Figure 1.24). The wake tends to spread near the ground and impacts the downwind aircraft further outboard compared to the forward flight case.

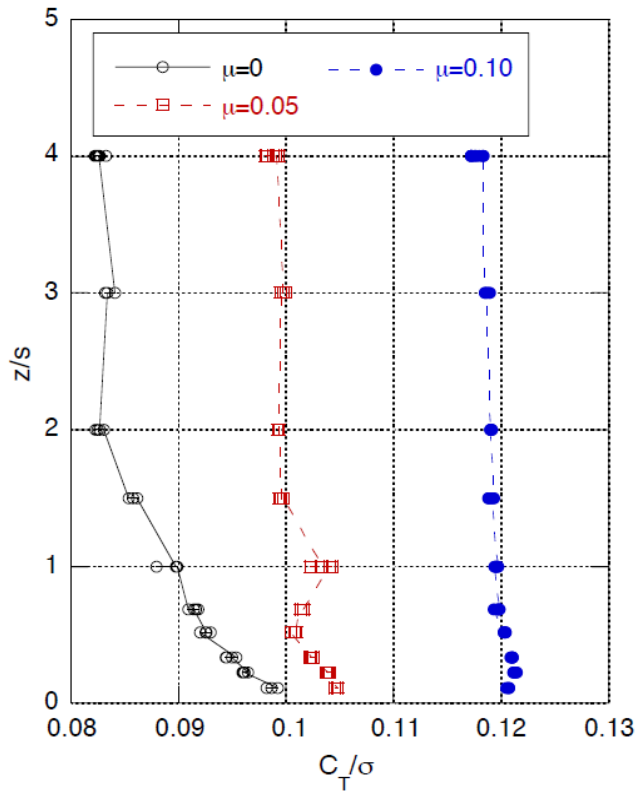

Figure 1.24: Effect of advance ratio on the thrust coefficient in ground effect (from Yamauchi *et al.* [39])

Later on, experiments were conducted on different helicopter configurations (simple, tilt-rotor and tandem-rotor) and with or without a low-fidelity model of LHA to study the problem of uncommand roll response due to another aircraft operating upstream. PIV data were extracted for different WOD conditions. They consist in maps of the instantaneous flow field, orthogonal to the wind axis, with or without the aircraft models, located at the deck landing spots. The roll moment is also extracted as it is the subject of the study. Critical configurations were found for specific positions of the upwind aircraft and were used to help solving the initial problem.

The results show the structure of the flow field induced by the presence of the upstream aircraft as well as the importance of the WOD angle (Figure 1.25).

The aircraft and ship geometries are only slightly simplified compared to the

full-scale vehicles; in particular, the rotors solidity is preserved and the advance ratios considered are realistic. However, both Reynolds and Mach numbers are still lower than expected in reality.

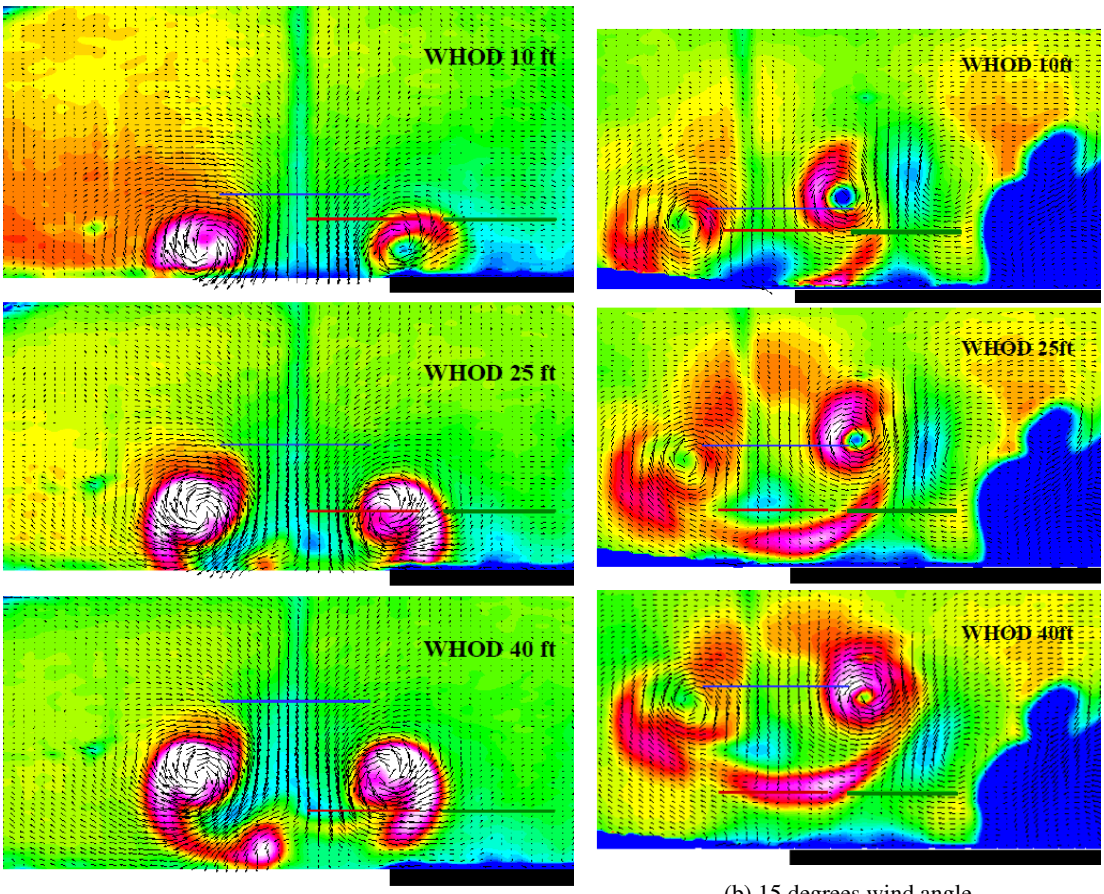

(a) 0 degrees wind angle

(b) 15 degrees wind angle

Figure 1.25: PIV maps behind a CH-46 in hover near the LHA flight deck (black area) at 35 knots for WOD angles of 0 and 15°. WHOD stands for Wheels Height Over Deck (from Silva *et al.* [37])

1.4 Computational Studies

1.4.1 Ship Airwakes

Many CFD computations on ship airwakes have been performed in the perspective of improving the accuracy of flight simulations. The velocities computed for various flow angles using CFD are usually compiled into "look-up" tables or modelled using simplified methods to be used as an input by the flight simulator to predict the helicopter behaviour in real time. The methods used do not take into account the coupling between the ship airwake and the rotor as they compute the ship airwake separately.

Model	References	Experimental conditions				Rotor data					Remarks
		Scaling	Velocity	Re	Wind angle	RPM	$M_{0.75}$	Re	μ	Characteristics	
SFS/SFS2	NRC, Cheney and Zan [30, 31]	1:60, 1:100				/	/	/	/	/	Wind tunnel experiments with flow visualisations and hot wire measurements.
SFS	ODU [a] Nacakli *et al.* [32, 33]	Length 1:50	5.14m/s	72000	0°	5000	0.1425	/	0.077	0.25m diameter	Wind tunnel experiments with rotor. Particle Imaging Velocimetry (PIV) survey of isolated SFS, isolated rotor and coupled system. Provides good validation data. Small experimental set-up, uses a model-scaled 4-bladed propeller, not articulated. SFS geometry too simple to provide realistic data. Low Reynolds number.
CPF	NRC [b], Zan [35]	Length 1:50, Speed 1:5, Frequency 10:1	5.8(28.8) m/s [c]	$30 \cdot 10^6$ FS, $107 \cdot 10^3$ WT	0° and 12°	/	/	/	/	/	Wind tunnel experiments with hot film anemometer measurements sampled at 100Hz. Small experimental set-up, Reynolds number does not match full-scale. Comparison with sea trial data at 20 and 30 knots but suffers from insufficient time averaging.
CPF + 4-bladed rotor	NRC, Zan [29]	Length 1:50, Speed 7:10, Frequency 35:1	7.2(10.3) and 19(27.14) m/s	/	/	11000 (313)	$M_{0.75} = 0.35$	$Re_{0.75} = 105 \cdot 10^3$	0.044646 / 0.118	Clark Y airfoil, 14° twist, 0.28m diameter, (chord calculated from Re: 15.4mm, AR: 9.03)	Wind tunnel experiments. Measurements of the thrust coefficient in the vicinity of the ship. Sampling at 100Hz for 10s. Small experimental set-up: Reynolds and Mach numbers do not match full-scale, C_T and μ too low.
CPF + CH-124 Sea King fuselage	NRC, Lee and Zan [9]	Length 1:50, Speed 5:4, Frequency 62.5:1	28.35(22.68) m/s	$Re_b = 10^6$	−25° to 25°	/	/	/	/	/	Wind tunnel experiments. Measurements of the loads (drag, side, yaw) on the fuselage in the ship airwake. Sampling at 1kHz for 34s (WT).
CPF + CH-124 Sea King fuselage + 5-bladed rotor	NRC, Lee and Zan [36]	Length 1:50, Speed 1.1:1, Frequency 55:1	up to 28.35(25.77) m/s	10^6	−45° to 45°	11200 (203.6)	/	$Re_{0.75} = 165 \cdot 10^3$		NACA 0012 airfoil, 0.378m diameter, 20mm chord, AR: 9.45	Wind tunnel experiments. Measurements of the loads (drag, side, yaw) and thrust on the rotor+fuselage in the ship airwake. Sampling at 1kHz for 34s (WT). Mach number and C_T match the full-scale values. Reynolds number and μ are too low.

Table 1.4: Summary of ship airwakes and shipborne rotors experiments

[a] Old Dominion University, US

[b] National Research Council, Canada

[c] First number denotes wind tunnel conditions, number between parenthesis denotes full-scale equivalent

Model	References	Experimental conditions				Rotor data					Remarks
		Scaling	Velocity	Re	Wind angle	RPM	$M_{0.75}$	Re	μ	Characteristics	
V-22 models	NASA Ames, US. Yamauchi *et al.* [39] and Johnson *et al.* [41]	Length 1:48	0, 13.15, 26.3 ft/s	/	0°	6355	0.17475	$Re_{\text{tip}} = 63 \cdot 10^3$	$0, 0.05, 0.1$	See table 1.6	Wind tunnel experiments of two tilt-rotor in interaction with and without ground effect for different relative positions. Thrust and roll moments measurements, oil and tuft flow visualisation (in ground effect). Realistic values for the rotors (σ, μ). Mach and Reynolds numbers too low.
LHA + V-22,CH-46,CH53 models	NASA Ames, US. Silva *et al.* [37]	Length 1:48	(up to 40 knots)	/	0°	See table 1.6					Wind tunnel experiments with PIV survey and rolling moment measurements for the different aircraft (V-22,CH-46,CH53) and a LHA models. Realistic values for the rotors (σ, μ). Mach and Reynolds numbers too low.
LHA + CH-46 models	NASA Ames, US. Wadcock *et al.* [38]	Length 1:48	14.1 to 25.3 ft/s (25 to 45 knots)	$\sim 2 \cdot 10^5$	0° and 15°	See table 1.6					Wind tunnel experiments with PIV survey for the isolated LHA and LHA with on-deck CH-46. Realistic values for the rotors (σ, μ). Mach and Reynolds numbers too low.
LHA + V-22,CH-46 models	NASA Ames, US. Rajagopalan *et al.* [42]	Length 1:48	19.7 ft/s (35 knots)	$\sim 2 \cdot 10^5$	0°	See table 1.6					Wind tunnel experiments with PIV survey of the different aircraft (V-22,CH-46) and a LHA models and comparison with numerical results. Realistic values for the rotors (σ, μ). Mach and Reynolds numbers too low.

Table 1.4: **Continued -** Summary of ship airwakes and shipborne rotors experiments

	V-22 Osprey	**CH46**	**CH-53E**
No. of rotors	2	2	1
No. of blades per rotor	3	3	7
Rotor radius [in]	228.5	306.0	474.0
Blade tip chord [in]	22.00	18.75	29.28
Rotor solidity	0.105[1]	0.059[2]	0.138[2]
Rotor RPM (100%)	397	264	177
Tip speed [$ft.s^{-1}$]	792	705	732
Blade tip Reynolds number	$9.26 \cdot 10^6$	$7.03 \cdot 10^6$	$11.39 \cdot 10^6$

Table 1.5: Properties of full-scale aircrafts used at NASA Ames (from Derby [40])

Parameter	**Tilt-rotor**	**Tandem Rotor Helicopter**	**Single Main Rotor Helicopter**
No. of rotors	2	2	1
No. of blades per rotor	3	3	5
Rotor radius [in]	4.687	6.311	10.220
Blade tip chord [in]	0.446	0.375	0.854
Rotor solidity	0.102[1]	0.057[2]	0.133[2]
Rotor RPM (100%)	6355	4224	2831
Tip speed [$ft.s^{-1}$]	260	233	252
Blade tip Reynolds number	61,616	46,366	114,604
Motor design speed [RPM]	12,313	4,224	11,324
Gear ratio	1.9375	1.0	4.0
Design power (with 25% margin) [W]	251	69	304

Table 1.6: Properties of equivalent scaled models used at NASA Ames (from Derby [40])

Simple Frigate Shape (SFS and SFS2)

Several papers report simulation attempts conducted on the SFS and SFS2 geometries. In 2008, Syms [43] performed numerical simulations on the SFS2 model using the Lattice-Boltzmann flow solver PowerFLOW. Results are compared with the experimental data from NRC [31]. The time-averaged results at 0 degrees yaw show good agreement both for the flow field on the flight deck (comparison with flying hot-film velocity data) and for the surface flow topology (comparison with oil flow visualisations). At 45 degrees yaw, the flow topology seems to be accurately predicted but the numerical results show higher mean velocity gradients and RMS values, probably due to a lack of dissipation in the solver.

Several studies were carried out at the University of Liverpool, using the SFS and SFS2 models. In 2005, Roper *et al.* [8,26] performed steady-state simulations of the flow around both models using the commercial CFD code Fluent. Results are then compared with data from NRC [30,31]. The results for pressure coefficient and velocities on the SFS show good agreement with the experimental flow visualisations (surface oil flow and off-surface smoke patterns). Simulations of the flow around the SFS2 were conducted and the results were implemented into a flight simulator as ”look-up” tables. Piloted trials have been carried out for different WOD angles and a SHOL diagram was plotted. It is reported that the lack of unsteadiness in the flow led in lower workloads than are normally experienced at sea.

The results highlighted the necessity of a time-accurate ship airwake to accurately predict the pilot workload. Computations were performed on the SFS2 using Fluent for two WOD angles and the results integrated into the FlightLab environment as previously. Pilots reported a workload higher than expected, suggesting that the wake unsteadiness was over-estimated and the accuracy of the computation should be assessed. However, it was found that the measured pilot activity correlated with the subjective workload rating given by the pilot, and the method may allow to extrapolate SHOL plots without depending on the pilot feedback, in particular when using a pilot model.

More recently, Forrest and Owen [34] investigated the airwake behind the Simple Frigate Shape (SFS2) and the T-23 frigate using Detached Eddy Simulation (DES) for different wind angles.

The SFS2 results were compared with experimental data from NRC and show good accuracy for both the mean velocities and turbulence intensities in each directions. Plots of Power Spectral Density (PSD) show good agreement for both level and frequency roll-off (Figure 1.26). The flow topology seems accurately predicted

when compared with experimental smoke visualisations.

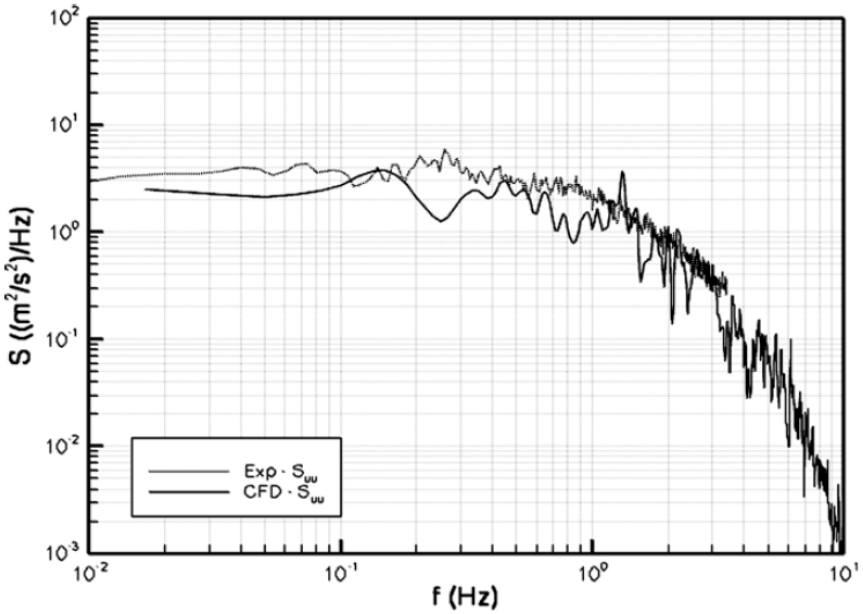

Figure 1.26: Power Spectral Density of longitudinal velocity over the SFS2 flight deck (from Forrest *et al.* [34])

As mentioned previously, such simple geometries are useful for validation purpose but can not pretend to represent a realistic scenario. The Type-23 frigate geometry is much closer to the geometry of a real ship, with only the smallest details removed such as antennas and weaponry. Differences are found between the very simplified SFS2 and the T23: smaller “turbulent” structures and less complex interaction between large-scale vortices. The assymetry in the geometry also impacts significantly the topology of the flow around the flight deck. The results are compared with full-scale at-sea testings and show good agreement, especially when the atmospheric boundary layer is taken into account in the simulation. As a conclusion, the study recommend the use of realistic models for CFD airwake simulations.

Following the work of Forrest and Owen, Kàària *et al.* [11] implemented the CFD data for the SFS2 into the FlightLab environment. The loads on the aircraft are calculated at different positions over the flight deck and the RMS values are calculated within the bandwidth 0.2-2Hz. Results show that the drag force, side force and yaw moment are more important for a 30 degrees green wind compared to a headwind. The value of the thrust coefficient plotted along a lateral line show the ”Deck effect”, with variations up to 10% between two positions.

Canadian Patrol Frigate

Two simulation attempts were conducted by Zan in 1999 [35] and Syms *et al.* in 2004 [10]. The steady states simulations both use the CFD-ACE solver and the atmospheric boundary layer is taken into account. Results show important discrepancies between wind tunnel experiments and at-sea trials as well as between wind tunnel data and CFD data. The first study points out that minor changes in the ship geometry affected significantly the results and the second one explains the discrepancies by the fact that steady simulations are not equivalent to time-averaged unsteady simulations.

Landing Helicopter Assault (LHA)

In 2001, Polsky and Bruner [44] performed both steady and unsteady simulations of the flow around a LHA model using the CFD code COBALT and a LES model. The numerical results are compared with experimental data collected at NASA Ames via velocity measurements. It was shown that the time-averaged results of the unsteady simulation compare very well with the experimental data when the steady state CFD show more discrepancy and are then not suitable for the study of highly unsteady flows. Comparison with full-scale data also showed that the LES simulation can predict the dominant frequencies in the flow where a $k-\omega$ model fails. Computation were conducted for two different wind speeds corresponding to two different Reynolds numbers; the results are very similar, showing again that for the Reynolds numbers of interest, the flow is largely Re independant.

The CFD data produced by Polsky and Bruner [44] has been implemented by Bunnell [45] in a blade-element model of a UH60 helicopter and the integrated simulation was used to simulate shipboard landings in the Vertical Motion Simulator at NASA Ames. This technique permits to create a realistic simulation environment, in particular to replicate the increase in pilot workload due to the flow unsteadiness.

Lee *et al.* [28] used the CFD code PUMA2 to compute the unsteady flow around the LHA and implemented the results into a flight simulation code which includes a model of UH60. A maneuver controller is used to simulate the pilot input. The results show the impact of the time-varying flow-field on the helicopter attitude and thus on the pilot workload.

1.4.2 Manoeuvre Simulations

Various multi-body dynamics comprehensive tools have been developed such as HOST (Eurocopter), CAMRAD II (Johnson Aeronautics), MBDyn (Politecnico di Milano),

Model	References	Solver	Numerical conditions		Wind angle	Remarks
			Method	Re		
SFS2	NRC, Syms [43]	PowerFlow	Lattice-Boltzmann, VLES	$500 \cdot 10^3$	0° and 45°	Comparison with surface visualisations and hot-wire measurements from [30,31]. Results compare well but the geometry is too simple to represent a realistic scenario.
SFS / SFS2	Liverpool University, UK. Roper *et al.* [8,26]	Fluent	Unstructured, Steady and unsteady, SIMPLEC algorithm with $k-\varepsilon$ and $k-\omega$	$20\,m.s^{-1}$ $17 \cdot 10^6$	−90° to 90° (SFS) 0° to 360° (SFS2)	Comparison with hot-wire measurements from [30,31]. Implementation of the results in FlightLab. Too simple geometry. Steady simulation unrealistic for this type of highly unsteady flow
SFS2 / Type-23	Liverpool University, UK. Forrest and Owen [34] and Kaaria *et al.* [11]	Fluent	DES, $\Delta t = 0.0188s$ (normalised by free-stream and beam)	$22.6 \cdot 10^6$	0° and 45°	Comparison of SFS results with smoke visualisations and hot-wire measurements from [30,31]. Comparison of T-23 results with at-sea testings. Implementation of the results in FlightLab.
CPF	NRC, Syms [10]	CFD-ACE	Steady, SIMPLEC algorithm with $k-\varepsilon$	/	0° and 12°	Comparison with hot-film anemometry data from Zan [35]. Boundary layer modelled. Steady simulation, results show important discrepancies.
LHA	Naval Air Warfare Center, US. Polsky and Bruner [44]	Cobalt (no precondi-tionning, Mach number set to 0.15 ∼ 0.2)	unstructured, Laminar RANS and LES, $\Delta t = 0.01s$ (frequencies up to 40Hz)	/	−90° to 90°	Comparison with wind tunnel and full-scale data. The steady simulation shows important discrepancies.

Table 1.7: Summary of ship airwake simulations

UMARC (University of Maryland), CHARM/RCAS (US Army). They include blade aero-elasticity, advanced wake modelling, empirical corrections and the low computational cost allows for the simulation of complex flight conditions, even in real time. However, some effects are not directly captured which are captured by the CFD: blade-vortex interaction, main/tail rotor interaction, main rotor/fuselage interaction, dynamic stall, etc.

Typically, comprehensive tools are used to predict the helicopter and rotor system states that are then used as baseline state for CFD simulations, although consistency between the two results can be obtained only by coupling the methods. A lot of work has been done in coupling CFD and comprehensive tools particularly for accurately predicting the rotor blade motion and deformation. Depending on the objective, different levels of coupling may be used. In the case of a weak/loose coupling, information is exchanged in a not time-accurate manner, usually every revolution. The concept of (very) strong/tight coupling requires that the two problems work with the same time-scales. Typically, data is exchanged at every time step or Newton steps of the CFD solver, so as to ensure consistency between the two methods. Weak coupling is sufficient to determine the trim state of a rotor system for a given flight condition but strongly coupled, time-accurate simulations are required if the system has no time-periodicity, such as during manoeuvres.

Rotorcraft blades are highly flexible elements and the deformations need to be taken into account using dedicated Computational Structural Dynamics (CSD) codes to predict the aircraft performance accurately. Numerous studies aimed at including blade aero-elasticity to a CFD solver to account for deformations in flapping, lead-lag and twist. To achieve CFD/CSD coupling, a finite element model is built to model the blades structural properties. The increased complexity of the system usually leads to longer convergence time but contributes to creating a model that better represent the real system.

Ananthan *et al.* [46] interfaced the UMARC code with two CFD codes, OVERTURNS and SUmb, in a loosely-coupled fashion and added acoustic predictions to the simulations of the SMART Rotor (Smart Materials Actuated Rotor Technology). The test case includes trailing edge flaps and experimental data was collected by DARPA/NASA/Boeing/Army in 2008. Results show good agreement, although the study focuses primarily on noise prediction.

The case of the UTTAS pull-up manoeuvre is frequently reported in the literature [47–49]. The manoeuvre was performed using an instrumented UH60 helicopter and is of great interest as it extends outside of the aircraft flight envelope. During the

manoeuvre, the aircraft experiences up to $2.1g$ acceleration with important stall events and transonic flow regions on the blades. In a key study from Baghwat *et al.* [48], the 40 revolutions of the UTTAS pull-up manoeuvre are analysed, in terms of blade loading, rotor hub forces and moments, blade flapping and lead-lag behaviour, pushrod and lag damper forces. The standalone RCAS code implementing a lifting line method and dynamic inflow model was compared with the coupled RCAS/OVERFLOW2 method. The coupled method consistently reduces the discrepancy with the experimental data, mainly due to the fact that it is a fast, highly loaded manoeuvre, with stalled and transonic flow regions that are poorly predicted using the lifting line theory. However it is noted that CFD does not always capture these effects and the improvements it offers may be more or less significant, depending on the flow conditions. Improving the grid and the turbulence modelling may further improve the results. The paper also concludes that quasi-steady simulations reproducing some specific instants of the manoeuvre gave good results at a much reduced computational cost. However this is based on the fact that the conditions of the flight are known, being derived directly from the experimental data. In case of a blind-test manoeuvre, the full simulation is still required. The simulations were carried out for the main rotor only: both the fuselage and the tail rotor have been ommited. By alleviating interactional effects, the simplification reduces the accuracy of the simulation, especially on the prediction of blade flapping at peak loading.

Abishek *et al.* [49] also studied the UTTAS pull-up manoeuvre using the UMARC/OVERFLOW2 coupled CFD/CSD method by predicting deformations from measured airloads and using these deformations for lifting-line and CFD analyses.

The control angles are determined *a priori* using the lifting line method, in an iterative fashion, to obtain the forces and moments recorded during the campaign. The study focuses on capturing and explaining dynamic stall events that occur the high-loading phase of the manoeuvre. Interestingly, the CFD simulations were performed in a non-inertial frame of reference and therefore the inertial effects are added to the Navier Stokes equations as a source term.

Masarati *et al.* [50] developed a multidisciplinary multi-body framework designed to handle multi-physics problem by interfacing any external code. The method found applications for rotorcraft studies: modelling of pilot arm dynamics, flapping wing fluid/structure coupling but has not been applied to helicopter rotor systems in manoeuvring flight as of yet.

Yu *et al.* [51] coupled the CHARM and RCAS analytical tools to combine the fast lifting surface method, free-wake and panel fuselage models of CHARM with the

deforming rotor system of RCAS. Increased accuracy is found by using CHARM's advanced methods over simple aerodynamic tables and lifting line theory. The method also benefits from being more computationally efficient than CFD.

Beaumier *et al.* [52] and Servera *et al.* [53] of ONERA coupled the HOST method with the CFD code elsA to include blade motion and aero-elasticity into the simulation. Results were compared against experimental data available for the 7A/7AD rotor. Weak "once-per-revolution" and strong "once-per-time-step" coupling methods were investigated. Similar results were reported in terms of rotor trim condition and the weak coupling is shown to converge more efficiently. However, it was noted that although the weak coupling method was good for periodic conditions, it was not appropriate for non-periodic flights.

A similar method was implemented in the HMB2 solver to couple NASTRAN and HMB2 [54]. The paper also gives an overview of the literature on CFD/CSD coupling. Results are limited to hover but show reasonable agreement with the experimental data available.

1.4.3 Coupled Simulations

As mentioned before, many factors are involved in the interaction between an aircraft and a ship. Hence, a fully-coupled simulation of the dynamic interface should include several parameters such as atmospheric boundary layer profile and turbulence levels, ship motion, pilot and flight mechanics models for the aircraft, accurate modelling of the rotor aerodynamics and blade motion. For the sake of simplicity, most of the simulation referred to as "coupled" take into account only a few of these parameters. The types of coupling defined previously (Table 1.3) are used in the following as a way of comparison.

An early attempt to compute the coupled ship airwake / helicopter downwash flow has been conducted in 1998 and 2001 by Wakefield *et al.* [4, 23]. The method used is based on the modification of the Navier-Stokes equations inside a specific area to take into account the (fictive) presence of the rotor in the CFD solver CFX (See Type-1 simulation). The modification applies a constant force to the fluid equal to the helicopter weight. The results are limited to the global flow topology and an estimate of the control and power requirements but do not describe any of the features of the actual flowfield.

More recently, a simulation of the fully-coupled interaction between the helicopter downwash and the ship airwake was conducted by Alpman, Bridges *et al.* [24, 25] in 2007 using the CFD code PUMA2 (Parallel Unstructured Maritime Aerodynamics)

for the ship wake concurrently with the helicopter flight dynamics code Genhel for the blade dynamics and loads (See Type-5 simulation). The three levels of coupling discussed above are compared together and with data from piloted simulations.

In the study, different scenarios are investigated. For the rotor in ground effect, the thrust coefficients are computed and show very good agreement with the experimental data by Zan [29]. The effect of the boundary layer on a rotor in forward flight near the ground is also quantified. The rotor is then studied in hover behind a hangar and the results show that the rotor significantly affect the oncoming velocity field. In particular, the vortices' influence on flight dynamics in case of a two-way coupling appears to be lessened as the vortices are forced down and away from the helicopter by the downwash.

The conclusions are only qualitative as many assumptions and simplifications are made. Nevertheless, the time history of the pilot input and helicopter attitude gives a lot of information and permits to point out that, even if a one-way coupling is computationally cheaper, it may be inaccurate in case of strong interaction (low velocity wind and aircraft close to the superstructure in particular). Despite the clear differences between the two levels of coupling, the superiority of the two-way coupling is not been clearly demonstrated. The flight test data results added in the second paper do not help to distinguish the improvements achieved by a fully-coupled simulation.

The work carried out by Polsky *et al.* [6, 7] [55] is of main interest for our purpose: the commercial flow-solver Cobalt has been used to simulate aircraft operations near the decks of the LHA, DDG (destroyer-class) ships and an aircraft carrier and includes a F-18, a V22 Osprey, a JSF "Harrier-like" VTOL aircraft and a H60 helicopter. Different configurations have been investigated: Fixed V22 aircraft above the LHA ship, F18 approach simulation with steady ship wake, JSF landing on the LHA and H60 hovering at different position above the DDG landing deck (Figure 1.27).

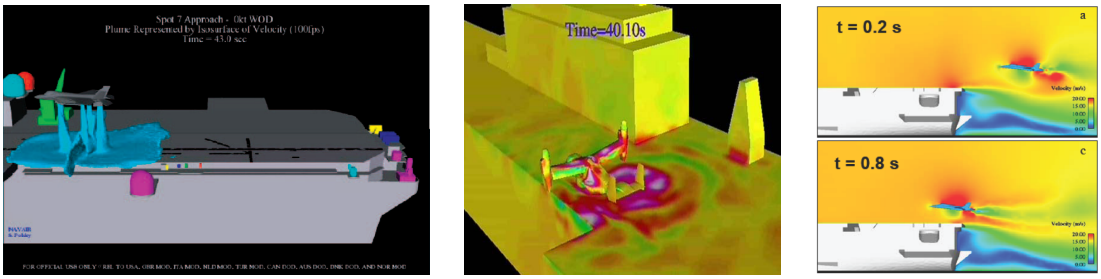

Figure 1.27: Three scenarios investigated: JSF and V22 in hover above the LHA flight deck, F-18 approaching an aircraft carrier deck (from Polsky [6, 7])

The CFD code Cobalt solves the Navier-Stokes equations on unstructured grids with an overset method for bodies in relative motion and a Large Eddy Simulation

method is used to model the turbulence as it has been proved to be well-suited for the computation of ship airwakes. In addition, the V22 and H60 rotors are modelled using an actuator-disc method (Type-2 simulation) but a blade-element method is being implemented.

The amount of data gathered throughout this programme is to be analysed using Reduced Order Modelling (ROM) methods [55] such as Proper Orthogonal Decomposition (POD) and Neural Network methods. This work could eventually permit to perform real-time fully coupled simulation.

This is the most advanced work carried out on the problem of ship/aircraft interactions. The computational cost is shown to be very important even with the simplifications made: actuator discs, no ship motion, no pilot and flight mechanics models.

1.5 Objectives

The present work aims at developing a method to study the interactional effects between ship and helicopter airwakes in the scenario of a helicopter operating in the vicinity of a ship.

The first objective is to validate the Helicopter Multi-Block (HMB2) solver developed at the University of Liverpool for the simulation of ship wakes and rotorcraft at low advance ratio. A comprehensive validation is carried out using the experimental data made available by NRC in Canada and the Georgia Institute of Technology in the US, for the Simple Frigate Shape model and by the European GOAHEAD Project for a full helicopter configuration.

The employed approach enables two-way coupled simulations where both the ship and the helicopter are solved simultaneously within the CFD. It has been coupled with a multi-body dynamics solver to provide the helicopter attitude and velocity during the simulation. Although it is possible to perform two-way coupled calculations using simplified models for the aircraft, this work focuses on using exclusively CFD and therefore modelling both the ship and the full aircraft. The relative motion between the different bodies makes use of the Chimera method for overlapping multiple meshes [56].

Capturing accurately the interactions that occur when a helicopter operates near a ship's landing deck requires unsteady simulations. The merits of various turbulence models have been assessed to find the right compromise between the accuracy of the solution and the stability and speed of the computation.

Investigating the Ship/Helicopter Dynamic Interface also requires the ability to

Model	References	Solver	Numerical conditions		Rotor model	Wind angle	Remarks
			Method	*Re*			
Helideck/Rotor	Wakefield *et al.* [23]	CFX	2D, steady	$\sim 10^7$ (30 and 60 knots)	actuator disc	/	Different positions of the actuator disc above the deck.
SFS/Rotor	Wakefield *et al.* [4]	/	3D	$16 \cdot 10^6$ (40 knots)	actuator disc	0° and 90°	Comparison of the ship airwake with smoke and oil flow visualisations from [30, 31]. Results are limited to the global flow topology, does not describe any realistic flowfield.
LHA/CH-46	Rajagopalan *et al.* [42]	Rot3DC	3D, unsteady, incompressible, laminar	19.7ft/s (35 knots)	actuator disc	0°	Comparison of the time averaged numerical results with PIV data from the same team for three different positions of the aircraft model. Numerical results compare acceptably in low WHOD but show discrepancies for higher WHOD.
Hangar and LHA / UH60 rotor model	Alpman and Bridges *et al.* [24, 25]	PUMA2 / Genhel	Coupled simulation CFD(PUMA2)/Flight mechanics(Genhel), unstructured	/	Pitt-Peters inflow + blade element theory	0° and 30°	Different levels of coupling investigated, boundary layer turbulence is taken into account by adding perturbations to the flowfield, use of a pilot model. Draw qualitative conclusions but make use of a lot of simplifications.
LHA, DDG (destroyer-class) and aircraft carrier / F-18, V22, JSF and H60 aircrafts	Polsky *et al.* [6, 7, 55]	Cobalt	Unstructured, LES	/	actuator discs	/	Fully coupled CFD simulations for different scenarios. Several simplifications are made (actuator disc, no pilot or flight mechanics). Most advanced work on ship/aircraft interaction: many scenarios investigated, realistic (although simplified) geometries.

Table 1.8: Summary of coupled simulations

simulate manoeuvring aircraft within the framework of CFD. This was achieved by implementing a versatile grid-motion method that allows articulated blade motion together with the motion of the airframe in an earth-fixed frame of reference. Simulations of the dynamic interface can be one-way coupled with one of the wakes being frozen - usually the ship's - or two-way coupled with the two wakes being resolved simultaneously. This is the preferred approach in this thesis.

The present research focuses on demonstrating the feasibility of coupling a comprehensive rotorcraft code with a CFD tool to achieve high-fidelity simulation of the challenging ship/helicopter flow interaction. While the simulation of full rotorcraft configurations and ship wakes using CFD has been demonstrated in past publications, the complexity associated to the coupling of the two wakes, and the accuracy and level of resolution required to perform manoeuvres have not been assessed. To the author's knowledge, this work is the first to attempt the simulation of manoeuvring helicopter during ship landing using a single framework to couple CFD and flight dynamics.

1.6 Novelty of the Work

CFD has seen rapid progress and acceptance as a tool for practical engineering design and development purposes. However, approximate models are still used for computationally expensive tasks. In the context of rotorcraft development, CFD is restricted to blade design and prediction of aircraft performance in steady flight conditions. This work aims at developing the tools and demonstrate the feasibility of coupling high-fidelity CFD tools and flight mechanics to solve the most complex cases, *i.e.* full helicopter configurations in manoeuvring flight. This area of work has gained traction in the past few years with the wider availability of high performance computer systems that can accommodate such expensive calculations. To the author's knowledge, no study has been published that simulate a full aircraft configuration in manoeuvring flight using a strongly-coupled Fluid Dynamics/Flight Mechanics approach. To emphasise the importance of developing such capabilities, the particularly challenging case of a shipborne landing was chosen. Simulations of the aircraft flying in the last leg of the manoeuvre, before touchdown, were performed with and without the ship wake. Although such computations are expensive in terms of CPU time, it is expected that they will provide valuable insight for future aircraft design, permit to foresee potential problems in certifying the aircraft for a particular ship and develop more accurate simulation tools for pilot training.

Chapter 2

Rotorcraft Flight Theory

In the first part of this section, first-principle mechanisms of helicopter flight are presented that take into account only basic design parameters and provide estimates of the rotorcraft performance for simple flight conditions. First principles includes considerations in terms of rotor flow momentum, blade motion, rotor inflow, distribution of lift in hover and forward flight. Despite their simplicity, these tools are still used to determine rotorcraft performance in early design stages.

In the second part, the expression of Euler's equations of motion for modelling rotorcraft fuselage and rotor blades is discussed. They are required to determine more accurately the performance of rotorcraft and simulate manoeuvring flight.

2.1 First Principle Mechanisms

2.1.1 Momentum Theory for Rotors in Hover

The momentum theory is an expression of the conservation principles and describes the rotor performance using only basic design characteristics: rotor radius, blade section, number of blades, rotational speed. It assumes a uniform, steady, incompressible and inviscid flow in a stream-tube that originates from the rotor disc as shown in figure 2.1. Under those assumptions, the principles of conservation of mass and energy permit to define thrust, torque and power coefficients, as well as flow velocity through the rotor disc [1].

For a closed surface S, we can write the conservation of mass principle:

$$\int\int_S \rho \mathbf{V} d\mathbf{S} = 0 \tag{2.1}$$

Considering the stream-tube as the reference surface, this gives an expression of the thrust:

$$T = \dot{m}(V_C + v_2) - \dot{m}V_C = \dot{m}v_2 \tag{2.2}$$

where $w = V_C + v_2$ is the flow velocity in the downstream section of the tube and V_C the climb velocity, i.e. the vertical speed of the aircraft.

The conservation of kinetic energy states that:

$$\int\int_S \frac{1}{2}(\rho \mathbf{V} d\mathbf{S})\|\mathbf{v}\| = 0 \tag{2.3}$$

This leads to a new expression for the thrust:

$$T(V_C + v_2) = \frac{1}{2}\dot{m}(V_C + V_2)^2 - \frac{1}{2}\dot{m}V_C^2 = \frac{1}{2}\dot{m}(2V_C v_2 + v_2^2) \tag{2.4}$$

This gives a relationship between the induced velocity at the disc plane v_i and the velocity in the far wake v_2:

$$v_2 = 2v_i \tag{2.5}$$

From the incompressibility hypothesis we can deduce that $A_\infty = \frac{1}{2}A_{\text{disc}}$. The wake contraction ratio is then defined by $\frac{r_\infty}{R} = \frac{1}{\sqrt{2}}$

The thrust T and power P in hover can be expressed as function of the induced velocity:

$$\begin{cases} T = 2\rho A v_i^2 \\ P = 2\rho A v_i^3 \end{cases} \tag{2.6}$$

Increasing thrust produced by unit of power spent, or power loading is done by reducing the induced velocity and hence increasing the rotor diameter:

$$\frac{T}{P} = \sqrt{\frac{2\rho A}{T}} = \frac{1}{v_i} \tag{2.7}$$

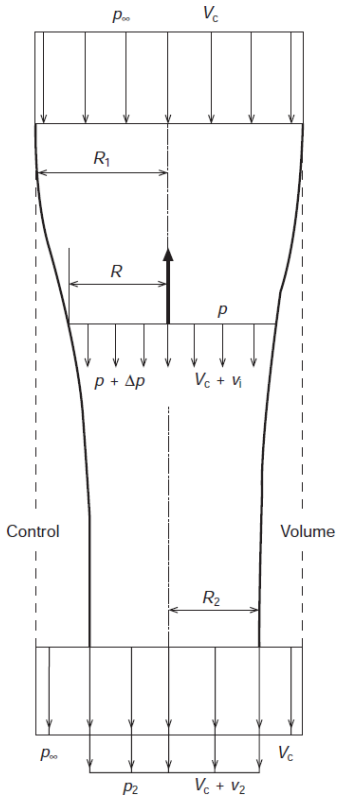

Figure 2.1: Stream tube defined by the rotor disc in axial flight. Reproduced from Bramwell [1].

The velocity of the flow through the rotor disc depends directly on the rotor radius and rotation speed. The rotor induced flow ratio in hover λ_h is given by:

$$\lambda_h = \frac{v_i^{\text{hover}}}{\Omega R} \tag{2.8}$$

where R and Ω are the rotor radius and rotational speed respectively. The tip velocity is given by $V_{\text{tip}} = \Omega R$.

The thrust, torque and power can be non-dimensionalised based on the rotor design parameters, radius and rotation speed. The corresponding coefficients are defined as follow, respectively:

$$C_{\text{T}}^{\text{UK}} = \frac{T}{\frac{1}{2}\rho A(\Omega R)^2} = \frac{T}{\frac{1}{2}\rho A V_{\text{tip}}^2} \tag{2.9}$$

giving:

$$lambda_h = \sqrt{\frac{C_T^{\text{UK}}}{2}} \tag{2.10}$$

$$C_{\mathrm{Q}}^{\mathrm{UK}} = \frac{Q}{\frac{1}{2}\rho A \Omega^2 R^3} \tag{2.11}$$

$$C_{\mathrm{P}}^{\mathrm{UK}} = \frac{P}{\frac{1}{2}\rho A (\Omega R)^3} = \frac{P}{\frac{1}{2}\rho A V_{\mathrm{tip}}^3} = \frac{C_{\mathrm{T}}^{3/2}}{2} \tag{2.12}$$

An empirical correction for the power coefficient, κ is often given to account for non-uniform inflow, tip losses, wake swirl, wake contraction, finite number of blades. A typical value is $\kappa \sim 1.15$.

$$C_{\mathrm{P}} = \frac{\kappa C_{\mathrm{T}}^{3/2}}{2} \tag{2.13}$$

Furthermore, the blade drag can be taken into account using the constant drag coefficient in the typical approximation:

$$D = \frac{1}{2}\rho c U^2 C_{\mathrm{D}} \tag{2.14}$$

where c is the chord of the blade. C_{P} can then be updated to take into account the power lost in the blade drag:

$$C_{\mathrm{P}} = \frac{\kappa C_{\mathrm{T}}^{3/2}}{2} + \frac{\sigma C_{\mathrm{D}}}{8} \tag{2.15}$$

σ is the rotor solidity given by the ratio of blade area over disc area:

$$\sigma = \frac{N_{\mathrm{blades}} c R}{\pi R^2} = \frac{N_{\mathrm{blades}} c}{\pi R} \tag{2.16}$$

The efficiency of a helicopter is difficult to define given the number of parameters involved. The Figure of Merit, FM gives an efficiency of the aircraft based on the amount of thrust generated for a given power, in hover (Ideal power required to hover over Actual power required to hover). With the definitions above, the momentum theory gives:

$$FM = \frac{\frac{C_{\mathrm{T}}^{3/2}}{2}}{\frac{\kappa C_{\mathrm{T}}^{3/2}}{2} + \frac{\sigma C_{\mathrm{D}}}{8}} \tag{2.17}$$

2.1.2 Rotor in Forward Flight

Helicopter rotors are designed to provide simultaneously the force required to lift the aircraft and the moments to control it. Moreover, in forward flight the loading changes, as the advancing and retreating blades operate in different flows, as shown in figure 2.2.

A region of reversed flow appears where the blade velocity is lower than the forward velocity. These effects lead to global pitching and rolling moments on the aircraft body.

A specific rotor assembly is required to achieve effective control while dealing with undesirable effects. The pilot controls the aircraft in altitude, pitch and roll by varying the blades pitch angle - hence varying the value of the lift - around the azimuth (feathering). The use of a swash-plate system ensures a consistent one-per-revolution pattern for the blade pitch angle. Fully-articulated rotor assemblies allow the blades to flap freely as a way to balance the lift and centrifugal force and reduce the loading at the hub.

Variations of the blade lift around the azimuth causes the blade to flap. The vertical motion changes the local angle of attack seen by the blade and reduces the loading. The coriolis effect associated to the flapping combined with variations of the drag causes a lead-lag motion, i.e. an in-plane oscillation of the blade Some rotor assemblies allow free motion in this direction although most include a damper to reduce the effect of resonance.

Two typical rotor assemblies are shown figure 2.3 that corresponds to fully-articulated and semi-rigid rotor hubs.

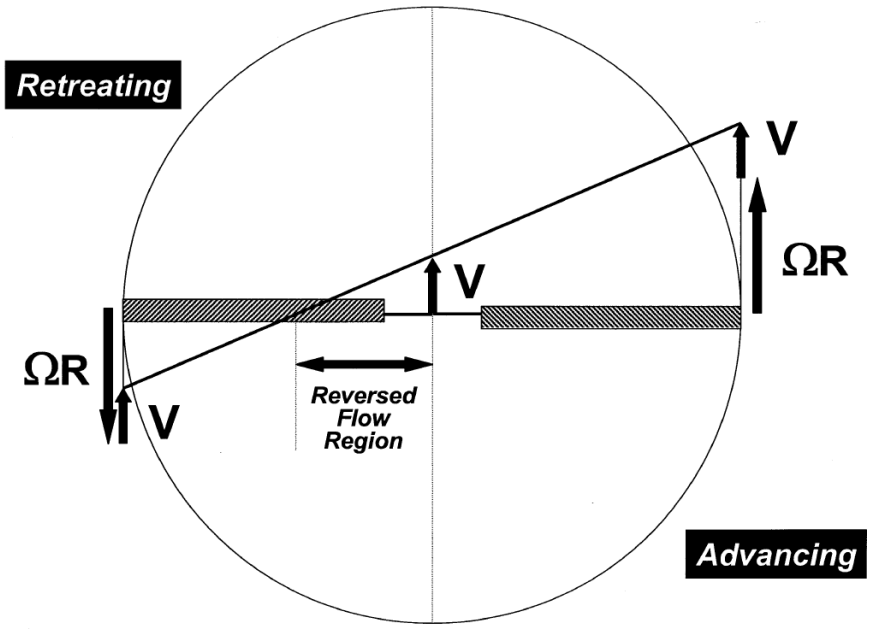

Figure 2.2: Rotor in forward flight. V is the aircraft speed, the rotor turns counter-clockwise with a tip speed of $V_{\text{tip}} = \Omega R$ where R is the rotor radius. The region where $V_{\text{blade}} < V$ sees reversed flow. From Bramwell [1]

In forward-flight, the rotor disc is tilted forward to use a fraction of the lift to produce the forward force necessary and counteract the drag of the fuselage, giving the

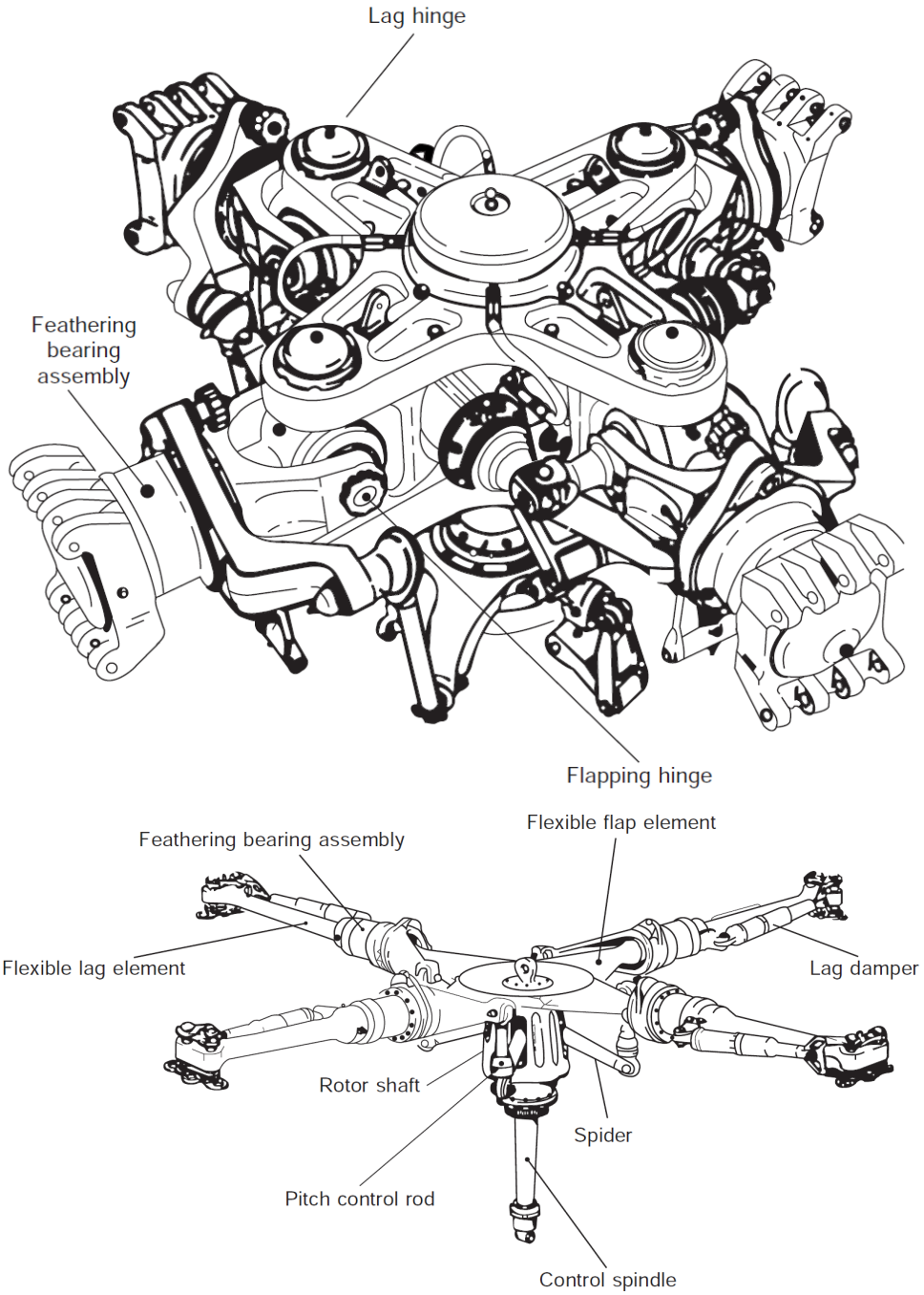

Figure 2.3: Two kinds of helicopter hubs: Fully-Articulated (Top) and Semi-Rigid (Bottom) (from Bramwell [1])

aircraft its forward speed. The distribution of forces on the rotor is more complex due to the loss of symmetry; it is the factor for determining the operational limitations of the aircraft.

Due to the forward speed, the advancing and retreating blades operate in two different flow conditions (Figure 2.2).

The one-per-revolution behaviour of the blade angles is often written as a Fourier decomposition,taking only the first harmonics:

$$\theta = \theta_0 + \theta_{1c}\cos(\Psi_i + \zeta) + \theta_{1s}\sin(\Psi_i + \zeta) + \beta tan(\delta_3) \tag{2.18a}$$

$$\beta = \beta_0 + \beta_{1c}\cos(\Psi_i) + \beta_{1s}\sin(\Psi_i) \tag{2.18b}$$

$$\zeta = \zeta_0 + \zeta_{1c}\cos(\Psi_i) + \zeta_{1s}\sin(\Psi_i) \tag{2.18c}$$

where θ is the pitch angle, β the flap and ζ the lead-lag. A description of each angle is given in figure 2.6 The subscripts 0, $1c$ and $1s$ designate the mean, cosine and sine components of the decomposition respectively. The δ_3 term added to the equation for θ is used in configurations where flap and lead-lag angles are coupled, which is often the case for tail-rotors.

2.1.3 Rotor in Ground Effect

The presence of a ground or deck under the rotor confines the development of the wake, increases the pressure and provides additional thrust. Using the method of images, Cheeseman and Bennett [57] gave an analytical estimate of the effect of the ground on the rotor thrust as function of the advance ratio and distance to the ground:

$$\frac{C_{\mathrm{T}}^{\mathrm{IGE}}}{C_{\mathrm{T}}^{\mathrm{OGE}}} = \frac{1}{1 - \frac{R^2}{16h^2\left(1+\left(\frac{\mu}{\lambda_i}\right)^2\right)}} \tag{2.19}$$

which can be simplified in hover with $\mu = 0$:

$$\frac{C_{\mathrm{T}}^{\mathrm{IGE}}}{C_{\mathrm{T}}^{\mathrm{OGE}}} = \frac{1}{1 - \frac{R^2}{16h^2}} \tag{2.20}$$

Using the previous analytical tool, curves of iso-distance and iso-μ are plotted in figure 2.4. Results show that the effect of the ground increases the thrust coefficient by about 7% in hover at one radius from the ground and less than 1% at three radiuses. At an advance ratio of 0.1, the beneficial effect of the ground drops by a factor 5 compared to the hover condition.

Experimental data were collected from Light *et al.* [17], Landgrebe [18], Fradenburgh [19] and Hayden [20], and are shown in figure 2.5. The rotors used for the experiments have different properties of solidity, specific loading and twist which explains some of the scatter in the data. Despite the differences, the beneficial effect of

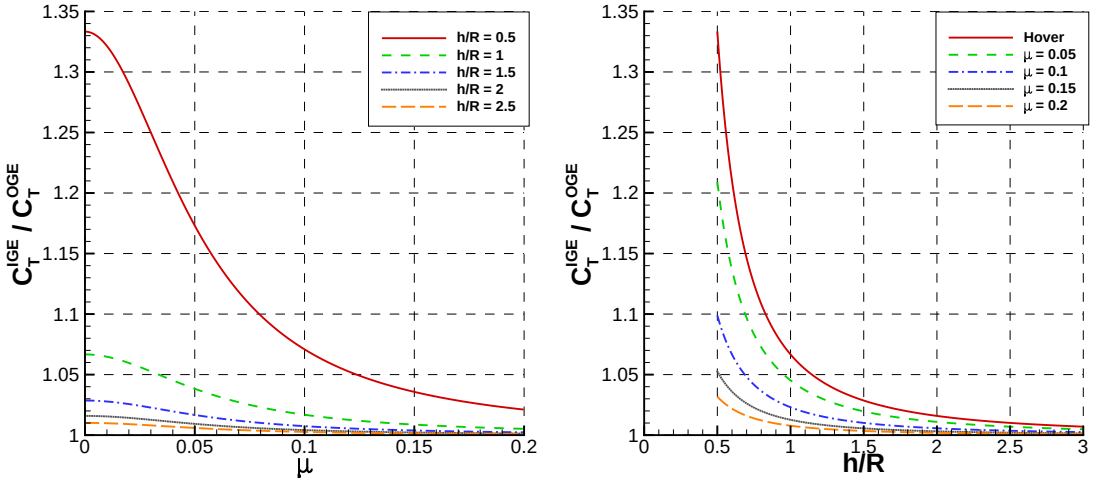

Figure 2.4: Effect of the distance and the advance ratio on the thrust coefficient in ground effect. λ_i in equation 2.19 corresponds to an arbitrary C_T^{UK} of 0.0144. (Theory from Cheeseman and Bennett [57])

the ground on the thrust is evident and follows reasonably closely the theoretical curve from Cheeseman and Bennett [57].

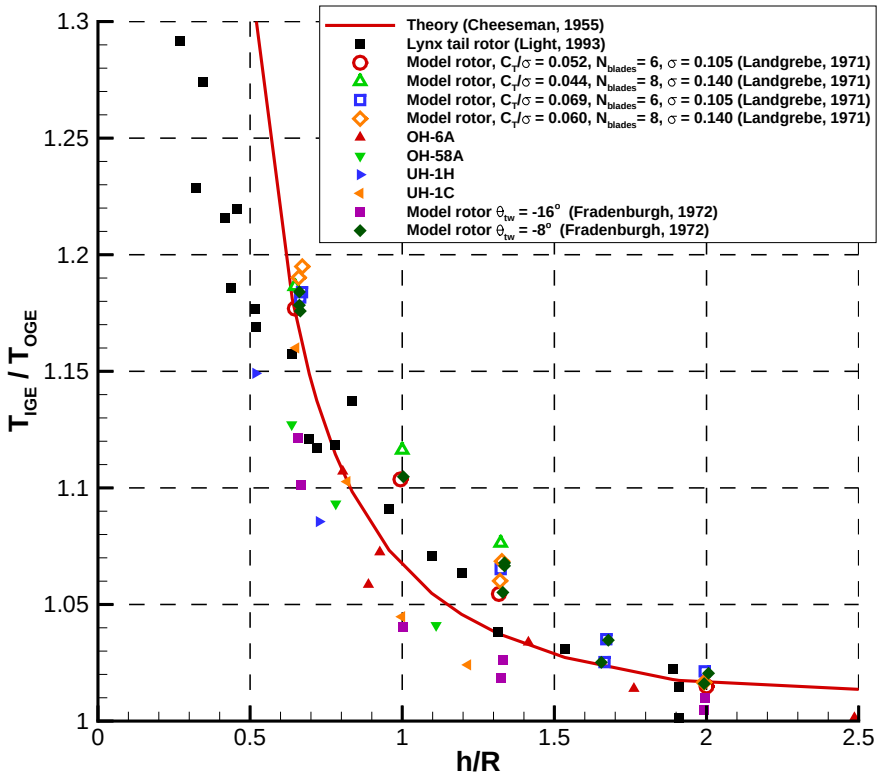

Figure 2.5: Effect of the ground on the thrust coefficient for a variety of rotors in hover. Theory from Cheeseman and Bennett [57]. Adapted from experimental data available in Landgrebe [18] and Light [17], Fradenburgh [19] and Hayden [20].

2.1.4 Blade Element Theory

The blade element theory assumes that each blade can be discretised and each blade section considered as a 2D airfoil (Figure 2.6).

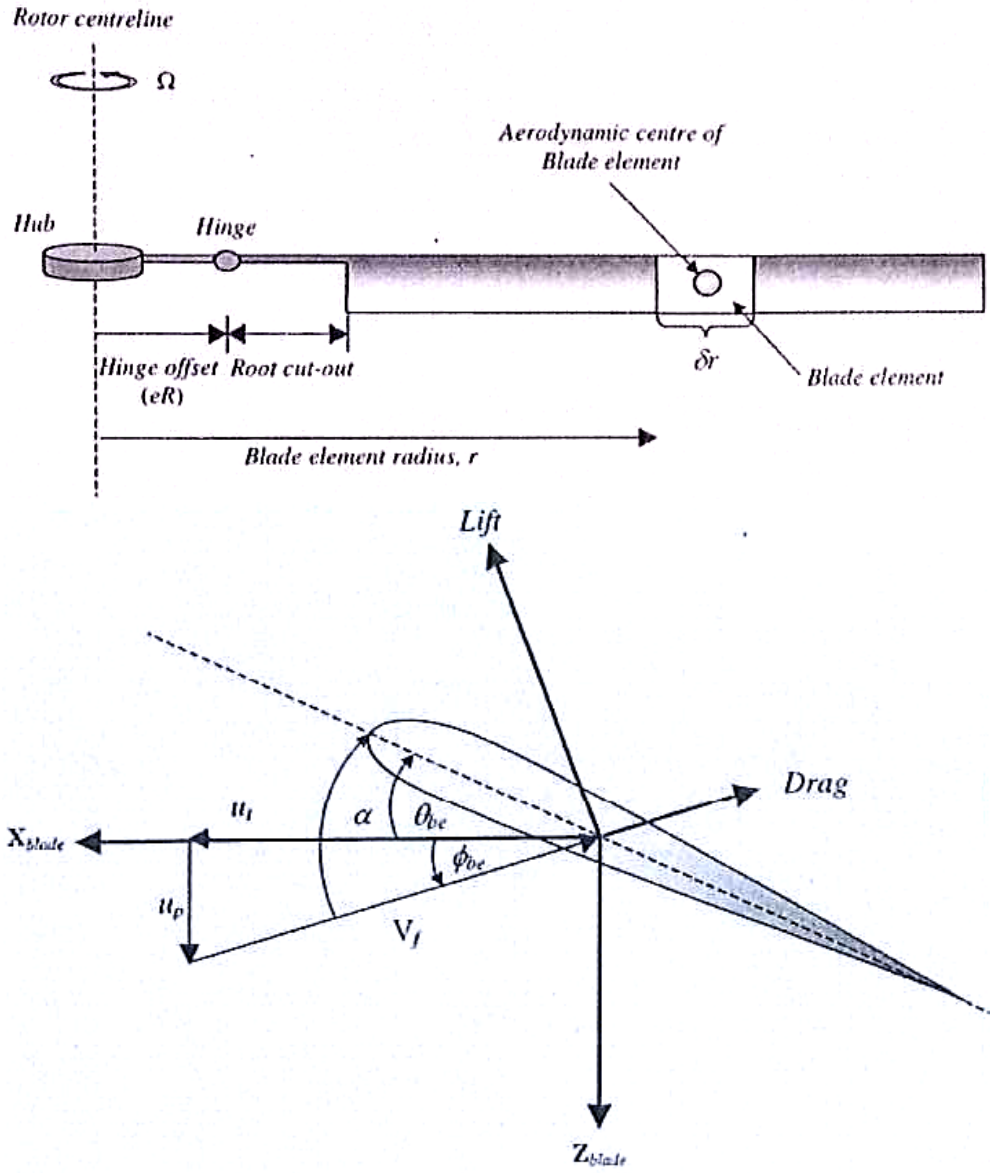

Figure 2.6: Notations used for the blade elements and aerofoils.

The rotation rate and flight conditions give the value and direction of the velocity applied on the section as function of the position on the blade (Figure 2.7). The local loads on the blade can be calculated and the total loads are obtained by integrating in the blade spanwise direction, for each blade [58].

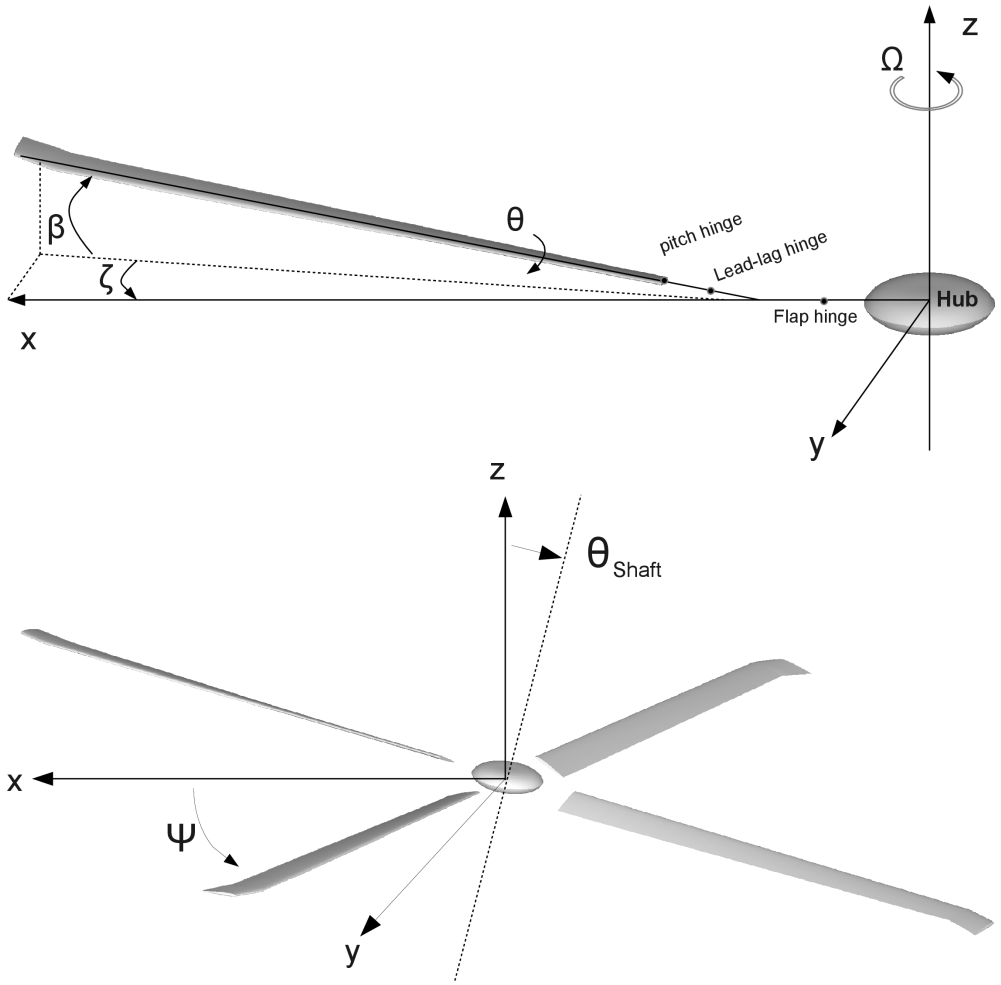

Figure 2.7: Notations used for the blade motion.

Lift and drag elements of force are calculated using the usual relations:

$$dL = \frac{1}{2}\rho U^2 c C_L dr \tag{2.21a}$$

$$dD = \frac{1}{2}\rho U^2 c C_D dr \tag{2.21b}$$

C_{L} and C_{D} are function of the angle of attack α, given by:

$$\alpha = \theta + \frac{r}{R}\dot{\beta} - tan^{-1}\frac{U_{\mathrm{P}}}{U_{\mathrm{T}}} \tag{2.22}$$

where θ is the blade incidence (function of the radius in case of twisted blades), $r\dot{\beta}$ is the flapping induced velocity and $U_{\mathrm{P}} = v_i + V_c$ is the velocity of the downwash (induced flow and climb velocity). $\phi = \frac{U_{\mathrm{P}}}{U_{\mathrm{T}}}$ is the contribution in angle of attack of the inflow.

Assuming $\phi = \frac{U_{\mathrm{P}}}{U_{\mathrm{T}}}$ is small, the drag contribution to the thrust is negligible and the thrust coefficient becomes:

$$C_T = \frac{1}{2}\sigma \int_0^1 C_L r^2 dr \tag{2.23}$$

Within a limited range of angles of attack, the lift coefficient of an airfoil is proportional to its angle of attack:

$$C_L = C_{L_\alpha}(\alpha - \alpha_0) \tag{2.24}$$

In forward flight at an advance ratio μ. The in-plane U_{T}, out-of-plane U_{P} and radial U_{R} velocities seen by each blade element are function of the azimuth:

$$U_{\mathrm{T}} = \Omega r + V_\infty \sin(\psi) = \Omega r + \mu \Omega R \sin(\psi) \tag{2.25}$$

$$U_{\mathrm{P}} = \underbrace{(\lambda_c + \lambda_i)\Omega R}_{\text{climb + induced flow velocities}} + \underbrace{y\dot{\beta}(\psi)}_{\text{flapping motion}} + \underbrace{\mu \Omega R \beta(\psi)\cos(\psi)}_{\text{coning effect}} \tag{2.26}$$

$$U_{\mathrm{R}} = \mu \Omega R \cos(\psi) \tag{2.27}$$

To be noted that in forward flight, the inflow is not uniform nor axisymmetric. To take this into account, inflow models are used such as linear ones:

$$\lambda_i = \lambda_0(1 + \lambda_{1c} r\cos(\psi) + \lambda_{1s} r \sin(\psi)) \tag{2.28}$$

2.1.5 Inflow Modelling

Several inflow models have been developed to study and predict the rotor behaviour without using CFD, hence reducing the computational cost. Dynamic inflow methods are still in use for real-time flight simulation, stability computations, flight mechanics and control[59]. It is a mathematical model that, given the history of blade loads on the rotor, will produce the induce flow normal to the rotor disc as a function of the coordinates: time, radial position and azimuthal position. It is expressed through a set of differential equations so that a linear model takes the following form:

$$[M]\left\{\frac{d\lambda_n}{dt}\right\} + [C]\{\lambda_n\} = \{F_m\} \tag{2.29}$$

with a number of variables that depends on the level of fidelity. The model by Pitt and Peters [60] assumes that the velocity through the disc is given by its mean value and first harmonic, so that:

$$\lambda = \begin{bmatrix} \lambda_0 \\ \lambda_{1c} \\ \lambda_{1s} \end{bmatrix} \tag{2.30}$$

$$\lambda_i = \lambda_0(1 + \lambda_{1c} r\cos(\psi) + \lambda_{1s} r\sin(\psi)) \tag{2.31}$$

The matrices of the system are then defined by

$$[M] = \begin{bmatrix} \frac{8}{3\pi} & 0 & 0 \\ 0 & \frac{16}{45\pi} & 0 \\ 0 & & \frac{16}{45\pi} \end{bmatrix} \tag{2.32}$$

$$[C] = V_\infty [L]^{-1} \tag{2.33}$$

with:

$$[L] = \begin{bmatrix} \frac{1}{2} & 0 & -\frac{15\pi}{64}X \\ 0 & 2(1+X^2) & 0 \\ \frac{15\pi}{64}X & 0 & 2(1+X^2) \end{bmatrix} \tag{2.34}$$

where V_∞ is the free-stream velocity.

$$\{F_m\} = \begin{bmatrix} C_T \\ -C_L \\ -C_M \end{bmatrix} \tag{2.35}$$

This models account for the wake skew angle χ via the constant $X = \tan(\frac{\chi}{2})$.

2.2 Dynamics modelling

The simulation of helicopter flight requires a multi-body motion solver to calculate the fuselage and main and tail rotor blades dynamics. The forces and moments applied on the various parts of the airframe are calculated using blade element theory, inflow model as well as models for the fuselage, tail plane and fins. Assuming no deformations, the resulting forces translate directly into accelerations. The resulting equations of motions can be written as a set of second order differential equations.

Equations of Motion

According to Newton's second law in a Cartesian coordinate system:

$$\dot{u} = \underline{\omega} \times \underline{u} + \frac{\sum \underline{F}^{ext}}{M} \tag{2.36}$$

where $\underline{\omega}$ is the vector of body rotations, $\underline{u}$ the body velocities and $\underline{F}^{ext}$ the sum of external forces. The conservation of angular momentum also gives:

$$\underline{\dot{H}} = -\underline{\omega} \times \underline{H} + \sum \underline{T}^{ext} \tag{2.37}$$

where $\underline{H} = \underline{\underline{I}}\underline{\omega}$, $\underline{H}$ is the momentum of the system, T^{ext} are the moments acting on the fuselage and $\underline{\underline{I}}$ is the inertia matrix of the vehicle, given by:

$$\underline{\underline{I}} = \begin{bmatrix} I_{xx} & I_{xy} & I_{xz} \\ I_{xy} & I_{yy} & I_{yz} \\ I_{xz} & I_{yz} & I_{zz} \end{bmatrix}. \tag{2.38}$$

Fuselage Equations of Motion

The velocities and rotation rates of the aircraft $[u\ v\ w\ p\ q\ r]$ are written as follows, in the aircraft frame of reference, at the Center of Gravity (CG) and taking into account the gravity separately [58]:

$$\begin{cases} \dot{u} = v\ r - q\ w + \frac{F_X^{\text{ext}}}{M} - g\ \sin\theta \\ \dot{v} = w\ p - u\ r + \frac{F_Y^{\text{ext}}}{M} + g\ \cos\theta\ \sin\phi \\ \dot{w} = u\ q - v\ p + \frac{F_Z^{\text{ext}}}{M} + g\ \cos\theta\ \cos\phi \end{cases} \tag{2.39}$$

$$\begin{cases} I_{xx}\dot{p} = I_{xy}\ p\ r + (I_{yy} - I_{zz})\ q\ r + I_{yz}\ (r^2 + q^2) + I_{xz}\ p\ q + L \\ I_{yy}\dot{q} = I_{yz}\ p\ q + (I_{zz} - I_{xx})\ r\ p + I_{xz}\ (p^2 - r^2) + I_{xy}\ q\ r + M \\ I_{zz}\dot{r} = I_{xz}\ q\ r + (I_{xx} - I_{yy})\ p\ q + I_{xy}\ (q^2 - p^2) + I_{yz}\ p\ r + N \end{cases} \tag{2.40}$$

The fuselage position and attitude written in the Galilean earth-fixed frame of reference $[x_e\ y_e\ z_e\ \theta\ \phi\ \psi]$ can be obtained by simple transformation of the previous quantities.

$$\begin{cases} \dot{\phi} = p + q\ \sin\phi\tan\theta + r\ \cos\phi\tan\theta \\ \dot{\theta} = q\ \cos\phi - r\ \sin\phi \\ \dot{\psi} = q\ \frac{\sin\phi}{\cos\theta} + r\ \frac{\cos\phi}{\cos\theta} \end{cases} \tag{2.41}$$

$$\begin{cases} \dot{x}_e = & u\ \cos\theta\cos\phi + v\ (\sin\phi\sin\theta\cos\psi - \cos\phi\sin\psi) \\ & +w\ (\cos\phi\sin\theta\cos\psi + \sin\psi\sin\phi) \\ \dot{y}_e = & u\ (\cos\theta\sin\psi) + v\ (\sin\phi\sin\theta\sin\psi + \cos\phi\cos\psi) \\ & +w\ (\cos\phi\sin\theta\sin\psi - \sin\phi\cos\psi) \\ \dot{z}_e = & -u\ \sin\theta + v\ \sin\phi\cos\theta + w\ \cos\phi\cos\theta \end{cases} \tag{2.42}$$

The forces $F_{\mathrm{X}}^{\mathrm{ext}}$, $F_{\mathrm{Y}}^{\mathrm{ext}}$ and $F_{\mathrm{Z}}^{\mathrm{ext}}$ include the rotor forces as well as fuselage drag and various appendices if accounted for separately.

Blade Flapping Equation

Newton's second law can be written for the specific case of a blade in flapping. We here consider a blade in pure flapping ($\dot{\theta} = 0$ and $\dot{\zeta} = 0$). The equation of motion reduces to:

$$I_\beta \ddot{\beta} = M_\beta \tag{2.43}$$

$$I_\beta = \int_0^R r^2 m(r) dr \tag{2.44}$$

where M_β is the sum of centrifugal force, hinge spring force with linear stiffness coefficient K and lift force, taken at the blade hinge:

$$I_\beta \ddot{\beta} = \underbrace{K_\beta \beta}_{\text{hinge spring force}} + \underbrace{\int_0^R rm(r)(r\Omega^2)dr}_{\text{centrifugal force}} \sin\beta - \underbrace{\int_0^R (\frac{1}{2}\rho V^2 c(r) C_{\mathrm{L}}) r dr}_{\text{moment due to blade lift force}} \cos\beta \tag{2.45}$$

The local lift at the blade radial position r depends on lift coefficient. A linear model is given by:

$$C_{\mathrm{L}} = \alpha_0 + a_0 \alpha(r) \tag{2.46}$$

where α_0 is the zero-lift angle and a_0 the lift slope. However, it is common to substitute this model with tabulated data in order to account for the loss of linearity at high angle of attack and the stall condition.

Blade Lead-lag Equation

Similarly, the equations for a blade in pure lead-lag ($\dot{\theta} = 0$ and $\dot{\beta} = 0$) are:

$$I_\zeta \ddot{\zeta} = M_\zeta \tag{2.47}$$

$$I_\zeta = \int_0^R r^2 m(r) dr \tag{2.48}$$

where M_ζ is the sum of centrifugal force, hinge spring force with linear stiffness coefficient K and blade drag force.

$$I_\zeta \ddot{\zeta} = \underbrace{K_\zeta \zeta}_{\text{hinge spring force}} + \underbrace{\int_0^R rm(r)(r\Omega^2)dr}_{\text{centrifugal force}} \sin\zeta - \underbrace{\int_0^R (\frac{1}{2}\rho V^2 c(r) C_D) r dr}_{\text{blade drag force}} \cos\zeta \tag{2.49}$$

The blade drag force is function of the drag coefficient defined by:

$$C_\mathrm{D} = C_\mathrm{D}^0 d_0 \alpha(r) \tag{2.50}$$

A fully-articulated, rigid rotor assembly is considered, with each blade articulated in flap and lead-lag via a hinge/damper system and actuated in pitch. The blade hinges are used as reference points to integrate the corresponding forces and moments calculated at each section of the blade. The contribution of each blade is then transported at the rotor hub and summed to obtain a set of forces and moments for the complete rotor. Finally, the equations of motion for the global system can be written with the contributions of the fuselage, fin and tail plane, main and tail rotor systems added explicitely at the center of mass.

Chapter 3

Helicopter Flight Dynamics

The basic principles of helicopter flight presented in section 2.1 are useful to calculate the theoretical performance of the aircraft as a function of various design parameters. However, these performance indices are valid for steady flight conditions: typically hover or forward flight.

Multi-body solvers are commonly used to better estimate the aircraft performance. Each part of the rotorcraft system is modelled independently and the system can be solved in a time-accurate fashion so as to enable simulation of non-steady flight.

A number of assumptions and approximations are made in the current approach:

1. All the components are fully-rigid and connected using ideal joints.
2. Blade and fuselage aerodynamic properties are tabulated functions of the flow angle and Mach number only.
3. The only aerodynamic interactions between components are the ones modelled directly, no free-wake model is used.

These assumptions are common in many analytical tools for rotorcraft and can be relaxed using advanced models: free-wake modelling, panel methods, deforming blades, etc.

This section presents the Helicopter Flight Mechanics (HFM) model developed for the purpose of this thesis.

3.1 Dynamics Model for Rotorcraft

A flight mechanics code for rotorcraft solves a set of equations of motion in time for the body position and attitude, as well as the blades rotations. An inflow model is added for each rotor as well as engine terms.

The assumptions are detailed in the introduction. The aircraft position and attitude is expressed by the coordinates of its center of gravity in the earth-fixed frame of reference (Figure 3.1)

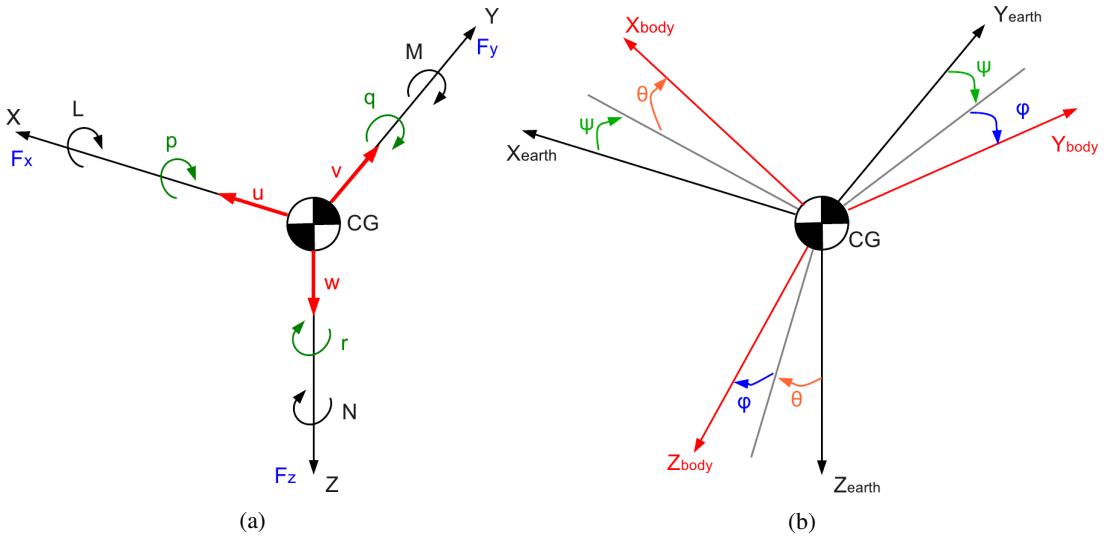

Figure 3.1: 3-axis and associated variables, Euler angles for earth-to-body transformation.

Earth-To-Body Transformation

The helicopter position and attitude is defined in the fuselage frame of reference by its three coordinates $[x\ y\ z]^{\mathbf{T}}$ and rotation angles $[\phi\ \theta\ \psi]^{\mathbf{T}}$ shown in figure 3.2. The velocities and rotation rates are the corresponding derivatives: $[u\ v\ w]^{\mathbf{T}} = [\dot{x}\ \dot{y}\ \dot{z}]^{\mathbf{T}}$ and $[p\ q\ r]^{\mathbf{T}} = [\dot{\phi}\ \dot{\theta}\ \dot{\psi}]^{\mathbf{T}}$.

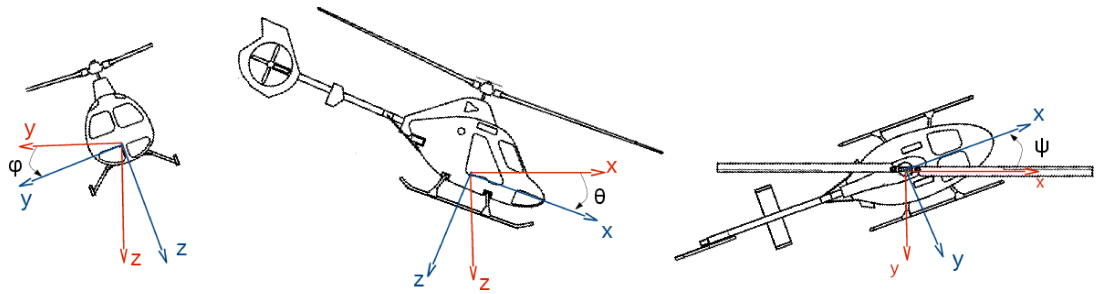

Figure 3.2: Helicopter-body axis system. Earth-based (red) and fuselage-based (blue) frames of reference

The velocities in the fuselage system of axes are then given by:

$$\begin{bmatrix} u \\ v \\ w \end{bmatrix} = \begin{bmatrix} \cos\theta\cos\psi & -\cos\theta\sin\psi & \sin\theta \\ \sin\phi\sin\theta\cos\psi - \cos\phi\sin\psi & -\sin\phi\sin\theta\sin\psi + \cos\phi\cos\psi & -\sin\phi\cos\theta \\ \sin\psi\sin\phi + \cos\phi\sin\theta\cos\psi & \cos\phi\sin\theta\sin\psi + \sin\phi\cos\psi & \cos\phi\cos\theta \end{bmatrix} \times \begin{bmatrix} u_e \\ v_e \\ w_e \end{bmatrix} \quad (3.1)$$

Inflow Model

The problem of inflow modelling has been described section 2.1.5. The inflow model chosen for this work is the one by Peter and HaQuang: The static inflow formulation of the model takes the following form:

$$\begin{pmatrix} \lambda_0 \\ \lambda_{1s} \\ \lambda_{1c} \end{pmatrix} = [L] \begin{pmatrix} C_\mathrm{T} \\ -C_\mathrm{L} \\ -C_\mathrm{M} \end{pmatrix} \tag{3.2}$$

An apparent mass term is introduced to obtained a dynamic inflow in a simple first order differential equation form:

$$[M] \begin{pmatrix} \dot{\lambda}_0 \\ \dot{\lambda}_{1s} \\ \dot{\lambda}_{1c} \end{pmatrix} + [L]^{-1} \begin{pmatrix} \lambda_0 \\ \lambda_{1s} \\ \lambda_{1c} \end{pmatrix} = \begin{pmatrix} C_\mathrm{T} \\ -C_\mathrm{L} \\ -C_\mathrm{M} \end{pmatrix} \tag{3.3}$$

with the matrices M and L as follow:

$$[M] = \begin{bmatrix} \frac{8}{3\pi} & 0 & 0 \\ 0 & \frac{16}{45\pi} & 0 \\ 0 & 0 & \frac{16}{45\pi} \end{bmatrix} \tag{3.4}$$

$$[L] = \begin{bmatrix} \frac{1}{2} & 0 & -\frac{15\pi}{64}\sqrt{\frac{1-\sin\alpha}{1+\sin\alpha}} \\ 0 & \frac{4}{1+\sin\alpha} & 0 \\ \frac{15\pi}{64}\sqrt{\frac{1-\sin\alpha}{1+\sin\alpha}} & 0 & \frac{4\sin\alpha}{1+\sin\alpha} \end{bmatrix} \tag{3.5}$$

Atmosphere model

Atmospheric properties are calculated as function of the aircraft altitude, pressure, and reference temperature:

$$\left(\frac{\rho}{\rho_\mathrm{ref}}\right) = \left(\frac{T_2}{T_\mathrm{QNH}}\right)^{\left(\frac{g-\Gamma R}{\Gamma R}\right)} \tag{3.6}$$

where Γ is the lapse rate and R the gas constant, and T_2 and ρ_ref as follow:

$$T_2 = T_\mathrm{QNH} - \Gamma h \tag{3.7}$$

$$\rho_\mathrm{ref} = P_\mathrm{QNH} R T_\mathrm{QNH} \tag{3.8}$$

$$\rho_{\text{ref}} = \frac{P_{\text{QNH}}}{R(T_2 + \Gamma h)} \left(\frac{T_2}{T_2 + \Gamma h} \right)^{\left(\frac{g-\Gamma R}{\Gamma R}\right)} \tag{3.9}$$

which gives:

$$\rho_{\text{ref}} = \frac{P_{QNH}}{R(273.15 + T_h + Lh)} \left(\frac{273.15 + T_h}{273.15 + T_h + Lh} \right)^{\left(\frac{g-LR}{LR}\right)} \tag{3.10}$$

P_{QNH} is the pressure setting in hPa, $T_h = T_{\text{QNH}} - \Gamma h$ is the temperature at the altitude h. The local speed of sound is given by:

$$a = \sqrt{\gamma R T_2} = \sqrt{\gamma R (273.15 + T_h)} \tag{3.11}$$

Solver

The equations of motion are written in the form of a linear system that contains body and blades equations of motion as well as the dynamic inflow model. The variables defined in equations 2.39 to 2.42 (body velocities and attitude), 3.3 (inflow velocities) and 2.18 (blade angles) of the system are shown figure 3.3.

Figure 3.3: Variables of the state vector z. $\dot{z}$ contains the respective derivatives. Blades variables are for each blades, q_e and $\dot{q}_e$ for each engine. Subscripts 1 and 2 correspond to the rotor index.

Since the variables are coupled, the system is written in state-space form:

$$\underline{z} = \underline{\underline{A}}^{-1} \, \underline{\dot{z}} dt \tag{3.12}$$

The form of the matrix $\underline{\underline{A}}$ is presented in figure 3.4. All differential equations are solved simultaneously, with the cross-terms taken into account. The method computes $\underline{\underline{A}}$ and $\underline{\dot{z}}$ from the body motion equations, inverse $\underline{\underline{A}}$ and pre-multiply $\underline{\dot{z}}$ before solving the system 3.12 in time using an Euler or Runge-Kutta fourth order method.

3.2 Building the Sea King Aircraft Model

The Sea King is a medium-lift transport and utility helicopter with a maximum take off weight of about 9700 kg. It was designed and is widely used for maritime operations, and was chosen for this work. Information about the MK50 model can be found in a series of DTIC reports [61–63]. The main characteristics of the aircraft are listed in table

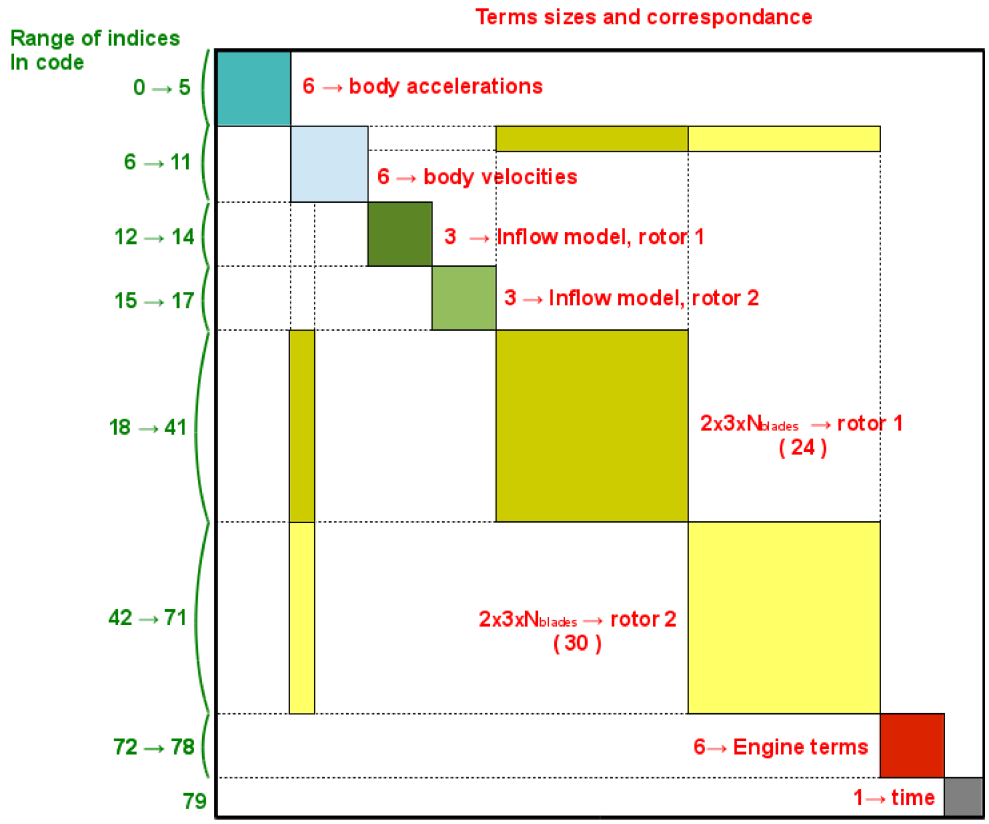

Figure 3.4: Pre-multiplication matrix.

3.1 A more comprehensive set of data and figures from the technical documents have been reproduced in appendix A

3.3 Helicopter Linear Model

Rotorcraft are complex systems and blade aero-elasticity, engine response, non-proportional control transfers and unsteady aerodynamics lead to a non-linear response of the aircraft to a given pilot input or external disturbance. It is not possible to determine a linear model for a helicopter that is representative of the behaviour consistently across the flight envelope. However, it is possible to determine a local linear approximation for a given flight condition. Despite the obvious limitations of such method, it is useful for many applications: development of simple and quick trimming methods and pilot models, prediction of the helicopter response to small disturbances, stability analysis, etc.

Given a set of state and control vectors, **x** and **u** respectively, a typical linear model consists in a set of coupled first order differential equations written in matricial form as:

Variable	Value	
All Up Weight (AUW)	8391.46	$[kg]$
Roll 2nd moment of inertia	19354.3	$[kg.m^2]$
Pitch 2nd moment of inertia	65587.69	$[kg.m^2]$
Yaw 2nd moment of inertia	53080.27	$[kg.m^2]$
Hub coordinates with respect to Center of Gravity	(0.31,0.0,-2.58)	$[m]$
Rotor radius	9.4488	$[m]$
Blade chord	0.4633	$[m]$
Hinge offset	0.32	$[m]$
Blade twist	-8.0	$[degrees]$
Blade mass	82.1	$[kg]$
Rotation speed Ω	21.89	$[rd.s^{-1}]$
Number of main rotor blades	5	
Number of tail rotor blades	5	
main rotor airfoil section	NACA0012	
tail rotor airfoil section	NACA0012	

Table 3.1: Physical characteristics of the Sea King MK50 helicopter [61–63]

$$\dot{\mathbf{x}} = A\mathbf{x} + B\mathbf{u} \tag{3.13}$$

The set of state $\mathbf{x}$ and control $\mathbf{u}$ vectors need to be determined depending on the case considered, and are usually defined as follows:

$$\mathbf{x} = [x_i]_{1<i<9} = [u\ v\ w\ p\ q\ r\ \Phi\ \theta\ \Psi]^{\mathbf{T}} \tag{3.14a}$$

$$\mathbf{u} = [b_j]_{1<j<4} = [\theta_0^{\mathrm{M}}\ \theta_{1s}\ \theta_{1c}\ \theta_0^{\mathrm{T}}]^{\mathbf{T}} \tag{3.14b}$$

This model gives the response of the aircraft in terms of accelerations for a given state and set of controls. This type of system is known as MIMO (Multiple-Inputs, Multiple-Outputs). It may be simplified further by decoupling some of the terms. For example, the heading is mainly controlled by the tail rotor collective and the effect of other controls may be neglected.

The following sections present the method employed in HFM to determine the matrices A and B and the applications of the different linear models to trimming and pilot modelling.

3.3.1 Feedback Linearisation

The feedback linearisation is a type of system identification method that consists in determining the set of matrices A and B used by the linear model that best-describes the response of a complex, non-linear helicopter model, in a given range of conditions.

If the non-linear system is simple, the linearisation may be achieved analytically or simply approximated from simple models [58] .

However, in most cases an iterative method is used that compares the inputs and outputs of a real or modelled aircraft and builds the matrix accordingly. An example of such tool is the CIFER (Comprehensive Identification from FrEquency Responses) package used at NASA that implements frequency-based signal analysis to find the suitable matrix.

As example, the linear model for the BO105 helicopter can be found in the literature [64], although using modified state and control vectors:

$$\mathbf{x} = [x_i]_{1<i<8} = [u\ w\ q\ \theta\ v\ p\ r\ \Psi]^{\mathbf{T}} \tag{3.15a}$$

$$\mathbf{u} = [b_j]_{1<j<4} = [\delta_0^{\mathrm{M}}\ \delta_{1s}\ \delta_{1c}\ \delta_0^{\mathrm{T}}]^{\mathbf{T}} \tag{3.15b}$$

where δ correspond to displacements at the pilot hand. The full A and B matrices are given below:

$$A = \begin{bmatrix} -0.0196 & 0.0148 & 0.5201 & -9.81 & 0.0 & -0.2907 & -0.0245 & 0.0 \\ -0.1320 & -0.3768 & 5.19 & 0.0 & 0.0025 & -0.0505 & 0.4668 & 0.0 \\ 0.0593 & -0.0012 & -3.4105 & 0.0 & -0.0158 & -0.86 & 0.0494 & 0.0 \\ 0.0 & 0.0 & 1.0 & 0.0 & 0.0 & 0.0 & 0.0 & 0.0 \\ 0.0037 & -0.0045 & -0.1595 & 0.0 & -0.1259 & -0.6369 & -5.019 & 9.81 \\ -0.0202 & -0.0111 & 2.3180 & 0.0 & -0.2290 & -9.4386 & 0.0537 & 0.0 \\ -0.0233 & 0.0079 & -0.601 & 0.0 & 0.0474 & 0.1119 & -0.4741 & 0.0 \\ 0.0 & 0.0 & 0.0 & 0.0 & 0.0 & 1.0 & 0.0 & 0.0 \\ 0.0 & 0.0 & 0.0 & 0.0 & 0.0 & 0.0 & 1.0 & 0.0 \end{bmatrix} \tag{3.16}$$

$$B = \begin{bmatrix} 0.0388 & 0.0957 & -0.0031 & -0.0144 \\ -1.1544 & 0.0364 & 0.0039 & 0.0024 \\ 0.0004 & -0.3844 & 0.0674 & 0.0248 \\ 0.0 & 0.0 & 0.0 & 0.0 \\ -0.0116 & 0.0011 & 0.0986 & -0.1919 \\ -0.0698 & 0.1739 & 1.0450 & -0.3902 \\ 0.2203 & 0.0080 & 0.0153 & 0.5353 \\ 0.0 & 0.0 & 0.0 & 0.0 \end{bmatrix} \tag{3.17}$$

Using the state and control vectors of equation 3.14 averaged over a period of the system, a simple linearisation method was implemented that derives a linear model for a Sea King helicopter from the full flight dynamics code presented in the previous chapter. The A and B are jacobian matrices defined as follows:

$$A = \left(\frac{\partial x_i}{\partial x_j} \right)_{i,j} \tag{3.18}$$

$$B = \left(\frac{\partial x_i}{\partial b_j} \right)_{i,j} \tag{3.19}$$

The linearisation operation consists in calculating individually each terms of the jacobian matrix using finite differences;

$$A = \left(\frac{x_i^{x_j+\varepsilon} - x_i^{x_j-\varepsilon}}{2\varepsilon} \right)_{i,j} \tag{3.20}$$

$$B = \left(\frac{x_i^{b_j+\varepsilon} - x_i^{b_j-\varepsilon}}{2\varepsilon} \right)_{i,j} \tag{3.21}$$

with $\varepsilon = 10^{-8}$. The resulting matrices are shown below:

$$A = \begin{bmatrix} -0.003 & -0.003 & 0.011 & 0.262 & -0.042 & 0.029 & -0.122 & -9.133 & 0.000 \\ 0.004 & -0.037 & 0.006 & -0.008 & 0.364 & -9.702 & 8.947 & -0.145 & 0.000 \\ 0.001 & 0.014 & -0.196 & 0.069 & 11.826 & -1.086 & -0.028 & -0.034 & 0.000 \\ 0.010 & -0.020 & 0.007 & -0.257 & 0.193 & 0.119 & -0.858 & -0.149 & 0.000 \\ 0.001 & 0.003 & -0.002 & -0.018 & -0.073 & -0.007 & 0.035 & -0.192 & 0.000 \\ -0.000 & 0.053 & 0.005 & 0.061 & 0.001 & -0.494 & 0.022 & -0.000 & 0.000 \\ 0.000 & -0.000 & 0.000 & 0.999 & 0.005 & 0.003 & -0.017 & 0.001 & 0.000 \\ 0.000 & 0.000 & -0.000 & -0.001 & 1.000 & -0.000 & -0.003 & -0.004 & 0.000 \\ 0.000 & 0.001 & 0.000 & 0.001 & 0.000 & 0.990 & -0.002 & -0.000 & 0.000 \end{bmatrix} \tag{3.22}$$

$$B = \begin{bmatrix} 0.491 & 4.079 & -5.204 & 0.011 \\ 0.774 & 5.164 & 2.399 & -3.253 \\ -13.634 & 0.712 & -1.327 & 1.507 \\ 1.051 & 13.466 & 0.940 & -1.254 \\ -0.032 & -0.737 & 3.781 & -0.072 \\ 0.418 & 0.089 & 0.022 & 5.286 \\ 0.011 & 0.180 & -0.012 & -0.026 \\ 0.001 & -0.002 & 0.046 & -0.001 \\ 0.005 & 0.001 & -0.000 & 0.107 \end{bmatrix} \tag{3.23}$$

3.3.2 Direct and Inverse Simulation

Aircraft models express the aircraft state (attitude, velocities, rotation rates) as function of control parameters; typically the pilot inputs. In the simplest cases, the relationship is linear and can be written as shown in equation 3.13 where **x** and **u** are the state and control vectors respectively.

Typical state and control vectors for rotorcraft are $\mathbf{x} = [u\ v\ w\ p\ q\ r\ \Phi\ \theta\ \Psi]$ and $\mathbf{u} = [\theta_0^{\mathrm{M}}\ \theta_{1s}\ \theta_{1c}\ \theta_0^{\mathrm{T}}]$. However, in many cases a higher order model is required to fully describe the aircraft behaviour across the flight envelope.

Inverse modelling consists in inverting the system of equations to express the pilot inputs as function of the aircraft attitude. For the linear model described previously, with 9 states and 4 controls, it is necessary to reduce the set of states. A "selection" matrix C is built to reduce the size of the problem to 4 states and 4 controls.

$$\mathbf{y} = C\mathbf{x} \tag{3.24}$$

By differentiating $\mathbf{y}$, we obtain

$$\dot{\mathbf{y}} = C\dot{\mathbf{x}} = CA\mathbf{x} + CB\mathbf{u} \tag{3.25}$$

For a prescribed $\mathbf{y}^*$ corresponding to a specific trajectory, we can write the controls $\mathbf{u}^*$ that guarantee that the output $\dot{\mathbf{y}} = \dot{\mathbf{y}}^*$ is achieved, as:

$$\mathbf{u}^* = (CB)^{-1}(\dot{\mathbf{y}}^* - CA\mathbf{x}) \tag{3.26}$$

In case of the linear model described earlier, only one differentiation of the output vector is necessary for $\mathbf{u}$ to appear. For more complex models, further differentiations might be required until the output is expressed as a function of u. The number of differentiations is called relative degree of the system. The method presented is usually referred to as SYCOS method in the literature [65,66] (SYnthesis through COnstrained Simulation).

In this case, the information that is prescribed to the system is contained in $\dot{\mathbf{y}}^*$. The calculated controls $\mathbf{u}^*$ are exact and uniquely defined within the limitations of the linear model. The SYCOS method can be modified to build a controller based on the linear model that can be applied to a wider range of helicopter models. The $\dot{\mathbf{y}}^*$ vector that contains the desired output is modified during the simulation to account for possible deviations from the desired flight path.

3.3.3 Linear Quadratic Regulator Pilot Model

The Linear-Quadratic Regulator [67] is an example of a widely used control method based on least-square minimisation that used a full linear model of the aircraft to provide control estimates during manoeuvre, given a prescribed objective trajectory. The inverse modelling method is presented here as it allows to *a priori* estimate the pilot controls but the LQR method was applied for piloted simulations, with or without CFD. The following state and control vectors, $\mathbf{x}$ and $\mathbf{u}$ respectively, are used:

$$\mathbf{x} = [u\ v\ w\ p\ q\ r\ x_\mathrm{e}\ y_\mathrm{e}\ z_\mathrm{e}\ \Phi\ \Theta\ \Psi] \tag{3.27}$$

$$\mathbf{u} = \left[\theta_0^\mathrm{M}\ \theta_{1\mathrm{c}}\ \theta_{1\mathrm{s}}\ \theta_0^\mathrm{T}\right] \tag{3.28}$$

and the linearised 6-DoF model of the rotorcraft around the trim state $(\tilde{\mathbf{x}}, \tilde{\mathbf{u}})$ is built as

$$\delta\dot{\mathbf{x}} = A\delta\mathbf{x} + B\delta\mathbf{u} \tag{3.29}$$

The nonlinear function $\mathbf{f}(\mathbf{x}, \mathbf{u})$ describes the evolution of the state space vector from the trim state $\tilde{\mathbf{x}}$ to the state $\mathbf{x}$ under the action of the fixed input $\mathbf{u}$, and is computed by integrating equation 3.29 over some revolutions of the rotor to allow the flapping motion transient be sufficiently damped.

The aim of an auto-pilot is to control the position $(x_\mathrm{e}, y_\mathrm{e}, z_\mathrm{e})$ of the helicopter in earth reference frame and its heading Ψ. We recast this trajectory tracking problem into the LQR setting as follows.

The matrices are calculated for a trim condition representative of the manoeuvre to perform. Then, if $\delta\mathbf{x}$ is the deviation of the state vector from the desired state, the variation $\delta\mathbf{u}$ of the controls is determined as the LQR optimal feedback due to the deviation $\delta\mathbf{x}$. The LQR controller will in fact drive $\delta\mathbf{x}$ to zero by minimising the quadratic cost function:

$$J = \int_0^\infty \left(\delta\mathbf{x}^\mathrm{T} Q \delta\mathbf{x} + \delta\mathbf{u}^\mathrm{T} R \delta\mathbf{u}\right) \mathrm{d}t \tag{3.30}$$

where Q and R are weighting matrices that define the importance of the the states and of the controls in the cost function. The solution to the minimisation problem is

$$\delta\mathbf{u}_\mathrm{LQR} = -K\delta\mathbf{x} \tag{3.31}$$

where K is the optimal feedback matrix given by

$$K = R^{-1}B^\mathrm{T}P \tag{3.32}$$

and P is the solution of the continuous algebraic Riccati equation:

$$A^\mathrm{T}P + PA - PBR^{-1}B^\mathrm{T}P + Q = 0 \tag{3.33}$$

As can be seen, the optimal LQR feedback matrix K does not depend on the solution and may therefore be calculated prior to the simulation for the various representative trim states. To achieve better tracking performance the LQR controller has been augmented with a simple PI controller:

$$\delta \mathbf{u}_{\mathrm{PI}} = -\mathrm{diag}(K_1^{\mathrm{P}}\ K_2^{\mathrm{P}}\ K_3^{\mathrm{P}}\ K_4^{\mathrm{P}})\mathbf{e} - \mathrm{diag}(K_1^{\mathrm{I}}\ K_2^{\mathrm{I}}\ K_3^{\mathrm{I}}\ K_4^{\mathrm{I}}) \int_{t-\Delta t}^{t} \mathbf{e}\ \mathrm{d}t \tag{3.34}$$

where $\mathbf{e}$ is the tracking error. The three coordinates of the trajectory $\mathbf{x}_{\mathrm{e}}$ and the heading angle Ψ are specified. The expression of the error is then:

$$\mathbf{e} = \left\{ \begin{array}{c} \mathbf{x}_{\mathrm{e}} - \hat{\mathbf{x}}_{\mathrm{e}} \\ \Psi - \hat{\Psi} \end{array} \right\} \tag{3.35}$$

where $\mathbf{x}_{\mathrm{e}}$ and $\hat{\mathbf{x}}_{\mathrm{e}}$ are the actual and desired trajectories in earth frame of reference, Ψ and $\hat{\Psi}$ the actual and desired headings. The coefficients K_i^{P} and K_i^{I} $(i = 1, \ldots, 4)$ are, respectively, the proportional and integral gains.

The values of the control angles at each time instant are therefore given by their value in the reference trimmed condition plus the feedback given by the LQR and PI controllers:

$$\mathbf{u} = \mathbf{u}^* + \delta \mathbf{u}_{\mathrm{LQR}} + \delta \mathbf{u}_{\mathrm{PI}} \tag{3.36}$$

3.3.4 Other Pilot Models

Unlike some other models, the LQR method provides optimal tracking without attempting to model the behaviour of a human pilot. The structural model is shown in figure 3.5 and is one of the most widely used pilot model. It provides a biological description of the human pilot, albeit simplified, in a closed-loop system, integrating vestibular and proprioceptive feedbacks, time delay and vehicle dynamics model. The vestibular system is part of the inner ear and is responsible for sensing body accelerations (linear and angular accelerations, angular rotation). It is a very sensitive and complex system: the perception depends on the level of acceleration as well as the duration, with different thresholds depending on the direction. During prolonged rotations, the apparent acceleration may decrease, leading to a false estimate of the rotation rate and an opposite post-turn illusion when the rotation stops. The gravity is also felt together with other accelerations and may give the pilot a false estimate of his position. The proprioceptive system gathers all the senses perceived through muscles and skin. It is felt by the pilot through the stick, pedals, seat, etc. and provides information about spatial position but also aircraft situation.

Optimal Control Models (OCM) consider the pilot as behaving in an optimal manner, while being subject to his psycho-physical limitations, modelled as a time delay and external noises (Figure 3.6). The motor and observation noises aim to model

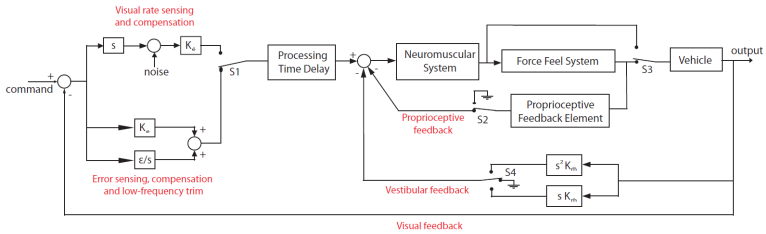

Figure 3.5: Compensatory structural model of the human pilot as proposed by Hess [68] (from Lone and Cook [69])

discrepancies in applying the desired command, distribution of attention towards each instrument, etc. that help modelling the pilot behaviour.

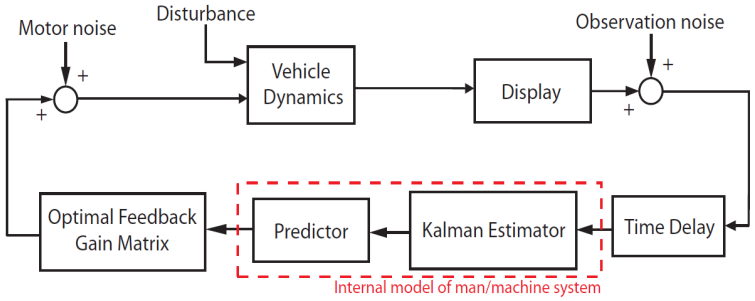

Figure 3.6: Compensatory optimal model of the human pilot as proposed by Kleinman [70] (from Lone and Cook [69])

The paper by Hess [71] presents the implementation of a pilot model for the simulation of a helicopter operating near a ship, with the introduction of models for the ship motion and the atmospheric turbulence.

3.3.5 Response to Pilot Inputs

Most trimming methods and pilot models rely on linearised models as they provide a good approximation of the aircraft instantaneous response for a given flight condition. The response of a free-flying aircraft to a disturbance in pilot input was calculated using the linear model and the full non-linear aircraft is shown in figure 3.7.

The disturbance is a two-second sinusoidal command of the main rotor collective angle with a integral value of zero. The linear model response is smooth and non-diverging by nature and predicts a gain in altitude. The full model is diverging due to the instable nature of the helicopter system.

The linear model only models the instantaneous response of the aircraft and therefore accurately describes the initial phase of the manoeuvre, between 1 and 1.5 seconds. However, the overall positive effect of the first half of the manoeuvre translates into a positive overall velocity for the aircraft, which is then cancelled-out

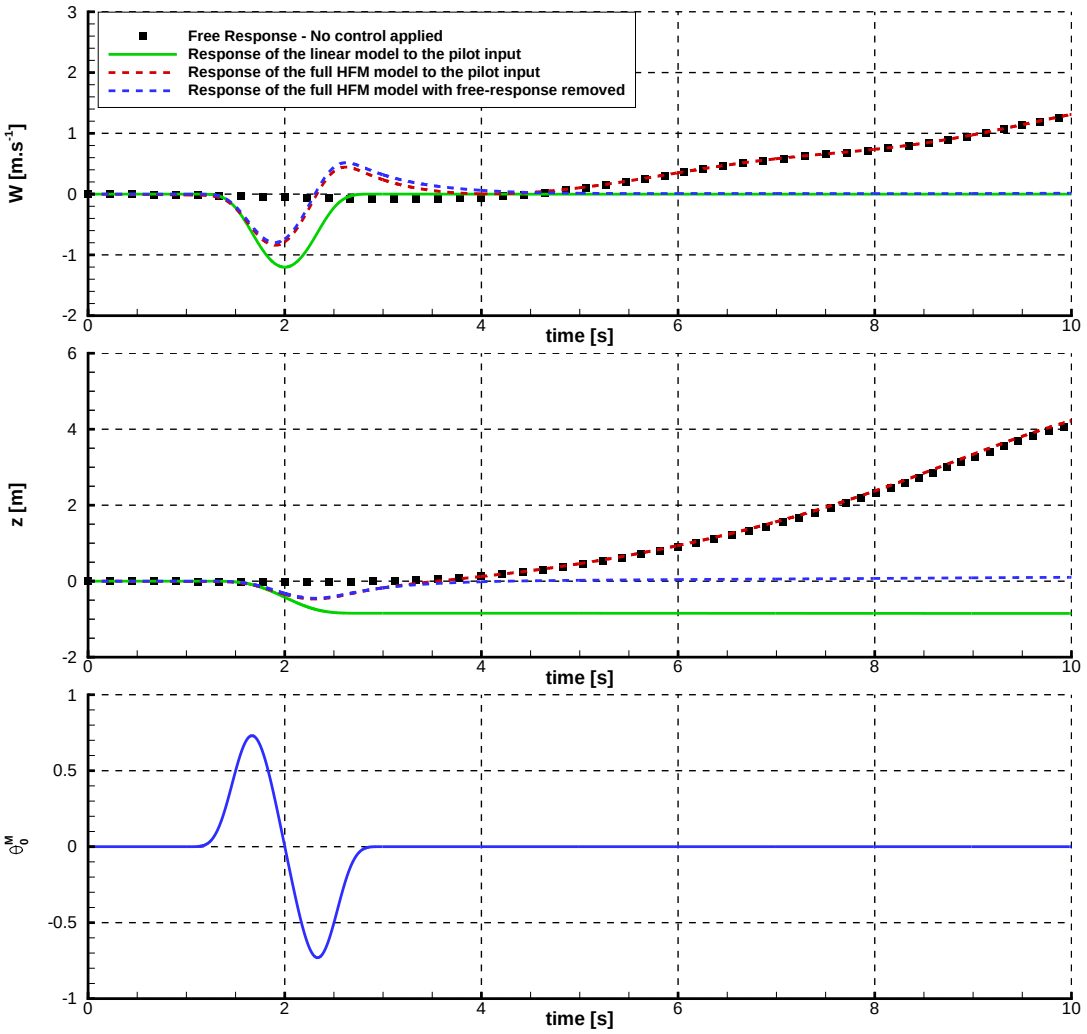

Figure 3.7: Pilot input and Aircraft response to a single-channel sinusoidal input on the main-rotor collective. Response of the linear model and HFM full aircraft are plotted. The free-flight response of the helicopter is also plotted and used to correct the response of the full aircraft.

during the second half and results in a gain of altitude. In the case of the full model, the first half of the manoeuvre translates into an acceleration, until a new equilibrium is reached, resulting in a given climb velocity and zero acceleration. The opposite effect occurs during the second half and returns the aircraft to its original position.

3.3.6 ADS33 Standard Manoeuvres

The Aeronautical Design Standard 33 (ADS33) document [72] provides comprehensive specifications regarding the performance and handling qualities requirements for military rotorcraft. In particular, it provides a set of elementary manoeuvres that any rotorcraft should be able to perform with a prescribed margin of error. The following sections present the results obtained by inverse modelling using 4 typical

ADS33 manoeuvres. Two different aircraft are simulated: the BO105 for which a linear model has been made available and largely used in the literature [64, 71, 73] and the Sea King helicopter for which a linear model was derived around the initial trimmed condition using HFM. The main difference between the two aircraft is the direction of rotation of the main rotor, with the Sea King rotor's advancing blade being on the right hand side from the pilot point of view. As a result, the θ_{1s} harmonic of the rotor changes sign between the two sets of results. Additionally, a typical landing manoeuvre has been designed that consists in a decelerating descent parallel to the ship midline, a translation above the deck and a final vertical descent and touchdown. Results highlight the benefits and limitations of the method and its applicability to more complex problems.

Lateral Reposition - ADS33/3.11.8

According to the ADS33, the manoeuvre starts in a stabilised hover at 35 ft wheel height (or no greater than 35 ft external load height) with the longitudinal axis of the rotorcraft oriented 90 degrees to a reference line marked on the ground. The pilot then initiates a lateral acceleration to approximately 35 knots groundspeed followed by a deceleration to laterally reposition the rotorcraft in a stabilised hover 400 ft down the course within a specified time. The position and velocities are prescribed to the system and shown in figure 3.8. The aircraft accelerates until it reaches 18 $m.s^{-1}$ lateral speed then decelerates and stops 120 m down the course. The total duration of the manoeuvre is 18 seconds.

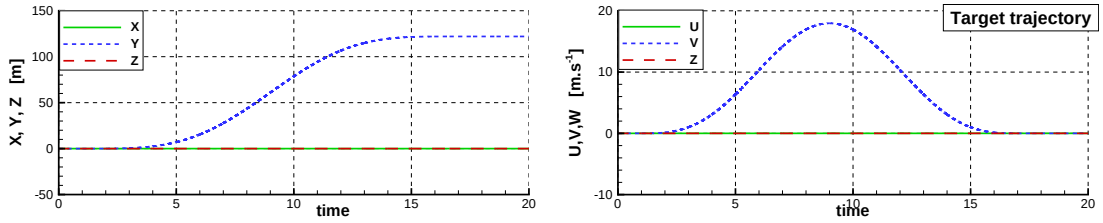

(a) Positions (b) Velocities

Figure 3.8: Positions and velocities prescribed to HFM for the lateral reposition manoeuvre. reference ADS-33/3.11.8

The history of the helicopter behaviour and predicted pilot inputs are shown figure 3.9.

The main characteristic of this manoeuvre is a large excursion in roll angle, up to about 25 degrees for both the Sea King and the BO105 aircraft. The roll/pitch coupling induces a response in pitch angle that is opposed in sign due to the inverted direction of rotation of the main rotor.

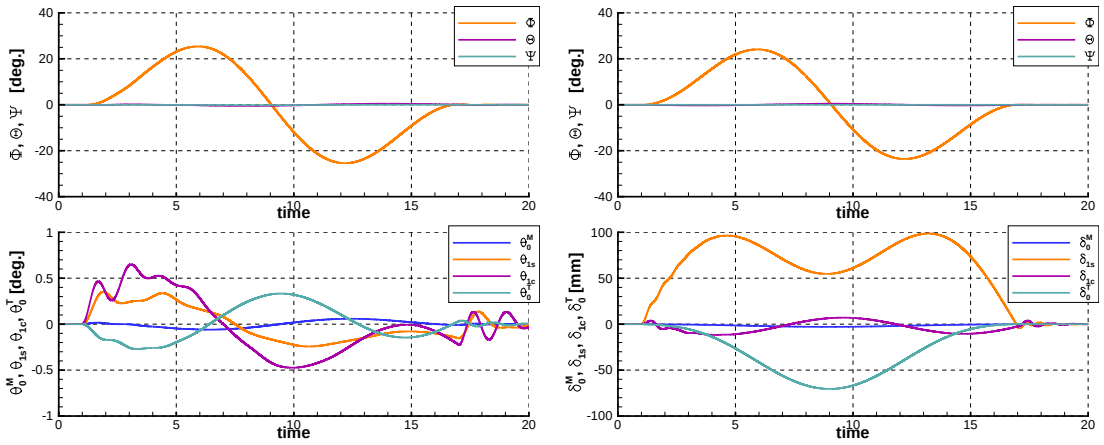

(a) Sea King (b) BO-105

Figure 3.9: Helicopter attitude and controls predicted through inverse-modelling for the lateral reposition manoeuvre. reference ADS-33/3.11.8

The lateral speed induces an important change in tail rotor inflow velocity and therefore an important correction is applied, as can be seen in the history of pedal activity. One important difference between the two aircraft is the lateral cyclic angle. For the Sea King, a small action is applied and cancelled out shortly after, while the BO105 pilot needs to apply a greater action and maintain the command throughout the manoeuvre. This suggests the BO105 has a more stable behaviour and cancelling the action would cause the helicopter to return to hover while the Sea King maintains its attitude when the controls return to a neutral position. Little action in terms of collective is required for this manoeuvre for both aircraft. In both cases the collective needs reducing as the aircraft accelerates. The collective is slightly increased at the end of the manoeuvre for the Sea King, possibly because of a greater inertia.

Acceleration and Deceleration - ADS33/3.11.11

According to the ADS33, the manoeuvre starts from a stabilised hover. In the GVE, the pilot rapidly increases power to approximately maximum, maintains altitude constant with pitch attitude, and holds collective constant during the acceleration to an airspeed of 50 knots. Upon reaching the target airspeed, he initiates a deceleration by aggressively reducing the power and holding altitude constant with pitch attitude. The peak nose-up attitude should occur just before reaching the final stabilised hover. In the DVE, the pilot accelerates to a groundspeed of at least 50 knots, and immediately decelerate to hover over a defined point. The maximum nose-down attitude should occur immediately after initiating the manoeuvre, and the peak nose-up attitude should occur just before reaching the final stabilised hover. The manoeuvre is then completed

with a stabilised hover for 5 seconds over the reference point at the end of the course.

The position and velocities are prescribed to the system and shown figure 3.10. The aircraft accelerates forward until it reaches about 30 $m.s^{-1}$ longitudinal speed then decelerates and stops 200 m down the course. The total duration of the manoeuvre is 18 seconds.

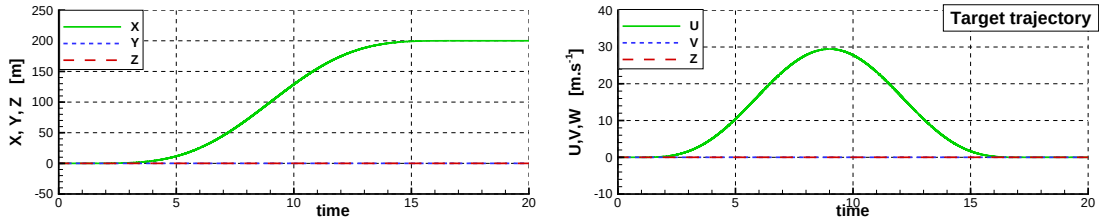

(a) Positions (b) Velocities

Figure 3.10: Positions and velocities prescribed to HFM for the acceleration-deceleration manoeuvre. reference ADS-33/3.11.11

The history of the helicopter behaviour and predicted pilot inputs are shown figure 3.11.

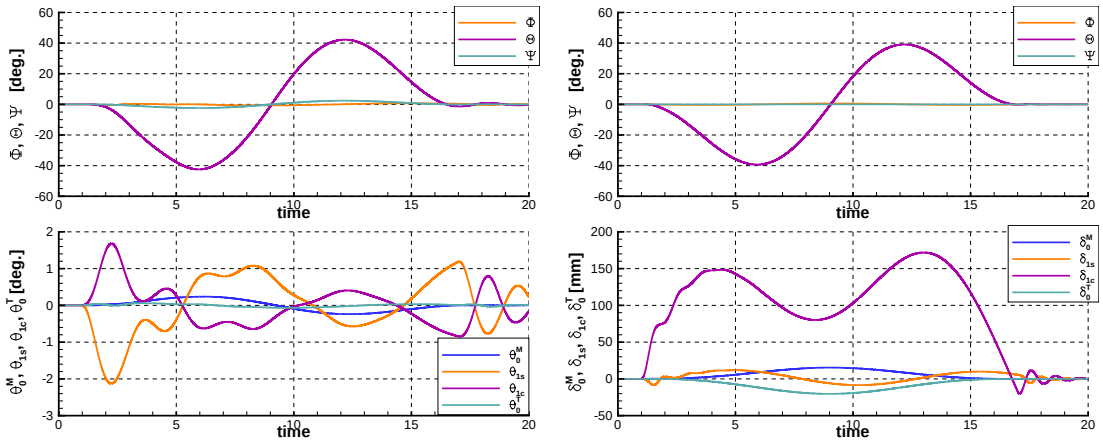

(a) Sea King (b) BO-105

Figure 3.11: Helicopter attitude and controls predicted through inverse-modelling for the acceleration-deceleration manoeuvre. reference ADS-33/3.11.11

The main characteristic of the manoeuvre is a large excursion in terms of pitch angle, reaching about 40 degrees in both cases. The roll and yaw angles deviations are the result of roll/pitch coupling and increase of main rotor torque but have much smaller amplitude. Similarly to the previous manoeuvre, a large excursion in cyclic - longitudinal in this case - is noticed for the BO105. This suggests that the aircraft model needs large and constant inputs to maintain forward flight while the Sea King model only needs an action to initiate the manoeuvre. Unlike the previous case, the collective needs increasing as the attained airspeed is much greater.

In both cases, the history of control highlights the typical limitations of the inverse modelling method. The linear model of both aircraft is defined for hover and slow flight such as “taxing” but the manoeuvre extends outside this domain. This leads to two phenomena: for the BO105 case the controls reach unrealistic amplitudes while for the Sea King it triggers oscillations due to the aggressiveness of the manoeuvre that are not damped efficiently.

Slalom - ADS33/3.11.9

According to the ADS33, the pilot initiates the manoeuvre in level unaccelerated flight and lined up with the center-line of the test course. He then performs a series of smooth turns at 500-ft intervals (at least twice to each side of the course). The turns shall be at least 50 ft from the center-line, with a maximum lateral error of 50 ft. The manoeuvre is to be accomplished below the reference altitude. The manoeuvre is then completed along the center-line, in coordinated straight flight.

The position and velocities are prescribed to the system and shown figure 3.12. The longitudinal velocity is kept constant at 26 $m.s^{-1}$ and only the lateral position is modified, using a sinusoidal function. The heading of the aircraft is kept to zero in this case but could be calculated so as to follow the direction of the trajectory.

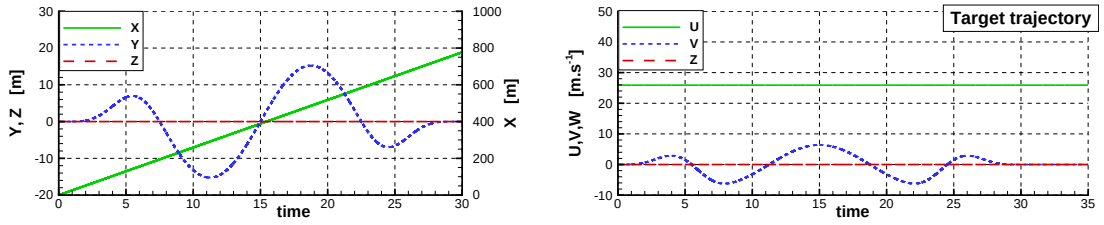

Figure 3.12: Positions and velocities prescribed to HFM for the slalom manoeuvre. reference ADS-33/3.11.9

The main characteristic of this manoeuvre is its aggressiveness in terms of roll angle, reaching up to 30 degrees. The behaviour of both aircraft is similar, although some oscillations can be noticed for the Sea King that are due to the aggressiveness of the manoeuvre, like in the longitudinal acceleration/deceleration case.

The oscillations that appeared in the pitch angle history are also present in the history of cyclic angles and it is difficult to draw conclusions in terms of pilot control. For the Sea King aircraft, the collective is consistently higher as the linear model is built around the forward flight case but the actual velocity during the manoeuvre is higher. The pedal history is similar for both aircraft with variations that correspond to the need to maintain heading despite the change in lateral velocity.

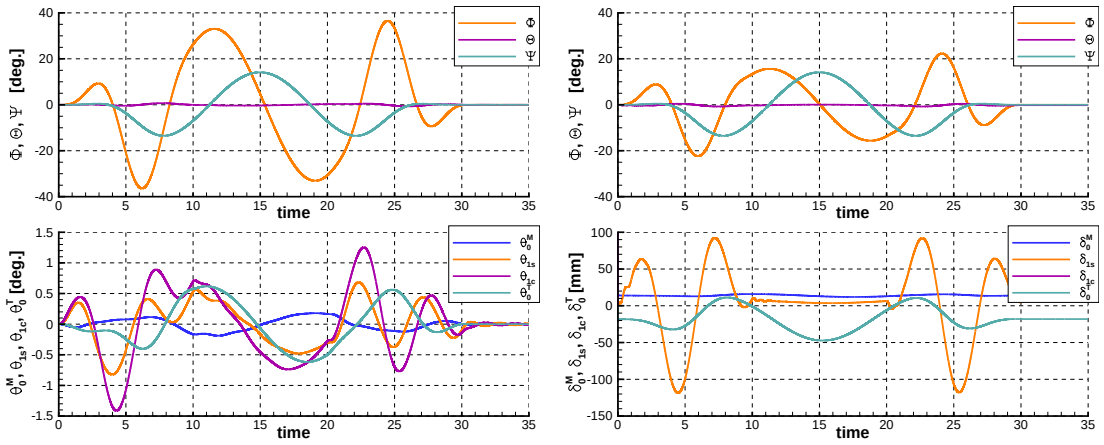

(a) Sea King (b) BO-105

Figure 3.13: Helicopter attitude and controls predicted through inverse-modelling for the slalom manoeuvre. reference ADS-33/3.11.9

The BO105 suffers from the use of the same linear model, tuned around hover, for a typical forward flight case. This leads to unrealistic controls, mainly in terms of cyclic.

Typical Landing Manoeuvre

A typical landing manoeuvre is simulated with a duration of 45 seconds. Approach: 100m forward, 20m downward, duration 15 seconds. Lateral reposition: 30m, 10 seconds. Descent: 20m, 20 seconds.

The position and velocities are prescribed to the system and shown figure 3.14. The three branches of the manoeuvre are clearly visible, with reasonable deviations when transitioning from one branch to the next. The history of the helicopter behaviour and predicted pilot inputs are shown figure 3.15. Each branch can be considered a standard steady-flight condition and, to some extent, they show similar behaviour as have been described previously. However, this manoeuvre is aggressive by design and the successive changes in trajectory and flight state induce oscillations and excursions that are likely unrealistic and make any conclusion in terms of pilot control very difficult.

3.3.7 Inverse Modelling Performances and Limitations

Inverse modelling is an efficient way to estimate the pilot activity from a prescribed flight path, however it suffers from several limitations. The linear model of the aircraft is usually valid around the trimmed flight condition of reference, this causes the method to misbehave and give unrealistic pilot controls in case the manoeuvre is too aggressive (See landing case 3.3.6) or away from the trimmed condition (See BO105

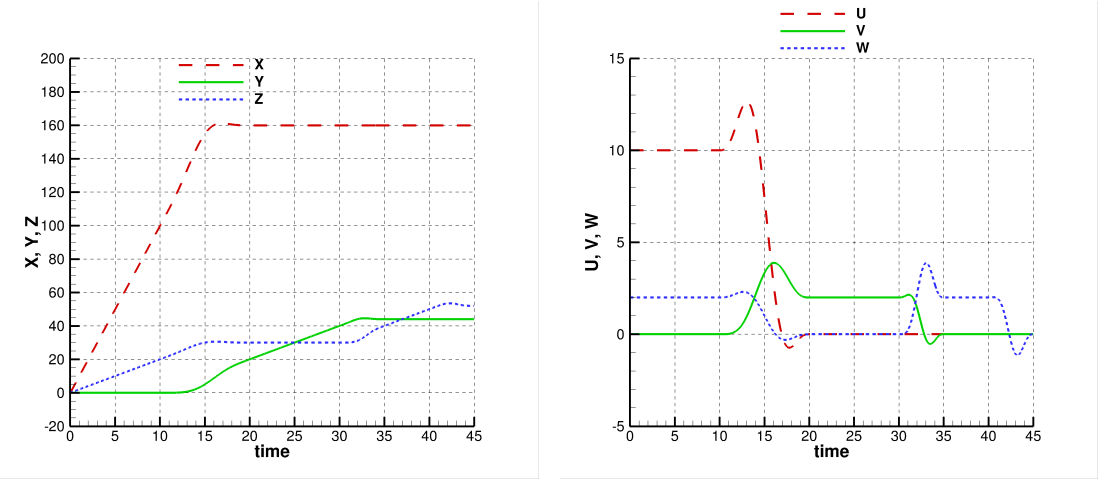

(a) Positions

(b) Velocities

Figure 3.14: Positions and velocities prescribed to the SYCOS method. Typical Landing Manoeuvre. Duration: 45s

results for the slalom case 3.3.6). As mentioned in Hess and Gao [74], the prescribed manoeuvre also needs to be smooth enough and high-order derivatives need to be continuous (typically $\mathscr{C}^2$) so that there are no discontinuities in acceleration throughout the manoeuvre. Any discontinuity causes the model to oscillate by a large amount, or diverge.

Despite its limitations, the method provides a realistic estimate of the pilot inputs required to follow a specific trajectory. It can then be used to devise more advanced control models such as the SYCOS method. The SYCOS method consists in adding a simple Compensatory Tracking Method (CTM) that permits to adjust the target trajectory fed to the inverse model and therefore provide pilot controls even if the helicopter does not behave exactly as the linear mode suggests.

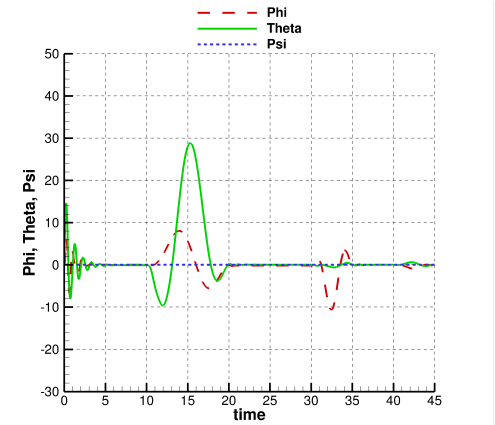

(a) Attitude - BO105

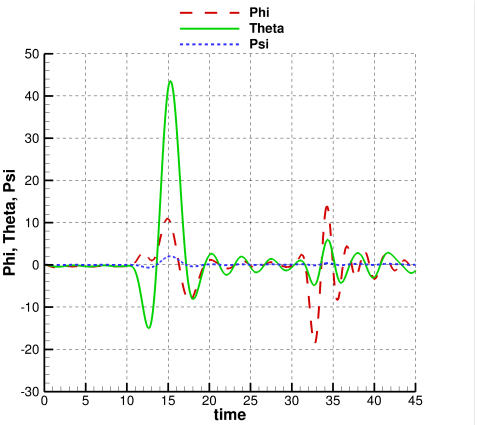

(b) Attitude - Sea King

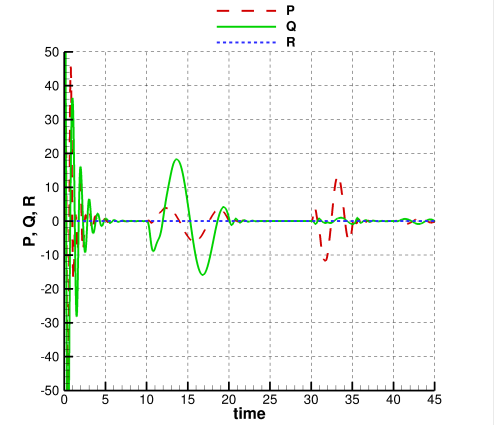

(c) Rotation Rates - BO105

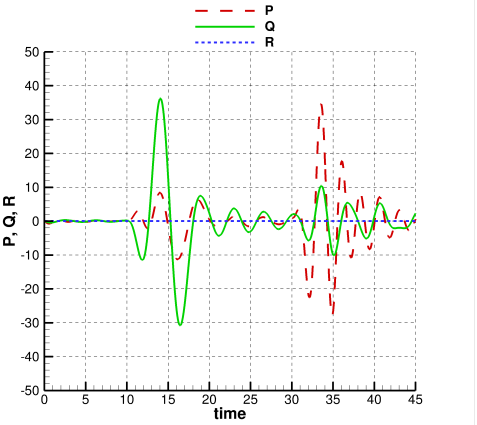

(d) Rotation Rates - Sea King

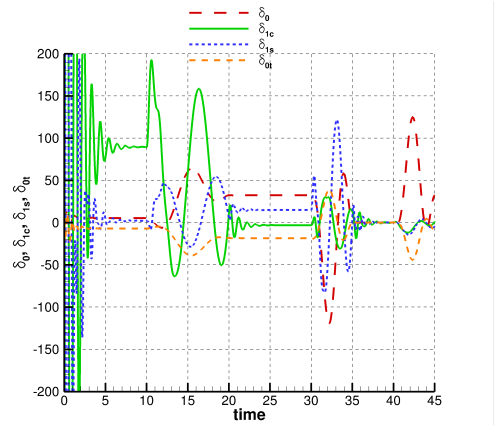

(e) Controls - BO105

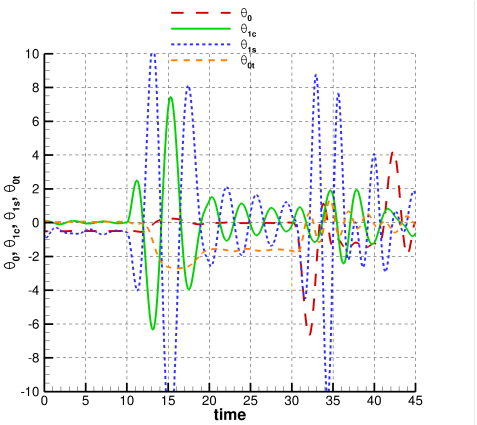

(f) Controls - Sea King

Figure 3.15: Pilot inputs and helicopter response. Responses are in meters, seconds, degrees. Controls are measured in degrees for the Sea King, cm at pilot hand for the BO105. Typical Landing Manoeuvre. Duration: 45s

3.4 Aircraft Trimming

Trimming is a recurrent problem for rotorcraft simulation. It consists in determining the appropriate set of pilot inputs and aircraft attitude so that the aircraft maintains steady hover or forward flight. The main problem arises from the fact that the trim condition is not always unique and several combinations of parameters may lead to valid trim states. Typical parameters are the 4 pilot inputs: collective, lateral and longitudinal cyclic and pedal, as well as the aircraft attitude in pitch, roll and yaw.

3.4.1 Model-Based Trimmer

A classic approach to the trimming problem consists in computing the Jacobian matrix that links helicopter attitude to pilot inputs and use it to cancel forces and moments. While this method is efficient, it usually finds only one trim state that depends on the initial trim state provided.

Other trimming methods have also been developed based on genetic algorithms or the non-linear Least-Square Minimisation Levenberg-Marquardt algorithm.

The current trimming algorithm is based on a Newton method for solving a system of 6 equations/6 unknowns. The derivatives of $\dot{u}$, $\dot{v}$, $\dot{w}$, $\dot{p}$, $\dot{q}$ and $\dot{r}$ with respect to θ_0^{M}, θ_{1c}, θ_{1s} θ, Φ and θ_0^{T} forms a 6×6 jacobian matrix J. The derivatives are computed using centered, second order differences and $\varepsilon = 10^{-8}$ and the jacobian matrix J is inverted before computing the updated values of the trim state:

$$J = \left(\frac{df_i}{dx_j}\right)_{i,j} = \begin{bmatrix} \frac{d\dot{u}}{d\theta_0} & \frac{d\dot{u}}{d\theta_{1c}} & \frac{d\dot{u}}{d\theta_{1s}} & \frac{d\dot{u}}{d\theta^{body}} & \frac{d\dot{u}}{d\Phi^{body}} & \frac{d\dot{u}}{d\theta_0^t} \\ \frac{d\dot{v}}{d\theta_0} & \frac{d\dot{v}}{d\theta_{1c}} & \frac{d\dot{v}}{d\theta_{1s}} & \frac{d\dot{v}}{d\theta^{body}} & \frac{d\dot{v}}{d\Phi^{body}} & \frac{d\dot{v}}{d\theta_0^t} \\ \frac{d\dot{w}}{d\theta_0} & \frac{d\dot{w}}{d\theta_{1c}} & \frac{d\dot{w}}{d\theta_{1s}} & \frac{d\dot{w}}{d\theta^{body}} & \frac{d\dot{w}}{d\Phi^{body}} & \frac{d\dot{w}}{d\theta_0^t} \\ \frac{d\dot{p}}{d\theta_0} & \frac{d\dot{p}}{d\theta_{1c}} & \frac{d\dot{p}}{d\theta_{1s}} & \frac{d\dot{p}}{d\theta^{body}} & \frac{d\dot{p}}{d\Phi^{body}} & \frac{d\dot{p}}{d\theta_0^t} \\ \frac{d\dot{q}}{d\theta_0} & \frac{d\dot{q}}{d\theta_{1c}} & \frac{d\dot{q}}{d\theta_{1s}} & \frac{d\dot{q}}{d\theta^{body}} & \frac{d\dot{q}}{d\Phi^{body}} & \frac{d\dot{q}}{d\theta_0^t} \\ \frac{d\dot{r}}{d\theta_0} & \frac{d\dot{r}}{d\theta_{1c}} & \frac{d\dot{r}}{d\theta_{1s}} & \frac{d\dot{r}}{d\theta^{body}} & \frac{d\dot{r}}{d\Phi^{body}} & \frac{d\dot{r}}{d\theta_0^t} \end{bmatrix} \tag{3.37}$$

where $x = (\theta_0^M \theta_{1c} \theta_{1s} \theta \Phi \theta_0^T)^{\mathbf{T}}$ and $f = (\dot{u}\ \dot{v}\ \dot{w}\ \dot{p}\ \dot{q}\ \dot{r})^{\mathbf{T}}$. The system to solve then reads:

$$[\Delta\theta_0^M \Delta\theta_{1c} \Delta\theta_{1s} \Delta\theta_0^T]^{\mathbf{T}} = J^{-1} \times [\Delta\dot{w} \Delta\dot{p} \Delta\dot{q} \Delta\dot{r}]^{\mathbf{T}} \tag{3.38}$$

The values of f are averaged over a $\frac{1}{N_{\text{blades}}}$ section of revolution to have meaningful loads. Less than 10 steps are usually enough to get convergence.

3.4.2 Hybrid Trimmer

The classic trimming method is based on the Helicopter model provided to HFM. At each iteration, it calculates the jacobian of the problem and the update for the controls based on the current estimate of the loads, aims to minimise them, or reach a prescribed target. The hybrid trimmer uses the last-computed jacobian but replaces the estimated loads by the loads calculated by the CFD solver. After convergence of the hybrid trimmer, the helicopter is trimmed, as far as the CFD loads are concerned.

The Sea King helicopter is trimmed in forward flight with a speed of 10 $m.s^{-1}$. The results in figure 3.16 show that the method constantly adjusts the pilot inputs to minimise the residual loads on the aircraft. The large overshoot in cyclic updates suggests that the Jacobian matrix do not accurately capture the coupling between the two cyclic angles and causes the solution to constantly vary around the correct trim state. However, the method is stable and the controls do not diverge so that a confinement method could be applied to progressively reduce the deviation and help the convergence. Future work will be carried out to ensure a better convergence of the method.

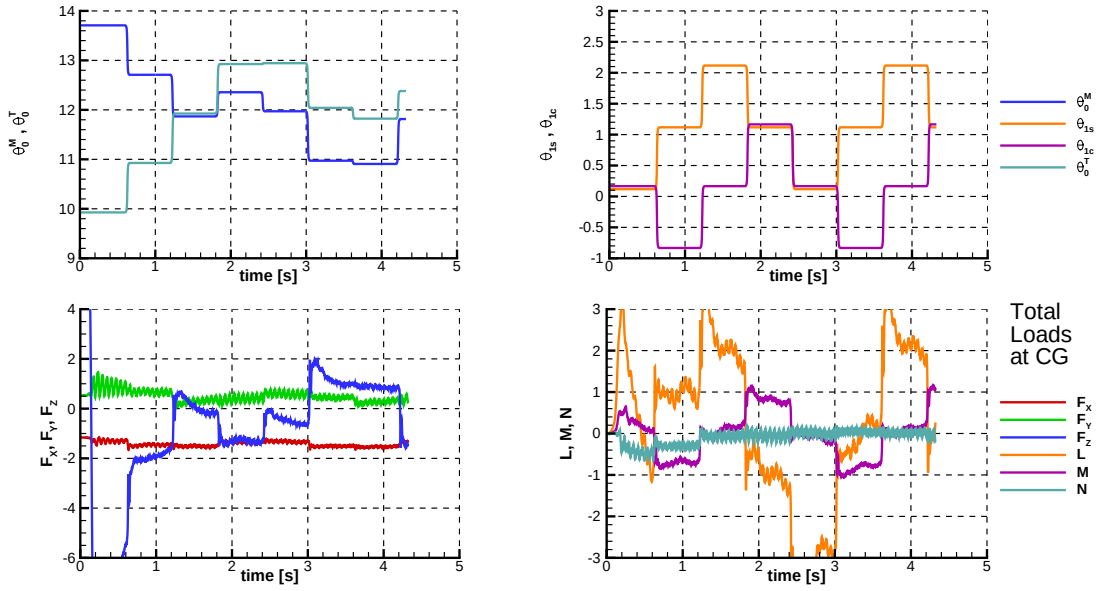

Figure 3.16: Convergence of pilot inputs and residual forces and moments on the aircraft during trimming in forward flight $u = 10\ m.s^{-1}$. Blade angles in degrees, forces and moments in arbitrary units.

Parameter	Standalone FM model	Coupled HFM/CFD
6DOF fuselage	✓	✓
Articulated blades	✓	✓
Atmospheric conditions	✓	✓
Inflow	✓(Linear model)	✓
Appendices	✓(bi-linear model)	✓
Blade aerodynamics	✓(Blade Element Theory)	✓
Rotor/fuselage interaction	✗	✓
Blade-tip losses	✗	✓
3D effects	✗	✓
Flexible body parts	✗	✗

Table 3.2: Comparison between standalone flight mechanics and CFD coupling approximations.

3.5 Developing the CFD/HFM Framework

This section presents the implementation of the flight dynamics model presented previously into the CFD framework HMB2. The Conventional Serial Staggered (CSS) approach was used, for which data is exchanged at every time iteration of the simulation, but is kept fixed between the Newton steps of the CFD solver. The communication between the two codes is shown in figure 3.17. After each CFD step the loads on each part of the aircraft are computed and passed on to the flight mechanics solver, which computes the position and attitude of the aircraft for the next time step. The grid is then moved to the given position.

3.5.1 Inertial and Non-Inertial Frames of Reference

A frame of reference is said inertial if an object in constant, rectilinear motion in this frame of reference undergoes no acceleration. The laws of physics take the same form in every inertial frame of reference and are homogeneous, isotropic and time-independent. In the opposite case, the frame of reference is “non-inertial”: in the presence of acceleration, the typical laws of physics are non-isotropic, non-homogeneous and additional effects appear such as centrifugal and Coriolis forces.

The Helicopter Multi-Block solver was designed to solve the non-dimensionalised Navier-Stokes equations for the case of forward-flying rotors in an inertial frame of reference commonly known as “wind-tunnel frame of reference”. The forward motion of the rotor is applied through the boundary conditions at the far-field so that the center of rotation is fixed. The rotor, however, is rotating around the shaft axis and undergoes acceleration.

For a flux vector The Navier-Stokes equations in integral form in the arbitrary Lagrangian Eulerian formulation read:

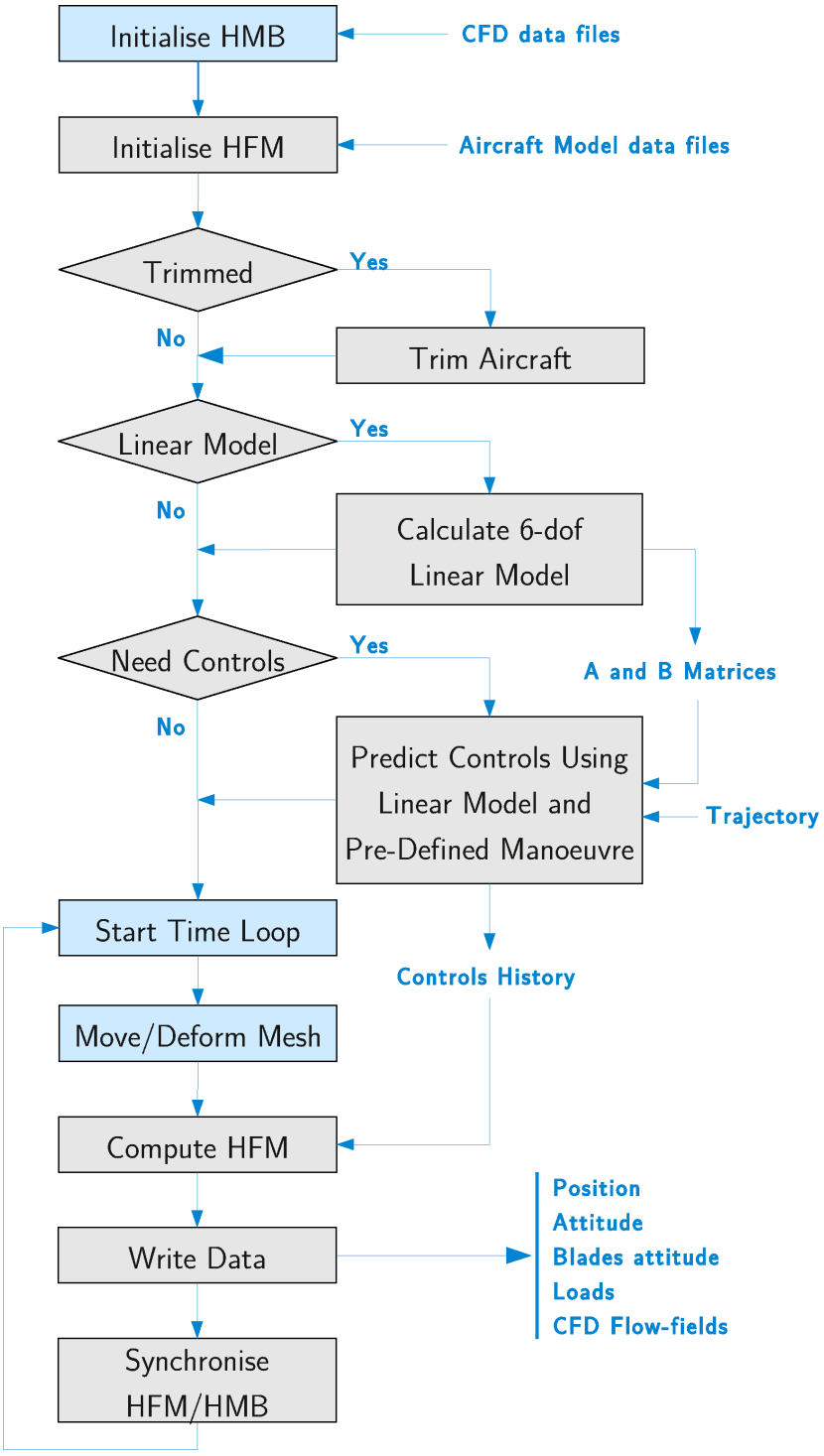

Figure 3.17: Flowchart of HMB2 and FM code communication.

$$\frac{d}{dt}\int_{V(t)} \mathbf{w} dV + \int_{\partial V(t)} \left(\mathbf{F}^i(\mathbf{w}) + \mathbf{F}^v(\mathbf{w})\mathbf{n} dS\right) = \mathbf{S} \tag{3.39}$$

with $\mathbf{F}^i$ and $\mathbf{F}^v$ the inviscid and viscous fluxes respectively. In the absence of volume forces and for an inertial frame of reference, $\mathbf{S} = \mathbf{0}$. The acceleration of the rotor is

taken into account when adding a mesh velocity to the velocity components of the vector of conserved variables $\mathbf{w} = [\rho, \rho u, \rho v, \rho w, \rho E]^{\mathbf{T}}$.

In the case of a rotor in hover, a blade-fixed frame of reference is chosen. It is inertial as the blade is in constant acceleration due to its rotation. In this case the mesh velocities comes directly as $\mathbf{u}_{\text{ref}} = \omega \times \mathbf{r}$ and the source term is $\mathbf{S} = [0, -\rho\omega \times \mathbf{u}_h]$.

Another inertial frame of reference is the "earth-fixed frame of reference". By definition it undergoes no acceleration with respect to the wind-tunnel frame of reference and can therefore replace it without reformulation of the solver. This particular frame of reference is useful when considering manoeuvring aircraft, as various regions of the flow undergo various accelerations. The non-dimensionalisation of the problem is modified as shown in figure 3.18. In manoeuvring flight, the advance ratio is not unique and is removed from the definition of the rotation velocity. It is applied through the farfield and the grid motion described in the nest section. The blade tip velocity and Mach number are chosen as reference values and the grid velocity comes from the fuselage velocities and rotations, as well as from the rotor rotation if in the rotor grid. The far-field velocity can be set to zero, or any value that accounts for additional effects (wind, constant velocity of the background, etc.)

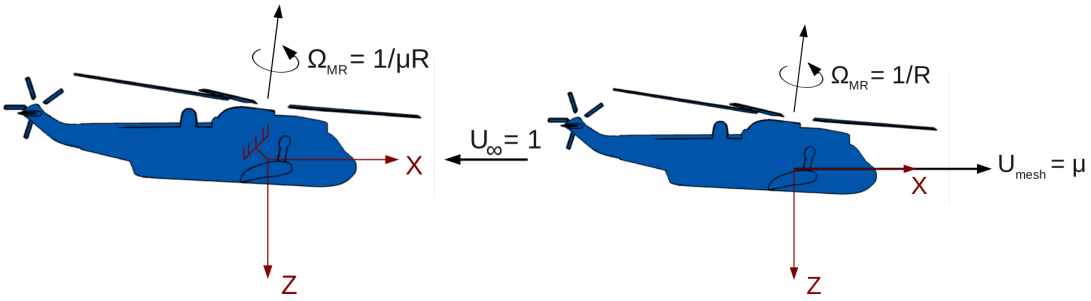

Figure 3.18: Wind-tunnel and earth-fixed frames of reference and differences in formulation.

3.5.2 Grid Motion Method

To simulate the flow around rotors in hover or forward flight, HMB2 uses a grid motion/deformation method for the blade articulations coupled with a rigid-body grid rotation. A general grid motion method is also implemented and can be used to simulate a pitching wing for example. The diagram of figure 3.19 shows the different cases that can be simulated.

The more general "Multi-body rotor case" is required for the simulation of manoeuvring aircraft. The wind-tunnel frame of reference is substituted with an earth-fixed frame of reference and a consequent change in the formulation is made as the rotor advance ratio is no longer uniquely defined:

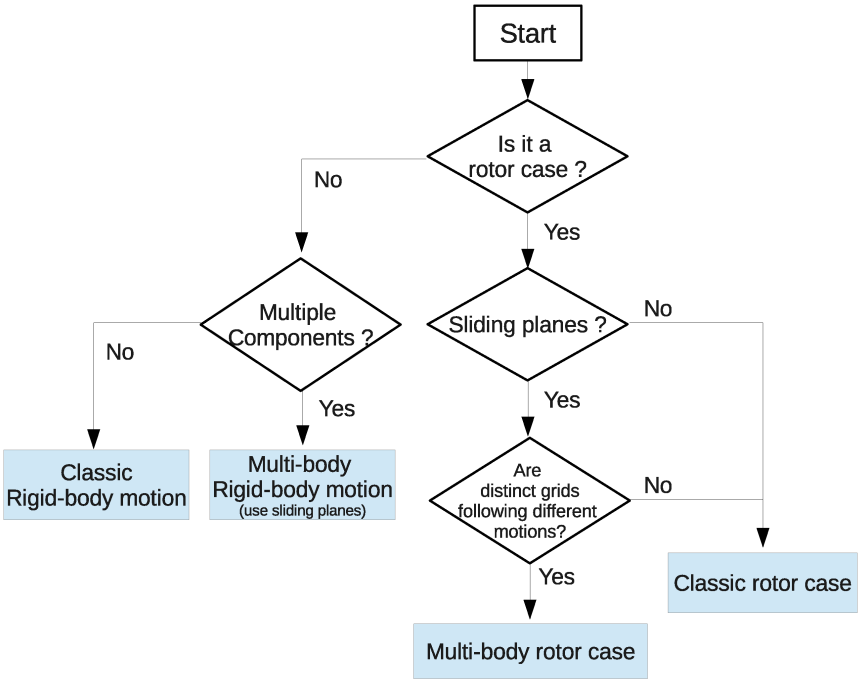

Figure 3.19: Diagram for Rotors and Rigid-Body motion cases

Non-dimensional variable	**Baseline HMB2**	**HMB2 in vehicle mode**	**Helicopter Flight Mechanics**
Rotational velocity	$\omega = \frac{1}{\mu R}$ ($V_{tip} = \frac{1}{\mu}$)	$\omega = \frac{1}{R}$ ($V_{tip} = 1$)	$\omega = \frac{V_{tip}}{R}$
Time step	$dt = \frac{2\pi\mu R}{N_{steps/cycle}}$)	$dt = \frac{2\pi R}{N_{steps/cycle}}$)	$dt = \frac{2\pi R}{N_{steps/cycle} V_{tip}} = \frac{2\pi}{\omega N_{steps/cycle}}$
Reference length	1 rotor chord length	1 meter	1 meter
Azimuthal step	$\Delta\Psi^{main} = \frac{360}{N_{steps/cycle}} = \omega dt$	$\Delta\Psi^{main} = \frac{360}{N_{steps/cycle}} = \omega dt$	$\Delta\Psi^{main} = \frac{360}{N_{steps/cycle}} = \omega dt$

Table 3.3: Definitions and correspondences between HFM and HMB2 codes. V_{tip} can be arbitrary but should be consistent with the provided Mach number.

The non-lifting ONERA rotor [75] is used as test case to validate the change of frame of reference in forward flight.

- 1. Forward-flight at $\mu = 0.5$, $M_{\text{tip}} = 0.625$, $M_\infty = 0.3125$ with no grid motion.
- 2. Forward-flight at $\mu = 0.25$, $M_{\text{tip}} = 0.625$, $M_\infty = 0.15625$ with -x translation at $U = 1$.
- 3. Forward-flight at $\mu = 0.25$, $M_{\text{tip}} = 0.625$, $M_\infty = 0.15625$ with x translation at $U = 1$.

The second case corresponds to $U_{\text{farfield}} + U_{\text{grid motion}} = 1 + 1 = 2$, hence $\mu = 0.5$, $M_\infty = 0.3125$.

The third case corresponds to $U_{\text{farfield}} + U_{\text{grid motion}} = 1 - 1 = 0$, hence $\mu = 0$, $M_\infty = 0$. Therefore it corresponds to a hover case, in forward-flight formulation.

Results are shown in figure 3.20. Cases 1 and 2 are equivalent and contours of the pressure coefficient show no difference, despite the differences in formulation. In particular, the Mach number used for the non-dimensionalisation of the solver, $\frac{1}{\gamma M_\infty^2}$, is different.

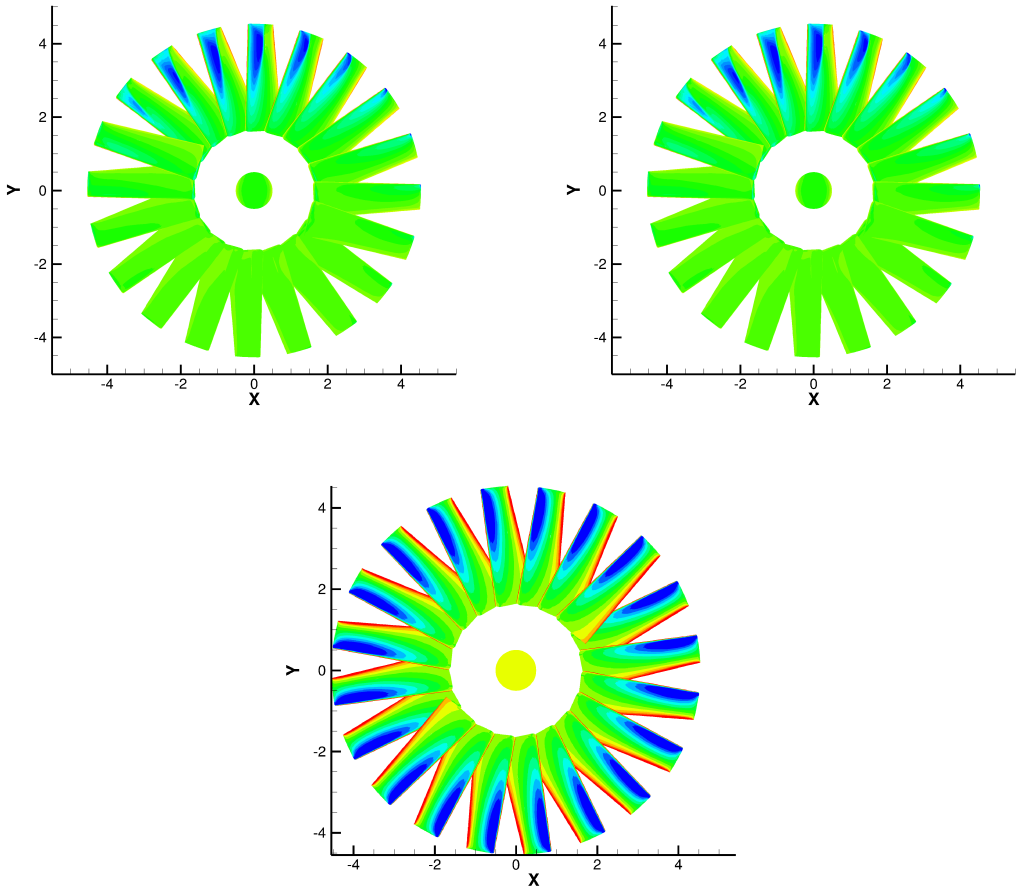

Figure 3.20: Pressure on the blades for cases 1, 2, 3.

Chapter 4

Mathematical Models for Rotor Flow Simulations

4.1 CFD Solver

All computations were performed using the HMB2 flow solver [76] developed at the University of Liverpool. The flow solver has been revised and updated over a number of years and has been successfully applied to a variety of problems including cavity flows, dynamic stall, rotors, wind turbines and full helicopter configurations amongst others. HMB2 is a 3D multi-block structured solver for the Navier-Stokes equations in the 3D Cartesian frames of reference. The Navier-Stokes equations consist of Partial Differential Equations (PDEs) describing the laws of conservation for:

- mass (continuity equation),
- momentum (Newton's 2nd Law), and
- energy (1st Law of Thermodynamics).

The continuity equation simply states that the mass must be conserved. In Cartesian coordinates, x_i, this is written as

$$\frac{\partial \rho}{\partial t} + \frac{\partial (\rho u_i)}{\partial x_i} = 0 \tag{4.1}$$

where ρ is the density of the fluid, t is the time and u_i is the velocity vector. In the above, Einstein's notation is used, which implies summation for repeated indices.

The second conservation principle states that momentum must be conserved. It is written in Cartesian coordinates as

$$\frac{\partial (\rho u_i)}{\partial t} + \frac{\partial \left(\rho u_i u_j\right)}{\partial x_j} = \rho f_i - \frac{\partial p}{\partial x_i} + \frac{\partial \tau_{ij}}{\partial x_j} \tag{4.2}$$

where f_i represents body forces, p the pressure and τ_{ij} the Newtonian stress tensor, which is defined as

$$\tau_{ij} = \mu \left[\left(\frac{\partial u_i}{\partial x_j} + \frac{\partial u_j}{\partial x_i} \right) - \frac{2}{3} \delta_{ij} \frac{\partial u_k}{\partial x_k} \right] \quad , \tag{4.3}$$

with μ the molecular viscosity and δ_{ij} the Kronecker delta, defined as

$$\delta_{ij} = \begin{cases} 1 & \text{if} \quad \text{i=j} \\ 0 & \text{otherwise} \end{cases} \tag{4.4}$$

The third principle can be written in Cartesian coordinates as

$$\frac{\partial \rho E}{\partial t} + \frac{\partial}{\partial x_j} \left[u_i \left(\rho E + p \right) \right] - \frac{\partial}{\partial x_j} \left(u_i \tau_{ij} - q_j \right) = 0. \tag{4.5}$$

where E is the total energy of the fluid per unit volume, defined as

$$E = \left[e + \frac{1}{2} u_i u_i \right] \tag{4.6}$$

and e is the specific internal energy with $u_i u_i$ representing the kinetic energy.

The heat flux vector, q_i, is calculated using Fourier's Law

$$q_i = -k \frac{\partial T}{\partial x_i} \tag{4.7}$$

where k is the heat transfer coefficient and T is the temperature of the fluid.

An ideal gas approximation is used, and the adiabatic index is set to $\gamma = 1.4$. Sutherland's law is used to assess the viscosity.

4.1.1 Vector Format

These three laws of conservation can be combined and written in the equation shown below, which is referred to as the Navier-Stokes equation of viscous flow. For brevity, vector notation is used

$$\frac{\partial \mathbf{W}}{\partial t} + \frac{\partial \left(\mathbf{F}^i + \mathbf{F}^v \right)}{\partial x} + \frac{\partial \left(\mathbf{G}^i + \mathbf{G}^v \right)}{\partial y} + \frac{\partial \left(\mathbf{H}^i + \mathbf{H}^v \right)}{\partial z} = S \tag{4.8}$$

where $\mathbf{W}$ is the vector of conserved variables and is defined by

$$\mathbf{W} = \left(\rho, \rho u, \rho v, \rho w, \rho E \right)^T \tag{4.9}$$

with the variables ρ, u, v, w, p and E having their usual meaning of density, the three components of velocity, pressure and total energy, respectively. The superscripts i and v in Equation 4.8 denote the inviscid and viscid components of the flux vectors $\mathbf{F}$ (in

the x-direction), **G** (in the y-direction) and **H** (in the z-direction). The inviscid flux vectors, $\mathbf{F}^i$, $\mathbf{G}^i$ and $\mathbf{H}^i$, are given by

$$\begin{aligned}\mathbf{F}^i &= \left(\rho u, \rho u^2 + p, \rho uv, \rho uw, u(\rho E + p)\right)^T \\ \mathbf{G}^i &= \left(\rho v, \rho uv, \rho v^2 + p, \rho vw, v(\rho E + p)\right)^T \\ \mathbf{H}^i &= \left(\rho w, \rho uw, \rho vw, \rho w^2 + p, w(\rho E + p)\right)^T\end{aligned} \tag{4.10}$$

while the viscous flux vectors, $\mathbf{F}^v$, $\mathbf{G}^v$ and $\mathbf{H}^v$, contain terms for the heat flux and viscous forces exerted on the body and can be represented by

$$\begin{aligned}\mathbf{F}^v &= \frac{1}{\mathrm{Re}}\left(0, \tau_{xx}, \tau_{xy}, \tau_{xz}, u\tau_{xx} + v\tau_{xy} + w\tau_{xz} + q_x\right)^T \\ \mathbf{G}^v &= \frac{1}{\mathrm{Re}}\left(0, \tau_{xy}, \tau_{yy}, \tau_{yz}, u\tau_{xy} + v\tau_{yy} + w\tau_{yz} + q_y\right)^T \\ \mathbf{H}^v &= \frac{1}{\mathrm{Re}}\left(0, \tau_{xz}, \tau_{yz}, \tau_{zz}, u\tau_{xz} + v\tau_{yz} + w\tau_{zz} + q_z\right)^T\end{aligned} \tag{4.11}$$

where τ_{ij} are the terms of the viscous stress tensor and S represents source terms. In most calculations, these terms are set to 0, however, for hovering rotors, a fixed grid approach is used and a source term is then added:

$$S = \left[0, -\rho\omega \times \mathbf{u_h}, 0\right]^T \tag{4.12}$$

where $\mathbf{u_h}$ is the local velocity field in the rotor-fixed frame of reference.

Although the Navier-Stokes equations completely describe turbulent flows, the large number of temporal and spatial turbulent scales associated with high Reynolds numbers make it difficult to resolve all the turbulent scales computationally[77]. In such circumstances, the number of turbulent scales are reduced by time averaging the Navier-Stokes equations to give the Reynolds-Averaged Navier-Stokes equations (RANS). This results in additional unknowns (called Reynolds stresses) which must be modelled[78]. The viscous stress tensor mentioned in Equation 4.11 is then approximated by the Boussinesq hypothesis[79], further details of which are provided in the following sections.

4.1.2 Numerical Methods

The HMB2 solver uses a cell-centred finite volume approach combined with an implicit dual-time method. In this manner, the solution marches in pseudo-time for each real time-step to achieve fast convergence. According to the finite volume method, the RANS equations can be discretised for each cell by

$$\frac{d}{dt}\left(\mathbf{W}_{i,j,k}\mathscr{V}_{i,j,k}\right) + \mathbf{R}_{i,j,k} = 0. \tag{4.13}$$

where $\mathscr{V}_{i,j,k}$ denotes the cell volume and $\mathbf{R}_{i,j,k}$ represents the flux residual.

The implicit dual-time method proposed by Jameson[80] is used for time-accurate calculations. The residual is redefined to obtain a steady state equation which can be solved using acceleration techniques. The following system of equations are solved in the implicit scheme during the time integration process

$$\frac{\Delta V\mathbf{W}_{i,j,k}^{m+1} - \Delta V\mathbf{W}_{i,j,k}^{m}}{\Delta V\Delta\tau} + \frac{\Delta V\mathbf{W}_{i,j,k}^{n+1} - \Delta V\mathbf{W}_{i,j,k}^{n}}{\Delta V\Delta t} = \mathbf{R}_{i,j,k}^{n+1} \tag{4.14}$$

where ΔV is the change in cell volume, $\Delta\tau$ is the pseudo time-step increment and Δt is the real time-step increment. The flux residual $\mathbf{R}_{i,j,k}^{n+1}$ is approximately defined by

$$\mathbf{R}_{i,j,k}^{n+1} \approx \mathbf{R}_{i,j,k}^{n} + \frac{\partial\mathbf{R}_{i,j,k}^{n}}{\partial\mathbf{W}_{i,j,k}^{n}}\left(\mathbf{W}_{i,j,k}^{n+1} - \mathbf{W}_{i,j,k}^{n}\right) \tag{4.15}$$

By substituting Equation 4.15 into Equation 4.14, the resulting linear system can be written as

$$\left(\frac{1}{\Delta t} + \left(\frac{\partial\mathbf{R}}{\partial\mathbf{W}}\right)^{n}\right)\Delta\mathbf{W} = -\mathbf{R}^{n} \tag{4.16}$$

where the subscripts i,j,k have been dropped for clarity and ΔW is used for $\left(\mathbf{W}_{i,j,k}^{n+1} - \mathbf{W}_{i,j,k}^{n}\right)$.

Osher's upwind scheme [81] is used to resolve the convective fluxes although Roe's flux-splitting scheme [82] is also available. The Monotone Upstream-centered Schemes for Conservation Laws (MUSCL) variable extrapolation method[83] is employed in conjunction to formally provide second-order accuracy. The van Albada limiter is also applied to remove any spurious oscillations across shock waves. The central differencing spatial discretisation method is used to solve the viscous terms. The non-linear system of equations that is generated as a result of the linearisation is then solved by integration in pseudo-time using a first-order backward difference. A Generalised Conjugate Gradient (GCG)[84] method is then used in conjunction with a Block Incomplete Lower-Upper (BILU)[84] factorisation as a pre-conditioner to solve the linear system of equations, which is obtained from a linearisation in pseudo-time.

The flow solver can be used in serial or parallel mode. To obtain an efficient parallel method based on domain decomposition, different methods are applied to the flow solver [85]. An approximate form of the flux Jacobian resulting from the linearisation in pseudo-time is used which reduces the overall size of the linear system by reducing the number of non-zero entries. Between the blocks of the grid, the BILU factorisation is also decoupled thereby reducing the communication between processors. Each processor is also allocated a vector that contains all the halo cells for all the blocks in the grid. Message Passing Interface (MPI) is

used for the communication between the processors in parallel. Most computations undertaken in this work have been performed on the Beowulf Pentium 4 130-processor workstations of the CFD Laboratory at the University of Liverpool. For very large grids, however, calculations were conducted on different supercomputing clusters such as HECToR[86] in Edinburgh, UK, and the necessary porting of the code onto these facilities performed. The Hector system is based on the Cray XE6 system and comprises 3712 12-core AMD Opteron 2.1GHz Magny Cours processors in 1856 XE6 compute nodes, delivering a peak-performance of 373 TeraFlops.

A number of linear and non-linear statistical turbulence models have been implemented into HMB2. The one-equation SA turbulence model[87] to realise the turbulent properties for DES computations, and the DDES approach as well as the SALSA modification of the SA turbulence model were implemented for this project. Options for DES with two-equation Wilcox $k-\omega$[88] and Menter's $k-\omega$ Shear-Stress Transport (SST)[89] turbulence models are also available. All these turbulence models and indeed the simulation techniques are described in greater detail in the following sections.

4.2 General Description of Turbulence and its Modelling

Turbulent flows contain structures which show rapid fluctuations in time and space. A broad range of scales are observed to exist at high Reynolds numbers where turbulence develops as an instability of the laminar flow. Starting with the laminar flow, fluid layers slide smoothly past each other and the molecular viscosity dampens any high-frequency small-scale instability. At high Reynolds number, the flow reaches a periodic state. The character of the flow also changes and becomes more diffusive and dissipative. This flow has increased mixing friction, heat transfer rate and spreading rate. Boundary layers consequently become thicker and less susceptible to separation.

The non-linearity of the Navier-Stokes equations leads to various interactions between the turbulent fluctuations of different wavelengths and directions. Wavelengths extend from a maximum comparable to the width of the flow to a minimum fixed by viscous dissipation of energy. A key process that spreads the motion over wide range of wavelengths is called vortex stretching[90]. Turbulent structures in the flow gain energy if the vortex elements are primarily orientated in a direction which allow the mean velocity gradients to stretch them. This mechanism is called production of turbulence. The kinetic energy of the turbulent structures is then convected, diffused and dissipated.

Most of the energy is carried by the large scale structures, the orientation of

which is sensitive to the mean flow. The large eddies cascade energy to the smaller ones via stretching. Small eddies have less pronounced preference in their orientation and statistically appear to be isotropic. For the shortest wavelengths, energy is dissipated by viscosity. This description corresponds to what is known as isotropic turbulence. For this flow, the ratio of the largest to smaller scale increases with Reynolds number[90].

If the unsteady Navier-Stokes equations are used to calculate the flow, a vast range of length and time scales would have to be computed. This would require a very fine grid and a very high resolution in time. This approach known as Direct Numerical Simulation of turbulence (DNS) is by today's computing speeds applicable only to flows at very low Reynolds number. One technique called Large-Eddy Simulation explicitly resolves the scales away from the wall and exploits modelling in the near-wall regions. A sub-grid scale (SGS) model is used to model the smaller scales which are assumed to be more isotropic. Although less computationally intensive than DNS, this is still expensive, especially for higher Reynolds number flows.

A turbulence model therefore needs to account for some part of the fluctuating motion in order to keep the computing cost down. The optimum model should therefore be simple to implement, general and derived out of the flow physics. It is equally important that the model is computationally stable and co-ordinate invariant. These statistical turbulence models are applied to a special form of the equations of motion called the Reynolds-Averaged Navier-Stokes (RANS) equations. These are obtained by Reynolds averaging the Navier-Stokes equations.

4.3 Reynolds Averaging

In a turbulent flow, the fields of pressure, velocity, temperature and density vary randomly in time. Reynold's approach involves separating the flow quantities into stationary and random parts. The quantities are then presented as a sum of the mean flow value and the fluctuating part[90]:

$$\phi = \overline{\phi} + \phi' \tag{4.17}$$

This formulation is then inserted into the conservation equations and a process known as Reynolds averaging is performed. Three averaging methods are possible:

- time averaging,
- spatial averaging,
- ensemble averaging.

Time averaging is the most common averaging method. It can be used only for statistically stationary turbulent flows, i.e. flows not varying with time on the average. For such flows, the mean flow value is defined as

$$\overline{u_i(x)} = \lim_{T\to\infty} \frac{1}{T} \int_i^{i+T} u_i(x,t)\,\mathrm{d}t \tag{4.18}$$

In practice, $T \to \infty$ means that the integration time T needs to be long enough relative to the maximum period of the assumed fluctuations.

4.4 Boussinesq-Based Models

The Boussinesq approximation is based on an analogy between viscous and Reynolds stresses and expresses the Reynolds stresses as a product of the eddy viscosity (μ_t) and the velocity gradient. Boussinesq's eddy viscosity hypothesis states that

$$-\rho\overline{u_i'u_j'} = \mu_t \left[\left(\frac{\partial u_i}{\partial x_j} + \frac{\partial u_j}{\partial x_i}\right) - \frac{2}{3}\delta_{ij}\frac{\partial u_k}{\partial x_k}\right] - \frac{2}{3}\rho\delta_{ij}k \tag{4.19}$$

where k represents the specific kinetic energy of the fluctuations and is given by

$$k \equiv \frac{u_i'u_i'}{2} \tag{4.20}$$

The key idea behind Boussinesq's hypothesis is that the Reynolds stresses can be calculated as a product of the dynamic eddy-viscosity, μ_t, and the strain-rate tensor of the mean flow, i.e.

$$-\rho\overline{u_i'u_j'} = 2\mu_t S_{ij} - \frac{2}{3}\delta_{ij}k \tag{4.21}$$

where

$$S_{ij} = \frac{1}{2}\left(\frac{\partial u_i}{\partial x_j} + \frac{\partial u_j}{\partial x_i} - \frac{2}{3}\delta_{ij}\frac{\partial u_k}{\partial x_k}\right) \tag{4.22}$$

Eddy viscosity, μ_t, is a scalar and consequently the Reynolds stress components are linearly proportional to the mean strain-rate tensor. What is also implied here is that compressibility plays a secondary rate in the development of the turbulent flow-field. According to Morkovin's hypothesis [91], compressibility affects turbulence only at hypersonic speeds.

To compute μ_t, further modelling is required and it is at this point that turbulence models come into play. Turbulence models are classified into categories based on the number of transport equations required to calculate μ_t. According to the number of transport equations needed for the calculation of the eddy viscosity, the Boussinesq-based models are classified as:

- algebraic or zero-equation models, such as the Cebeci-Smith[92] and Baldwin-Lomax[93] models,

- one-equation models, such as the Spalart-Allmaras (SA)[87] and Baldwin-Barth (BB)[94] models.
- two-equation models, such as the $k-\omega$[88], $k-\varepsilon$[95], $k-\omega$ baseline (BSL) and shear-stress transport (SST)[89] and $k-g$[96] models.
- multi-equation models: three-equation[97–99], four-equation[100], five-equation [101] and multiple time-scale [102–104] models.

An additional family of models solves equations for all components of the Reynolds stress tensor. These are also known as Reynolds Stress Models (RSM), second-order closures or second-moment closures.

4.5 Viscosity-Dependent Parameters

Non-dimensionalised wall distances for turbulent flow, y^*, and non-turbulent flow, y^+, are defined by the following

$$y^* \equiv \frac{y_n k^{1/2}}{\nu}, \qquad y^+ \equiv \frac{y_n u_\tau}{\nu}, \tag{4.23}$$

where y_n is the distance from the nearest wall, $u_\tau \equiv \sqrt{\tau_w/\rho}$ is the friction velocity and τ_w represents the dynamic wall shear stress. Turbulent Reynolds numbers for the $k-\varepsilon$ model (denoted by R_t) and for the $k-\omega$ model (denoted by R_ω) are given by the following equation

$$R_t \equiv \frac{k^2}{\nu\varepsilon}, \qquad R_\omega \equiv \frac{k}{\nu\omega} \quad , \tag{4.24}$$

which represents the importance of the eddy over molecular viscosity.

4.6 One-Equation Models

This type of turbulence model was designed to improve the ability of algebraic models to account for the convection and diffusion of turbulence. This was accomplished by employing an additional transport equation, usually for the realisation of the kinetic energy of turbulence, k. The general form of this transport equation takes the following form

$$\frac{\partial k}{\partial t} + u_j \frac{\partial k}{\partial x_j} = \tau_{ij}\frac{\partial u_i}{\partial x_j} - \varepsilon + \frac{\partial}{\partial x_j}\left[\frac{\mu}{\rho}\frac{\partial k}{\partial x_j} - \frac{1}{2}\overline{u_i' u_i' u_j'} - \frac{1}{\rho}\overline{p' u_j'}\right] \tag{4.25}$$

The first term in Right-Hand Side (RHS) $\left(\tau_{ij}\frac{\partial u_i}{\partial x_j}\right)$ represents the production of turbulence. From the terms in the square brackets, the first $\left(\frac{\mu}{\rho}\frac{\partial k}{\partial x_j}\right)$ is the molecular

diffusion term, the second $\left(\overline{u_l' u_i' u_j'}\right)$ is the turbulent flux of the turbulent kinetic energy, modelled as a function of the gradient of the turbulent kinetic energy, and the third $\left(\frac{1}{\rho}\overline{p' u_j'}\right)$ is the pressure diffusion term, which is usually neglected due to its small contribution. The term ε is the dissipation rate of k per unit mass of fluid, and is usually defined by

$$\varepsilon = \frac{\mu}{\rho}\overline{\frac{\partial u_i'}{\partial x_k}\frac{\partial u_i'}{\partial x_k}} \tag{4.26}$$

Eddy viscosity for one-equation turbulence models is usually calculated by

$$\mu_t = \rho C_\mu l_{mix}\sqrt{k} \tag{4.27}$$

where C_μ is a coefficient specific to the model.

BB[94] and SA[87] are the most common types of one-equation models. History effects of the turbulent kinetic energy profile are better accounted for in one-equation models due to the additional differential equation. Specifically tuned for aerodynamic flows with adverse pressure gradients and transonic flow conditions, one-equation models also work well for flow regions where the mean velocity gradient is zero. Better prediction of near-wall effects and transition, for instance, can simply be integrated into the model's formulation by adding extra relevant terms because of its modular design. For these reasons, one-equation models have gained much popularity in aerospace applications. The disadvantage of one-equation models is that no mechanism for the computation of the length scale, l, is included, making the prediction of highly turbulent flows (with a broad range of length scales) difficult. In that respect, one-equation models are still similar to algebraic models.

Many modifications have been undertaken to one-equation turbulence models, especially to the SA model, with the view of extending their range of applications. Extensions to compressible supersonic flows over complex configurations have been addressed by Deck[105] while rotational and curvature effects to account for the change on turbulent shear stress have been addressed by Spalart and Shur[106]. The SA model has also been modified to be used in DES computations[107].

4.6.1 Spalart-Allmaras Model

The one-equation SA turbulence model [87] solves a transport equation for the undamped eddy viscosity directly. The kinematic eddy viscosity, (ν_t), in the SA model is calculated by

$$\nu_t = \tilde{\nu} \cdot f_{v1} \tag{4.28}$$

where

$$f_{v1} = \frac{\chi^3}{\chi^3 + c_{v1}^3} \qquad \text{and} \qquad \chi = \frac{\tilde{\nu}}{\nu} \tag{4.29}$$

In the above equations, and hereafter, the term f refers to a function, c refers to a constant, ν is the molecular viscosity and $\tilde{\nu}$ is the undamped eddy viscosity that obeys the following transport equation

$$\begin{aligned} \frac{D\tilde{\nu}}{Dt} &= c_{b1}(1-f_{t2})\tilde{S}\tilde{\nu} + \frac{1}{\sigma}\left(\bigtriangledown\cdot((\nu+\tilde{\nu})\bigtriangledown\tilde{\nu}) + c_{b2}(\bigtriangledown\tilde{\nu})^2\right) \\ &\quad - \left(c_{w1}f_w - \frac{c_{b1}}{\kappa^2}f_{t2}\right)\left(\frac{\tilde{\nu}}{d}\right)^2 + f_{t1}\Delta U^2 \end{aligned} \tag{4.30}$$

The first term on the right-hand side is the production term, the second is the diffusion term and the third is the near-wall term. The last term models transition downstream of tripping. The subscript b stands for basic, w for wall and t for trip. The parameter σ represents the turbulent Prandtl number and d is the wall-distance.

The term $\tilde{S}$ in Equation (4.30) is defined by the following equation, where S is the magnitude of vorticity

$$\tilde{S} = S + \frac{\tilde{\nu}}{k^2 d^2} f_{v2}, \qquad f_{v2} = 1 - \frac{\chi}{1+\chi f_{v1}} \tag{4.31}$$

The function f_w in Equation (4.30) is given by

$$f_w = g\left(\frac{1+c_{w3}^6}{g^6+c_{w3}^6}\right)^{1/6}, \qquad g = r + c_{w2}\left(r^6 - r\right), \qquad r = \frac{\tilde{\nu}}{\tilde{S}k^2d^2} \tag{4.32}$$

For large r, the function f_w approaches a constant value. Values for r where this occurs can be truncated to approximately 10. The wall boundary condition is satisfied where $\tilde{\nu} = 0$. In the free-stream, 0 is the best value to use for the working variable ($\tilde{\nu}$), provided that numerical errors do not push $\tilde{\nu}$ to negative values near the edge of the boundary layer (the exact solution cannot go negative). Values below $\nu/10$ are also acceptable. The same applies to the initial condition. The f_{t2} function is defined by

$$f_{t2} = c_{t3} \cdot e^{-c_{t4}\cdot\chi^2} \tag{4.33}$$

The trip function f_{t1} is defined as

$$f_{t1} = c_{t1} g_t \cdot e^{-c_{t2}\frac{\omega_t^2}{\Delta U^2}\left(d^2 + g_t^2 d_t^2\right)} \tag{4.34}$$

where d_t is the distance from the field point to the trip, ω_t is the wall vorticity at the trip, ΔU is the difference between the velocity at the field point and that at the trip and $g_t = \min(0.1, \Delta U/\omega_t \Delta x)$, in which Δx is the grid spacing along the wall at the trip.

Coefficient	c_{b1}	σ	c_{b2}	κ	c_{w2}	c_{w3}	c_{v1}	c_{t1}	c_{t2}	c_{t3}	c_{t4}
Value	0.1355	2/3	0.622	0.41	0.3	2	7.1	1	2	1.1	2

Table 4.1: Closure coefficients for the SA model

Values used in HMB2 for the SA turbulence model constants are given in Table 4.1.

The constant c_{w1} is defined as

$$c_{w1} = \frac{c_{b1}}{k^2} + \frac{(1+c_{b2})}{\sigma} = 3.2391. \tag{4.35}$$

A value of 2/3 has been used for the turbulent Prandtl number, σ.

4.7 Two-Equation Models

By far the most popular type of turbulence model used is the two-equation type. Two-equation models are 'complete', i.e. can be used to predict properties of a given flow with no prior knowledge of the turbulence structure or flow geometry. Two transport equations are used for the calculation of the turbulent kinetic energy, k, and turbulence length scale, l, or a function of it. The choice of the 2nd variable is arbitrary and many proposals have been presented. The most popular involves using:

- ε — specific dissipation rate of turbulence.
- ω — k-specific dissipation rate.
- τ — turbulent time-scale.

A description of the different types of two-equation models is provided in Table 4.2 below. As well as indicating the variable used for the second transport equation, Table 4.2 includes the equation used to calculate the eddy viscosity.

Two-Equation Model	Equation	2nd Variable Used
Kolmogorov (c. 1942) [108]	$k^{1/2}l^{-1}$	ω (Frequency Length Scale)
Rotta (c. 1950)	l	
Harlow-Nakayama (1967) [109]	$k^{3/2}l^{-1}$	ε (Energy Dissipation Rate)
Spalding (1969) [110]	kl^{-2}	ω'^2 (Vorticity fluctuations squared)
Speziale (1992) [111]	$lk^{-1/2}$	τ (Time-Scale)
Nee	kl	kl (k times length scale)
Harlow-Nakayama	$lk^{-1/2}$	ν_t (Eddy viscosity)

Table 4.2: Different types of two-equation turbulence models and the corresponding second variable.

One of the most widely used two-equation turbulence models is the $k-\varepsilon$ model. One of the original versions of this model was developed by Jones and Launder [95] in 1972. The turbulent scale in the $k-\varepsilon$ model is calculated using a second transport equation for the turbulent dissipation rate, ε. The eddy viscosity for the $k-\varepsilon$ model is typically derived from

$$\mu_T = C_\mu \rho \frac{k^2}{\varepsilon} \tag{4.36}$$

where C_μ is the model coefficient. The advantage of the $k-\varepsilon$ model is that it performs well for attached flows with thin shear layers and jets but fails to predict the correct flow behaviour in many flows with adverse pressure gradients, extended separated flow regions, swirl, buoyancy, curvature secondary flows and unsteady flows.

The other class of two-equation turbulence models that is widely used is the $k-\omega$ model. In 1988, Wilcox[88] developed the famous $k-\omega$ model originally conceived by Kolmogorov. The $k-\omega$ model is similar to the $k-\varepsilon$ model but instead uses the k-specific dissipation rate as a second variable to compute the turbulent length scale. The eddy viscosity is obtained by

$$\mu_T = \rho \frac{k}{\omega} \tag{4.37}$$

Although the $k-\omega$ model provides better performance in adverse pressure gradient flows, it suffers largely from the same problems as the $k-\varepsilon$ model. Hybrid versions of the $k-\omega$ and $k-\varepsilon$ models called the $k-\omega$ baseline (BSL) and $k-\omega$ shear-stress transport (SST) models were later introduced by Menter[89]. These, in particular the $k-\omega$ SST version, perform well in separated flows. The idea behind the $k-\omega$ BSL model is to exploit the robust and accurate formulation of the $k-\omega$ model near the wall but to also take advantage of the lack of sensitivity to free-stream values of the $k-\varepsilon$ model away from the wall. Menter[89] achieved this by transforming the $k-\varepsilon$ model into the same format as the $k-\omega$ formulation. This process generated an additional cross-diffusion parameter in the ω transport equation. For the SST model[89], the idea was to improve the $k-\omega$ BSL model by including terms to account for the transport of the principal shear stress. This term is incorporated in Reynolds Stress Models (RSM) and was also applied in the Johnson-King model[112]. Its importance was realised based on the significantly improved results for adverse pressure gradient flows[89].

4.7.1 Model Equations: Linear $k-\omega$ Model

Mathematical formulations of the different types of the linear $k-\omega$ two-equation turbulence models discussed in the previous sections are described here. More

information on the $k-\varepsilon$ and $k-g$ models can be obtained from [113].

Since the introduction of the linear $k-\omega$ model by Wilcox in 1988[88], the other notable modification to the $k-\omega$ model came from Menter in 1994[89] who proposed the hybridisation of the $k-\omega$ model with the $k-\varepsilon$ model, as described previously. Table 4.3 lists the four notable versions of the $k-\omega$ models and further describes if they include parameters to compute the low Reynolds number properties.

Type of Model	**Low-Re**
Wilcox (1988)[88]	Yes
Wilcox (1994)[114]	Yes
Menter (1994)[89] **— (i) BSL Model**	Yes
Menter (1994)[89] **— (ii) SST Model**	Yes

Table 4.3: Different types of linear $k-\omega$ turbulence models

Turbulence transport equations used in the formulation of the $k-\omega$ models are given by the following:

$$\frac{\partial}{\partial t}(\rho k)+\frac{\partial}{\partial x_j}\left(\rho U_j k\right)=\frac{\partial}{\partial x_j}\left[\left(\mu+\frac{\mu_t}{\sigma_k}\right)\frac{\partial k}{\partial x_j}\right]+\rho\left(P_k-\beta^*\omega k\right) \tag{4.38}$$

$$\frac{\partial}{\partial t}(\rho\omega)+\frac{\partial}{\partial x_j}\left(\rho U_j \omega\right)=\frac{\partial}{\partial x_j}\left[\left(\mu+\frac{\mu_t}{\sigma_\omega}\right)\frac{\partial \omega}{\partial x_j}\right]+\rho\left(\frac{\alpha}{\nu_t}P_\omega-\frac{\beta}{\beta^*\omega^2}\right)+\rho S_l \tag{4.39}$$

In the transport equation for k and ω above, the production of turbulence, P, and the dissipation rate specific to k, P_ω, is defined by

$$P_k=\tau_{ij}^R\frac{\partial u_i}{\partial x_j},\qquad P_\omega=\rho\frac{\alpha}{\nu_t}P_k. \tag{4.40}$$

Values for the coefficients used in all the four types of linear $k-\omega$ models discussed here are given in the Table 4.4.

Type of Model	α^*	β^*	α	β
Wilcox (1988)[88]	1	$\frac{9}{100}$	$\frac{5}{9}$	$\frac{3}{40}$
Wilcox (1994)[114]	$\frac{\frac{1}{40}+\frac{R_\omega}{6}}{1+\frac{R_\omega}{6}}$	$\frac{9}{100}\frac{\frac{5}{18}+\left(\frac{R_\omega}{8}\right)^4}{1+\left(\frac{R_\omega}{8}\right)^4}$	$\frac{5}{9}\frac{\frac{1}{10}+\frac{R_\omega}{2.7}}{1+\frac{R_\omega}{2.7}}$	$\frac{3}{40}$
Menter (1994)[89] ***(BSL)***[1]	1	0.09	$B\begin{pmatrix}0.553\\0.440\end{pmatrix}$	$B\begin{pmatrix}0.075\\0.083\end{pmatrix}$
Menter (1994)[89] ***(SST)***[2]	$\min\left(1,\frac{0.31}{F_2}\frac{\omega}{\bar{w}}\right)$	0.09	$B\begin{pmatrix}0.553\\0.440\end{pmatrix}$	$B\begin{pmatrix}0.075\\0.083\end{pmatrix}$

Table 4.4: Values of constants used in linear $k-\omega$ models.

Menter's models[89] are constructed as a 'blend' of the $k-\omega$ and $k-\varepsilon$ models. Here the $k-\varepsilon$ model is phrased in the same form as the $k-\omega$ model so as to exploit its independence of free-stream values. Blending of the $k-\varepsilon$ and $k-\omega$ model values

Type of Model	σ_k	σ_ω	S_l
Wilcox (1988)[88]	2	2	0
Wilcox (1994)[114]	2	2	0
Menter (1994)[89]***(BSL)***[1]	$\frac{1}{B\begin{pmatrix}0.5\\1.0\end{pmatrix}}$	$\frac{1}{B\begin{pmatrix}0.5\\0.856\end{pmatrix}}$	$B\begin{pmatrix}0\\\frac{1.71}{\omega}\nabla k\cdot\nabla\omega\end{pmatrix}$
Menter (1994)[89]***(SST)***[2]	$\frac{1}{B\begin{pmatrix}0.85\\1.0\end{pmatrix}}$	$\frac{1}{B\begin{pmatrix}0.5\\0.856\end{pmatrix}}$	$B\begin{pmatrix}0\\\frac{1.71}{\omega}\nabla k\cdot\nabla\omega\end{pmatrix}$

Table 4.4: **Continued -** Values of constants used in linear $k-\omega$ models.

for α, β, σ_k^{-1} and σ_ω^{-1} is (in this notation) given by the following equation

$$B\begin{pmatrix}a\\b\end{pmatrix} \equiv F_1 a + (1-F_1)\, b. \tag{4.41}$$

The blending function is defined by

$$F_1 = \tanh\left(\arg_1^4\right), \tag{4.42}$$

where

$$arg_1 = min\left[\max\left(\frac{k^{1/2}}{\beta^*\omega y}, \frac{500\nu}{y_n^2\omega}\right), \frac{2k\omega}{y_n^2 \max\left(\nabla k\cdot\nabla\omega, 0.0\right)}\right]. \tag{4.43}$$

The $k-\omega$ SST model places an additional vorticity-dependent limiter on the shear-stress

$$F_2 = \tanh\left(arg_2^2\right), \qquad arg_2 = \max\left(\frac{2k^{1/2}}{\beta^*\omega y}, \frac{500\nu}{y^2\omega}\right). \tag{4.44}$$

Note that this model also uses a slightly different value of σ_k.

For low-Reynolds number versions of the $k-\omega$ model and Menter's $k-\omega$ BSL and SST models, the following boundary conditions are assumed for a direct integration to the wall

$$\text{For } k: \quad k_w = 0, \qquad flux(k)_w = 0 \quad , \tag{4.45}$$

$$\text{For } \omega: \quad \omega = 0, \qquad flux(\omega)_w = -\nu\nabla\omega \quad . \tag{4.46}$$

where the subscript w denotes the value *at* the wall.

4.7.2 Model Equations: SST-SAS Model

The Scale-Adaptive Simulation (SAS) approach [115–119] differs from the conventional RANS formulation as it "adjusts the turbulence length scale to the local inhomogeneities" [115]. Two SAS models have been developed through the DESIDER project: the SST-SAS and the KSKL-SAS.

The SST-SAS model is based on the Shear-Stress Transport (SST) formulation of the $k-\omega$ model with the adjunction of a new term that uses a quadratic length-scale ratio $(\frac{L}{L_{vK}})^2$.

$$\frac{\partial}{\partial t}(\rho k)+\frac{\partial}{\partial x_j}\left(\rho U_j k\right)=\frac{\partial}{\partial x_j}\left[\left(\mu+\frac{\mu_t}{\sigma_k}\right)\frac{\partial k}{\partial x_j}\right]+\rho\left(P_k-\beta^*\omega k\right) \tag{4.47}$$

$$\begin{aligned}\frac{\partial}{\partial t}(\rho\omega)+\frac{\partial}{\partial x_j}\left(\rho U_j\omega\right)=&\frac{\partial}{\partial x_j}\left[\left(\mu+\frac{\mu_t}{\sigma_\omega}\right)\frac{\partial\omega}{\partial x_j}\right]+\alpha\frac{\omega}{k}\rho P_k-\rho\beta\omega^2\\&+Q_{SAS}+(1-F_1)\frac{2\rho}{\sigma_{\omega 2}}\frac{1}{\omega}\frac{\partial k}{\partial x_j}\frac{\partial\omega}{\partial x_j}\end{aligned} \tag{4.48}$$

The additional term Q_{SAS} in given by:

$$\begin{aligned}Q_{SAS}=max\Bigg[&\rho\zeta_2\kappa S^2\left(\frac{L}{L_{vK}}\right)^2\\&-C_{SAS}\frac{2\rho k}{\sigma_\Phi}max\left(\frac{1}{k^2}\frac{\partial k}{\partial x_j}\frac{\partial k}{\partial x_j},\frac{1}{\omega^2}\frac{\partial\omega}{\partial x_j}\frac{\partial\omega}{\partial x_j}\right),0\Bigg]\end{aligned} \tag{4.49}$$

with $\zeta_2=3.51$, $\sigma_\Phi=2/3$, $C_{SAS}=2$
For a boundary layer, L_{vK} is given by $L_{vK}=\kappa\frac{U'(y)}{U''(y)}$. A generalisation for 3D cases is proposed:

$$L_{vK}=max\left(\kappa\left|\frac{U'}{U''}\right|,C_S\sqrt{\frac{\kappa\zeta_2}{((\beta/C_\mu)-\alpha)}}\Delta\right) \tag{4.50}$$

where Δ is the grid size parameter given by the cubic root of the control volume size: $\Delta=\Omega_{CV}^{1/3}$

C_S is a new closure parameter.

Coefficient	ζ_2	σ_Φ	C	Δ	α	β	C_μ	C_S
Value	3.51	2/3	2	$\Omega_{CV}^{1/3}$	0.44	0.0828	0.09	0.11

Table 4.5: Closure coefficients for the SST-SAS model

4.8 Detached-Eddy Simulation

4.8.1 Original Detached-Eddy Simulation

The original idea of DES was postulated by Spalart *et al.* [106]. The RANS equations with a modified length scale are used in the whole domain. This length scale is now

also depending on the mesh length scale. In the RANS areas, the usual RANS length scale will be used, but in the LES zones, the length scale will now depend on the mesh length scale, forcing the turbulence model to behave like LES. This concept is called Detached-Eddy Simulation (DES). DES does not need an interface between the RANS and LES part.

Spalart introduced the mesh length scale Δ as a function of the cell size following the three axis Δ_x, Δ_y and Δ_z:

$$\Delta = max(\Delta_x, \Delta_y, \Delta_z) \quad . \tag{4.51}$$

The new length scale for DES is then:

$$l_{DES} = min(l_{RANS}, C_{DES}\Delta) \quad , \tag{4.52}$$

where C_{DES} is an arbitrary constant. For example, in the case of the Spalart-Allmaras model, the scale length d is the wall distance. In the new DES model, the length scale $\tilde{d}$ is defined as:

$$\tilde{d} = \min(d, C_{DES}\Delta) \quad . \tag{4.53}$$

Therefore, when close enough to the wall, the model will use the RANS equations, and if we go further from the wall, the length scale will switch to the grid length scale and the model will behave like LES.

This modification aims at increasing the dissipation term of the turbulent kinetic energy and thus decrease the production term. The Dissipation term is now equal to:

$$-C_{w1} f_{w1} \left(\frac{\tilde{\nu}}{\tilde{d}}\right)^2 \quad . \tag{4.54}$$

This process can be generalised to other RANS models, like the $k-\omega$ ones as described by Strelets[120]. In this case, the length scale is changed from $\frac{\sqrt{k}}{\omega\beta}$ to:

$$l_{DES} = \min\left(\frac{\sqrt{k}}{\omega\beta}, C_{DES}\Delta\right) \quad . \tag{4.55}$$

A similar idea put forward by Batten *et al.* [121] is called LNS: Limited Numerical Scales and has several advantages compared to the original DES. For instance, LNS claims to be 'automatic' by detecting the areas of application of the RANS and LES without *a priori* knowledge of the location of walls or wall-distances. Furthermore, LNS approaches DNS as $\Delta \to 0$ and reverts back to RANS at the far-field of the flow if the grid there is coarse. Ref. [113] describes how to implement LNS.

For DES with the two-equation $k-\omega$ model, the only modification, as with the one-equation Spalart-Allmaras DES variant, is in the dissipation term

$$-\beta^* \rho \omega k \tag{4.56}$$

The turbulent length scale is defined by

$$l = \frac{k^{1/2}}{\beta^* \omega} \tag{4.57}$$

Re-arranging for $\beta^* \omega$ and substituting into equation 4.56 gives

$$-\rho \frac{k^{3/2}}{l} \tag{4.58}$$

where l is given by

$$l = \min\left(l, C_{DES}\Delta\right). \tag{4.59}$$

C_{DES} is set to 0.78 and Δ is as before.

4.8.2 Delayed Detached-Eddy Simulation (DDES)

The DES can have difficulties to handle the transition between the LES and RANS zones. In the case of coarse mesh around the wall, the DES will work as expected with a transition outside the boundary layer. If the mesh is very fine ($\Delta = \delta/20$, with δ the boundary layer thickness), then the simulation will behave like a Wall-Modelled LES (LES with a wall model, RANS in this case). The problem appears for mesh size in between these two cases. The transitions takes place at about the first third of the boundary layer , and the two upper thirds of the boundary layer will then be in LES mode. This will reduce the turbulent viscosity and therefore the Reynolds strains.

Therefore, Spalart [122] developed the Delayed Detached-Eddy Simulation (DDES). The DDES introduce a limiter in the length scale ($\frac{\sqrt{k}}{\omega}$ in the $k-\omega$ model) that ensures that the transition will not take place in the boundary layer. In the Spalart-Allmaras model, this limiter modifies the parameter r (root of the ratio between the length scale and the wall distance):

$$r_d = \frac{\nu_t + \nu}{\sqrt{\frac{\partial U_i}{\partial x_j}\frac{\partial U_i}{\partial x_j}\kappa^2 d^2}} \tag{4.60}$$

with κ the Kàrmàn constant. The term $\nu_t + \nu$ can be replaced with $\tilde{\nu}$ in the Spalart-Allmaras model. Now r_d equals 1 in the logarithmic part of the boundary layer and equals 0 outside the boundary layer. ν avoids this term to tend to 0 very close to the wall. A new function f_d is defined as:

$$f_d = 1 - \tanh\left(\left[8 r_d\right]^3\right) \tag{4.61}$$

f_d equals 1 in the LES zones and 0 elsewhere. The values of 8 and 3 are arbitrary and set the shape of f_d. These value were chosen in order to obtain good results for a planar wall flow.

The new value of the length scale un the Spalart-Allmaras model is now set at:

$$\tilde{d} = d - f_d \max\left(0, d - C_{DES}\Delta\right). \tag{4.62}$$

The RANS zone is defined by $f_d = 0$ and the LES zone by $f_d = 1$. In the case of highly detached flows, the detached zone is calculated in LES mode and the transition is quicker, allowing a smaller grey zone.

4.9 Summary of the Turbulence Models Used in this Thesis

A list of the turbulence models available in HMB2 and used in this paper, and the acronyms used to designate them is shown in Table 4.6.

Acronym	Description
SA	Spalart-Allmaras model[87]
DES	Detached-Eddy Simulation[106]
$k-\omega$	Wilcox's $k-\omega$ (1994) model[114]
$k-\omega$ BSL	Menter's $k-\omega$ Baseline model[89]
$k-\omega$ SST	Menter's $k-\omega$ Shear-Stress Transport
$k-\omega$ SAS	Menter's $k-\omega$ Scale-Adaptive Simulation model [115]

Table 4.6: Summary of the turbulence model used in this thesis, as well as their acronyms.

4.10 Actuator Disc Method

The actuator disc theory appeared with the work of Froude over a century ago. Froude's description of the rotor disc was that of a permeable surface "covered" with a uniform normal load that corresponds to the weight to be lifted by the rotor. The prediction of the loading is derived from momentum theory principles and tend to underestimate the value of the loading by around 15% [123].

The work by Glauert on propellers [124] helped improve the model thanks to the Blade Element Theory. With Blade Element Modelling (BEM), each blade section along the span is approximated to an airfoil and the loading of the global rotor can be expressed as function of the span-wise position. The concept of actuator "annulus" is introduced as an extension of the classic stream-tube defined by the momentum theory.

The application of the actuator disc method to helicopter rotors requires one further step to achieve a reasonable description of the flow characteristics. Due to the advancing speed of the aircraft, a variation in loading appears around the azimuth, especially in the retreating side where a reverse flow region appears. The rotor is out of balance since the advancing blade creates more lift than the retreating blade. This is

accounted for by modifying the pitch of the blade in a one-per-rev fashion. A realistic description of an actuator disc for forward-flying rotors should take into account this effect so that the rotor loading ΔP is function of the radial position x_R on the blade and the azimuth Ψ (equation 4.63).

$$\Delta P = f(x_R, \Psi) \tag{4.63}$$

Shaidakov [125] used the distribution given in equation 4.64 to give a realistic model of actuator disc. P_0, P_s and P_{2c} coefficients are functions of the radius, advance ratio, rotor tilt and thrust coefficient. His model was tuned for realism using results from flight tests.

$$\Delta P^* = P_0 + P_s \sin\Psi + P_{2c} \cos 2\Psi \tag{4.64}$$

Actuator discs have been used extensively in conjunction with CFD [4, 7, 23, 55] to estimate the effect of the rotor without the complexity and computational cost of actual rotor blades. In the CFD framework, source terms are added to the momentum and energy equations to impose a jump of pressure across the rotor disc that is representative of the loading. The size, position and attitude (tilt, roll) of the rotor disc can be adjusted depending on the flight condition and the global distribution depends on the thrust coefficient $C_{\mathrm{T}}^{\mathrm{UK}}$ and advance ratio μ:

$$C_{\mathrm{T}}^{\mathrm{UK}} = \frac{T}{\frac{1}{2}\rho U_{tip}^2 \pi R^2} \tag{4.65}$$

$$\mu = \frac{U_\infty}{U_{tip}} \tag{4.66}$$

In case of a uniform disc, the source term for the momentum equation is expressed, in dimensionless form:

$$\Delta P^* = \frac{\Delta P}{\rho_\infty U_\infty^2} = \frac{\frac{1}{2} T U_{tip}^2}{\frac{1}{2}\rho_\infty U_\infty^2 A U_{tip}^2} = \frac{1}{2}\frac{C_{\mathrm{T}}^{\mathrm{UK}}}{\mu^2} \tag{4.67}$$

The model by Shaidakov described earlier was implemented to achieve better distribution of loading than a uniform disc. The load distribution as function of the radius for the advancing and retreating blades are shown figure 4.1. Features such as blade tip offload due to the tip vortex, reverse flow region and presence of the hub are accounted for by the model.

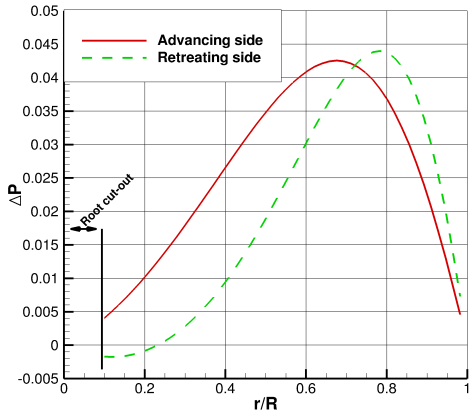

Figure 4.1: Distribution of loading as function of radius for advancing ($\Psi = \frac{\pi}{2}$) and retreating ($\Psi = \frac{3\pi}{2}$) blades.

More advanced actuator disc models describe the rotor wake in a time-accurate manner by localising the position of the blade at each instant in time and distributing the effect of the blade loading accordingly. The lifting line or lifting surface theories may be used to improve the accuracy of the model by accounting for the local flow velocity. They provide an estimate of the loading for each blade section at each instant in time depending on the flow condition. As for the steady actuator model used for this work, the blade loading is applied by adding a source term to the CFD computation. Since the flow condition is taken into account to calculate the loading, it acts as a closed-loop system, as opposed to the previous - open-loop - definitions of an actuator disc.

4.10.1 Atmospheric Boundary Layer

In the context of shipborne rotorcraft, accounting for the profile of the atmospheric boundary layer is important to determine the exact flight conditions. Wells [126] gives the tools to estimate the shape of the boundary layer over the ocean. A mean wind profile is shown in figure 4.2 and is defined by:

$$U = \frac{U_*}{k} \ln\left(\frac{z}{z_0}\right) \tag{4.68}$$

where U_* is the friction velocity, k the Von Kàrmàn constant and z_0 the roughness coefficient. The friction velocity is given by:

$$\tau = \rho U_*^2 \tag{4.69}$$

Over the sea surface, the roughness coefficient can be estimated from the friction velocity as well:

$$z_0 = \frac{\alpha U_*^2}{g} \tag{4.70}$$

where α is the Charnock constant = 0.016.

The problem depends on τ which can be measured directly or via the following relationship:

$$\tau_0 = \rho_{air} C_{\mathrm{D}} (U_{10} - U_S)^2 \tag{4.71}$$

where C_D is given by $C_D = (0.61 + 0.063 U_{10}) \cdot 10^{-3}$. U_{10} is the velocity at 10 meters above the sea and U_S is about 2% of U_{10}.

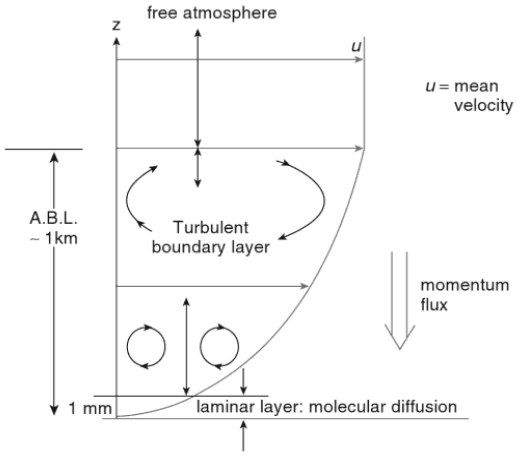

Figure 4.2: Typical ocean atmospheric boundary layer (from Wells [126])

The atmospheric boundary layer contains a wide range of turbulent scales. To take into account the larger scales that are to be resolved in the calculation, the synthetic turbulence model implemented in HMB2 can be used. The method uses "turbulent spots", generated randomly and the velocity field is generated by superposition of each spot's influence:

$$u_i^k(x_j) = \varepsilon_i^k f_{\sigma_j}(x_j - x_j^k) \tag{4.72}$$

which can be read as "the contribution of spot k to the velocity field u_i at position x_j is given by a function $f(r)$, where r is the distance between the velocity point and the spot location $x_j - x_j^k$. ε_i^k is the sign applied to the perturbation"

The velocity distribution around the spot k is given by $f(r)$, which includes a length scale σ_j and is defined either as a Gaussian or Tent function:

$$f_{\sigma_j}(r) = \frac{1}{\sqrt{2\pi}} e^{-\frac{3r^2}{2\sigma_j^2}} f_{\sigma_j}(r) = \sqrt{\frac{3}{2\sigma_j}} \left(1 - \left|\frac{r}{\sigma_j}\right|\right) \tag{4.73}$$

The overall velocity fluctuation is given by the sum of all the spots contributions. Each spot position and sign are generated randomly.

Chapter 5

GOAHEAD Validation

Most CFD studies of the helicopter flight emphasise the most challenging flight conditions, which usually correspond to the edges of the flight envelope. Hover and fast forward flight conditions are representative of most of the helicopter flight-time and should be studied carefully for optimal performance.

However, ship/helicopter operations are typically performed at low or moderate speed with constant action from the pilot required due to the unsteady nature of the ship wake. In these conditions, the combination of regions of low-speed, incompressible flow around the fuselage and high-speed, compressible flow around the rotor blades as well as stronger interactions between each element of the airframe may affect the accuracy of the CFD results.

In this chapter, validation calculations are carried out to demonstrate the capability of HMB2 to simulate full helicopter configurations at moderate advance ratio using the experimental data gathered during the GOAHEAD campaign [127].

5.1 Experimental Setup

The GOAHEAD experiments aimed at providing extensive data for the validation of full helicopter configurations for various flight conditions. Eight test cases were first considered to cover different flight speeds and rotor loadings. Their characteristics are presented in table 5.1. Further details about the campaign and the experimental set-up can be found in Antoniadis *et al.* [127]. The flight state of the highlighted test case "TC2" is the most representative of ship/helicopter operations and was chosen for the validation of the CFD solver.

The free-stream Mach number of 0.059 corresponds to an advance ratio of 0.096 and the fuselage has a nose-up pitch attitude of 1.9 degrees. The helicopter model (approx 1:8 scale) was trimmed in the wind tunnel to minimise forces and moments

Test Case	**data point**	$M_\infty^{\mathbf{WT}}$	$\Theta^{\mathbf{Fus}}$	$C_T^{\mathbf{M}}$	$M_{tip}^{\mathbf{M}}$	$C_T^{\mathbf{T}}$	$M_{tip}^{\mathbf{T}}$	C_D
TC1a - Isolated fuselage	136	0.059	+4.8					
TC1b - Isolated fuselage	151	0.204	-2.0					
TC1c - Isolated fuselage	185	0.258	-1.0					
TC2 - Low-speed pitch-up	392	0.059	+1.9	0.071	0.617	0.087	0.563	0.176
TC3-4 - Cruise and high-speed tail shake	396	0.204	-2.5	0.071	0.617	0.080	0.563	0.185
TC5 - Highly loaded dynamic stall	424	0.194	+1.0	0.084	0.617	0.040	0.563	0.050
TC6 - Very high speed	416	0.25	-1.0	0.071	0.617	0.040	0.563	0.050

Table 5.1: List of the GOAHEAD test cases and the corresponding flow conditions (Reproduced from Antoniadis *et al.* [127]).

θ_0	θ_{1c}	θ_{1s}	β_0	β_{1c}	β_{1s}
9.76	-1.76	2.56	1.96	-0.76	1.29

Table 5.2: Main rotor trim condition of the GOAHEAD TC2 test case (NLR Report NLR-TP-2007-604 [129]).

on the mast. The exact trim state of the TC2 case was calculated *a posteriori* using the comprehensive code HOST [128] and is shown table 5.2.

The experimental rig is built around a fuselage model similar to the one of the NH90 helicopter, mounted on a streamlined strut. The 4-bladed main rotor is based on the 7AD blade geometry previously used in the literature [130], with a radius of $2.04m$. The tail rotor has two un-cambered, non twisted blades and the ratio of rotation rate between the two rotors is set to 5, albeit with no mechanical connection between them.

The experimental data collected includes recordings of unsteady pressure levels at 130 different locations on the fuselage, fin, tail plane and main rotor blade, as shown figure 5.1. PIV measurements were also carried out in a frame above the tail plane that shows the location of the vortices shed by the main rotor.

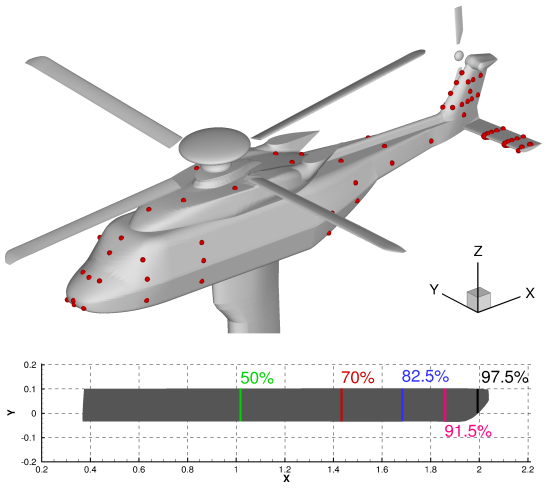

Figure 5.1: Position of pressure sensors on the GOAHEAD fuselage and 5 radial stations of the instrumented blade.

5.2 Grid and Parameters

The grid used for this work was split in three parts. The fuselage grid also serves as background and contains the strut used to hold the model in the wind tunnel. The main and tail rotor are created separately and assembled to the final grid using the sliding plane method. The sliding plane method was designed to exchange information between rotor and background grids while they rotate.

For preliminary calculations, a baseline mesh was generated that contains 23.8 million cells. It was further refined and particular attention paid to the region of the tail to capture the main rotor blades vortices and the interaction with the tail plane, fin and tail rotor. The final grid contains a total of 64 million cells. Table 5.3 gives a summary of the number of blocks and cells for each component of the two meshes used in this work.

The fine mesh version of the GOAHEAD grid is shown in figure 5.2 and a view of the sliding planes is given in figure 5.3.

	Fuselage	**Main Rotor**	**Tail Rotor**
Number of blocks	2308	1112	376
Number of cells of baseline grid (millions)	11.8	9.6	2.4
Number of cells of refined grid (millions)	38.6	21.9	3.5

Table 5.3: Sizes of the baseline and refined GOAHEAD grids.

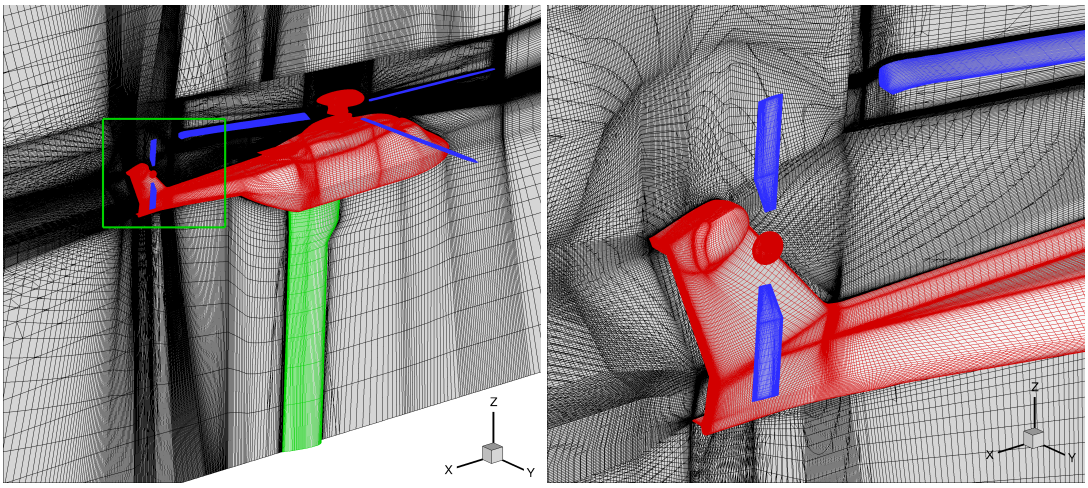

Figure 5.2: Fine version of the GOAHEAD grid used for this work.

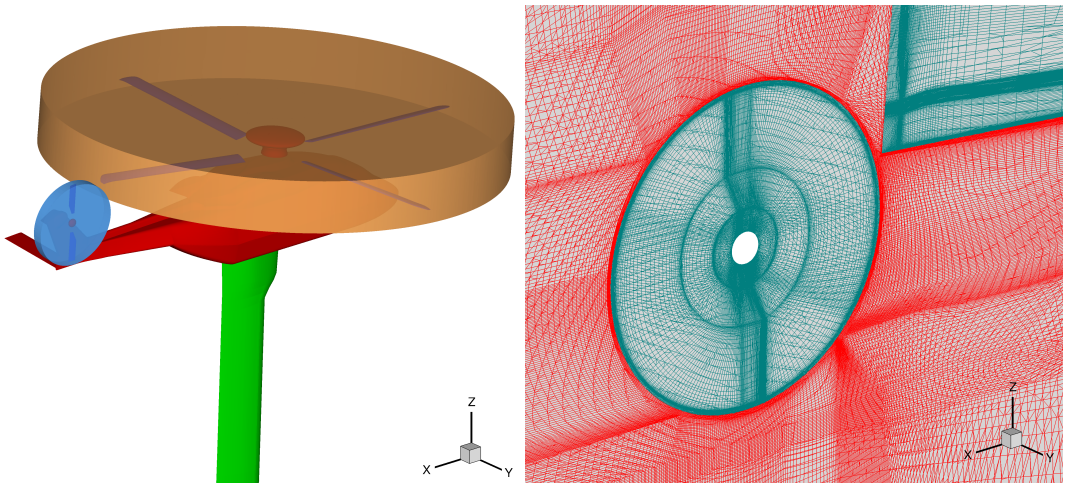

Figure 5.3: Positions of the sliding planes used to interface the main and tail rotors grids with the background.

The low-speed case ”TC2” of the GOAHEAD database is used to validate HMB2 for helicopter configurations at low advance ratio [127].

The advance ratio is close to 0.1 and the aircraft has a nose-up pitch angle of 1.9 degrees. The main rotor pitch and flap harmonics were predicted using HOST and the same values are used here, without re-trimming. This case is characterized by important blade/vortex and vortex/tail interactions due to the low advance ratio, since the rotor wake vortices do not clear the airframe as quickly.

The experimental data available includes recordings of unsteady pressure on the fuselage, fin, tail and main rotor blades, as well as PIV measurements in the region above the tail plane.

The computation parameters and aircraft attitude and controls are given tables 5.4 and 5.2. The computation ran for a total of 10 revolutions on the baseline grid and

Mach Number	**Fuselage pitch**	**Rotor loading**	M_{tip}^{M}	M_{tip}^{M}	**Reynolds number**	**Turbulence model**	$\frac{\Omega^M}{\Omega^T}$
0.059	+1.9 deg.	0.071	0.617	0.566	10^6	$k-\omega$	5.0

Table 5.4: Flight conditions and parameters of the GOAHEAD TC2 test case (NLR Report NLR-TP-2007-604 [129]).

convergence of the loads is achieved after about 5 revolutions, i.e. when the main rotor wake has cleared the airframe (Figure 5.4).

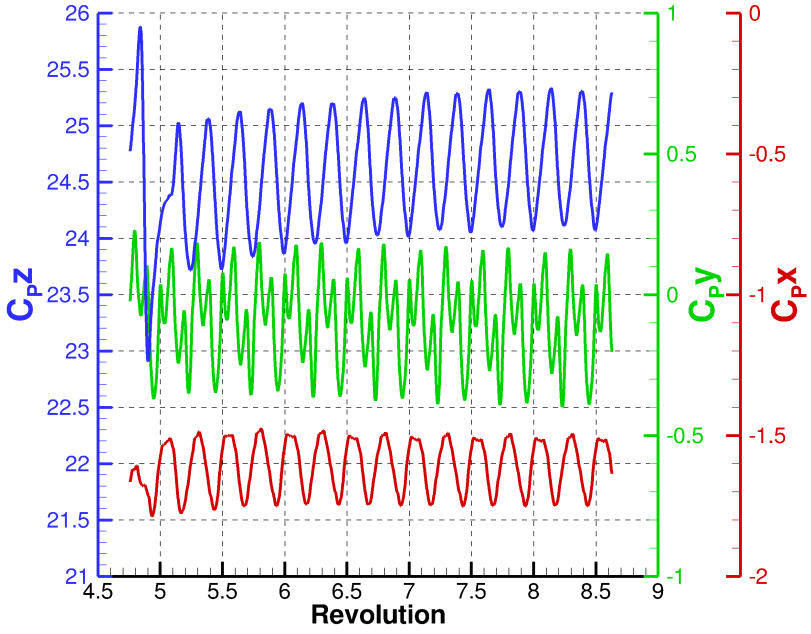

Figure 5.4: Convergence of the integrated forces for the last 4 revolutions.

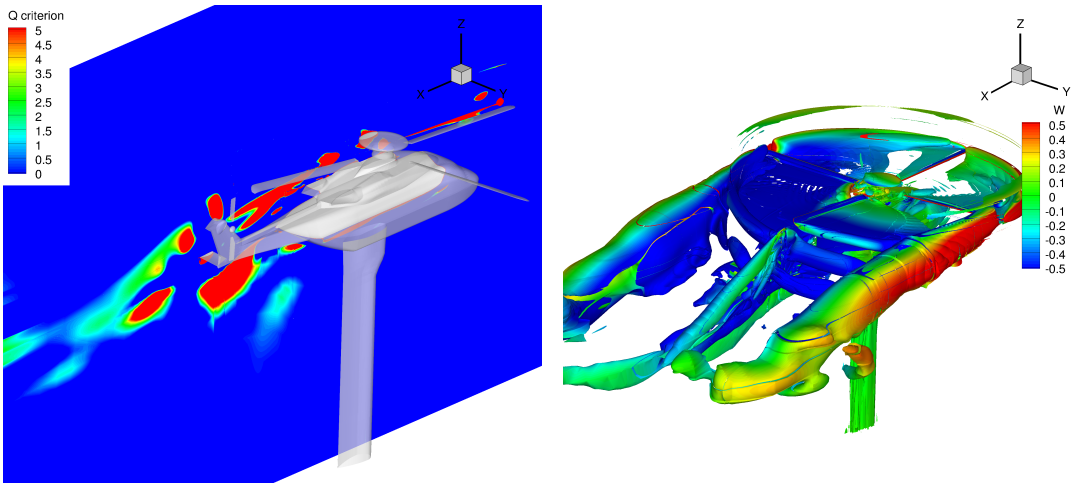

(a) (b)

Figure 5.5: Characterisation of the flow using Q-criterion. (a) Slice of the flow at y=-0.225 and (b) Iso-contour of Q-criterion=5 colored by non-dimensional vertical velocity $\frac{w}{U_\infty}$.

5.3 Fuselage Results

Figure 5.7 shows the distribution of instantaneous pressure at three different sections of the fuselage for two positions of the main rotor, 0 and 45 degrees azimuth. Error bars are added to account for the uncertainty of the experimental measurements. The largest uncertainties are found in the region immediately behind the main rotor, between the two exhausts where the flow is extremely unsteady. Overall, the distribution of pressure coefficient on the fuselage is predicted within the margin of error of the experimental data, with both the coarse and fine grids.

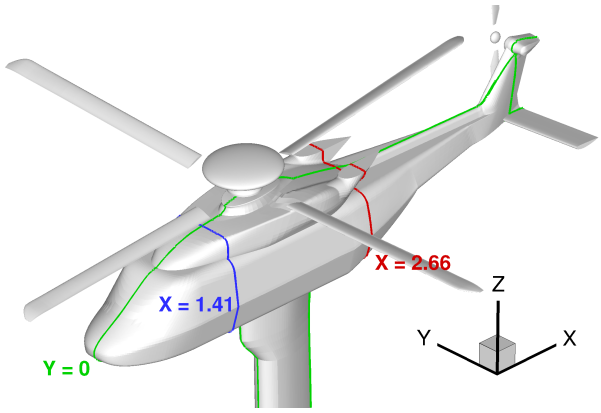

Figure 5.6: Positions of slices

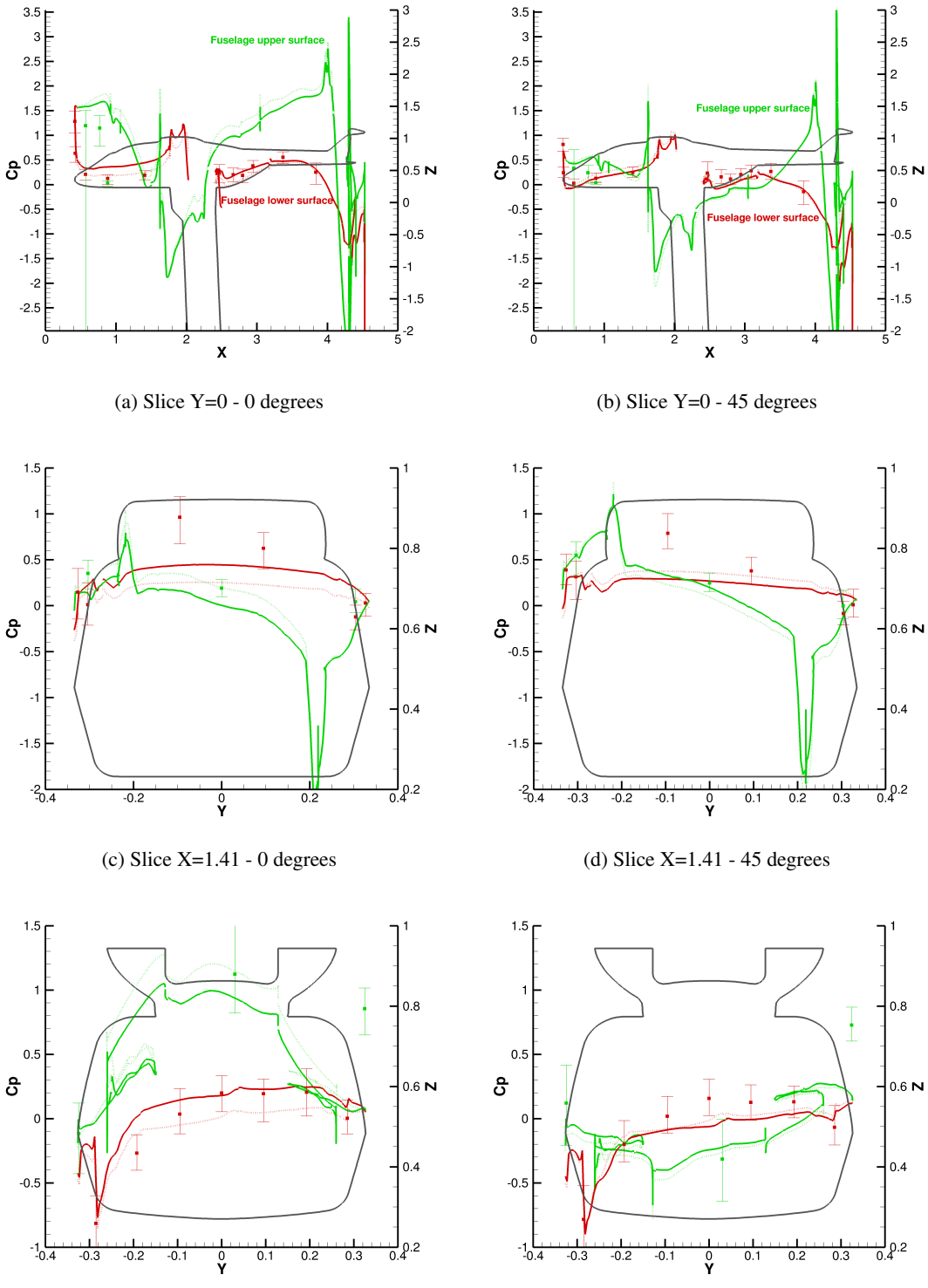

(a) Slice Y=0 - 0 degrees

(b) Slice Y=0 - 45 degrees

(c) Slice X=1.41 - 0 degrees

(d) Slice X=1.41 - 45 degrees

(e) Slice X=2.66 - 0 degrees

(f) Slice X=2.66 - 45 degrees

Figure 5.7: Distribution of pressure coefficient at three sections of the fuselage for 0 and 45 degrees of main rotor azimuth. Coarse (plain lines) and fine (dashed lines) mesh results.

The time-dependant signals of pressure coefficients are plotted at the 8 different

locations on the fuselage indicated in figure 5.8 with the corresponding Fourier decompositions. The results shown in figure 5.3 are characterised by a dominance of 4-per-rev and 10-per-rev signals corresponding to the main and tail rotors blade-passing frequencies respectively. It is important to note the uncertainty on the tail rotor thrust that has not been trimmed to the experimental value (C_T^{UK} of 0.075 for CFD instead of 0.174 during the tests).

Points 20, 25, 26 and 42 show a dominance of the main rotor signal and a very good prediction of the peak-to-peak values. The points 79, 90, and 91 located at the tail are dominated by the tail rotor signal on the CFD data. The amplitude of the tail rotor signal is much lower on the experimental dataset, which may be explained by the values used for trimming the rotor (lower collective, no flapping). The point 120 is located further along the tail plane and shows a phase offset which is due to the main rotor wake being convected faster in the CFD, possibly because of the uncertainty in main rotor collective.

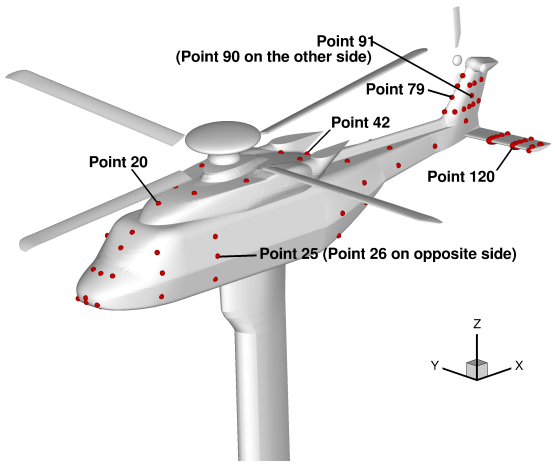

Figure 5.8: Positions of the pressure sensors on the fuselage.

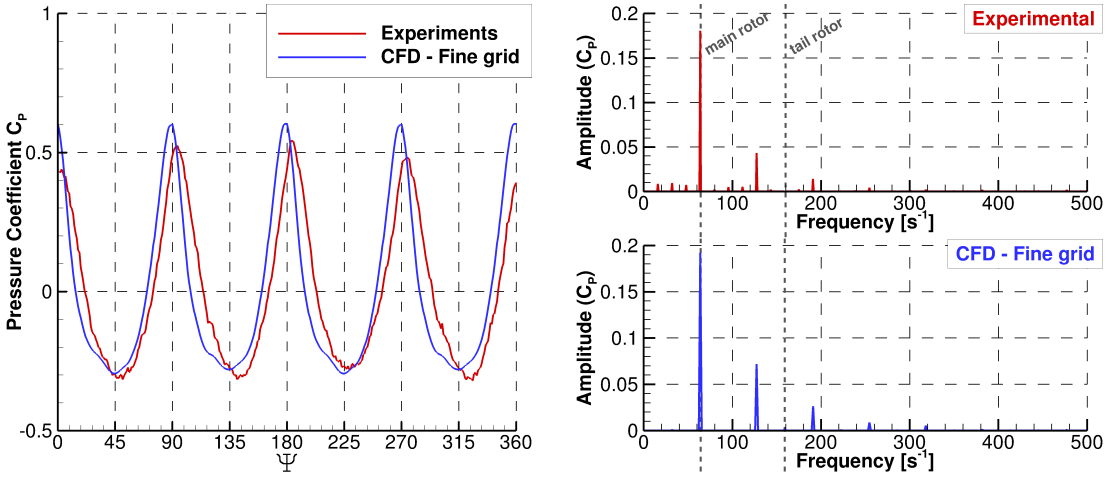

(a) Point 20

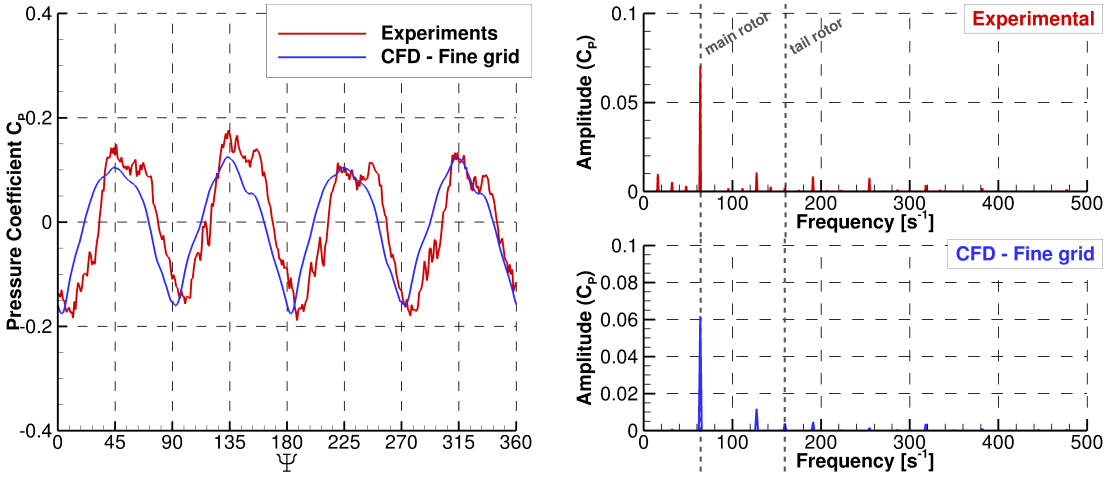

(b) Point 25

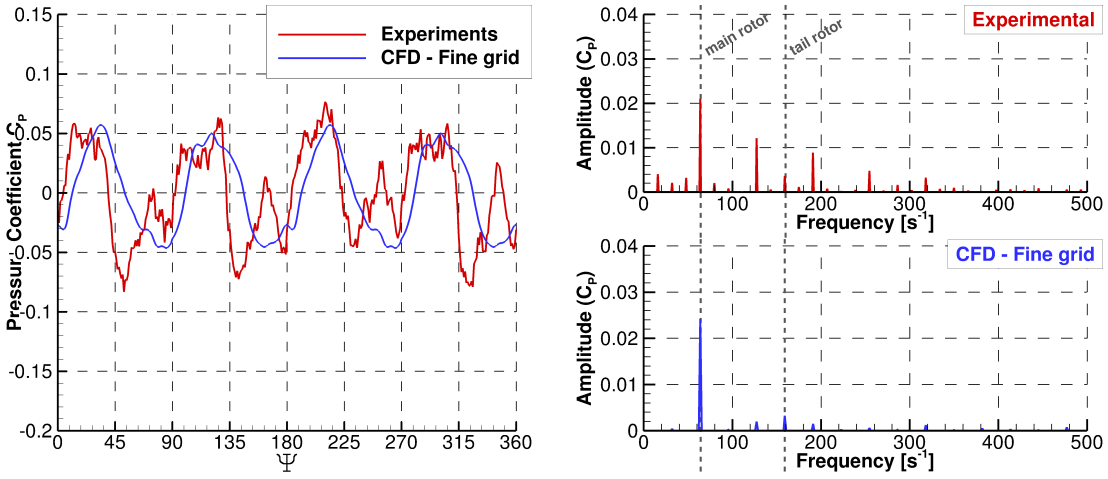

(c) Point 26

Figure 5.9: Signal of pressure and FFT analysis at different locations on the fuselage. Eight different points on the fuselage. Mean value removed

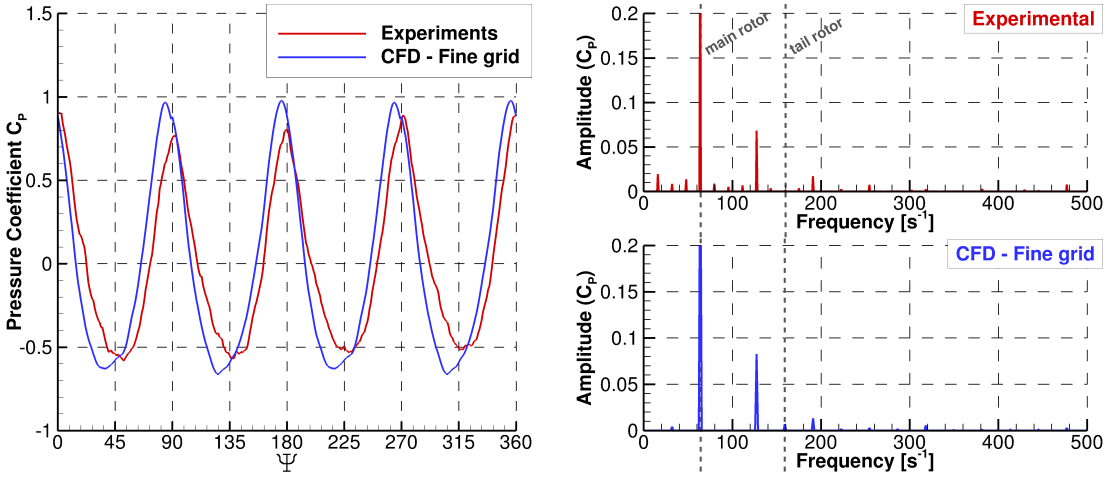

(d) Point 42

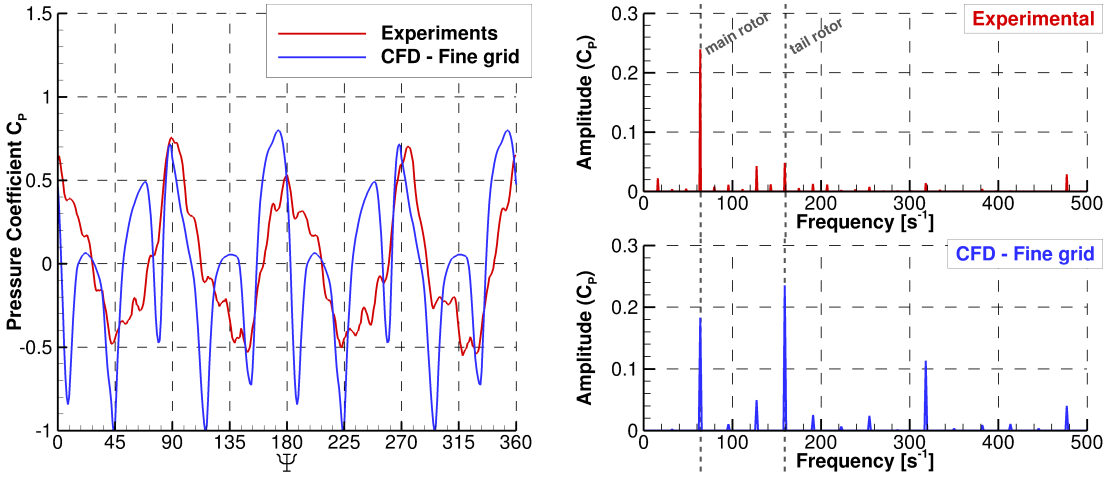

(e) Point 79

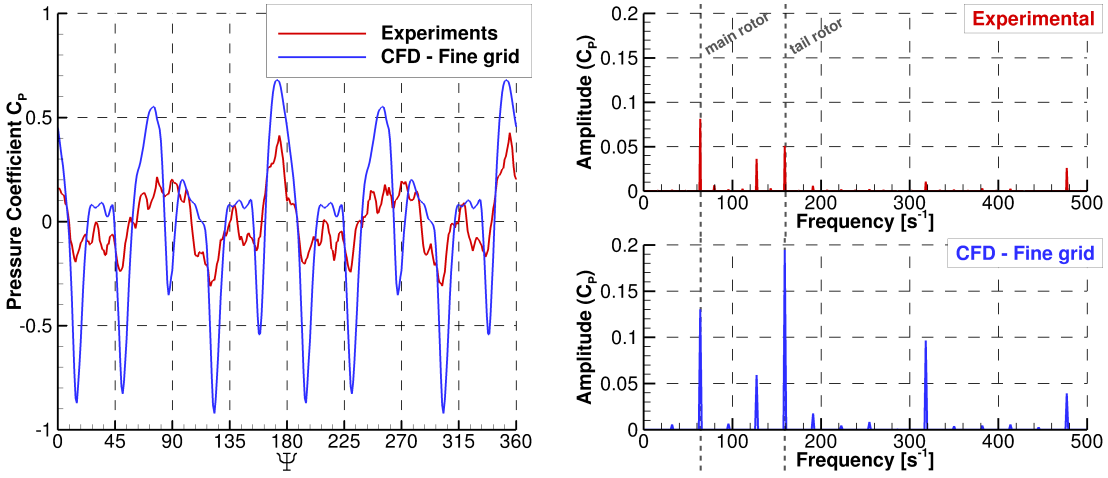

(f) Point 90

Figure 5.9: **Continued -** Signal of pressure and FFT analysis at different locations on the fuselage. Eight different points on the fuselage. Mean value removed

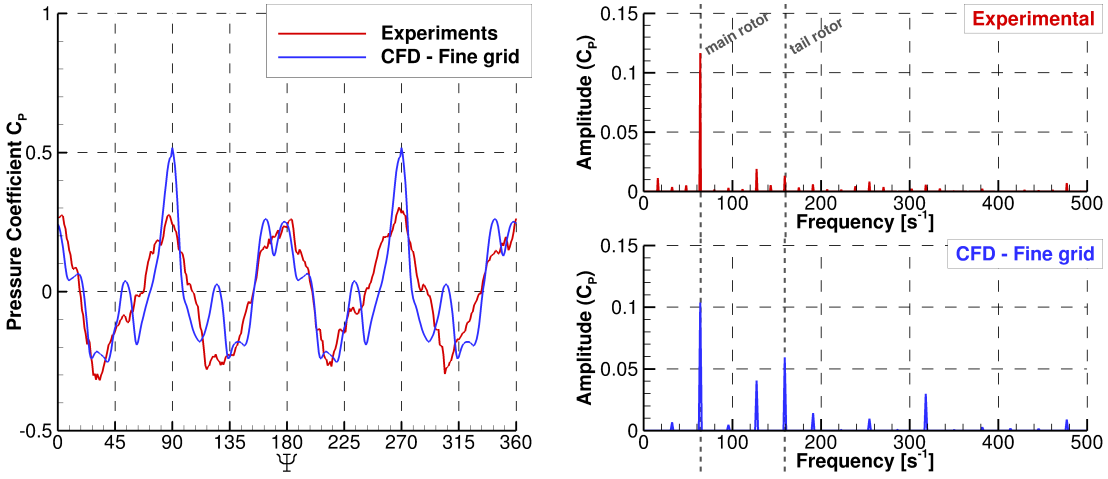

(g) Point 91

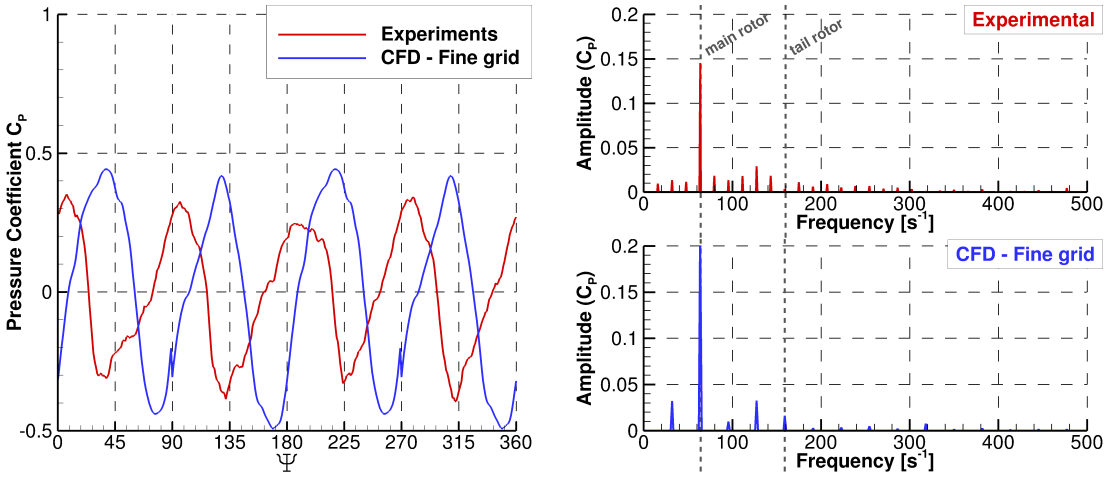

(h) Point 120

Figure 5.9: **Continued -** Signal of pressure and FFT analysis at different locations on the fuselage. Eight different points on the fuselage. Mean value removed

5.4 Main Rotor Results

The instantaneous pressure coefficients at different sections of the main rotor blades were also measured. The sections are positioned at 50%, 70%, 82.5%, 91.5% and 97% of the blade span. Figures 5.10 and 5.10 show the first 4 sections at every 30 degrees of azimuth. The results show good agreement, especially for the inboard sections and are consistent around the azimuth.

Figure 5.11 show the distribution of loading across the rotor disc for the main and tail rotors. The blade loading in integrated at each section and the value is represented in the disk plane as function of the spanwise and azimuthal position. The main rotor shows high loadings at the front and the back and is almost symmetric in left/right loading at the trim condition specified. The final values of thrust for the main and tail rotors are shown table 5.5. With the trim conditions provided by HOST [127], the main rotor shows a loading 19.7% higher than in the experiments. As mentioned previously, the tail rotor is significantly less loaded.

	σ	C_T^{UK}	C_T^{UK}/σ **(CFD)**	C_T^{UK}/σ **(experiments)**	**Difference**
Main rotor	0.085	0.0143	0.170	0.142	19.7%
Tail rotor	0.115	0.0087	0.075	0.174	331%

Table 5.5: Summary of main and tail rotor characteristics and comparison with experimental results.

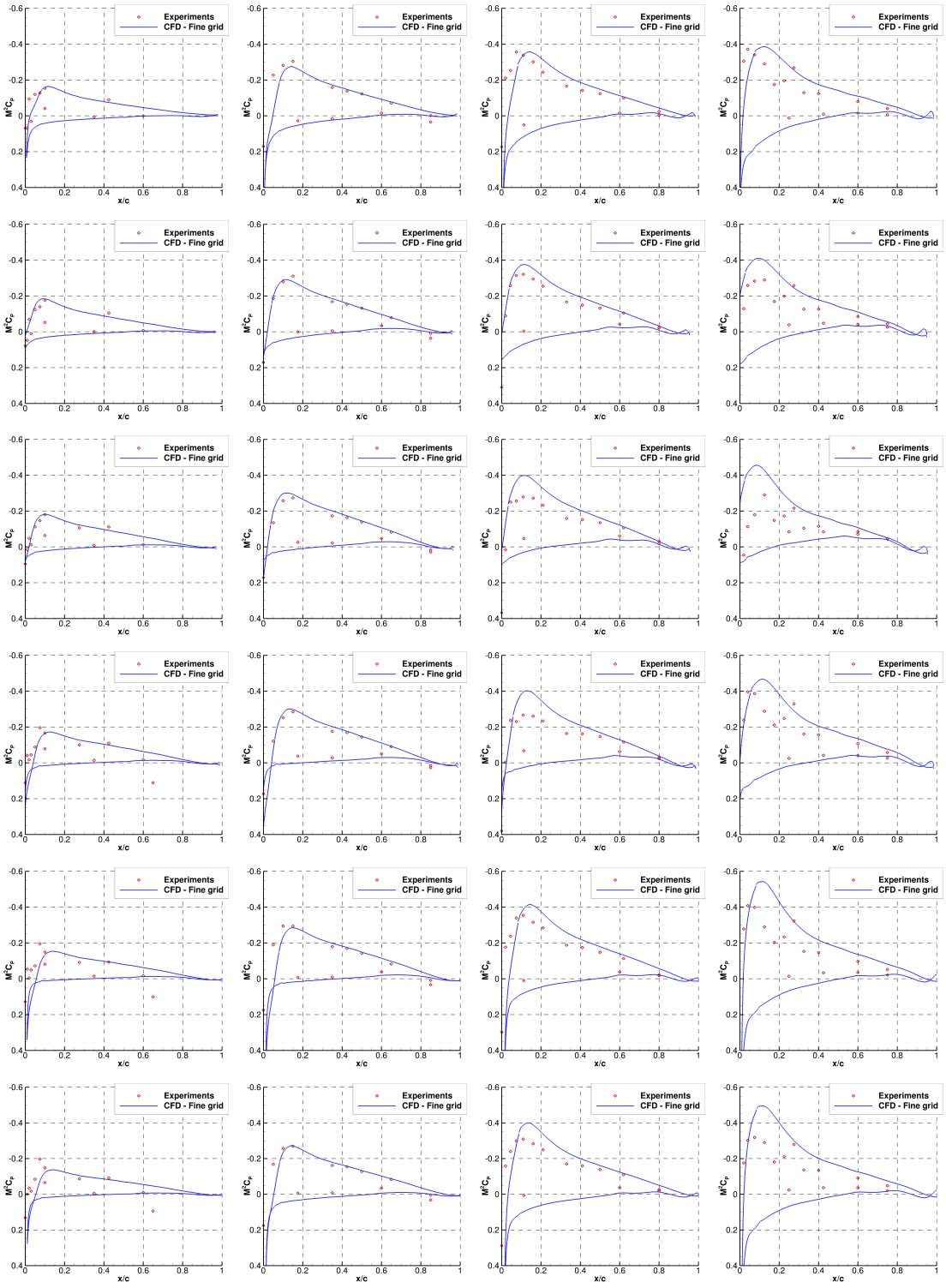

Figure 5.10: Curves of experimental and numerical pressure coefficient between 0 and 150 degrees at 4 different locations: 50%, 70%, 82.5% and 91.5% span.

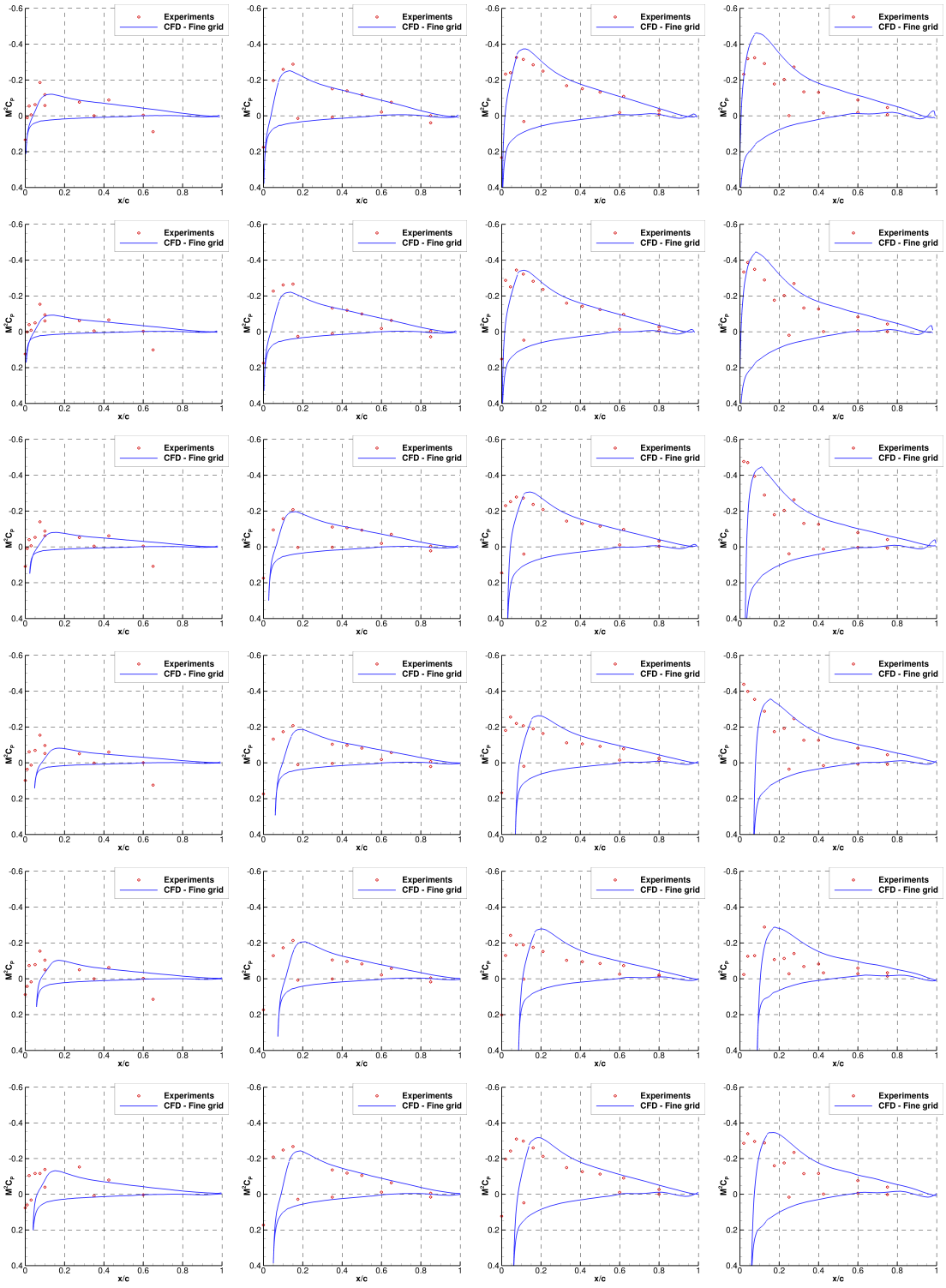

Figure 5.10: **Continued -** Curves of experimental and numerical pressure coefficient between 180 and 330 degrees at 4 different locations: 50%, 70%, 82.5% and 91.5% span.

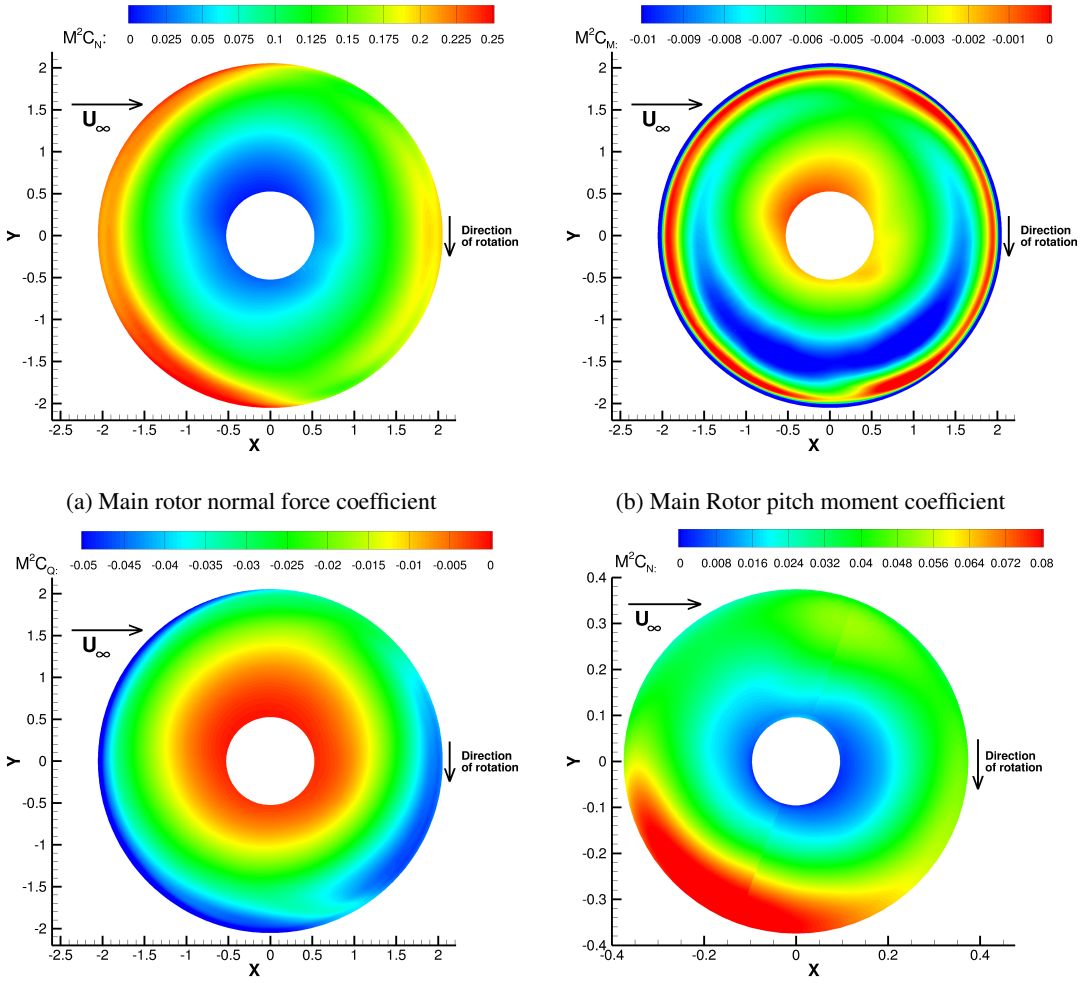

(a) Main rotor normal force coefficient

(b) Main Rotor pitch moment coefficient

(c) Main Rotor torque moment coefficient

(d) Tail rotor normal force coefficient

Figure 5.11: Main and tail rotors loading coefficients as function of azimuth and radial position. Low-speed TC2 case of GOAHEAD.

5.5 PIV Comparisons

One objective of the low speed case was to observe the tip vortices of the main rotor blades passing in proximity to the tail. PIV planes were taken in the region above the tail plane. Figure 5.12 shows the PIV region at three time instants corresponding to 60, 70 and 80 degrees azimuth of the main rotor, along with the corresponding CFD results.

The red and black crosses point at the center of the vortex core in the experimental and numerical datasets respectively. The vortex cores follow the same trajectory in CFD and experiments but the offsets suggest faster convection in the CFD simulations, which is consistent with the pressure signals of figure 5.3.

The mesh is perhaps not fine enough to preserve the high vorticity level at the vortex core and the intensity is significantly lower in the CFD data.

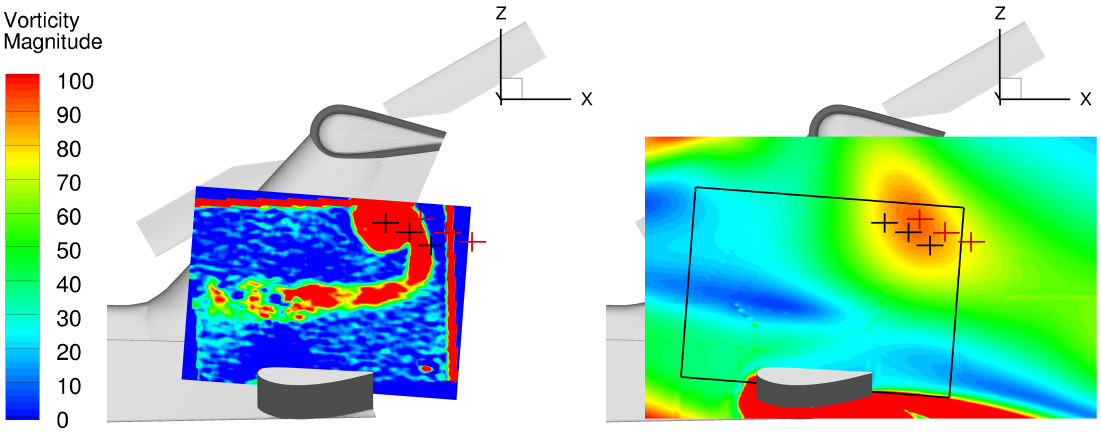

(a) 60 degrees

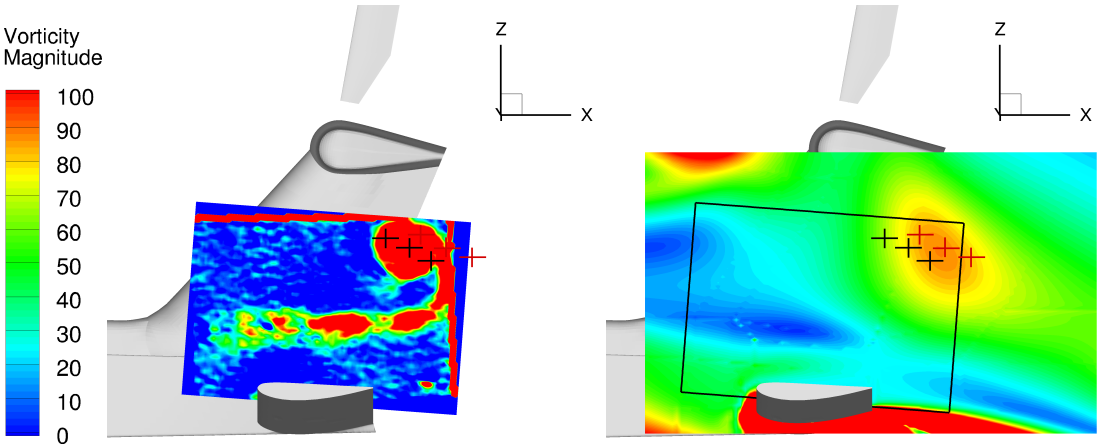

(b) 70 degrees

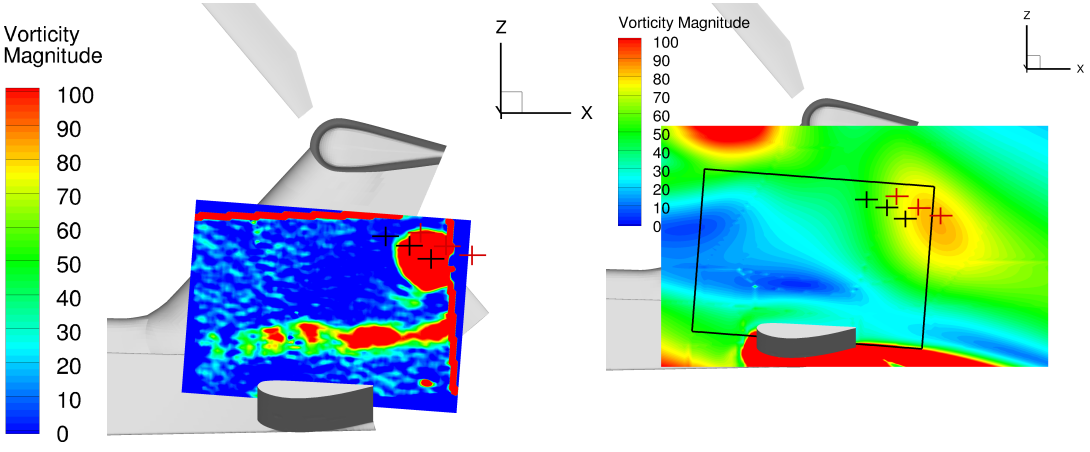

(c) 80 degrees

Figure 5.12: Comparison between PIV data (left) and numerical results (right) in the region of the tail for 3 different azimuth of the main rotor. Crosses indicate centers of vortices: red CFD, black experiments. Vorticity shown in $deg.s^{-1}$

Chapter 6

Ship-Wake Computations

The content of this chapter was published in:
C. Crozon, R. Steijl and G. Barakos,
Numerical Study of Rotors in Ship Airwake,
The American Institute of Aeronautics and Astronautics Journal of Aircraft, 2013.

The study of the ship/helicopter dynamic interaction requires to capture accurately the steady and unsteady characteristics of the ship wake. Ship wakes are highly turbulent, low-speed flows, with Mach numbers below 0.1 and Reynolds numbers in the 10-100 million range based on the ship length.

The sharp edges typical of most ship geometries are known to fix the points of separation in the flow and generate large zones of recirculation in the vicinity of the ship superstructure. The wake is typically unsteady, with shedding frequencies in the range 0.2-2Hz depending on the size of the elements of the superstructure and the wind speed. The Reynolds number based on the ship length is around 100 millions for a frigate while the Mach number is below 0.1.

Most of the turbulence energy of the wake correspond to structures in the 0.2-2Hz range [3]. This corresponds to the typical range of frequency a pilot responds to, and therefore plays an important role in increasing the pilot workload when manoeuvring the aircraft in the vicinity of the ship

This work focuses on frigate-like ship (see figure 6.1) with a landing deck at the aft end. A comprehensive validation of the Helicopter Multi-Block (HMB2) solver for the simulation of ship airwakes is carried out using the modified Simple Frigate Shape (SFS2) geometry. The results for three turbulence models - URANS $k-\omega$, DES Spalart-Allmaras and SAS - and three different grid densities are compared with the experimental data available. The steady and unsteady characteristics permit to

determine the numerical models and grid densities required to capture accurately the characteristics of the flowfield.

Figure 6.1: Example of a frigate: The Type-23 HMS Richmond of the Royal Navy. From http://www.defenceimagery.mod.uk, under Open Government License.

A campaign of measurements was conducted at the Naval Surface Warfare Center Carderock Division (NSWCCD) [131, 132]. Published results include mean values of streamwise velocity, local flow pitch and yaw angle along 8 vertical lines positioned in the direct vicinity of the ship, above the landing deck (Figure 6.12(a)). Experiments were conducted at 0 and 60 degrees wind angle. A set of numerical simulations have been conducted that reproduce the two experimental conditions using Detached Eddy Simulation with Spalart-Allmaras turbulence model (DES-SA) and the Scale-Adaptive Simulation (SAS). Results for each of the two wind angle have a similar level of agreement and only the 60 degrees case is reproduced in this chapter.

6.1 Unsteady Ship Airwake Validation

6.1.1 Grid and Parameters

The employed grids were structured multi-block, and generated using ICEMCFD. Their sizes were generated for the purposes of this work and are shown figure 6.2: coarse, medium and fine that contain 4.2, 7.9 and 14.8 million cells respectively. The conditions reproduce those of the experimental campaign and are shown in table 6.1.

Reynolds number	Mach number	Ship beam length	Time step
658000	0.1	1	0.01

Table 6.1: Parameters used for the SFS2 simulations to match the experimental conditions from NRC [30,31]

The Mach number was set to 0.1, which is suitable for incompressible flows and does not compromise the stability of the solver. All simulations were performed for the three turbulence models - URANS $k-\omega$, DES Spalart-Allmaras and SAS - and on the three different grids.

The maps in the experimental dataset are shown in figure 6.3. The first section analyses the statistical convergence of each calculation based on the time-histories of the velocity signals obtained at 2 probe positions. The second section compares the time-histories of the velocity signals obtained at 2 different probe positions for each turbulence model and grid density. Finally, mean and RMS values of the velocity are calculated on the converged part of the signals and compared with the experimental data. Conclusions are given in terms of accuracy of the solution, stability of the simulation and minimum grid density required to capture the flow features.

Figure 6.4 shows example of velocity signals taken along the center-line at points 39 and 171. Although they are not completely periodic, most of the signals show periodic behaviours and are homogeneous in term of variations.

6.1.2 Statistical Convergence

To assess the statistical convergence of each dataset, the time-history of the velocities at 2 probe positions were used for each turbulence model and grid size. The mean and RMS quantities were calculated on "time-windows" of 5, 10, 15 or 20 seconds and the values were plotted as function of the window position. The process was repeated for different window sizes to alleviate the uncertainty on the sampling size. Figures 6.5 and 6.6 explain the method and the results obtain for the case of a DES simulation on the baseline grid.

6.1.3 Grid Sensitivity Study

A grid sensitivity study was conducted using the DES-SA model and results are reproduced in figures 6.7 and 6.8. Although no experimental data have been published that help estimate the level of unsteadiness to expect in the flow, the simulations show that a fine grid containing 15 million cells was required to capture a reasonable level of unsteadiness that is typical of ship wakes when using DES. The frequency analysis in

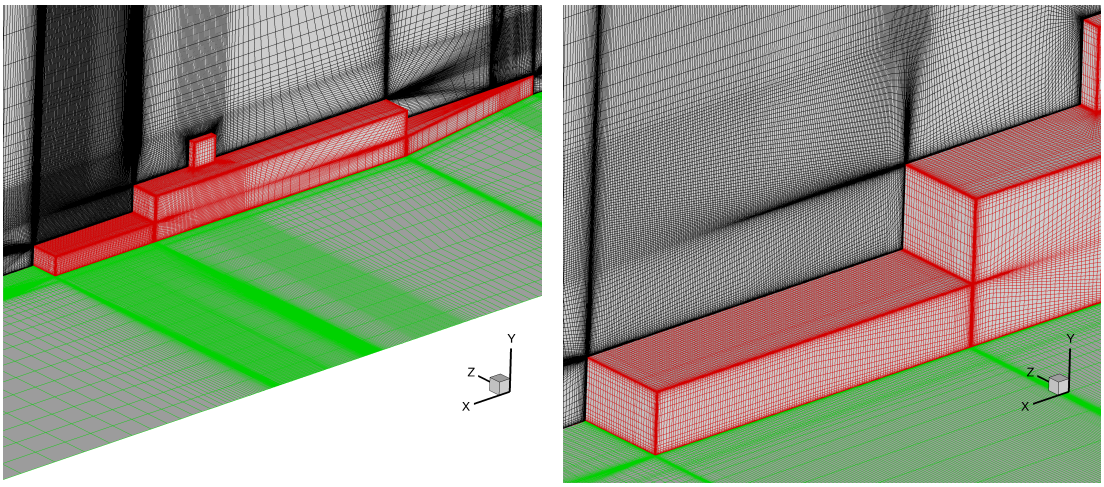

(a) Fine grid - 14.8M cells

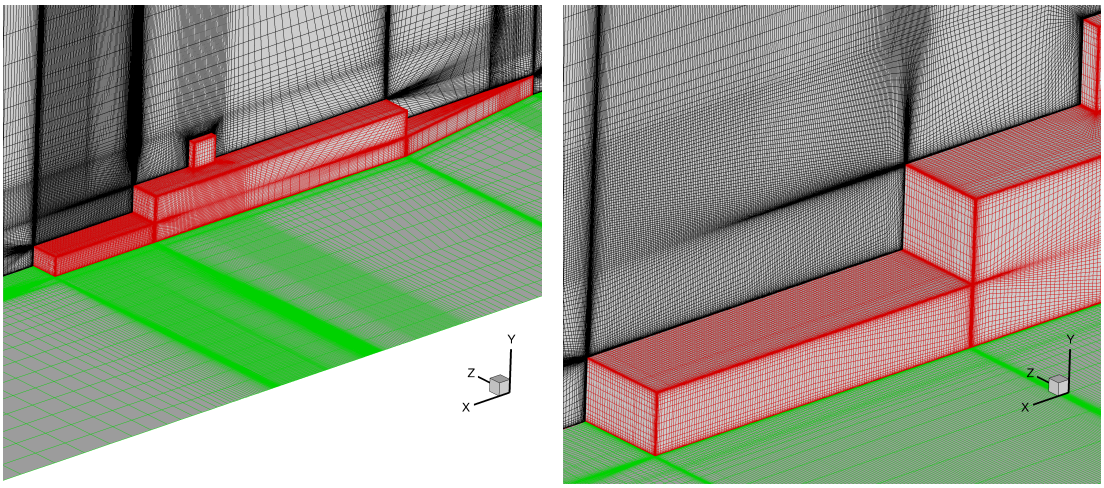

(b) Intermediate grid - 7.9M cells

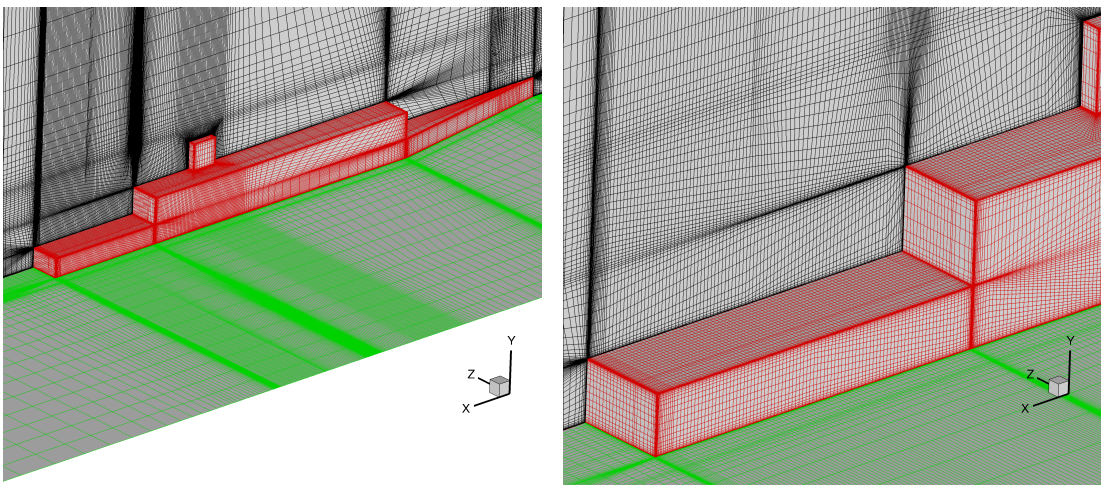

(c) Coarse grid - 4.2M cells

Figure 6.2: Simple Frigate Shape (SFS2) grids of three different densities.

6.8(b) and (c) show that similar levels of unsteadiness are found when using the SAS

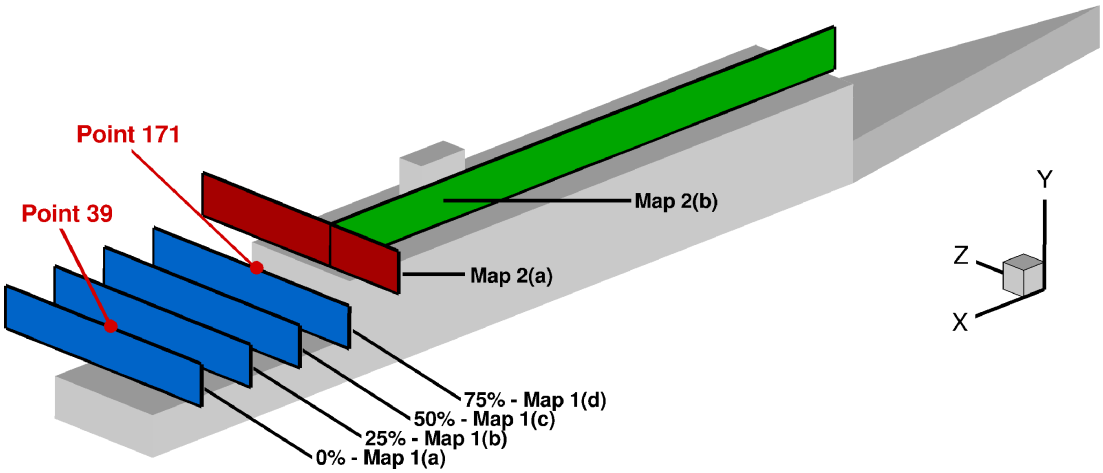

Figure 6.3: Velocity maps of the experimental dataset.

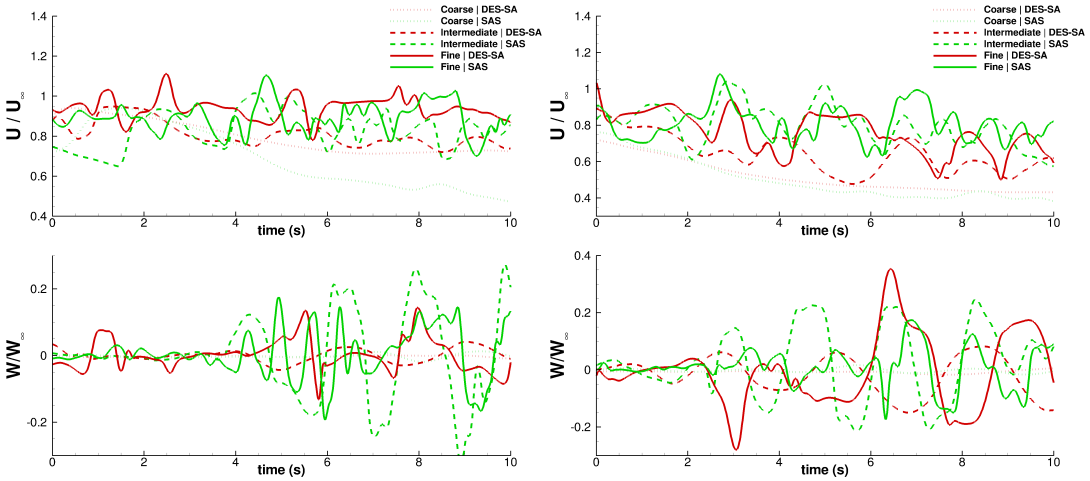

(a) Probe 39

(b) Probe 171

Figure 6.4: History of axial and lateral velocity for 2 probe positions, $WOD = 0°$, $Re = 6.58 \cdot 10^5$

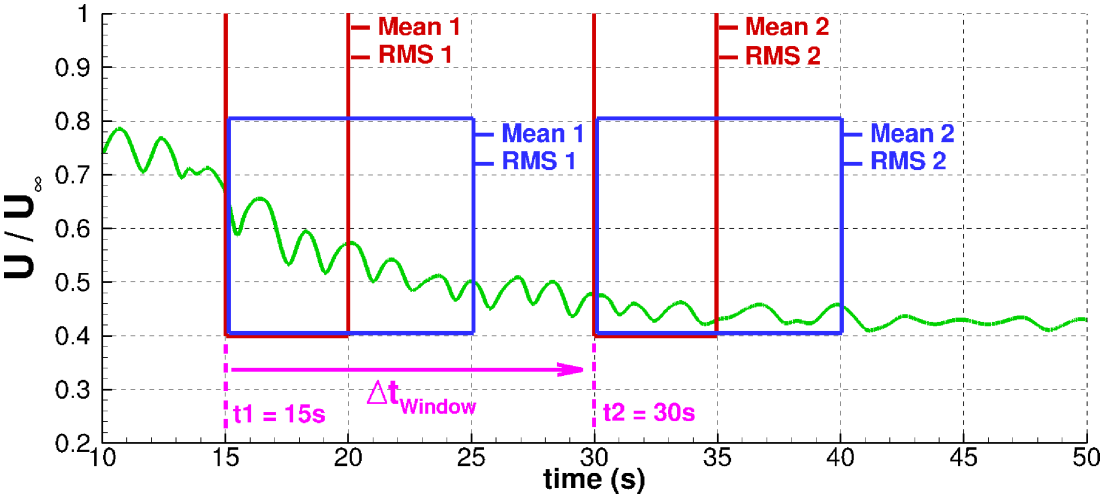

Figure 6.5: Principle of the statistical analysis used to assess the convergence of the data.

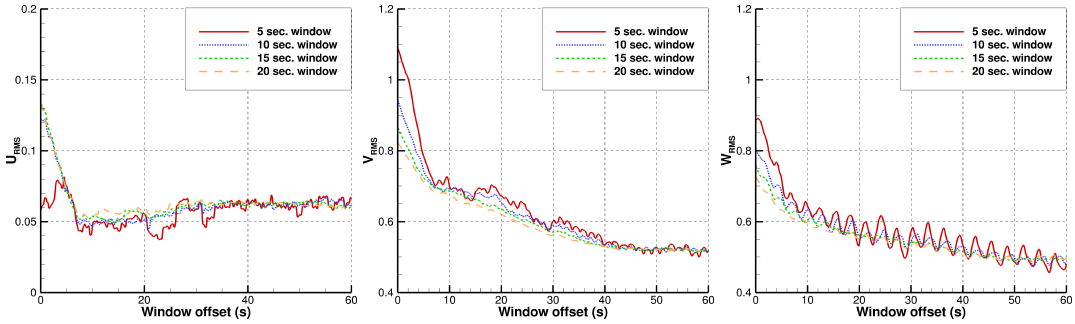

Figure 6.6: Statistical convergence of DES results on baseline grid at probe 39.

model with the intermediate and fine grid densities.

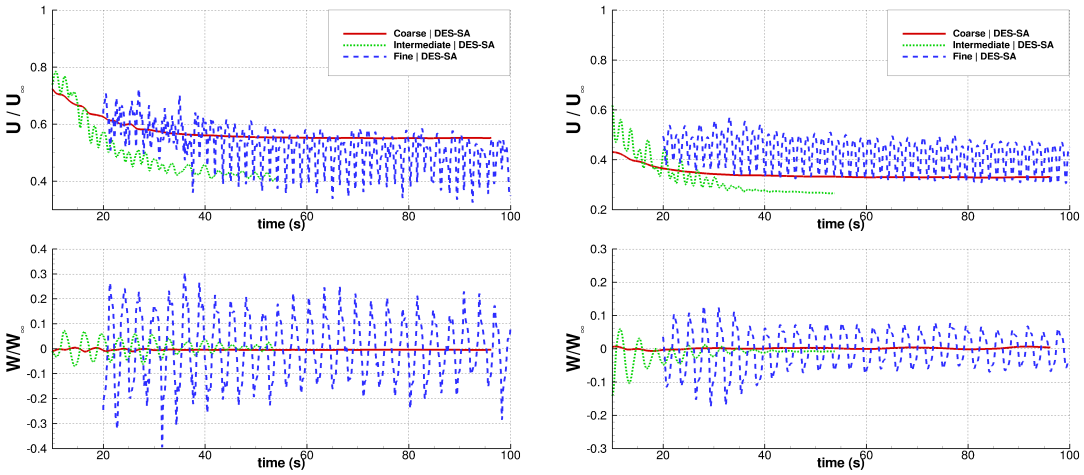

(a) Probe 39

(b) Probe 171

Figure 6.7: Comparison of 2 velocity signals using DES for 3 grid densities at 2 probe positions. $WOD = 0^{\circ}$, $Re = 6.58 \cdot 10^5$

Figures 6.9, 6.10 and 6.11 show the velocity signals obtained for each of the three grids using various turbulence models. The coarse and intermediate-density grid fail to produce a realistic level of turbulence in the ship wake. However, DES and SAS models produce similar levels of turbulence using the finer baseline mesh. The URANS model consistently produces a steady-state solution with very low levels of turbulence, and is therefore not suitable for unsteady simulations of highly turbulent flows such as ship wakes.

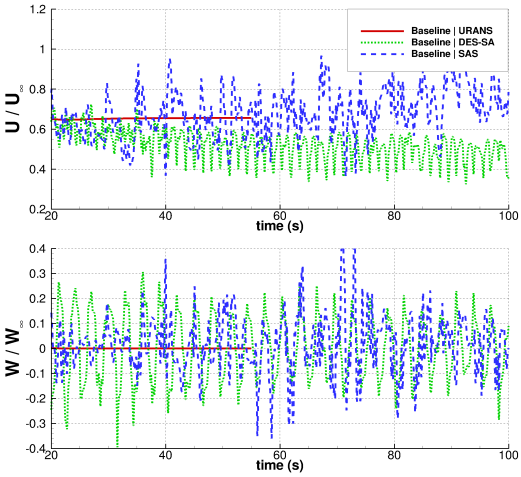

(a) Velocity history

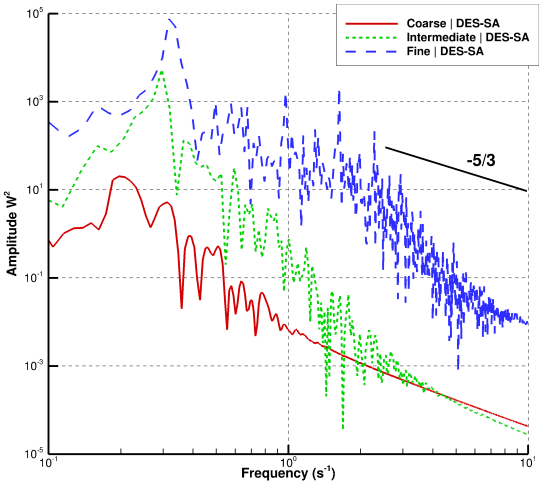

(b) DES Frequency analysis

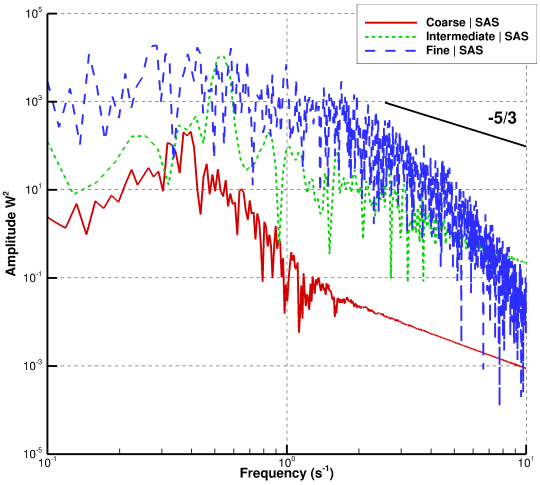

(c) SAS Frequency analysis

Figure 6.8: Comparison of URANS, DES-SA and SAS models and grid density study using DES-SA and SAS models on the Simple Frigate Shape. The typical shedding frequency is 0.6Hz as can be seen in the SAS results of (c). Headwind case, $Re = 6.58 \cdot 10^5$, probe 39. Part of the signal in the grey area were not used for the frequency analysis.

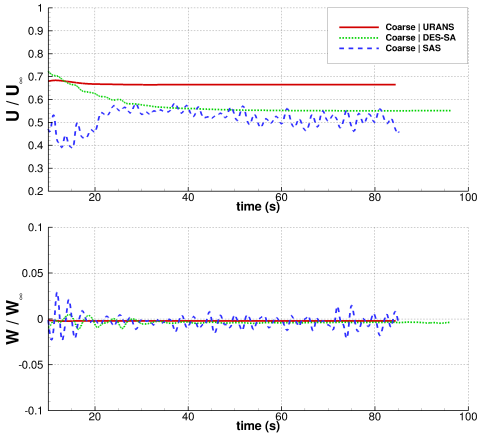

(a) Probe 39

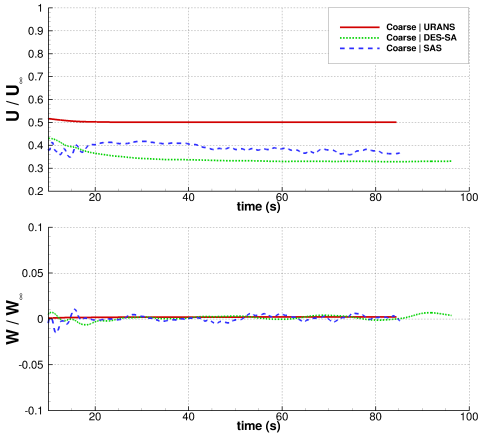

(b) Probe 171

Figure 6.9: Comparison of 2 velocity signals for the coarse density grid using 3 different turbulence models: URANS $k-\omega$, DES Spalart-Allmaras, SAS. $WOD = 0°$, $Re = 6.58 \cdot 10^5$

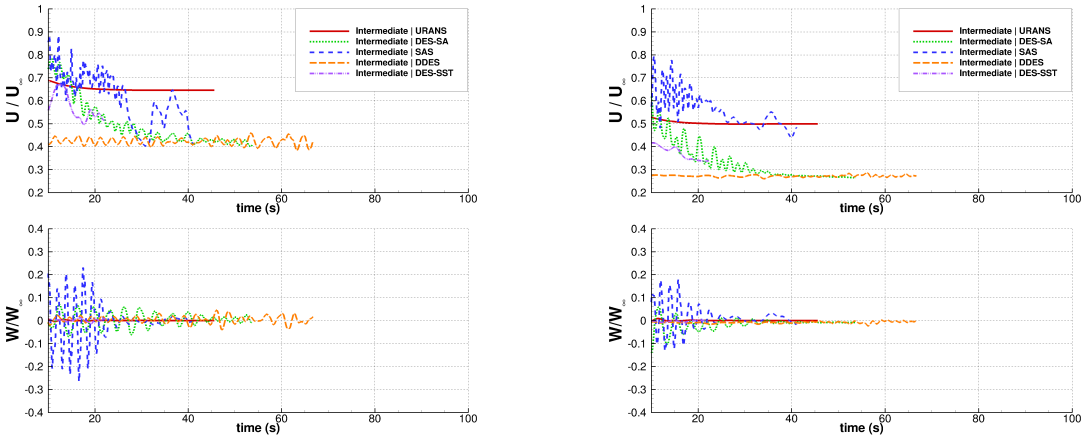

(a) Probe 39 (b) Probe 171

Figure 6.10: Comparison of 2 velocity signals for the intermediate density grid using 5 different turbulence models: URANS $k-\omega$, DES Spalart-Allmaras, SAS, Detached-DES Spalart-Allmaras and DDES SST. $WOD = 0°$, $Re = 6.58 \cdot 10^5$

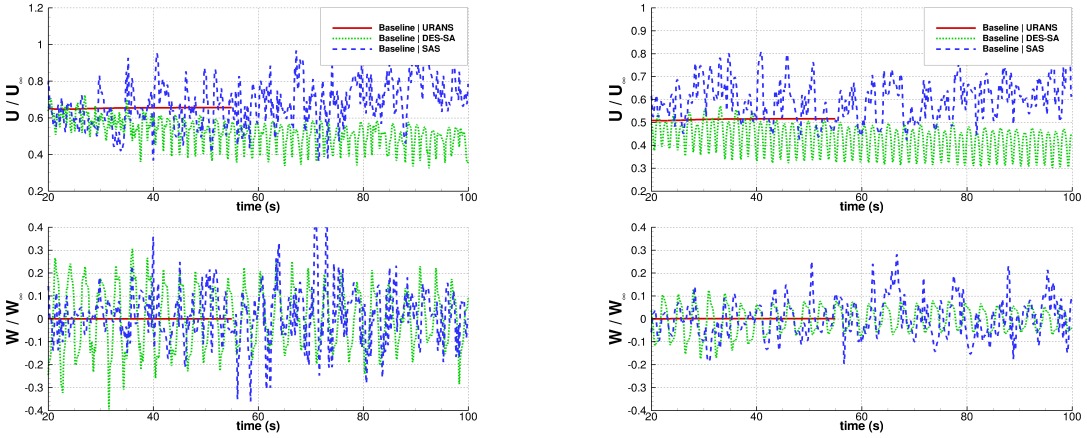

(a) Probe 39 (b) Probe 171

Figure 6.11: Comparison of 2 velocity signals for the intermediate density grid using 3 different turbulence models: URANS $k-\omega$, DES Spalart-Allmaras, SAS. $WOD = 0°$, $Re = 6.58 \cdot 10^5$

6.1.4 SFS2: Comparison with Experiments

Figure 6.12 shows the results obtained using the DES-SA and SAS models. Plots show the non-dimensional wind velocity ($\frac{V}{V_\infty}$), and the pitch (Φ_{wind}) and yaw (Ψ_{wind}) angles of the flow. By definition, the pitch angle represents the downwash velocity while the yaw contains the lateral velocity with respect to the free-stream. The agreement between experimental and CFD data is good for both models. The DES-SA results show that the recirculation zone is slightly over-predicted by the CFD, with globally larger deficits of velocity and more discrepancies in terms of the downwash angle (See mean velocity along the lines F and G).

Considering that the SAS model performs well, and is also both numerically more stable and maintain a reasonable level of unsteadiness in coarser regions of the grid, it will be preferred over the DES model for the coupled helicopter/ship simulations.

Figures 6.13 and 6.14 show the frequency spectrum of the x- and z-velocities at two probe locations in the wake of the ship. DES results show discrete peaks of frequency while the SAS model produces a broadband signal. The coarse mesh shows much lower levels of turbulence compared to the intermediate and fine meshes. Figure 6.15 shows a comparison of the previous DES and SAS results on the fine mesh. The SAS consistently shows a higher level of turbulence across the spectrum.

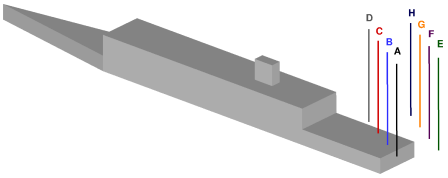

Figure 6.16 shows instantaneous iso-surfaces of Q-criterion colored with streamwise velocity to highlight the structures in the flow. The DES-SA and $k-\omega$ SAS models show structures of similar sizes and a similar extent of the wake downstream and laterally. The various structures that pass over the deck appear to be large enough to directly affect the aerodynamics of a helicopter in the region of the deck.

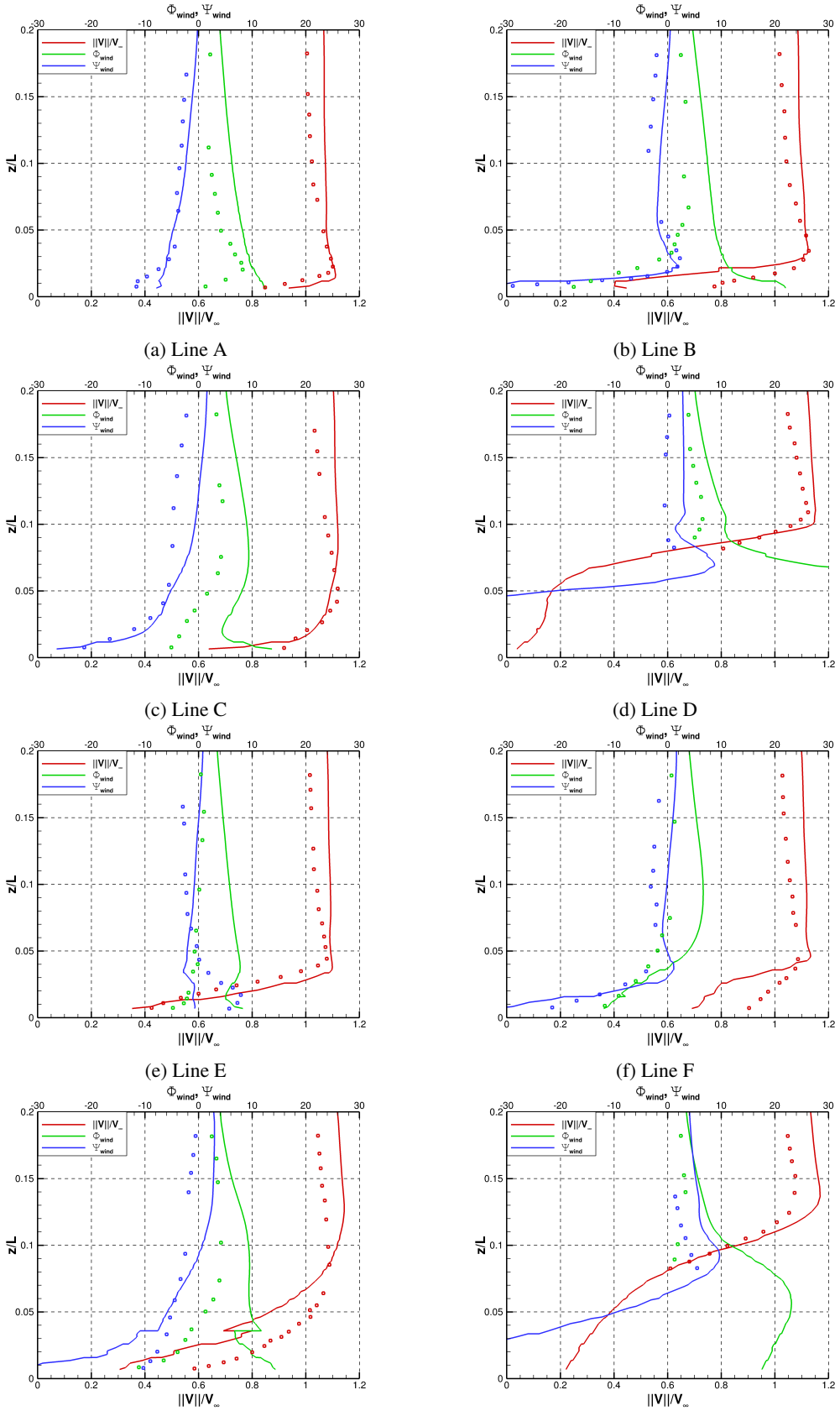

(a) Line A

(b) Line B

(c) Line C

(d) Line D

(e) Line E

(f) Line F

(g) Line G

(h) Line H

Figure 6.12: Time-averaged values of velocity and flow angles along 8 vertical lines. CFD (plain lines) and experimental (dots) results. DES-SA model, $WOD = 60$ *degrees*, $Re = 6.58 \cdot 10^5$

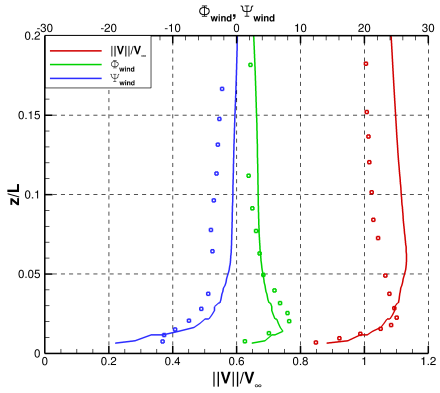

(i) Line A

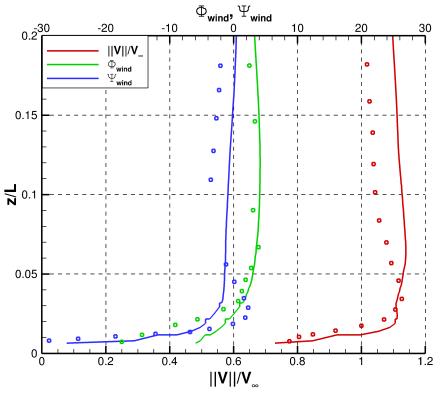

(j) Line B

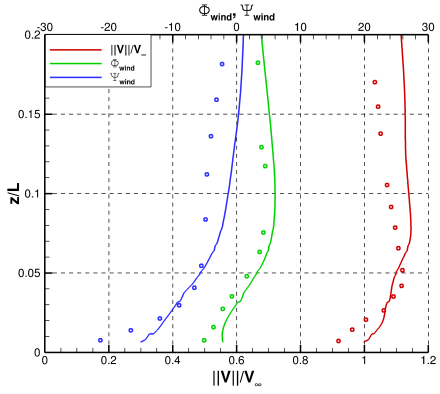

(k) Line C

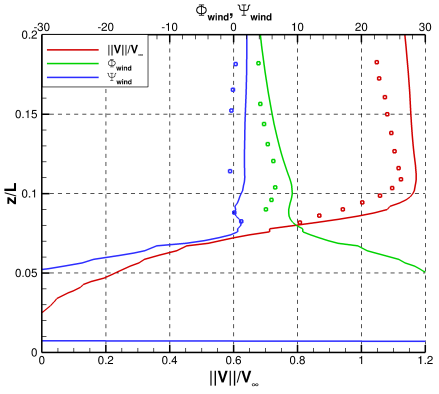

(l) Line D

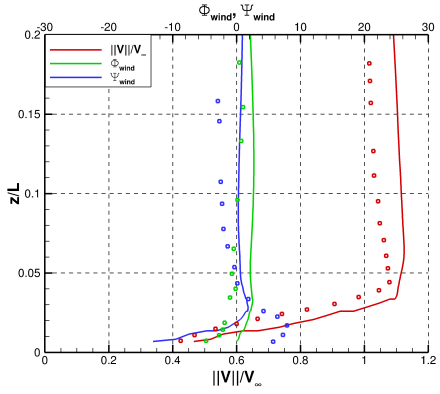

(m) Line E

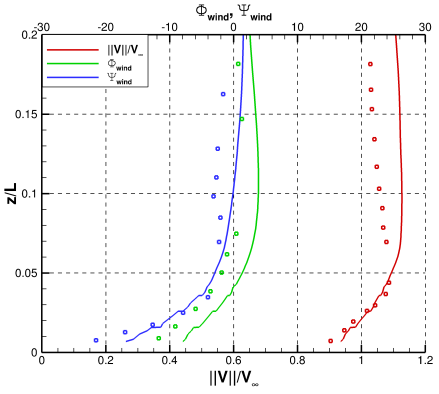

(n) Line F

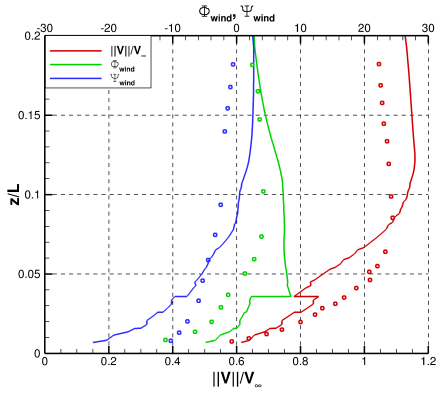

(o) Line G

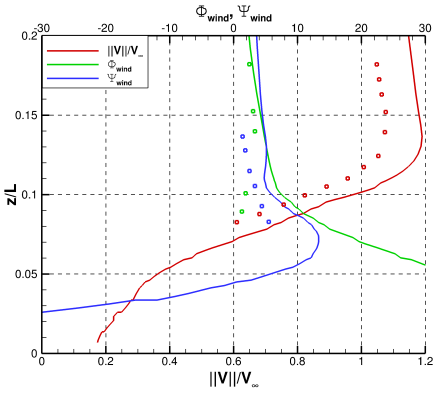

(p) Line H

Figure 6.12: **Continued -** Time-averaged values of velocity and flow angles along 8 vertical lines. CFD (plain lines) and experimental (dots) results. SAS model, $WOD = 60$ *degrees*, $Re = 6.58 \cdot 10^5$

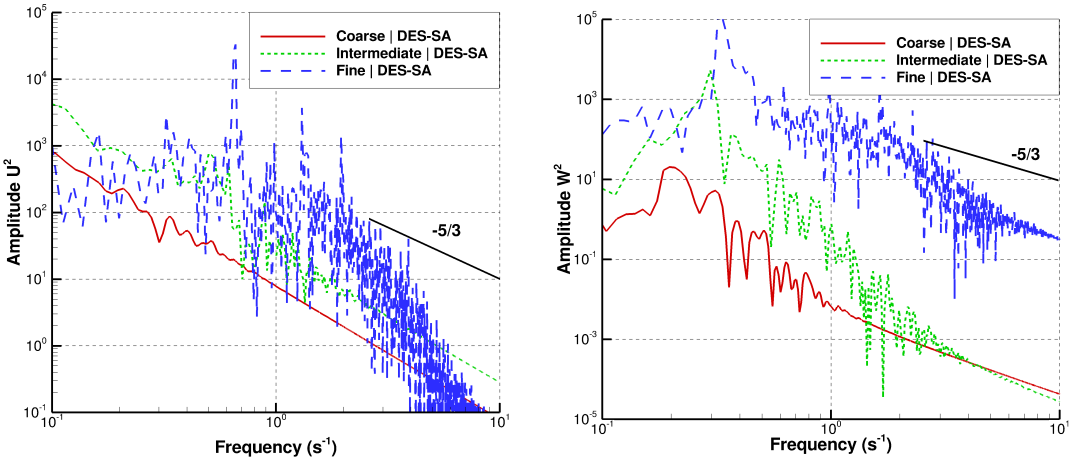

(a) Probe 39

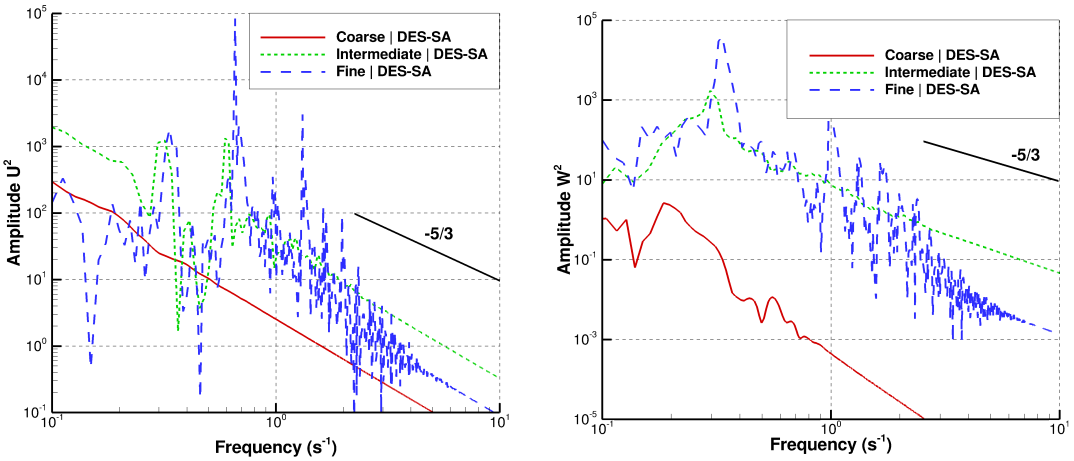

(b) Probe 171

Figure 6.13: Frequency analysis of the flow for two velocity directions using different grid densities at two probe positions along the center-line. DES-SA model, $WOD = 0°$, $Re = 6.58 \cdot 10^5$

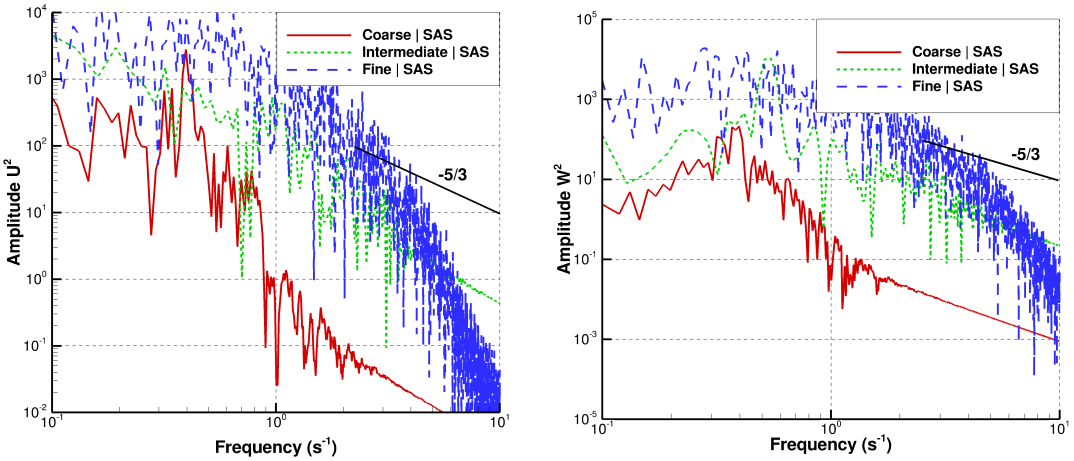

(a) Probe 39

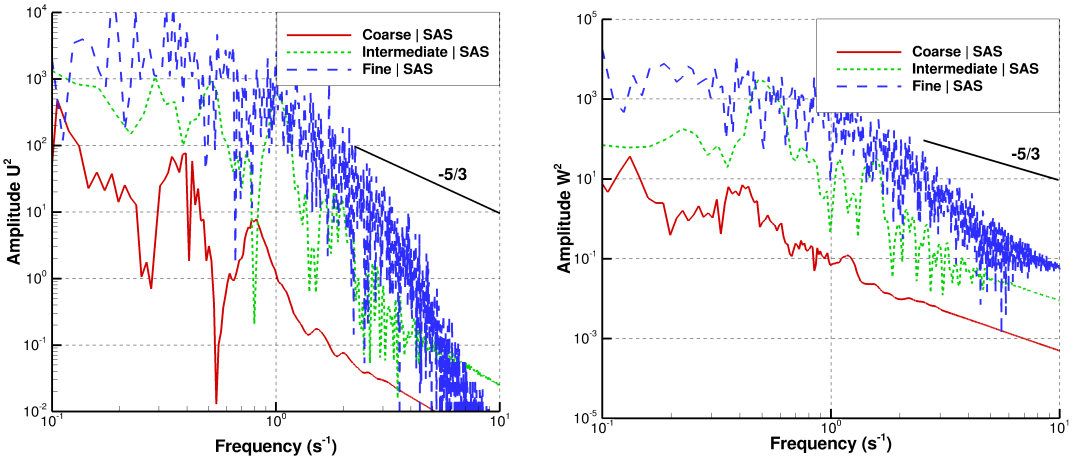

(b) Probe 171

Figure 6.14: Frequency analysis of the flow for two velocity directions using different grid densities at two probe positions along the center-line. $k-\omega$ SAS model, $WOD = 0°$, $Re = 6.58 \cdot 10^5$

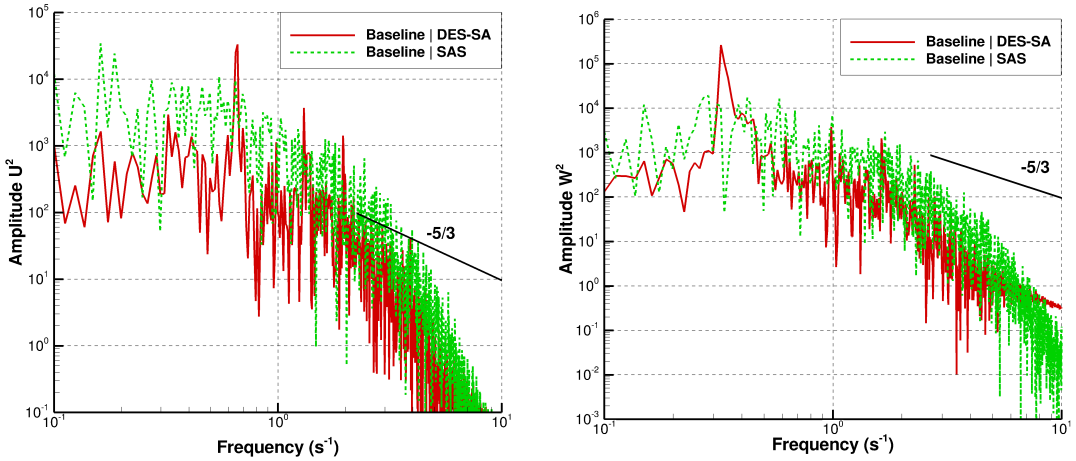

(a) Probe 39

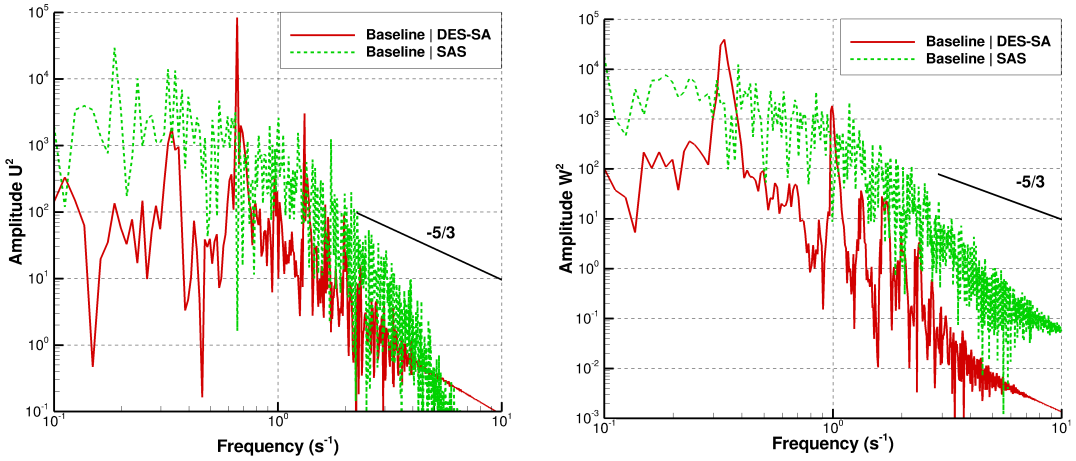

(b) Probe 171

Figure 6.15: Frequency analysis of the flow for two velocity directions using different turbulence models on the baseline grid. $WOD = 0°$, $Re = 6.58 \cdot 10^5$

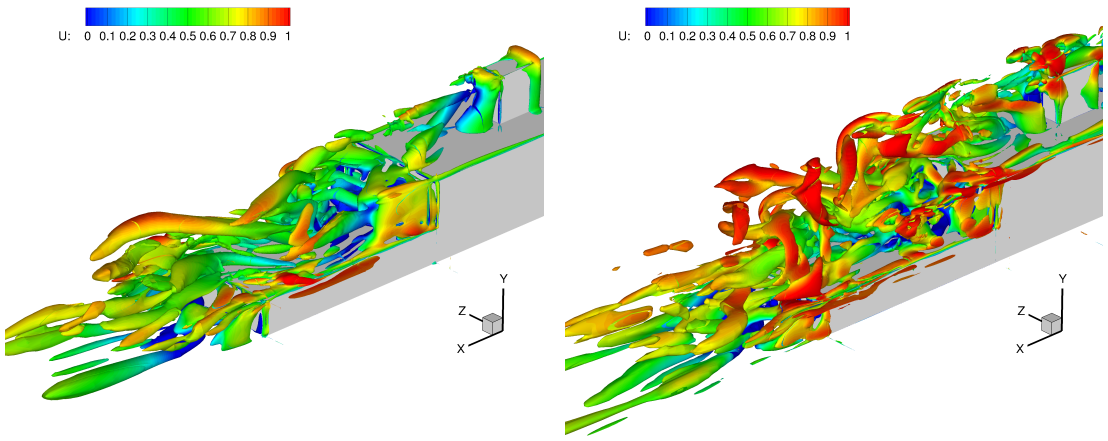

(a) DES-SA (b) $k-\omega$ SAS

Figure 6.16: Instantaneous Iso-Q criterion (Q=10) colored by streamwise velocity obtained with DES-SA and $k-\omega$-SAS models. $WOD = 0°$, $Re = 6.58 \cdot 10^5$ based on ship beam.

6.2 Ship/Rotor Wake Interaction

6.2.1 Grids and Parameters

The current line of investigation is inspired by the experiments of Zan[29] at NRC Canada: the actuator discs are horizontal (no shaft angle) and the positions reproduce the 8 extrema of the measurements domain. These extrema correspond to 14 meters off the center-line on each side, 10.5 and 45.5 meters downstream of the hangar door, 9 and 15 meters above the deck. The wind angles are 0 and 12 degrees from portside, the thrust coefficient is $C_T^{UK} = 0.00734$ and the rotor advance ratio reproduces the experimental case with a 19m/s wind, giving $\mu = 0.118$.

Experiments employed a standalone four-bladed rotor [29] as well as a five-bladed rotor with Sea King fuselage [36]. Both rotors were horizontal, non-articulated and have high values of solidity. Only the rotor is included in the present work and its geometry as well as trim-state are set to realistic values for a full scale rotor in forward flight.

Table 6.2 gives the flow conditions used for the wind tunnel experiments and the present CFD study compared to estimated full-scale values. For numerical stability and mesh economy, the Reynolds numbers chosen for CFD stand between 1 and 10 million for both the ship and the rotor, which represents a necessary compromise between model-scale and full-scale values. A comprehensive comparison of ship wakes with experimental data was performed in Lawson *et al.* [133] and showed reasonable agreement.

All results presented below are non-dimensionalized so that $U_\infty = 1$, $P_\infty = \frac{1}{\gamma M^2}$, and $b = 1$ where b is the ship beam, which gives a length scaling of 1:16.4 to obtain the full-scale results in meters.

Ship and rotor wakes are characterized by their high levels of vorticity. The vorticity magnitude as defined by equation 6.1 is used in this paper. The levels of vorticity have been chosen arbitrarily to highlight the flow features; in the case of the ship wake alone, the non-dimensionalized values of the vorticity magnitude can be rescaled to full scale by multiplying by $\frac{U_\infty}{b}$ where b is the ship beam. This is made possible by the fact that the flow over the ship is largely Re-independant.

$$\Omega_{magnitude} = \sqrt{\left(\frac{dW}{dy} - \frac{dV}{dz}\right)^2 + \left(\frac{dU}{dy} - \frac{dW}{dx}\right)^2 + \left(\frac{dV}{dx} - \frac{dU}{dy}\right)^2} \qquad (6.1)$$

where all quantities are dimensionless. Most of the results are plotted for a dimensionless vorticity magnitude of $\Omega_{magnitude} = 2$, which corresponds to $2.5s^{-1}$,

Variable	Exp. values	CFD		Full-scale values
		isolated rotor	ship and rotor	
Ship length	2.68 m	-	134.1 m	134.1 m
Ship beam	0.328 m	-	16.4 m	16.4 m
Rotor blade chord	$\approx$ 2 cm	1	0.344 m	0.5 m
Rotor diameter	28 cm	20.33	14.0 m	20.33 m
V_∞	19 m/s	1 (non-dim)	1 (non-dim)	$\approx$ 50 knots
Re_{meters}	1.3M	440,000	500,000	1.7M
Re_{beam}	424000	-	8.2M	28M
Re_{chord}	12,400	150,000	172,000	600,000
Re_{tip}	105000	1.27M	1.46M	5.0M
M_∞	0.055	0.055	0.055	$\approx$ 0.07
M_{tip}	0.466	0.466	0.466	$\approx$ 0.64
μ	0.118	0.118	0.118	0.118

Table 6.2: Comparison of flow conditions corresponding to wind-tunnel experiments, CFD calculations and full-scale equivalent.

i.e. 0.4 Hz in a 40 knots wind.

The Canadian Patrol Frigate (CPF) geometry represents a good compromise between geometric realism and mesh complexity. The ship baseline grid contained 5.8 million cells and was refined in the vicinity of the ship, resulting in 15.6 million cells. The isolated actuator disc was run in pure forward flight (no ground effect) using a 1.4 million cell grid.

Figure 6.17 shows the baseline and refined versions of the grid. The sea and ship are considered as walls, a coarser background grid is used and the actuator disc in its centered position is shown in the figure 6.17b.

Steady-state calculations were performed using the CPF and an actuator-disc method for modelling the effect of the rotor. Twenty calculations have been performed: 1 baseline isolated ship, 1 baseline actuator disc and 8 different positions of the actuator disc are examined for 2 different wind angles: 0 and 12 degrees from portside. For each case, the actuator disc is in "station-keeping" flight, i.e. steady with respect to the ship.

The actuator disc method together with steady-state simulation were chosen as a first approach to tackle ship rotor wake coupling. Further simulations were performed using a five-bladed Sea King rotor and the URANS method and present the advantage of predicting the loads applied on the rotor blades. The modified ship grid and rotor grid sizes were 7.6 and 14 million cells respectively (Figure 6.18).

The rotor grid is a drum embedded in the ship grid using three sliding planes to allow rotation. Similarly, the ship grid is also embedded in a background grid via the use of sliding planes (Figure 6.19). The rotor spins at constant speed and was resolved using 720 time steps per revolution.

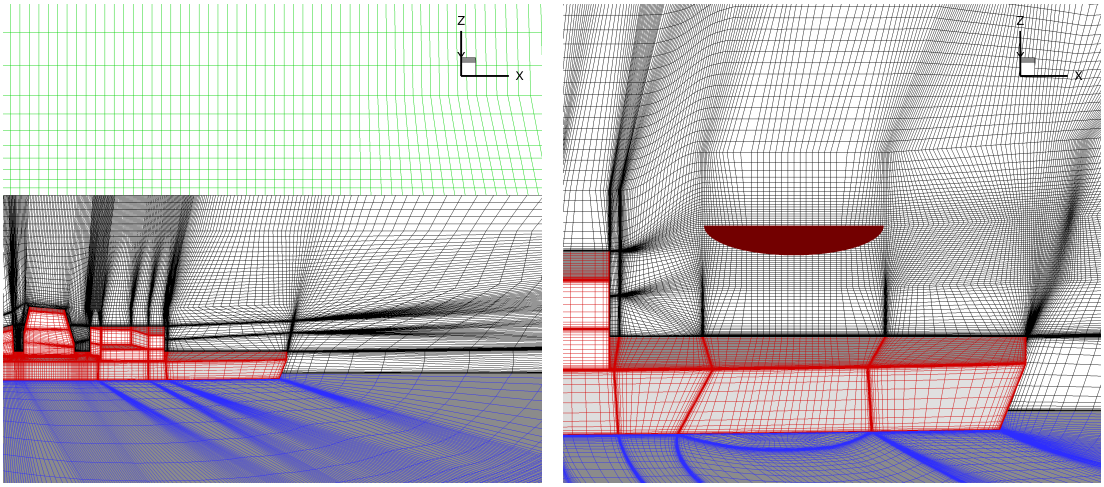

(a) (b)

Figure 6.17: Views of the grids used for actuator disc simulations. (a) overview and (b) close view on the refined grid showing the position of the actuator disc.

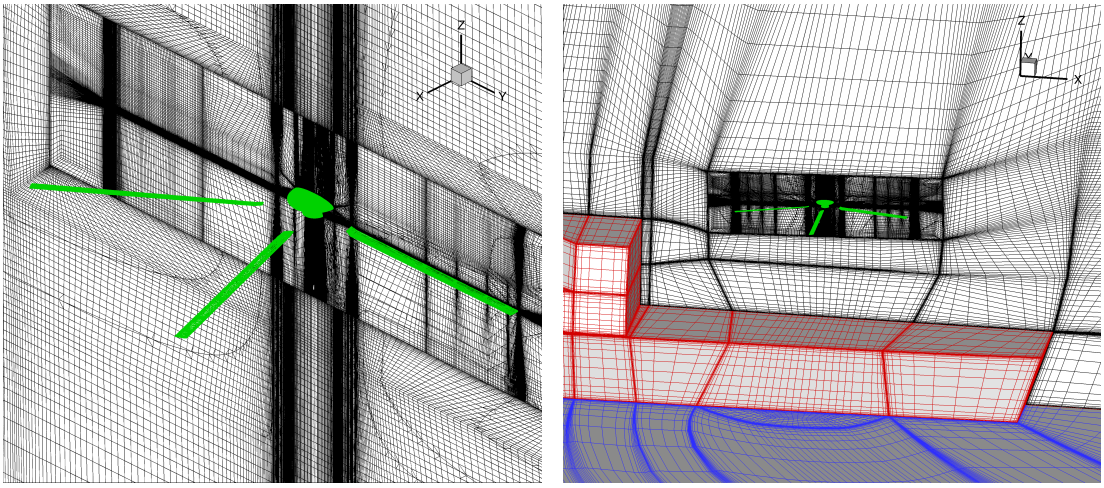

Figure 6.18: Views of the grids used for rotor calculations. The rotor grid is identical in both cases, and consists of a drum that is embedded in a background grid (a) for isolated forward-flying rotor calculations, or the ship grid (b) for shipborne simulations. Sliding planes are used to interface the two grids.

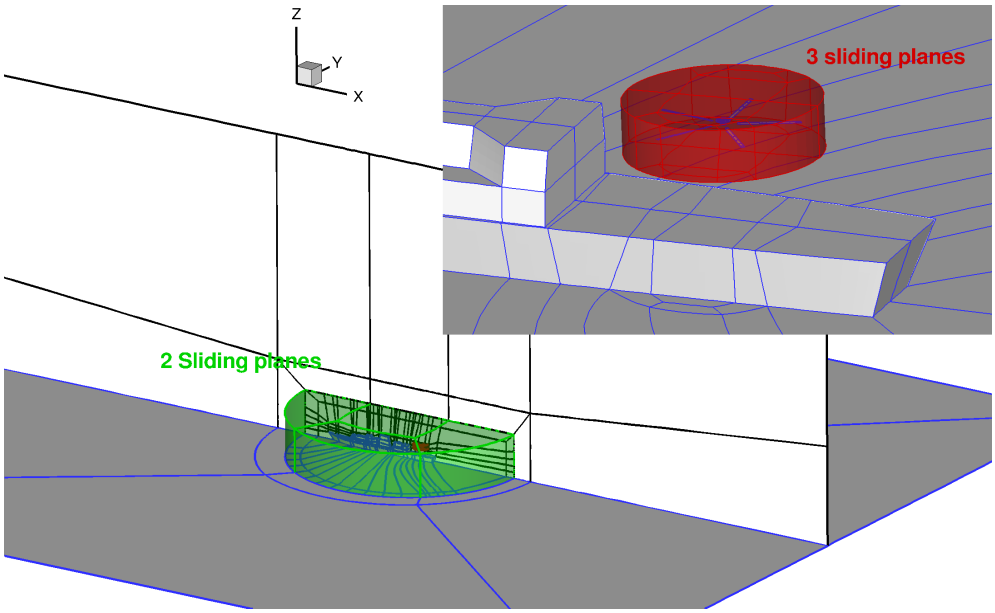

Figure 6.19: Sliding plane interfaces used for the shipborne rotor grid. The rotor drum is embedded in the ship grid using three sliding planes (in red) and the ship grid itself is included in a background grid via two sliding planes (in green).

6.2.2 CPF with Headwind and Sidewind

A grid of the CPF geometry was created and is symmetrical with respect to the longitudinal axis. The 0° and 20° wind angle cases have been tested. The topology of the flow is shown by plotting the contours of iso-velocity along the axis of the ship (Figure 6.20). The global flow topology is very similar to the one sketched by Syms [10], with large recirculation bubbles behind the hangar, the hull and the different parts of the ship superstructure. The sidewind gives an asymmetry to the flow with the formation of a large vortex over the deck, which contrasts with the almost uniform flow in the 0° case.

6.2.3 Comparison between URANS and DES

One characteristic of ships is the presence of unsteady structures in the airwake. The frequency of these structures is usually below 1Hz, and will impact directly the helicopter aerodynamics and pilot workload when operating in the vicinity of the ship. The large difference in frequency between the rotor aerodynamics and the wake means that coupled calculations require a large number of rotor revolutions to cover one period of the ship wake.

Time-averaged DES and URANS results show very similar flow features as seen figures 6.22 and 6.23. The flow structures are of similar sizes and intensity in terms of mean flow characteristics. The URANS model captures very little unsteadiness

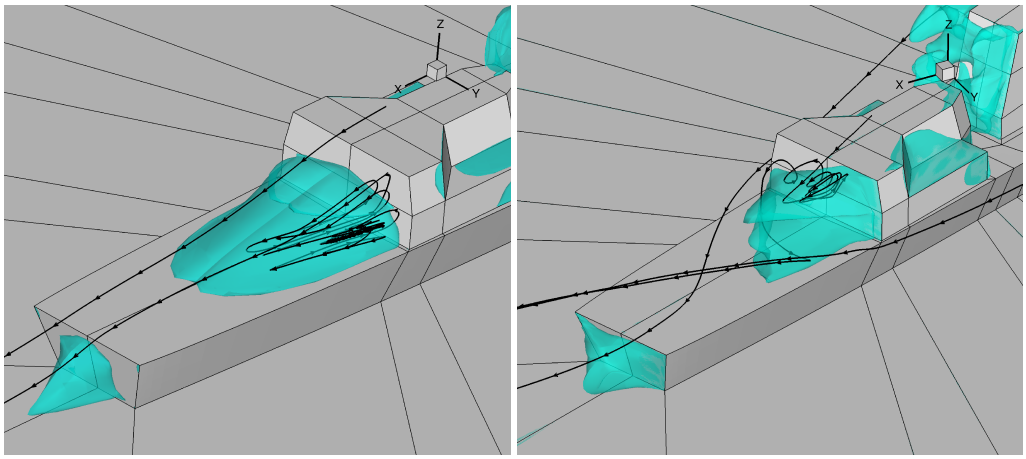

Figure 6.20: Flow topology above the deck of the Modified Canadian Patrol Frigate. Iso-surfaces U=0 and streamlines. Steady calculation, $k-\omega$ model, 0° and 20° WOD, $Re = 10^6$, $Mach = 0.1$

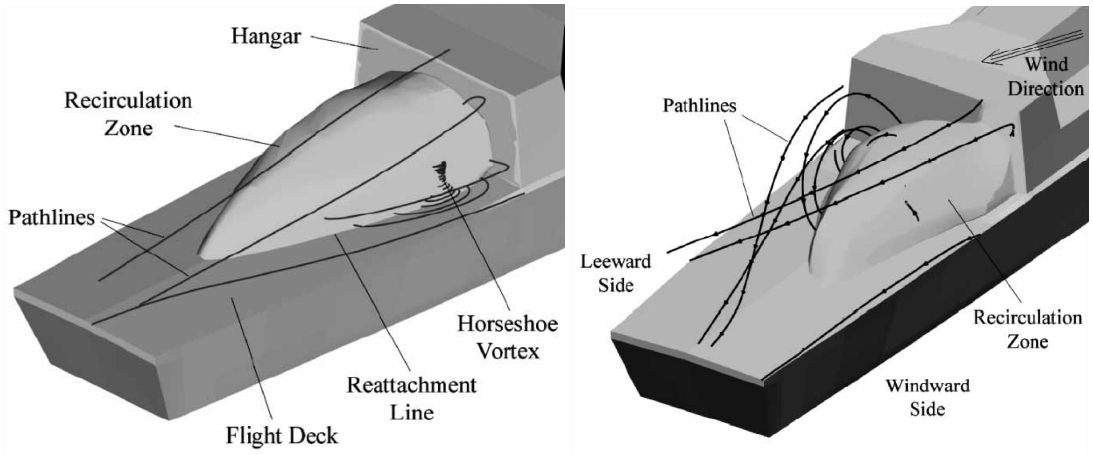

Figure 6.21: Flow topology above the deck of the Modified Canadian Patrol Frigate as presented by Syms [10]

compared to the DES model but shows that it is suitable for estimating the mean flow characteristics of a ship wake. Following this observation, the URANS model is chosen for the following work as the required grid size is much smaller than for DES.

6.2.4 Actuator Disc Results

Coupling Effect

A common method for simulating the Dynamic Interface is to use a simple rotor method (Blade Element Model) and add the velocities from a steady or unsteady but ”frozen” ship wake. This wake is computed separately, hence neglecting the effect of the rotor on the final ship wake.

The case of a rotor in ”station-keeping” flight at one rotor radius above the deck (just before touchdown) is chosen and each set of figures shows the 4 possible

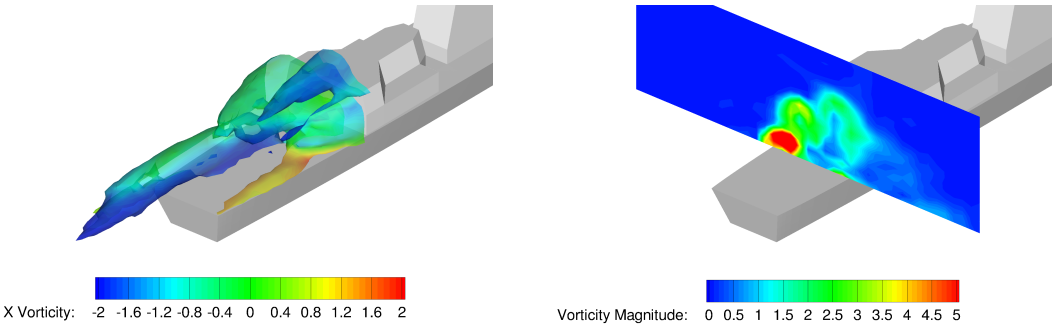

Figure 6.22: (a) Contours of iso-vorticity $\Omega_{\text{magnitude}} = 2$ colored with streamwise vorticity to highlight the direction of rotation and (b) map of vorticity. Isolated ship using Detached Eddy Simulation, 12 degrees WOD.

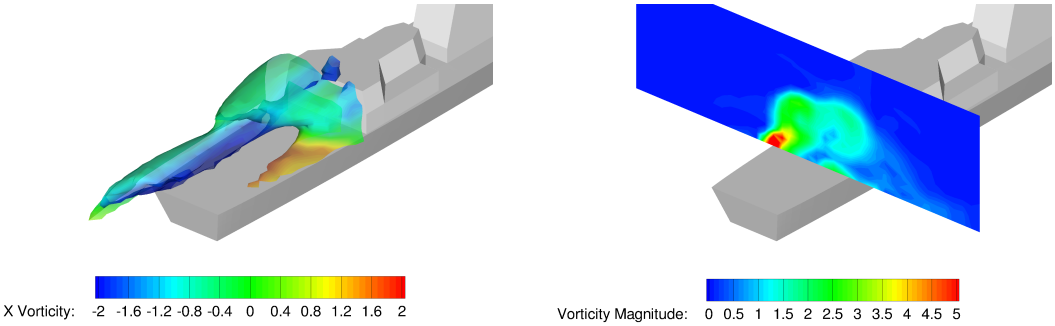

Figure 6.23: (a) Contours of iso-vorticity $\Omega_{\text{magnitude}} = 2$ colored with streamwise vorticity to highlight the direction of rotation and (b) map of vorticity. Isolated ship using Unsteady RANS calculation, 12 degrees WOD.

configurations: isolated ship, isolated actuator disc in forward flight, superposition of the two cases and coupled simulation. As mentioned previously, two wind angles are considered: 0 and 12 degrees from portside.

The superposition was performed by combining the flowfield variables mesh point by mesh point. The non-dimensional velocities ($\underline{u} = [u,v,w]^T$) are written as $u = U + \tilde{u}$ where U is the mean value and $\tilde{u}$ is the perturbation. Since the mean value is identical for both case:

$$\underline{u}^{Superposition} = \underline{U} + \underline{\tilde{u}}^{CPF} + \underline{\tilde{u}}^{AD} \tag{6.2}$$

With $\underline{U} = [1,0,0]^T$ for the 0 degrees wind angle case, and $\underline{U} = [\cos(12), \sin(12), 0]^T$ for the 12 degrees wind angle case. The pressure and density are averaged locally:

$$p^{combination} = \frac{p^{CPF} + p^{AD}}{2} \tag{6.3}$$

$$\rho^{combination} = \frac{\rho^{CPF} + \rho^{AD}}{2} \tag{6.4}$$

The vorticity is then recomputed in each of the cases from the new variables.

The isolated actuator disc in forward flight is computed out of ground effect. According to Cheeseman's work [57], the difference in thrust for a rotor at the present conditions (one rotor radius from the ground, advance ratio 0.118) is 0.7%. Since the rotor near the deck is partially in ground effect and under the influence of the hangar and ship, it is difficult to distinguish the influence of each contribution, and thus outside the scope of this work.

Figures 6.24 and 6.25 show iso-surfaces of vorticity with streamlines and maps of the vorticity at the back of the rotor for each of the 4 cases at 12 degrees wind angle. Although a corresponding set of results were computed at 0 degrees, it showed similar characteristics. The main characteristic of the isolated ship wake (a) is the presence of the mixing layer that separates the recirculation zone, made visible by the streamlines behind the hangar, from the rest of the flow that passes over the hangar roof and on the side of the ship. The portside wind generates a larger vortex starting on the windward side of the hangar. The baseline rotor (b) shows typical contra-rotating super-vortices that are convected downstream with very little weakening. The superposition (c) shows the same flow characteristics as the two previous cases, with no visible coupling effects. However, the coupled case (d) shows an interaction between rotor and ship wakes: in particular, the velocity seen by the actuator disc is greatly reduced compared to the isolated case. The presence of the hangar creates blockage to the flow and reduces the convection. As a result, the super-vortices are pushed further downward and pair with vortical structures from the ship wake downstream. While the isolated rotor shows well-confined vortical structures, the coupled case shows lower levels of vorticity, with a larger spatial extent. The streamlines also suggest a recirculation zone behind the hangar door reinforced by the effect of the rotor blowing over the deck.

Figure 6.26 shows the difference in terms of inflow velocity between the shipborne rotor and superposition cases. Results show that the superposition method over-predicts the inflow in the center of the disc by over 50% and under-predicts it on each side, because of much stronger supervortices.

Effect of the Rotor Thrust

The 12 degrees wind angle was re-computed with 4 times the value of the thrust coefficient, i.e. $C_{\mathrm{T}}^{\mathrm{UK}} = 0.02936$ to demonstrate the effect of the rotor thrust on the global wake. Figure 6.27 shows the results in terms of vorticity for the isolated ship and shipborne actuator disc at $C_{\mathrm{T}}^{\mathrm{UK}} = 0.00734$ and $C_{\mathrm{T}}^{\mathrm{UK}} = 0.02936$. The deck creates an effective blockage that can be seen as a "partial ground effect" and forces the wake

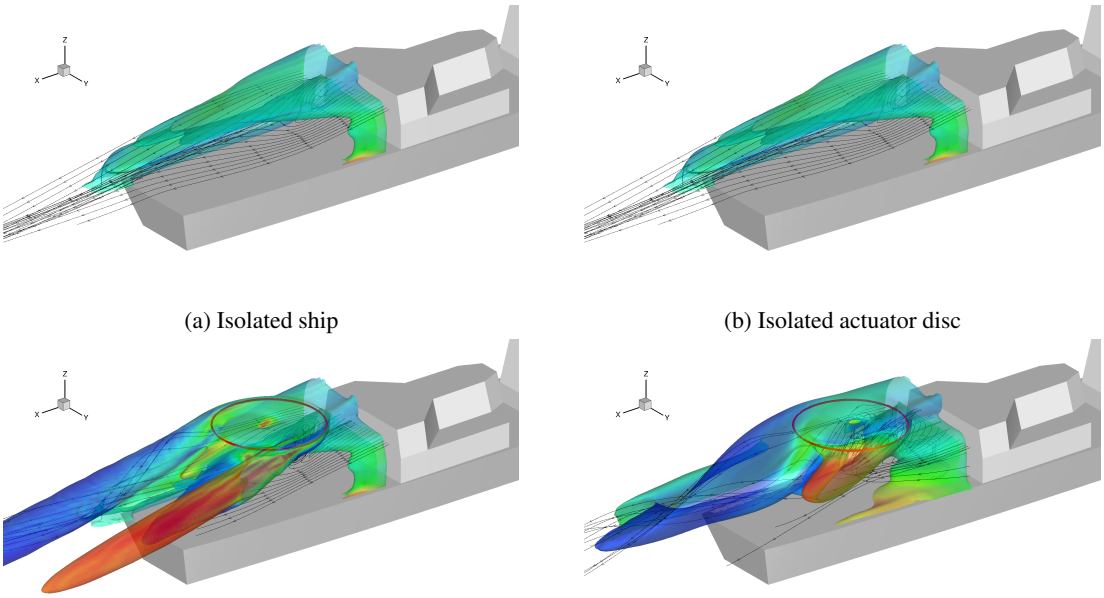

(a) Isolated ship

(b) Isolated actuator disc

(c) Superposition actuator disc and ship wakes

(d) Actuator disc on ship

Figure 6.24: Iso-vorticity $\Omega_{\text{magnitude}} = 2$ of isolated ship, isolated actuator disc, shipborne actuator disc and superposition of isolated AD and ship at 12 degrees WOD, $C_{\text{T}}^{\text{UK}} = 0.00734$.

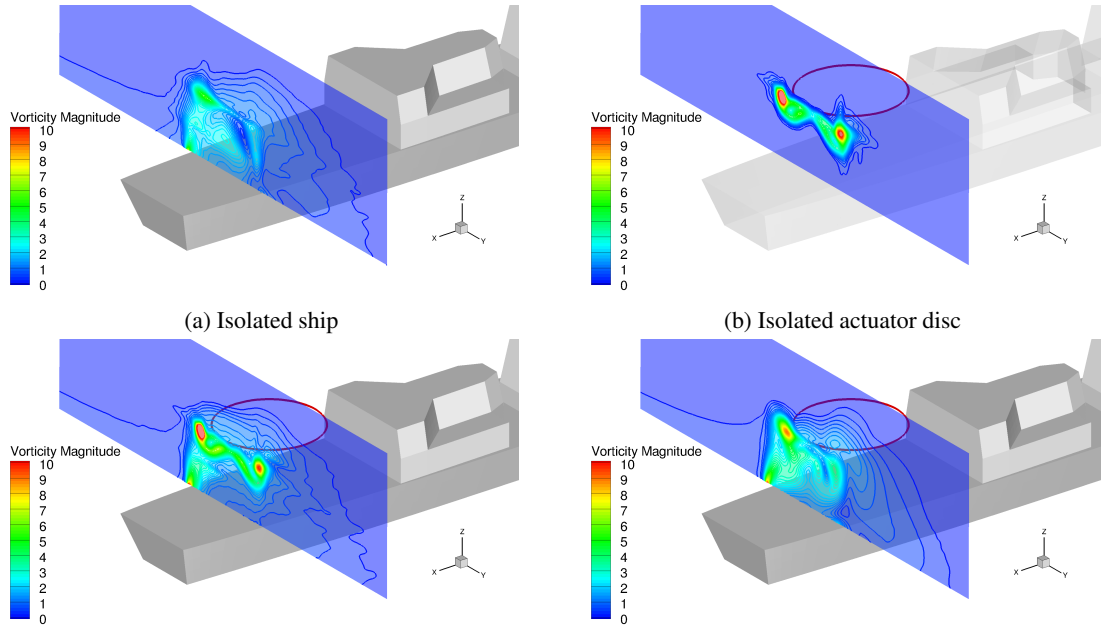

(a) Isolated ship

(b) Isolated actuator disc

(c) Superposition actuator disc and ship wakes

(d) Actuator disc on ship

Figure 6.25: Maps of vorticity at back of the disc of isolated ship, isolated actuator disc, shipborne actuator disc and superposition of isolated AD and ship at 12 degrees WOD, $C_{\text{T}}^{\text{UK}} = 0.00734$.

to expand laterally. As a result, the wake remains closer to the deck, in a zone of low velocity behind the hangar, showing little super-vortices, especially on the leeward side.

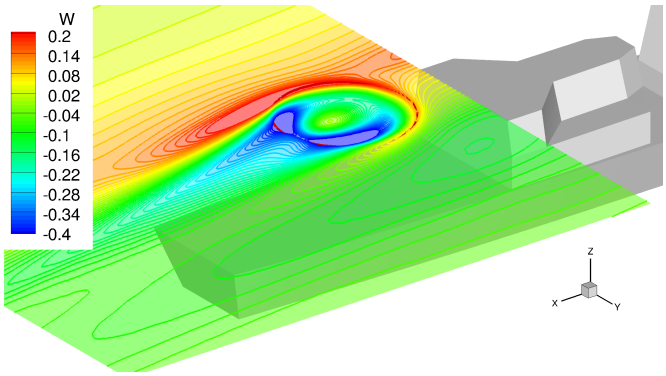

(a) Actuator disc on ship

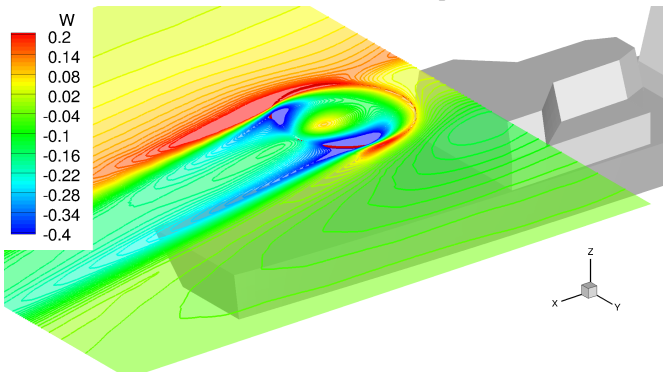

(b) Superposition actuator disc and ship wakes

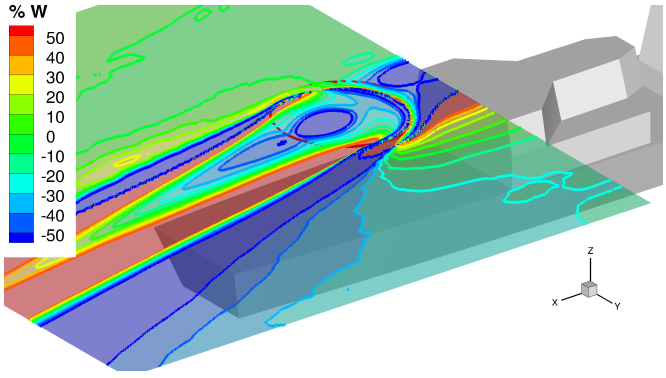

(c) Percentage of difference

Figure 6.26: Comparison of the distribution of downwash velocity in the plane of the actuator disc for a shipborne rotor and superposition case. The difference is shown in (c) and was calculated via $\frac{(b)-(a)}{(a)}$, $C_{\mathrm{T}}^{\mathrm{UK}} = 0.00734$.

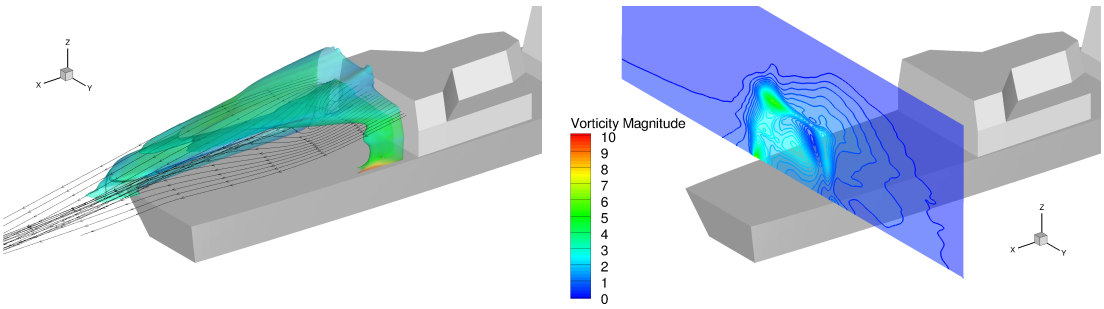

(a) Isolated ship wake

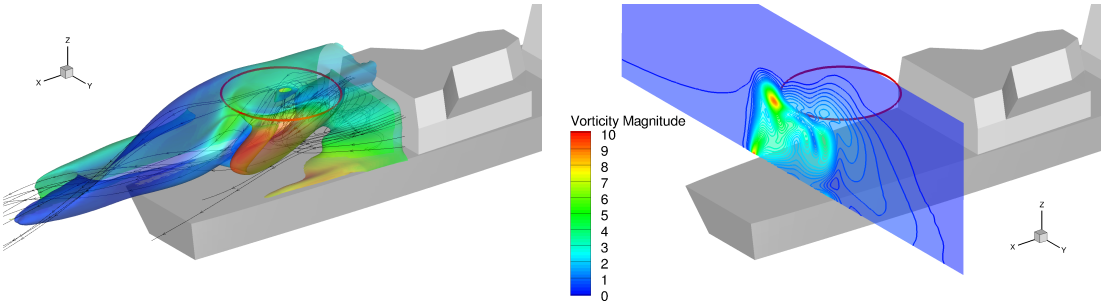

(b) Coupled simulation at $C_{\mathrm{T}}^{\mathrm{UK}} = 0.00734$

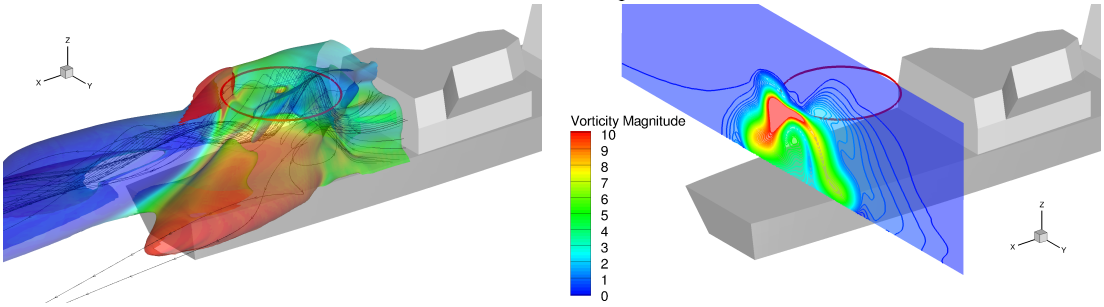

(c) Coupled simulation at $C_{\mathrm{T}}^{\mathrm{UK}} = 0.02936$

Figure 6.27: Iso-vorticity $\Omega_{\mathrm{magnitude}} = 2$ and maps of vorticity at the back of the actuator disc of isolated ship and shipborne actuator disc at two different thrust coefficients, 12 degrees WOD.

Although the simulations were steady and used a simplified rotor model, this study of the coupling effect between a rotor and ship wake suggests that the case of a rotor ”station-keeping” over the deck before touchdown cannot be simulated by superimposing the flowfield obtained for an isolated rotor to the wake of the isolated ship.

The following section aims at estimating the extent of the mutual influence between the ship and rotor wakes.

Influence of the Rotor Position

A parametric study was conducted on the coarse version of the grid. Eight positions of the rotor disc have been chosen that correspond to full-scale values of 14 meters off the center-line on each side, 10.5 and 45.5 meters aft the hangar door, 9 and 15 meters above the deck. Figure 6.28 shows the distribution of downwash velocity $\frac{w}{U_\infty}$ in the region of the disc for 8 different positions of the actuator disc at 0 degrees WOD angle. Important differences in terms of downwash velocity are found between the inboard and outboard regions of the disc, especially for upwind cases. This suggests an important variation of rotor trim-state as the aircraft maneuvers in this particular region.

At 12 degrees, (Figure 6.29) the distribution of velocity is no longer symmetric and the windward and leeward rotors operate in, and contribute to very different flowfields: upwash with strong vortical structure on the windward side, downwash on the leeward side.

The inflow distribution in the plane of the isolated actuator disc is given for comparison in both cases. At the considered advance ratio, the inflow is almost completely symmetrical but loses this symmetry when shipborne, due to the influence of the ship wake. The upwind rotor, on the leeward side of the ship in ”station-keeping” at 9 meters can be seen as a worst-case scenario as the rotor operates in a strong downwash, therefore reducing the control and power margins. The effect of the ship wake is stronger at 9 meters above the deck but shows a significant effect even above the level of the hangar roof, at 15 meters, suggesting that the interactional effect between the ship and the helicopter extends outside the deck area delimited by the size of the landing pad and the hangar wall.

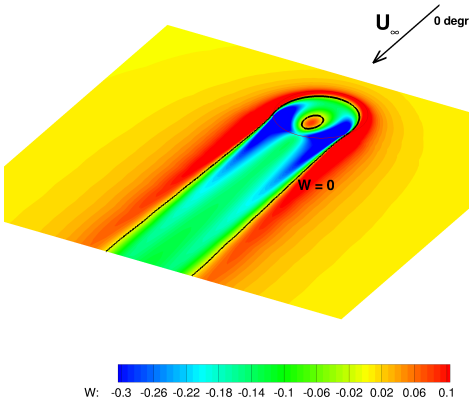

(a) Baseline actuator disc

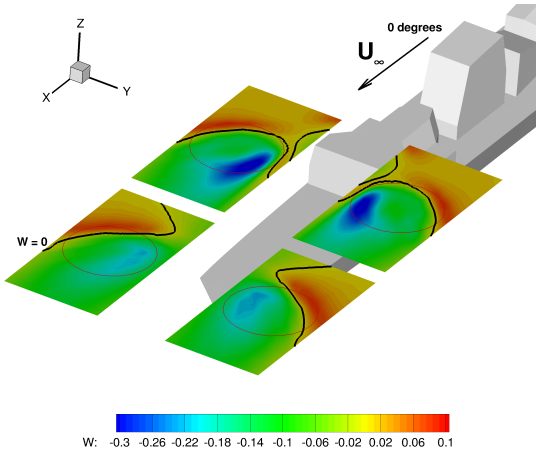

(b) 9 meters above deck

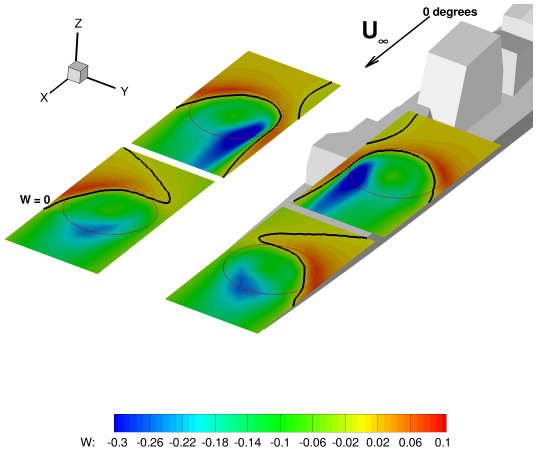

(c) 15 meters above deck

Figure 6.28: Contours of dimensionless downwash velocity projected on a plane that coincides with the actuator disc. Actuator disc without ship is given for comparison. The black line separates the regions of upwash and downwash. 0 degrees WOD.

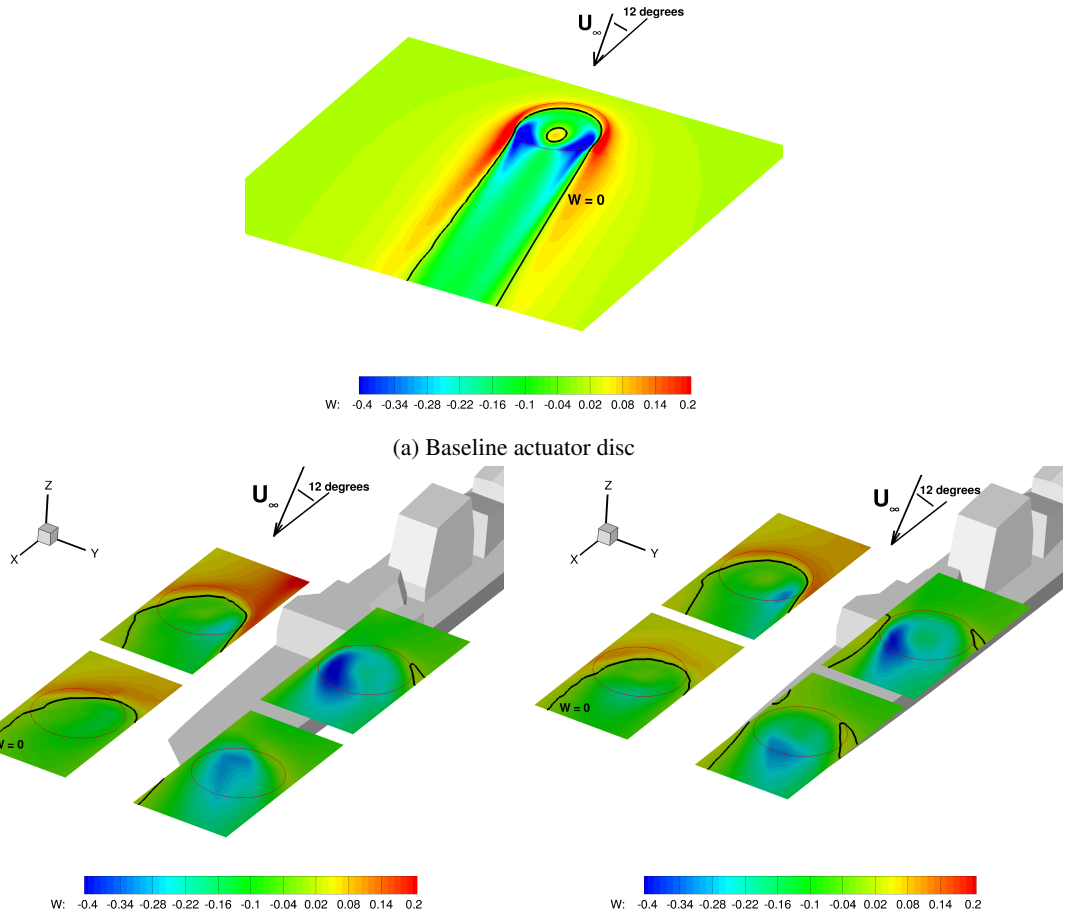

(a) Baseline actuator disc

(b) 9 meters above deck

(c) 15 meters above deck

Figure 6.29: Contours of dimensionless downwash velocity projected on a plane that coincides with the actuator disc. Actuator disc without ship is given for comparison. The black line separates the regions of upwash and downwash. 12 degrees WOD.

To compare the relative strength of the rotor and ship wakes, maps of the vorticity are plotted at the back of each upstream actuator disc, demonstrating the impact of the rotor on the ship wake (Figure 6.30). The baseline cases are given for comparison and correspond to the ship airwake with no actuator disc.

Overall, at the chosen thrust coefficient, ship and rotor wakes show similar levels of vorticity. At 0 degrees (left-hand-side figures), the downwash effect of the actuator disc causes the ship wake to lose its symmetry and cases at 9 meters above the deck clearly show interaction between the two wakes that is less visible at 15 meters. However, for every case, the corresponding rotor and ship vortices are contra-rotating, preventing them from pairing and therefore limiting the interactional effects: in snapshot (c) and (d), the rotor super-vortex on the right-hand side of the disc rotates in the counter-clockwise direction whilst the left-hand side of the ship wake rotates clockwise.

As mentioned before, the case of a rotor in an upwind position on the leeward side of the ship is believed to be the most demanding for the aircraft as the rotor is directly in the vicinity of the ship, in a region of strong downwash that reduces significantly the power and control margins of the aircraft. This situation was chosen to assess the effect of the rotor thrust: 3 different values of thrust are used (1, 2 and 4 times the thrust used for previous cases) at $C_{\mathrm{T}}^{\mathrm{UK}} = 0.00734$, 0.01468 and 0.02936. Figure 6.31 shows the results in terms of vorticity magnitude. The vorticity clearly increases with the thrust as well as the interactional effect with the ship wake. However, the influence remains limited to a region of the flow close to the rotor and does not extend enough upstream to change significantly the topology of the ship wake itself.

The actuator disc method is an efficient tool for capturing the main flow characteristics of coupled ship/rotor simulations. The results also show that for a rotor in close proximity to the ship wake, two-way coupled calculations are necessary as they capture coupling effects that are not represented by combinations of the ship and rotor wakes. On the other hand, the use of steady calculations and a simplified model of an actuator disc that has been tuned to be representative of forward-flying rotors may not be satisfactory for high fidelity simulations. To overcome the limitations of the actuator disc model and predict accurate helicopter loads, coupled simulations with fully-articulated rotor blades and a helicopter fuselage are necessary.

6.2.5 Shipborne Sea-King Rotor

This section addresses the case of a rotor in ”station-keeping” at 1 rotor radius above the deck (i.e. just before touchdown) using an unsteady simulation that includes a full

Variable	Isolated rotor trim state	Shipborne rotor trim state	Difference
μ	0.118	0.118	N/A
$C_{\mathrm{T}}^{\mathrm{UK}}$	0.00734	0.00734	N/A
$C_{\mathrm{M}}^{\mathrm{pitch}}$	≈ 0	≈ 0	N/A
$C_{\mathrm{M}}^{\mathrm{roll}}$	≈ 0	≈ 0	N/A
C_{Q}	0.00162	0.00173	6.8%
θ_0	4.885	5.852	19.8%
θ_{1c}	-1.558	-1.596	2%
θ_{1s}	0.806	0.521	35%

Table 6.3: Values of the rotor characteristics after isolated and shipborne trimming.

5-bladed Sea King rotor.

Rotor Trimming

First, the isolated rotor is trimmed in terms of blade collective and cyclic using the previous target thrust coefficient $C_{\mathrm{T}}^{\mathrm{UK}} = 0.00734$ and zero moment in pitching and rolling (figure 6.32). The propulsive and side forces are not accounted for during the trimming. The rotor hub is assumed to be rigid in flap to reproduce the experimental set-up and therefore no blade flapping harmonics are applied. The isolated rotor case was computed for 6 revolutions to reach a converged state and then was trimmed over 4 additional revolutions. The operation was repeated for the shipborne rotor; after convergence using the previous trim state (10th revolution), only 2 more revolutions were necessary to adjust the trim state to the new flow conditions. The final trim state of both rotors is presented table 6.3. and shows that the collective angle required to maintain thrust increases by almost 20% because of the additional inflow and despite the additional ground effect which, as mentioned before, should tend to increase the thrust by 0.7% in the present flight conditions. The torque shows an increase of 7% and the lateral cyclic changes significantly because of the large vortex initiating on the windward corner of the hangar and passing over the deck. The shipborne rotor was also re-trimmed to a new target thrust coefficient of $C_{\mathrm{T}}^{\mathrm{UK}} = 0.01468$, corresponding to exactly twice the previous value, as for the actuator disc case. This is referred to as ”high-thrust” case.

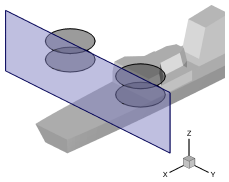

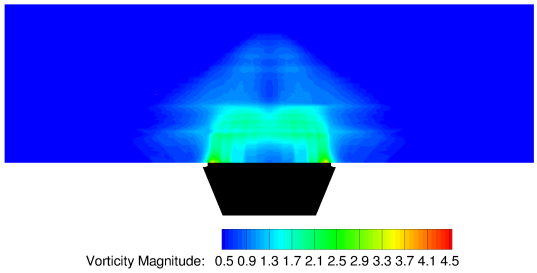

(a) Baseline, 0 degrees

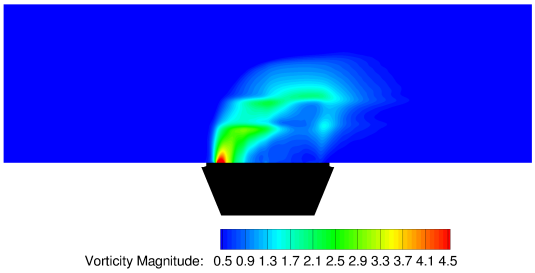

(b) Baseline, 12 degrees

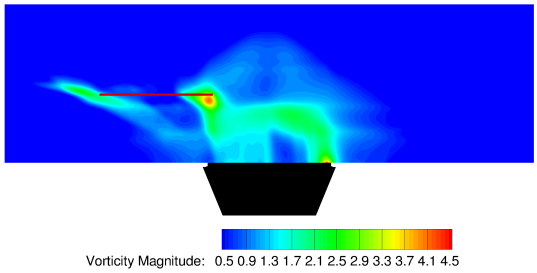

(c) 9 meters, portside, 0 degrees

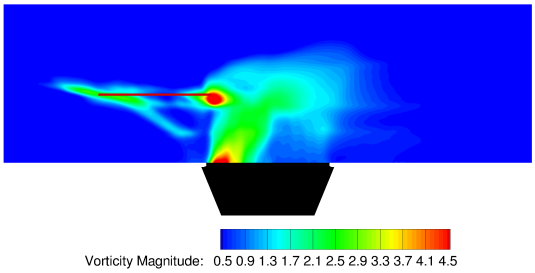

(d) 9 meters, portside, 12 degrees

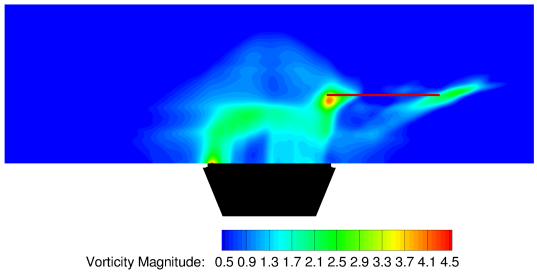

(e) 9 meters, starboard, 0 degrees

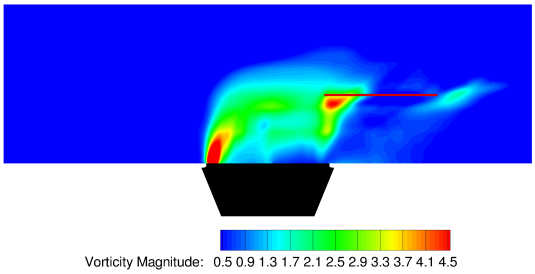

(f) 9 meters, starboard, 12 degrees

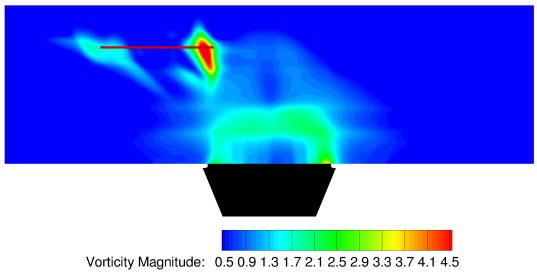

(g) 15 meters, portside, 0 degrees

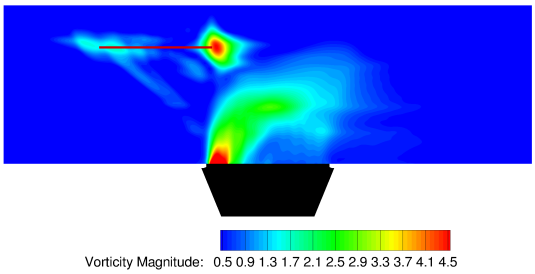

(h) 15 meters, portside, 12 degrees

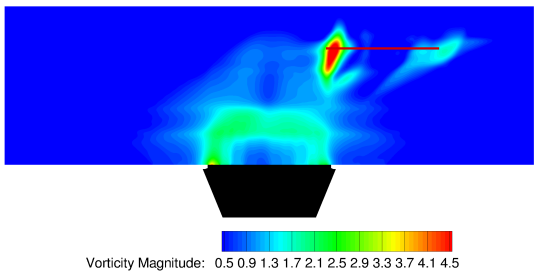

(i) 15 meters, starboard, 0 degrees

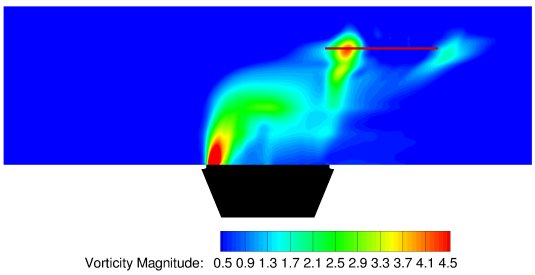

(j) 15 meters, starboard, 12 degrees

Figure 6.30: Maps of vorticity behind the ship for upstream cases. (a)(b) Baseline case (no actuator disc).

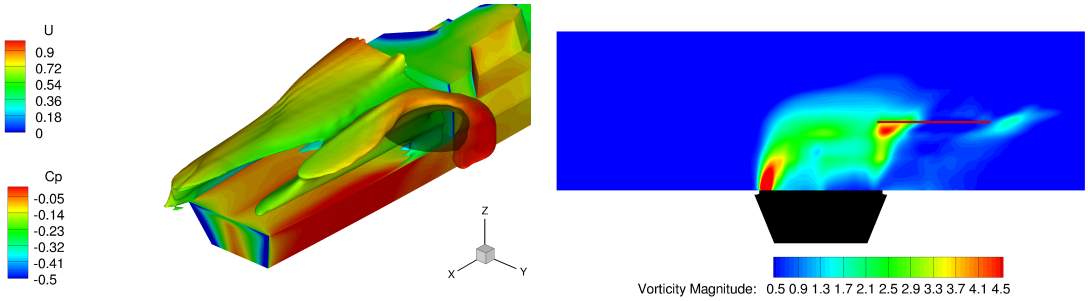

(a) $C_{\mathrm{T}}^{\mathrm{UK}} = 0.00734$

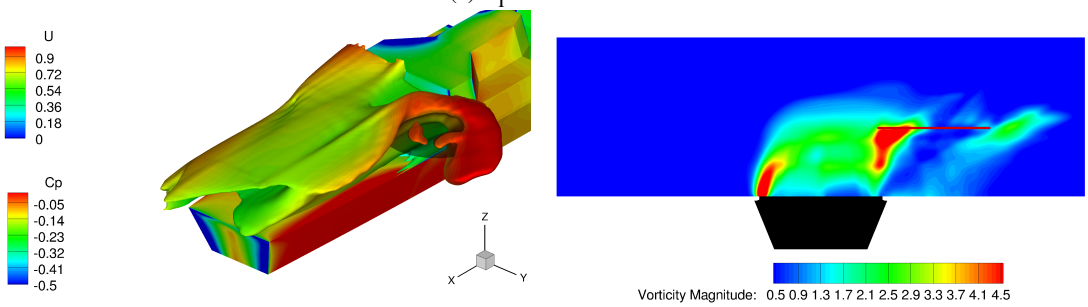

(b) $C_{\mathrm{T}}^{\mathrm{UK}} = 0.01468$

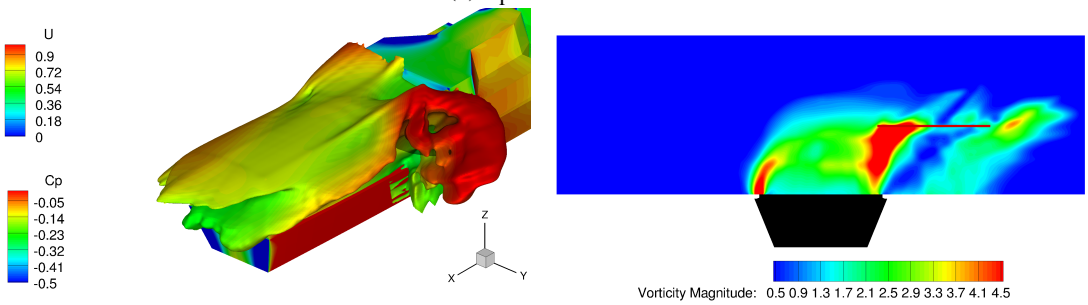

(c) $C_{\mathrm{T}}^{\mathrm{UK}} = 0.02936$

Figure 6.31: Maps of vorticity and iso-contours $\Omega_{\mathrm{magnitude}} = 2$ behind the ship at the back of an upwind, leeward actuator disc at 9 meters above deck, 12 degrees WOD for 3 different thrust coefficients.

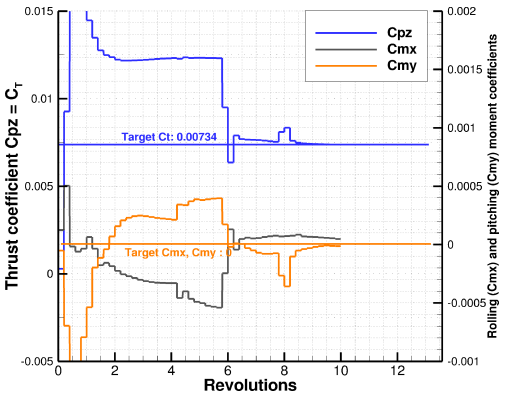

(a) Isolated rotor

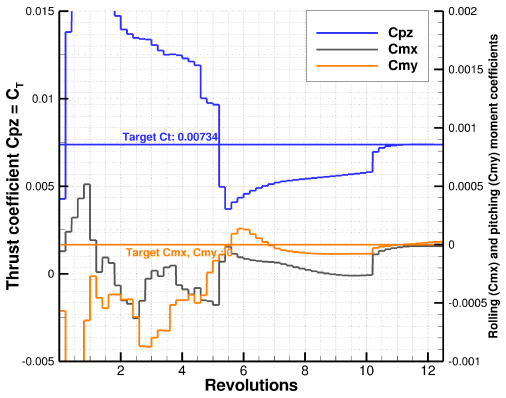

(b) Shipborne rotor

Figure 6.32: Curves of thrust, pitch and roll moments coefficients for the main rotor as function of the number of revolutions. Values used by the trimmer (average value over a fifth of a revolution) for the isolated and shipborne rotors, compared with their respective target values.

The values of collective and cyclic pitch θ_0, θ_{1c}, θ_{1s} correspond to the amplitude of the mean, cosine and sine components of a negative Fourier decomposition:

$$\theta = \theta_0 - \theta_{1c}\cos\Psi - \theta_{1s}\sin\Psi \tag{6.5}$$

Shipborne Rotor Flow Topology

Figure 6.33 shows iso-contours and maps of vorticity for the ship alone, rotor alone, ship and rotor combined using superposition method and coupled calculation with a portside 12 degrees wind. The super-vortices on each side of the isolated rotor are clearly visible, as well as the signature of the blade tip vortices in the rotor wake. The superposition method shows similar results as with the actuator disc study: the flow topology after superposition shows no additional effect due to an interaction between the two wakes. In the case of a coupled simulation, the super-vortices seem to be altered by the ship wake and do not persist long enough to be convected with the ship wake.

Maps of vorticity show a slice of the rotor wake with values of vorticity and a wake topology similar to the actuator disc cases. The rotor wake appears to be significantly stronger in terms of vorticity than the ship wake for this rotor location and therefore the effect of the rotor onto the ship wake is expected to be strong, ruling out the use of the superposition method.

The high-thrust case presented in figure 6.33(e) shows an increase of vorticity in the wake. The wake is also pushed further down underneath the rotor but the flow topology remains similar.

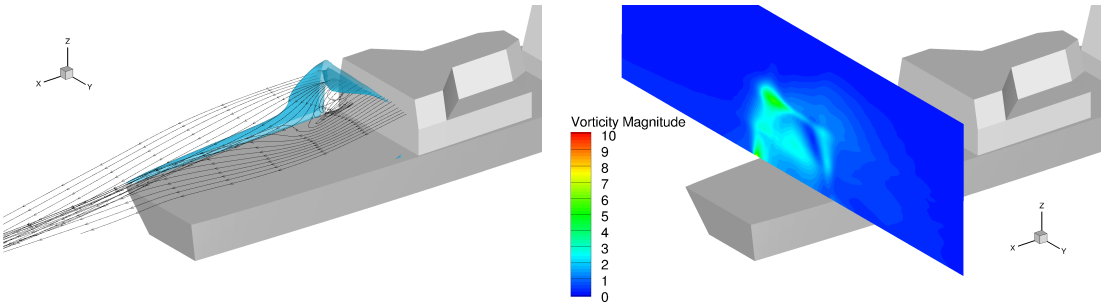

(a) Isolated ship

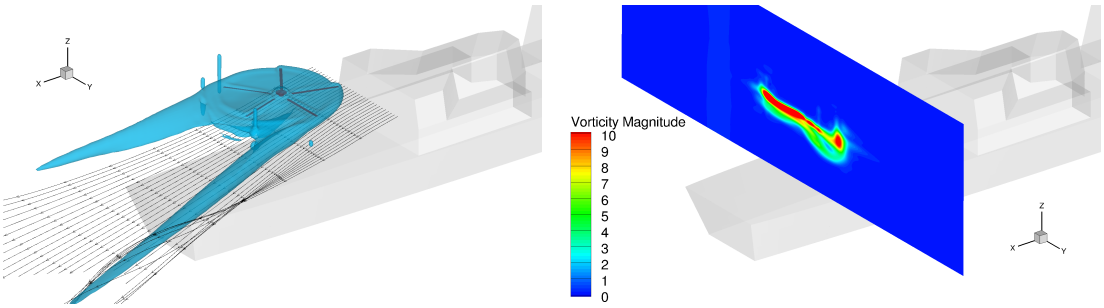

(b) Isolated rotor

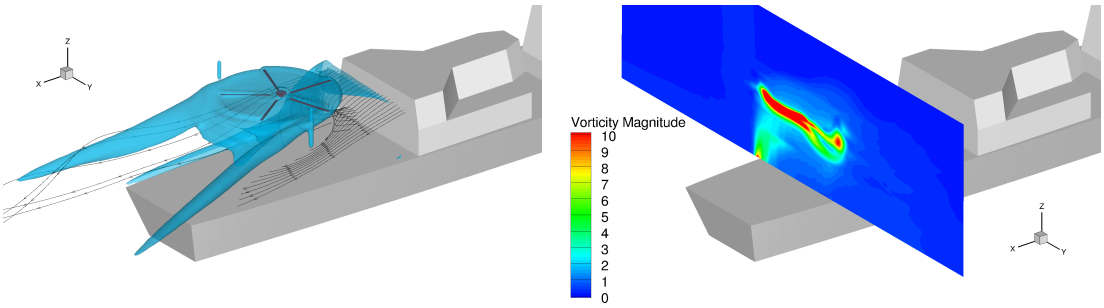

(c) Superposition

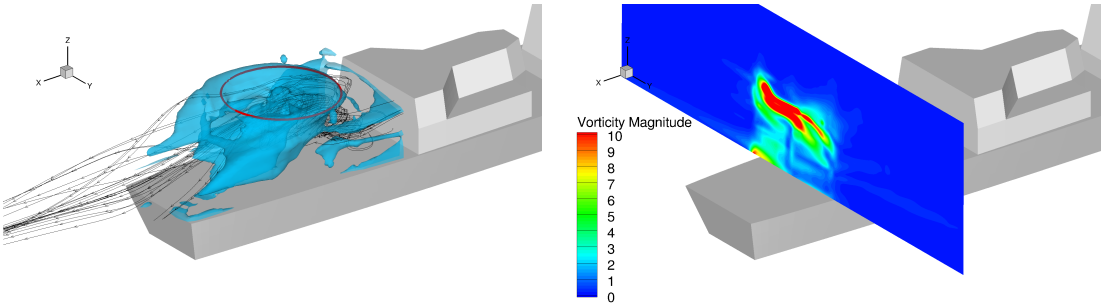

(d) Coupled

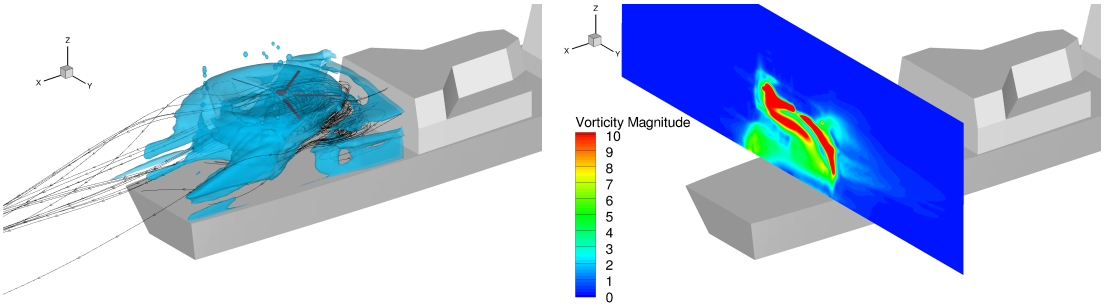

(e) Coupled at high thrust

Figure 6.33: Contours of iso-vorticity $\Omega_{\text{magnitude}} = 6$ with streamlines and maps of vorticity for isolated ship, isolated Sea King rotor, superposition and coupled cases at 12 degrees WOD, $C_{\text{T}}^{\text{UK}} = 0.00734$.

Figure 6.34 shows a comparison of the flow topology with an actuator disc and a rotor at the same position over the deck. Differences are found in the recirculation zone behind the hangar that is located further downstream in the rotor calculation. The isolated rotor flow is included for comparison and shows significant differences with the shipborne rotor case in terms of downwash intensity. The effect of the blade tip vortices is also visible on both isolated and shipborne rotors. The downwash intensity is also much stronger in the high-thrust case, the wake extends further and the ground effect is expected to play a more important role in this case.

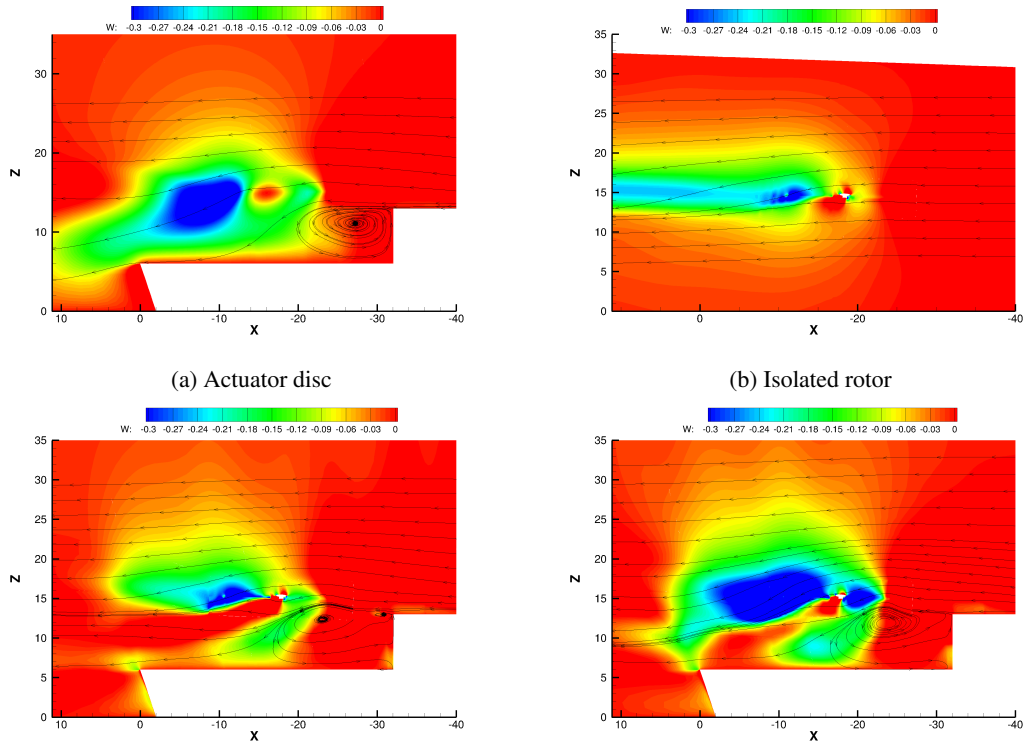

(a) Actuator disc

(b) Isolated rotor

(c) Shipborne rotor

(d) Shipborne rotor at high thrust

Figure 6.34: Slice of z-velocity normalised by the streamwise velocity with streamlines for actuator disc, isolated Sea King rotor, shipborne rotor at $C_{\mathrm{T}}^{\mathrm{UK}} = 0.00734$ and shipborne rotor at $C_{\mathrm{T}}^{\mathrm{UK}} = 0.01468$. 12 degrees WOD.

Figures 6.35 and 6.36 show maps of downwash velocity through the rotor disc for an isolated rotor, shipborne actuator disc and 4 different azimuthal positions of the shipborne rotor. The ship hull is outlined when the ship is present in the simulation.

The difference in inflow distribution due to the ship is visible and will impact directly the rotor performance by changing the angle of attack seen by the blades (See section 6.2.5). The actuator disc method shows good agreement in terms of downwash distribution across the disc with the 5-bladed rotor.

The surface flow topology is presented in figure 6.37 using contours of pressure

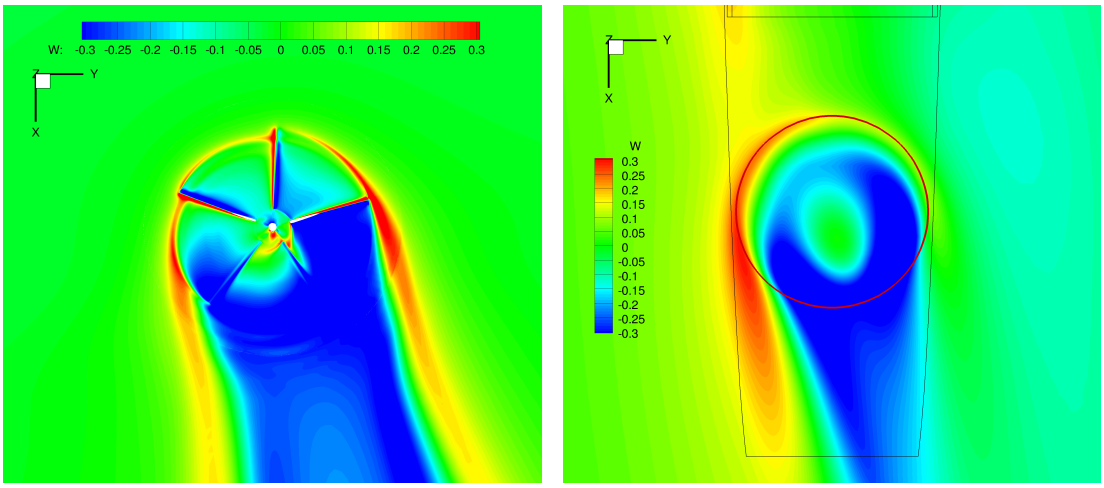

(a) Isolated Sea King Rotor

(b) Shipborne Actuator Disc

Figure 6.35: Maps of non-dimensional downwash velocity in a z-plane crossing the rotor disc. $C_{\mathrm{T}}^{\mathrm{UK}} = 0.00734$.

coefficient on the deck. Firstly, a recirculation zone is located behind the hangar and reattaches in the middle of the deck, showing a rise of pressure on the deck. This pressure rise is more important and is located further downstream with the presence of the rotor blowing over the deck.

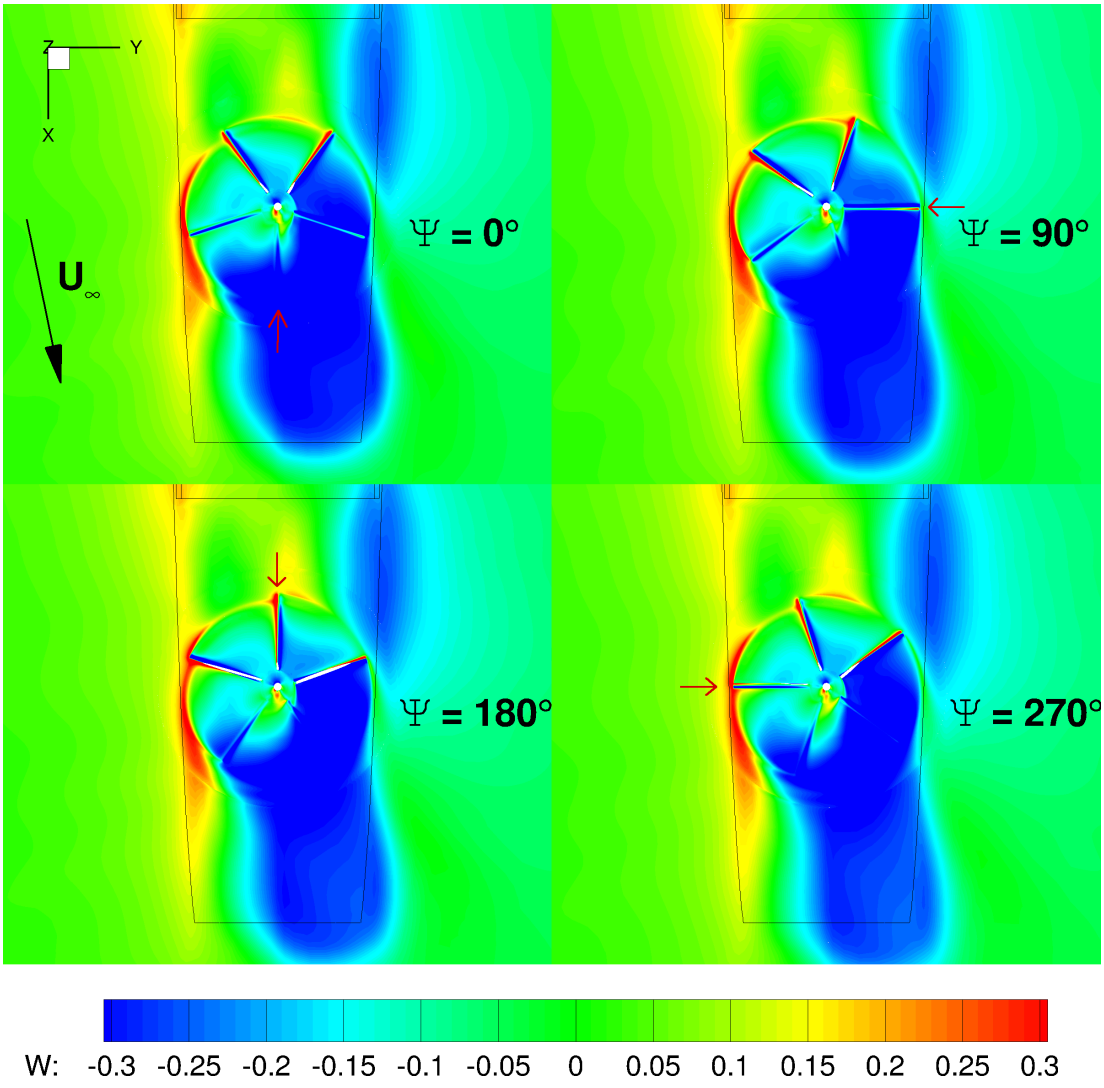

Figure 6.36: Maps of non-dimensional downwash velocity in a z-plane crossing the rotor disc. The red arrow points at the blade that starts at 0 degrees azimuth. $C_{\mathrm{T}}^{\mathrm{UK}} = 0.00734$.

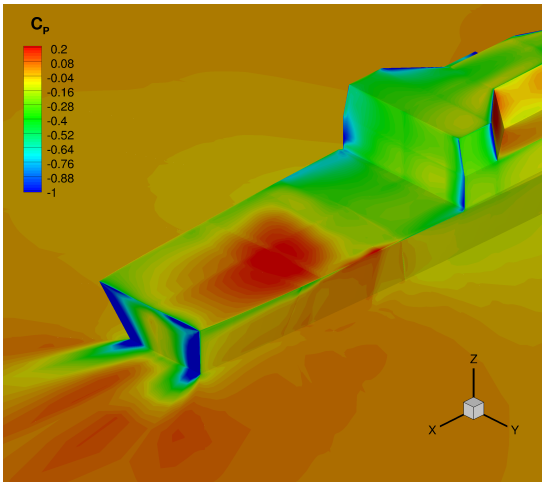

(a) Isolated ship

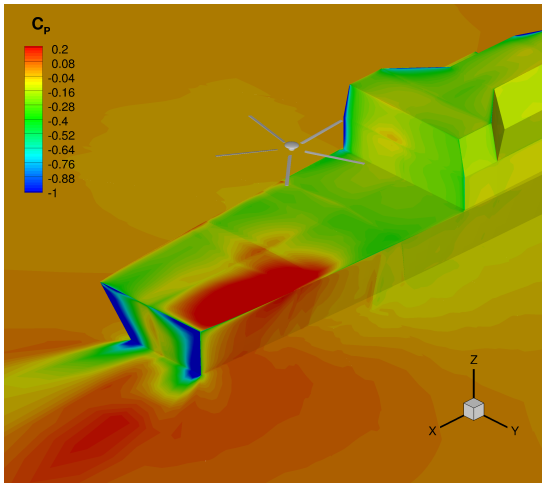

(b) Ship with Sea King rotor at $C_{\mathrm{T}}^{\mathrm{UK}} = 0.00734$

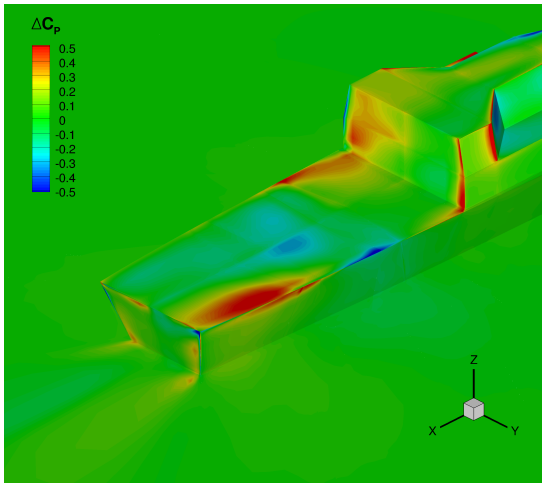

(c) Difference

Figure 6.37: Surface pressure coefficient in the region of the deck for isolated ship and coupled case. The third figure shows the variation of C_{P} between the two cases, calculated via $\Delta C_P = \frac{C_P^{(b)} - C_P^{(a)}}{C_P^{(a)}}$.

Rotor Loading

Actuator disc methods assume a fixed rotor loading, which has been tuned for forward-flying rotors. Full rotor calculations are used to determine the actual rotor loading for any flight conditions. It is therefore possible to compare isolated and shipborne rotor loadings.

Figures 6.38, 6.39 and 6.40 show the distribution of loading for an isolated rotor in trimmed forward flight, the same rotor, under the same conditions, behind the Canadian Patrol Frigate and after a second trimming in the ship wake. There are significant differences in terms of thrust at the front and starboard side of the disc, where the downwash behind the hangar tends to decrease the angle of attack of the blades. On the port side, the upwash caused by the side-wind deviated by the hull maintains a high loading. This is consistent with pilot feedback that indicates a tendency of the aircraft to roll when entering the region of the flow directly behind the hangar [3]. The second trimming imposes a higher collective to balance the loss of thrust and changes both the cyclic terms to restore the rotor balance in terms of pitch and roll moments (table 6.4). The fourth element of each figure corresponds to the high-thrust case. The observed distributions of normal force, pitching moment and torque coefficients are similar, although with less variations around the azimuth.

Results obtained for the shipborne rotor show a reduction of thrust of about 20% compared to the isolated rotor in forward flight at the same trim state. This is consistent with the observations of Zan [29] that showed a reduction of about 10% for the headwind case and a further reduction when the rotor was located in the leeward side of the ship with a 12 degrees wind angle. For comparison, Cheeseman theory predicts a 0.7% increase in thrust for a forward-flying rotor at the same distance, 1 rotor radius, above a ground plane.

Case	θ_0	θ_{1s}	θ_{1c}
Isolated rotor $C_T^{UK} = 0.00734$	4.885	0.806	-1.558
Shipborne rotor $C_T^{UK} = 0.00734$	5.852	0.521	-1.596
Shipborne rotor $C_T^{UK} = 0.01468$	12.522391	1.656754	-3.241754

Table 6.4: Values of the estimated rotor trim states for the 2 values of C_T^{UK} tested.

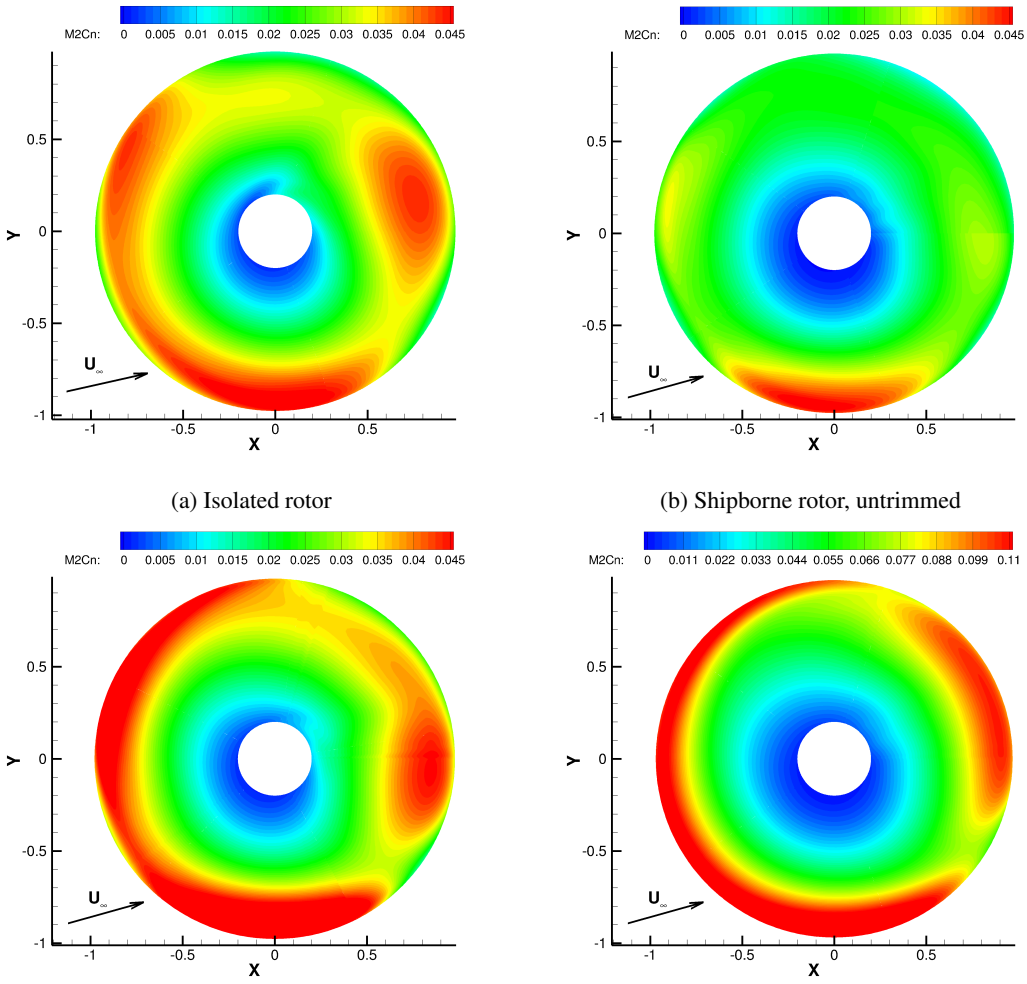

(a) Isolated rotor

(b) Shipborne rotor, untrimmed

(c) Shipborne rotor $C_{\mathrm{T}}^{\mathrm{UK}} = 0.00734$

(d) Shipborne rotor $C_{\mathrm{T}}^{\mathrm{UK}} = 0.01468$

Figure 6.38: Normal force coefficient $M^2 C_{\mathrm{N}}$ for (a) isolated rotor, (b) shipborne rotor and (c,d) shipborne rotor after re-trimming for two thrust coefficients.

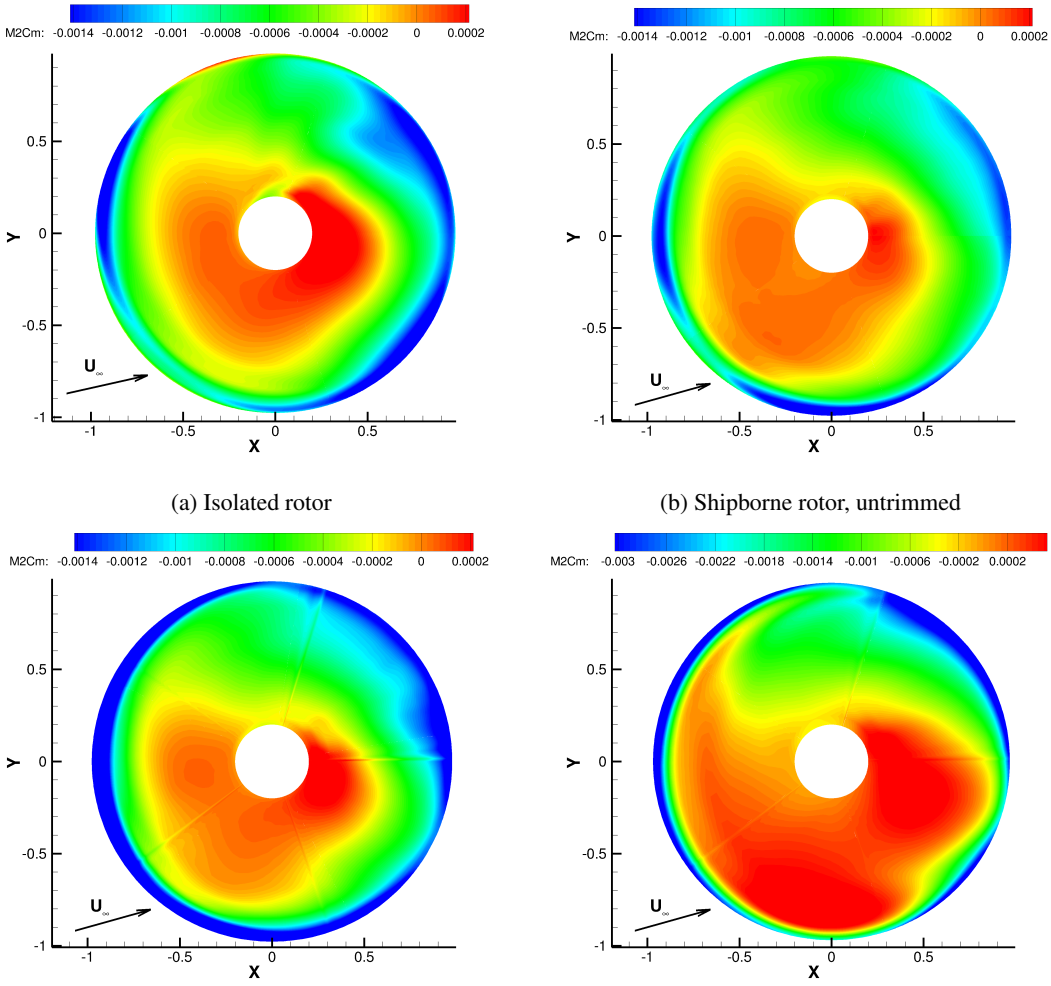

(a) Isolated rotor

(b) Shipborne rotor, untrimmed

(c) Shipborne rotor $C_{\mathrm{T}}^{\mathrm{UK}} = 0.00734$

(d) Shipborne rotor $C_{\mathrm{T}}^{\mathrm{UK}} = 0.01468$

Figure 6.39: Pitch moment coefficient $M^2 C_{\mathrm{M}}$ for (a) isolated rotor, (b) shipborne rotor and (c,d) shipborne rotor after re-trimming for two thrust coefficients.

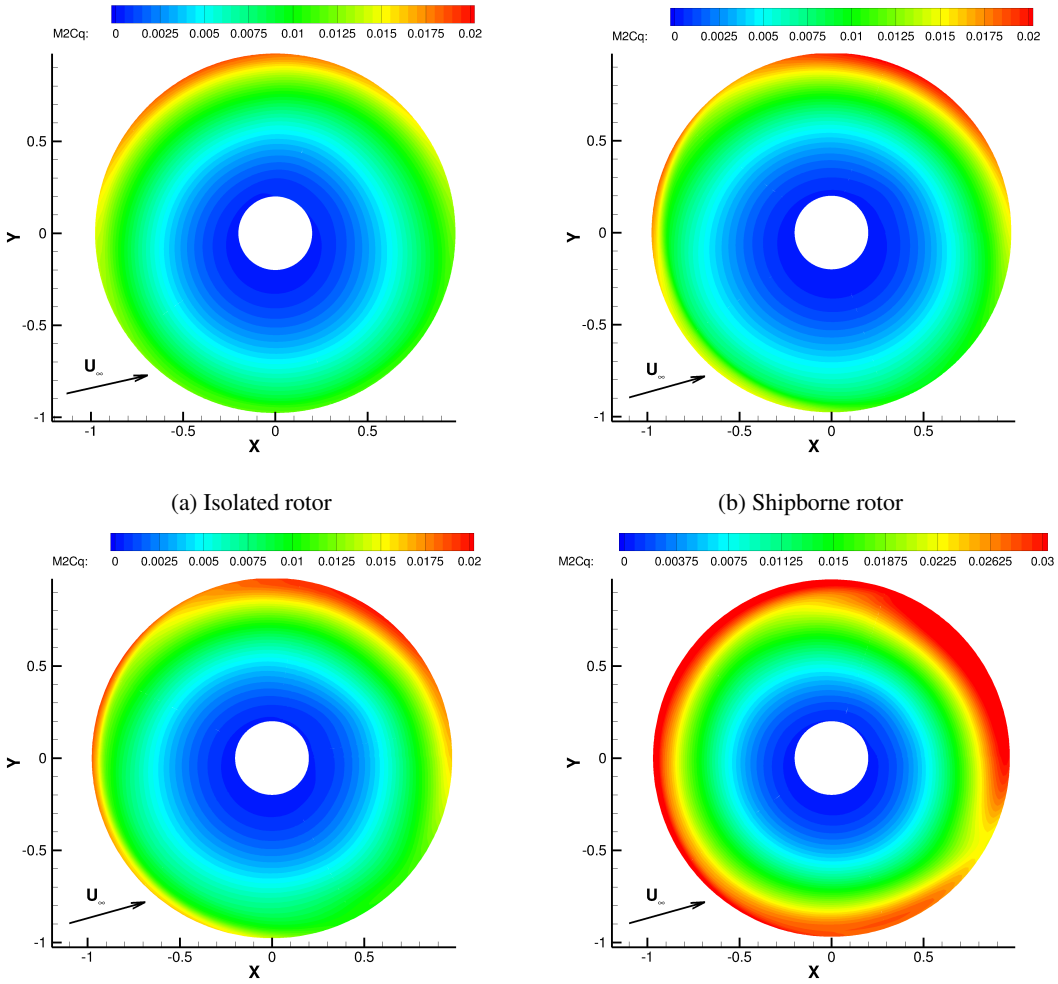

(a) Isolated rotor

(b) Shipborne rotor

(c) Shipborne rotor $C_{\mathrm{T}}^{\mathrm{UK}} = 0.00734$

(d) Shipborne rotor $C_{\mathrm{T}}^{\mathrm{UK}} = 0.01468$

Figure 6.40: Torque coefficient $M^2 C_{\mathrm{Q}}$ for (a) isolated rotor, (b) shipborne rotor and (c,d) shipborne rotor after re-trimming for two thrust coefficients.

Chapter 7

Coupled Ship Helicopter Manoeuvre

The content of this chapter was submitted for publication in:
C. Crozon, R. Steijl and G. Barakos,
Coupled Flight Dynamics and CFD - Demonstration for Helicopters in Shipborne Environment,
Journal of the American Institute of Aeronautics and Astronautics.

The staggered coupled HFM/HMB2 method described in section 3.5 is demonstrated in this chapter for the simulation of manoeuvring rotorcraft aerodynamics. Coupled simulations are carried out by substituting the simplified models used to model the blades, fuselage aerodynamics and inflow with the loads predicted by the CFD. The CFD loads predicted by HMB2, and the aircraft position and attitude predicted using HFM and helicopter flight dynamics are exchanged at every time iteration of the simulation but are kept fixed during the Newton steps of the CFD. The non-dimensional time step of $dt = \frac{2\pi R}{N_{steps/cycle}} = 0.1636$ was chosen, with $N_{steps/cycle} = 360$ and $R = 9.3759$. These values give one-degree and five-degree azimuthal steps of the main and tail rotors respectively, which is enough to ensure the stability of the CFD solver. The helicopter is trimmed before every attempt to simulate a manoeuvre and the linearised aircraft model required by the pilot model is computed around the trim state. The matrices used by the trimmer and the auto-pilot model are computationally expensive to generate using CFD if finite differences are used. Instead, the HFM method and simplified aerodynamics models are used when a linearised model is calculated, and the Jacobian matrices are computed using finite differences.

Variable	Value	
All Up Weight (AUW)	8391.46	$[kg]$
Roll 2nd moment of inertia	19354.3	$[kg.m^2]$
Pitch 2nd moment of inertia	65587.69	$[kg.m^2]$
Yaw 2nd moment of inertia	53080.27	$[kg.m^2]$
Hub coordinates with respect to CG	(0.31,0.0,-2.58)	$[m]$
Rotor radius	9.4488	$[m]$
Blade chord	0.4633	$[m]$
Hinge offset	0.32	$[m]$
Blade twist	-8.0	$[degrees]$
Blade mass	82.1	$[kg]$
Rotation speed Ω	21.89	$[rd.s^{-1}]$
Number of main rotor blades	5	
Number of tail rotor blades	5	
main rotor airfoil section	NACA0012	
tail rotor airfoil section	NACA0012	

Table 7.1: Some of the HFM model parameters for the Sea King MK50 [61–63].

7.1 Presentation of the Simulations

A model of the Sea King MK50 helicopter was created for HFM from the data made available by the Aeronautical Research Laboratory of the Australian Defence Science and Technology Organisation (DSTO) [61–63]. Key parameters are presented in table 7.1 and the full model is presented in appendix A.

A CFD mesh of the Sea King helicopter was created for the calculations with HMB and is shown in figure 7.1. The fuselage, main and tail rotors were generated separately, and assembled using sliding planes. The fuselage was split in three sections for ease of meshing and assembled using the sliding plane method of HMB [134]. For simulations of the helicopter flight without the ship, a background grid was added to further extend the computational domain. Shipborne simulations use the Halifax-Class "Canadian Patrol Frigate" (CPF) model presented in chapter 6. The grid was refined in the region of the deck and upstream to capture potential vortices shed from the ship superstructure. A background grid was added to lower the CPU cost of extending the computational domain. The mesh is shown in figure 7.2. For shipborne calculations, the grid of the Sea King helicopter, without the background, was embedded into the ship mesh and the chimera method was used between the two grids to allow the helicopter to manoeuvre. The characteristics of each component of the CFD mesh are summarised in table 7.2.

The helicopter is trimmed before each calculation. If the LQR auto-pilot is used, the required matrices are calculated around the trim state, using HFM, before the manoeuvre and are not recalculated. For CFD calculations, the hybrid trimmer

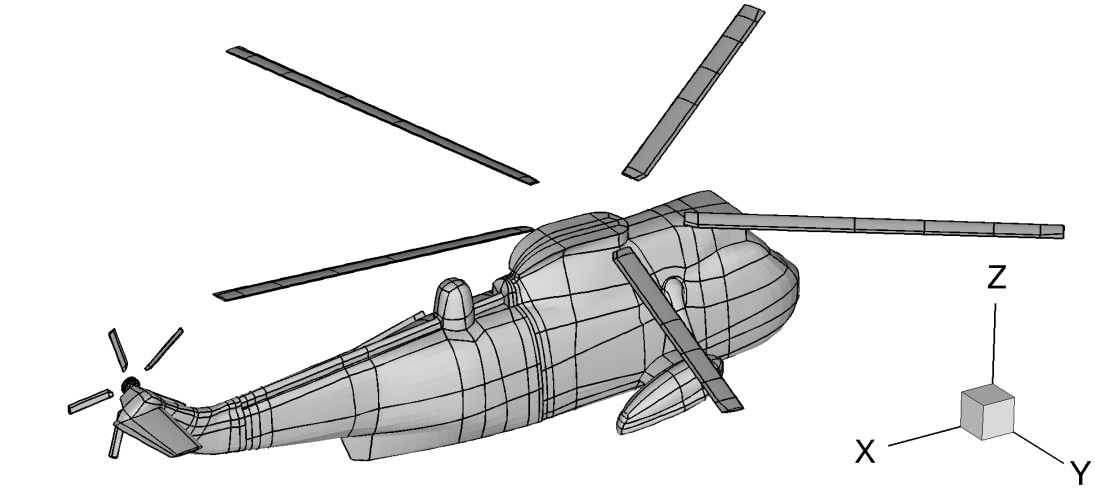

(a)

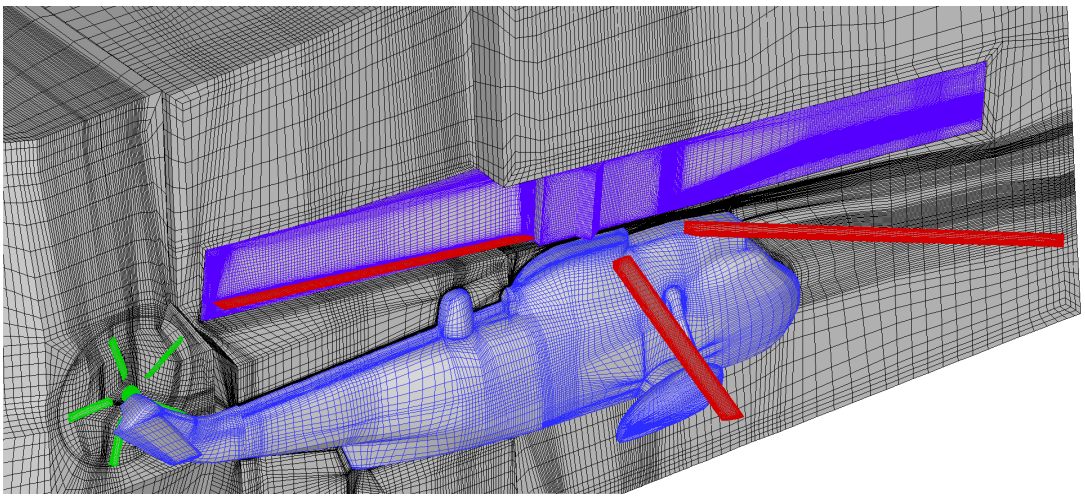

(b)

Figure 7.1: (a) Surface blocking and (b) CFD mesh of the Sea King helicopter.

described in section 3.4.2 was used to find a trim state that best minimises the residual loads on the aircraft.

The case of a shipborne landing manoeuvre was chosen to demonstrate the coupled HFM/HMB2 method. An idealised landing trajectory is shown in figure 7.3 and consists in three branches:

- **A-B**: Approach and deceleration to come to station keeping at the nominal speed of the ship.
- **B-C**: 15 to 20 meters lateral reposition over the landing point.
- **C-D**: 10 to 15 meters slow descent and touchdown.

The approach **A-B** is performed on the portside of the ship to give the pilot a good visibility of the deck and ship superstructure. The lateral reposition **B-C** and

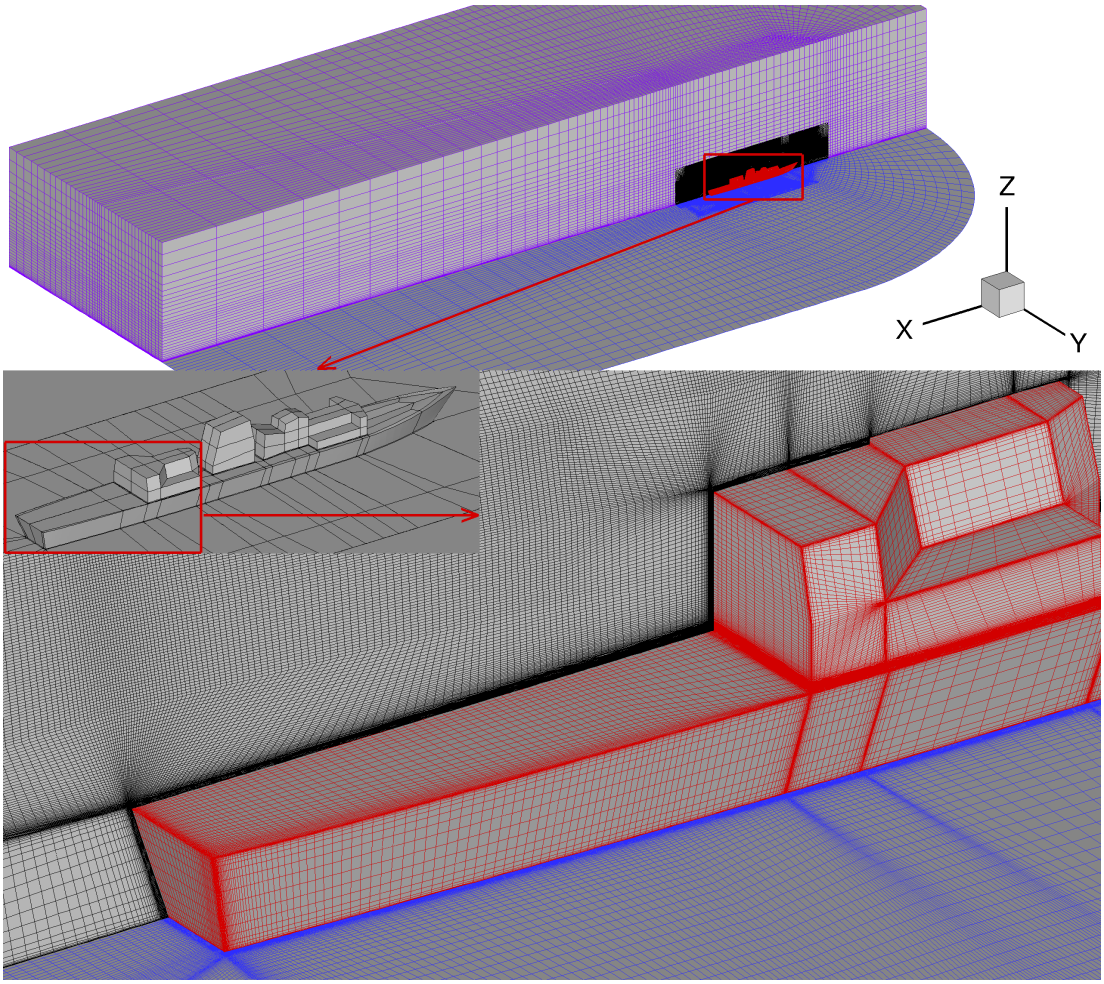

Figure 7.2: Grid of the CPF model used in this section.

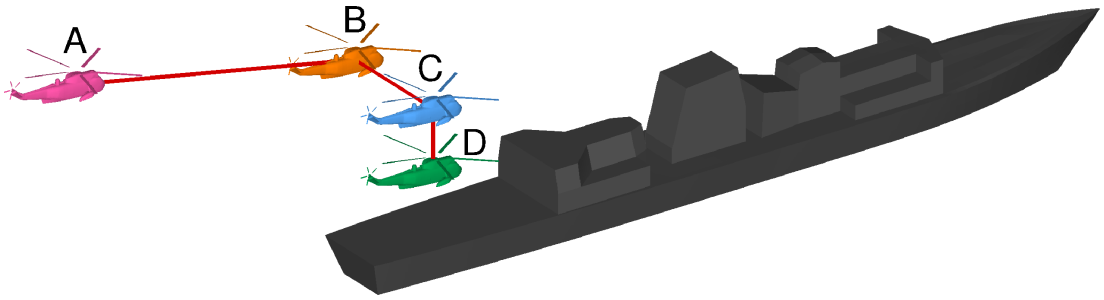

Figure 7.3: Typical landing manoeuvre as performed by the UK Royal Navy. **A-B** Descending approach on portside. **B-C** Lateral reposition and station-keeping. **C-D** Descent and touchdown.

descent **C-D** are performed at the nominal speed of the ship to maintain a stationary position relatively to the deck. The last two branches are critical as the helicopter must enter the ship wake and descend while maintaining an appropriate position and attitude to touchdown without over-stressing the aircraft or compromising the crew safety. The reported maximum speed for the Halifax-Class Frigate like the CPF is 29 knots and

Grid Part	Blocks	Cells (millions)
Sea King Fuselage Front	2146	1.43
Sea King Fuselage Middle	1940	0.53
Sea King Fuselage Tail	1533	0.39
Sea King Main Rotor (per blade / total)	260 / 1300	3.39 / 16.95
Sea King Tail Rotor (per blade / total)	230 / 1150	0.85 / 4.25
Sea King Background	34	1.3
Sea King Total	**8103**	**24.85**
Canadian Patrol Frigate	1026	30.72
Canadian Patrol Frigate Background	18	0.23
Canadian Patrol Frigate Total	**1044**	**30.95**

Table 7.2: Number of blocks and cells for mesh components used for the Sea King computations.

a nominal speed of 10 $m.s^{-1}$, or 19.4 knots, was chosen. This speed accounts for the combination of wind and ship motion but no variation due to the atmospheric boundary layer profile was taken into account. A headwind case is considered.

First, the **B-C** and **C-D** segments of the idealised landing trajectory are simulated using the standalone HFM code, with the pilot controls predicted using the embedded LQR auto-pilot model presented in section 3.3.3. Then, the coupled HFM/HMB2 method is demonstrated by simulating a short "single-input" response and comparing the results obtained with the trajectory predicted using the HFM method. Simulations of the shipborne helicopter in station-keeping flight at the first and last positions of the manoeuvre are performed and the flowfields are compared. This was carried out to ensure that the Chimera method [56] used to interface the helicopter and ship grids was performing well and to develop the flowfield in the wake of the ship. No flight mechanics model was used for these computations.

The descent manoeuvre was then performed with or without the presence of the CPF. The results are compared to identify the differences in pilot input and aerodynamic loads due to the presence of the ship wake. In both cases, the LQR pilot model was used to track with the best accuracy possible the target trajectory.

7.2 Free-Response to Single Pilot Input

The coupled HFM/HMB2 method is first demonstrated by calculating the response of the aircraft to a single-channel pilot input. The command is a simple two-seconds sinusoidal pull-up action that increases the value of the collective by five degrees and then returns it to the original value as shown in figure 7.4. Other control angles are kept fixed to the initial trimmed condition.

The trimming methods only find a trim state of the aircraft that minimises the average loading. Since the HFM helicopter model is unsteady, it does not maintain

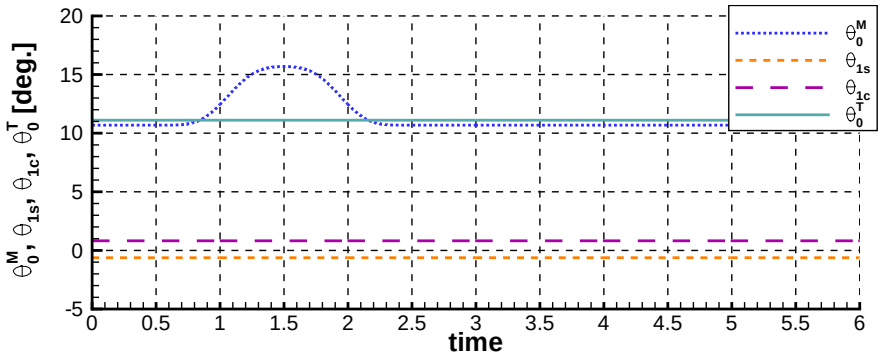

Figure 7.4: Control input used to characterise the aircraft response to a single-channel pilot input.

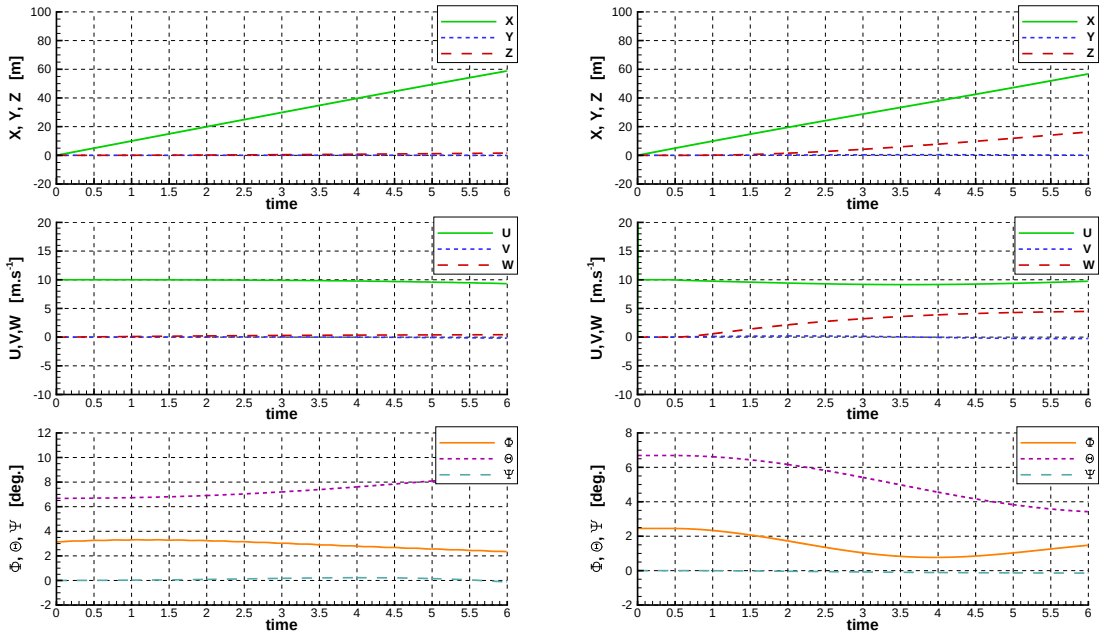

(a) HFM Response

(b) HMB response

Figure 7.5: Aircraft free-response calculated with HFM and HMB if a constant pilot input is applied. This is referred to as "drift".

steady flight conditions even under those trimmed conditions, and "drifts" if no active control is applied. This response was calculated using HFM and HMB and the resulting trajectory and attitude are shown in figure 7.5. To characterise the intrinsic response of the aircraft to the pilot input, results are presented with and without the "drift". Results obtained using the standalone code HFM, and coupled CFD simulation are shown in figures 7.6 and 7.7 respectively.

The HFM results show a clear increase in vertical velocity and a final altitude gain of about 12 meters after six seconds. The aircraft rolls and pitches as a consequence of the change in rotor loading.

The results obtained using the coupled method show a similar behaviour, albeit

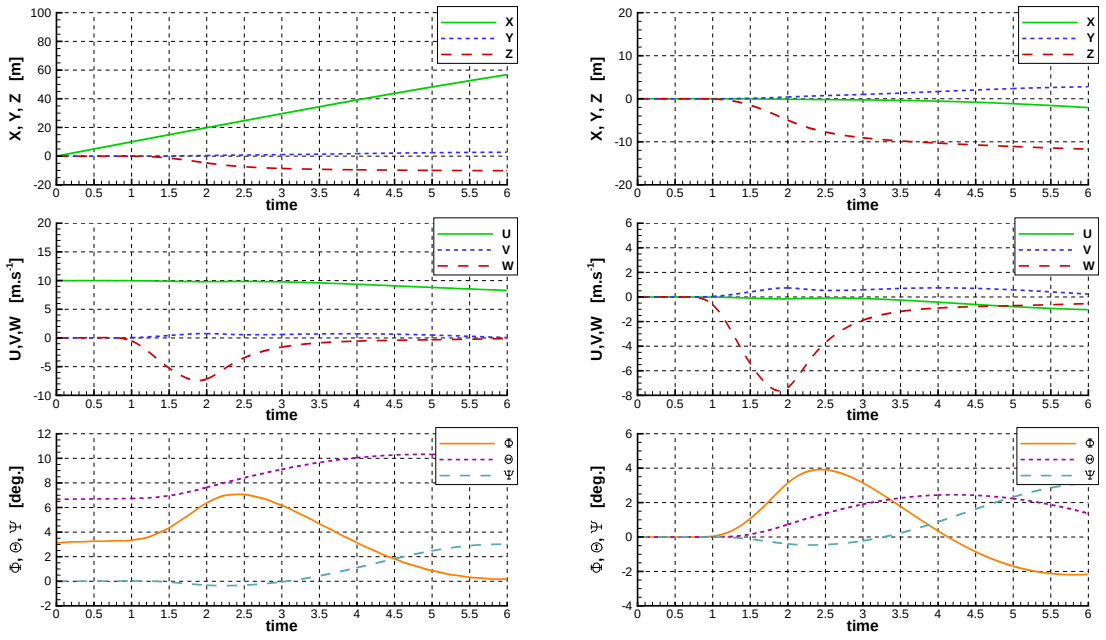

(a) HFM Response

(b) HFM response without drift

Figure 7.6: Aircraft response to a collective input (Fig. 7.4) with and without "drift". Position, velocities and attitude calculated using the standalone HFM method.

of lower amplitude. The total gain in altitude is about 7 meters after 6 seconds and the rolling and pitching moments are significantly lower than predicted by the HFM simulation.

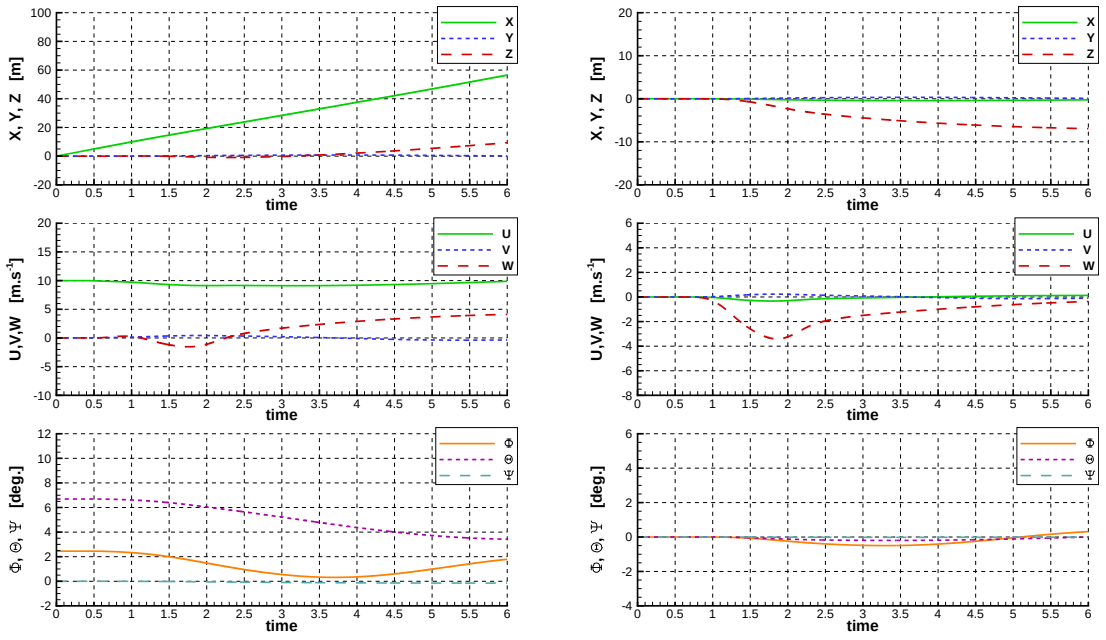

(a) HFM/HMB2 Response

(b) HFM/HMB2 response without drift

Figure 7.7: Aircraft response to a collective input (Fig. 7.4) with and without natural drift. Position, velocities and attitude calculated using the coupled HFM/HMB2 method.

7.3 LQR Simulation of the Landing using HFM

Figures 7.8 and 7.9 show the results of a LQR-piloted simulation of the **B-C** and **C-D** branches of the manoeuvre respectively. The standalone HFM code is used to trim the aircraft, calculate the linearised model required for the LQR pilot model and perform the manoeuvre. The trimming and the calculation of the linearised model are performed using HFM prior to the calculation using finite differences as described in section 3.3.1, equations 3.14, 3.20 and 3.21.

The Aeronautical Design Standard 33 "Handling Qualities Requirements for Military Rotorcraft" (ADS-33E-PRF) document [72] specifies a series of manoeuvres that rotorcraft need to be able to perform and the associated tolerances. Results show that the LQR pilot model accurately maintains stable flight and follows the target trajectories within the tolerance set for similar manoeuvres in the ADS33 document. Since the ADS33 does not include a landing, the lateral reposition and the descent manoeuvres were used for comparison.

Results for the lateral reposition manoeuvre show some overshoot in the lateral position.To alleviate this problem, some pilot models add a predictive method to "look-ahead" and anticipate changes in the trajectory, as in the Generalised Predictive Control (GPC) method of Hess and Jung [135]. This limits overshoots and gives a behaviour more representative of a human pilot, but it is not implemented in the current LQR

model.

Moreover, accelerations of the aircraft are typically oscillatory due to the blades rotation. The position, velocities and accelerations are time-averaged over one blade-passing period (one fifth of main rotor revolution). This is done to avoid an oscillatory response of the pilot model but introduces delays in the response. No correction was applied to account for this delay, as it does not impact the stability of the method.

The target trajectory given to the LQR method only specifies the required change in y-position. Other targets in position and attitude angle are kept to their original value. By minimising the overall error in positioning, the LQR method allows for some deviation in every direction. To achieve the repositioning target, the helicopter needs to roll to the right to engage in translation, and to the left to exit the manoeuvre. The two peaks in attitude angle are clearly visible in figure 7.8(b) with a deviation of about 12 degrees on each side. Forces at the rotor hub clearly show the change in lateral force as well as a high-frequency "blade-passing" signal. The pilot input in the tail rotor collective shows significant variation as a result of the changes in inflow due to the lateral velocity. There are also smaller pilot inputs on the main rotor lateral cyclic and collective to engage and exit the manoeuvre.

The target trajectory for the descent manoeuvre begins after one second of flight and covers a distance of 10 meters in four seconds, as can be seen in figure 7.9 (a). However, the constraint was that the manoeuvre should be completed in under eight seconds. Results show that the aircraft crosses the 10 meters line six seconds after the beginning of the manoeuvre. The aircraft reaches 4 $m.s^{-1}$ peak descent velocity, and it slows down to about 0.4 $m.s^{-1}$ at the seven seconds mark.

The collective inputs are reduced by two degrees to engage the manoeuvre before returning to the initial value. An increase in normal force can be seen at the four-second mark, which is a consequence of the reduced downwash through the rotor disc during the descent. As a consequence, no increase in rotor collective is necessary to slow down the descent and stabilise the aircraft.

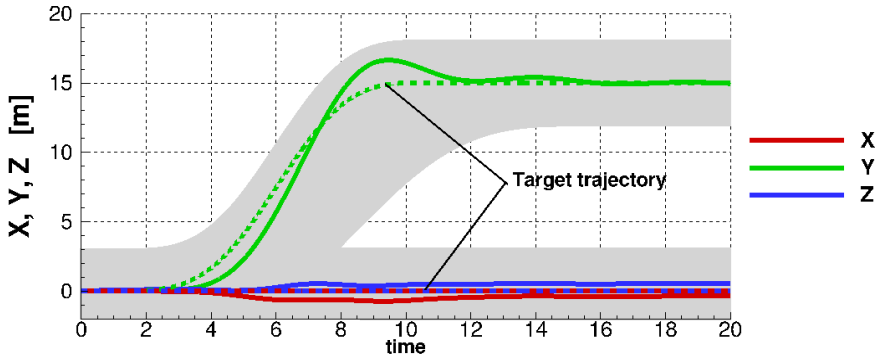

(a) Positions

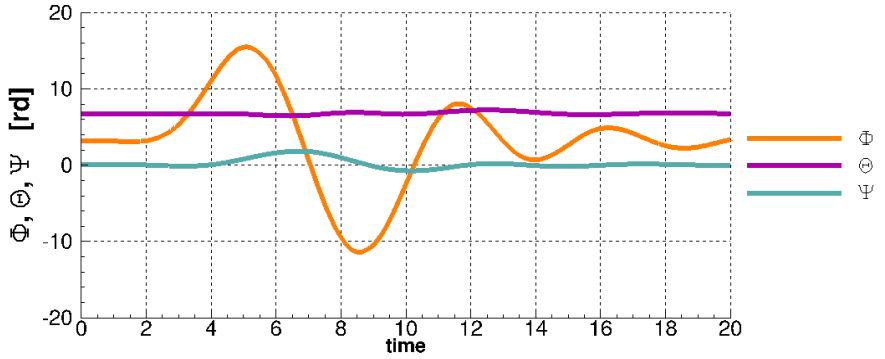

(b) Attitude Angles

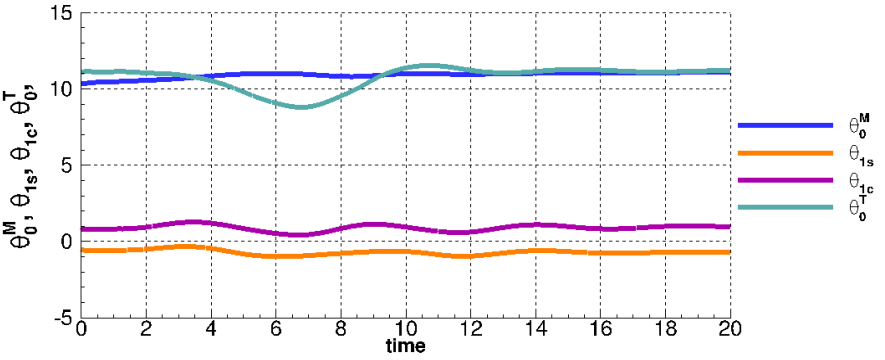

(c) Control Angles

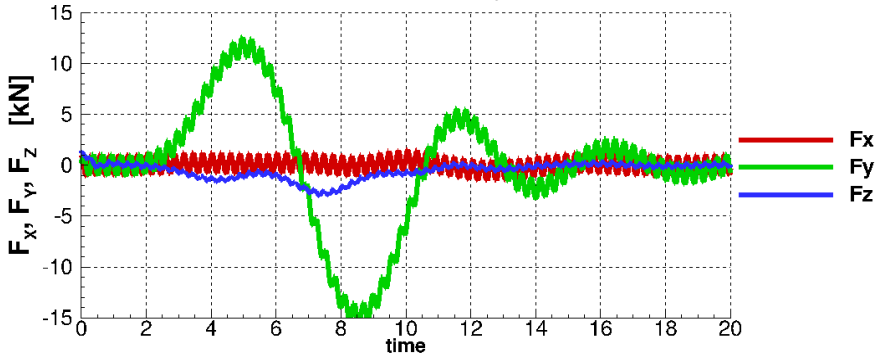

(d) Main Rotor Forces

Figure 7.8: Aircraft position, attitude, controls history and global forces during a LQR piloted lateral reposition simulation with HFM, compared with the target trajectory. The manoeuvre performed at a forward speed of 10 $m.s^{-1}$ and should be performed in 4 to 8 seconds. The error in x-position is shown in (a). The shaded area corresponds to the acceptable margin of error determined in ADS33 rapid descent manoeuvre.

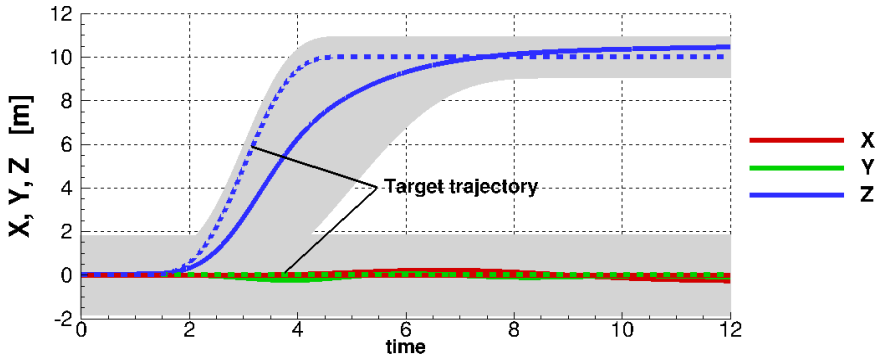

(a) Positions

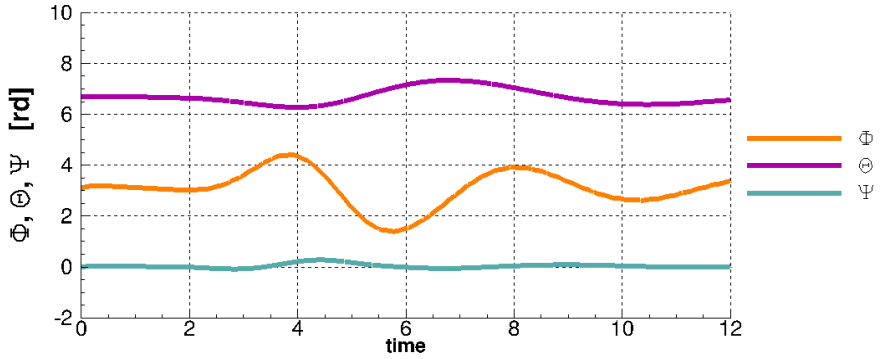

(b) Attitude Angles

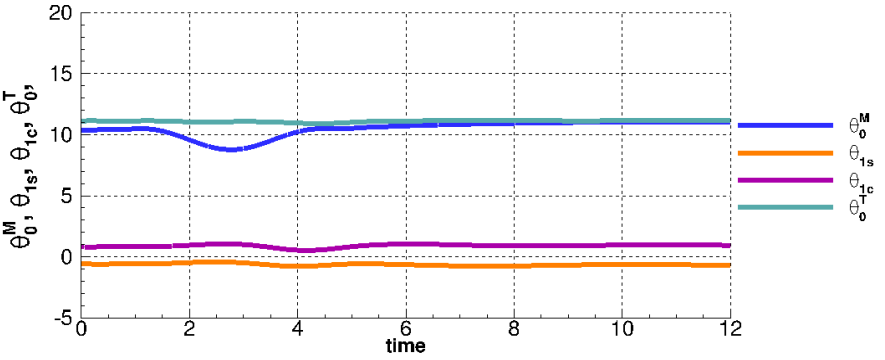

(c) Control Angles

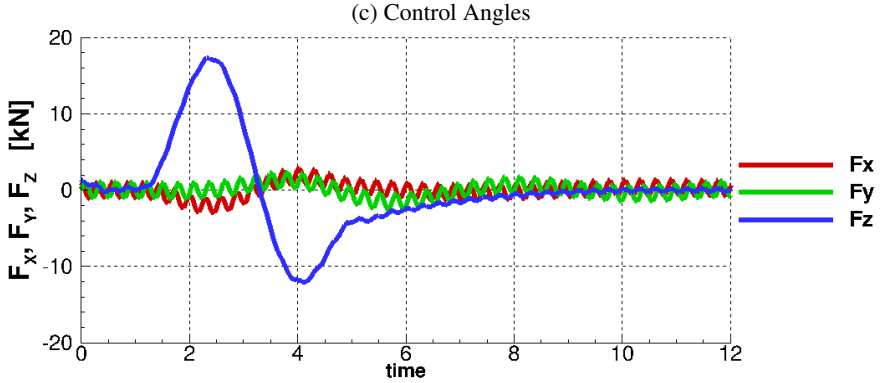

(d) Main Rotor Forces

Figure 7.9: Aircraft position, attitude, controls history and global forces during a LQR piloted landing simulation with HFM, compared with the target trajectory. The manoeuvre is performed at a forward speed of 10 $m.s^{-1}$ and should be performed in 4 to 8 seconds. The error in z-position is shown in (a). The shaded area corresponds to the acceptable margin of error determined in ADS33 rapid descent manoeuvre.

7.4 Coupled HFM/HMB2 Simulation in Free Air

Figure 7.10 presents the test case of the final descent and landing of figure 7.9 using the coupled HFM/HMB2 method. The LQR pilot model is set to start after three revolutions to allow some time for the flowfield to converge. Any residual load is then cancelled to start the manoeuvre in trimmed flight, as can be seen in figure 7.10 (d), at the one-second mark.

The results suggest that the LQR pilot model is able to accurately follow the specified trajectory with minimal deviation in terms of helicopter attitude and lateral and longitudinal positions. The LQR inputs in the main rotor cyclic and collective angles remain lower than 5 degrees, suggesting a mild pilot activity throughout the manoeuvre. It should be noted that, by construction, the LQR method acts as a filter that limits high-frequency changes in control and provides optimal tracking. It is therefore not representative of the behaviour of a human pilot.

The large excursion in tail rotor collective is caused by a change in moment around the yaw axis at the beginning of the manoeuvre, probably due to a still-converging inflow on the tail rotor and an overestimated tail rotor thrust. The pilot model corrects for the deviation, without affecting the global behaviour of the aircraft.

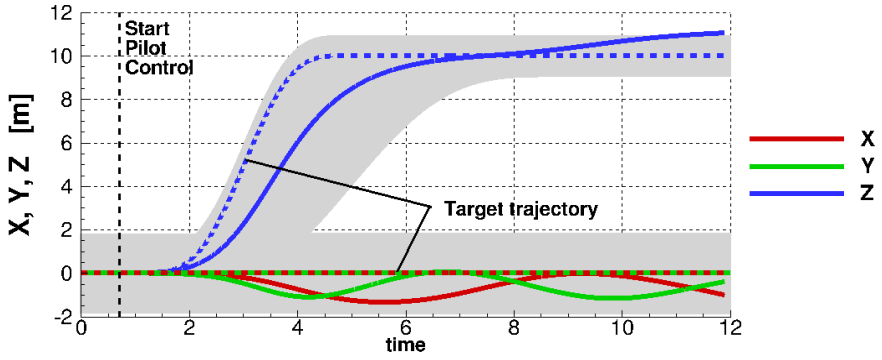

(a) Positions

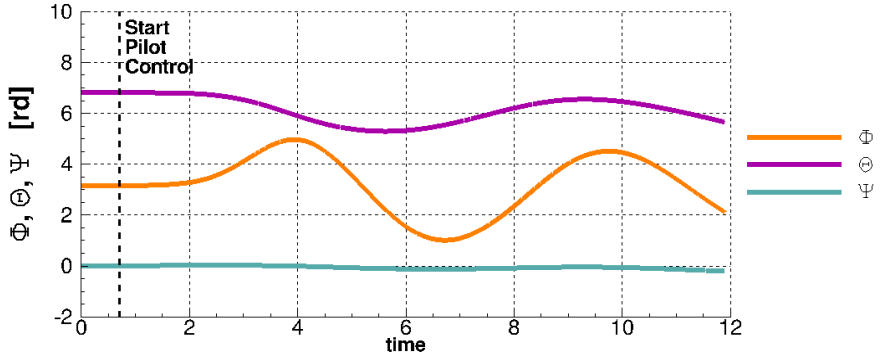

(b) Attitude Angles

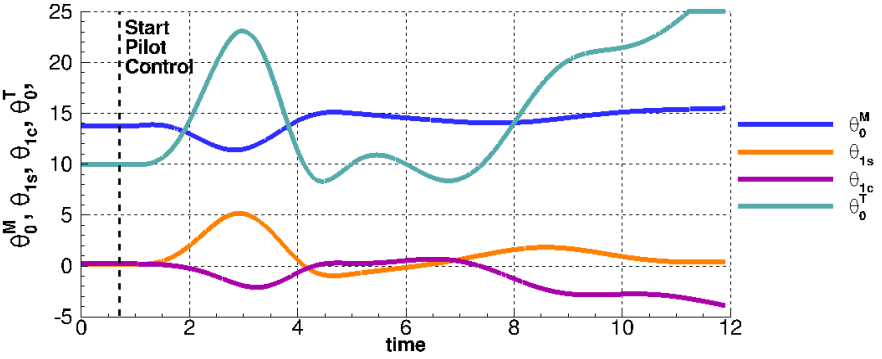

(c) Control Angles

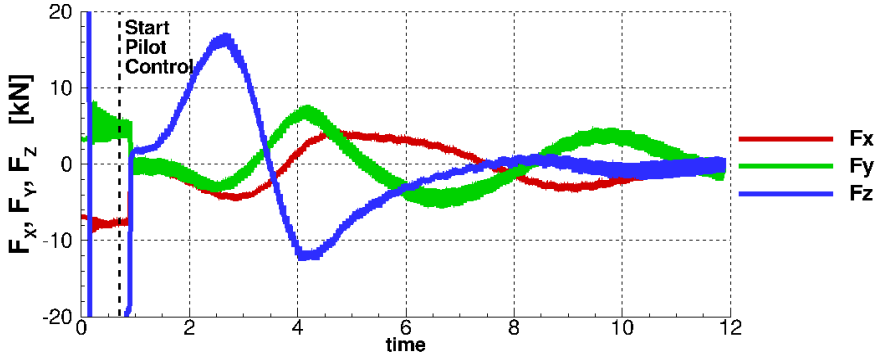

(d) Main Rotor Forces

Figure 7.10: Aircraft position, attitude, controls history and global forces during coupled CFD simulation with LQR control, compared with target trajectory. Manoeuvre performed at a forward speed of 10 $m.s^{-1}$ and should be performed in 4 to 8 seconds. Error in x-position is shown in (a). Shaded area corresponds to the acceptable margin of error determined in the ADS33 rapid descent manoeuvre.

7.5 Coupled Shipborne Simulations

7.5.1 Station-keeping Flight

Because of the two vastly different timescales between ship and helicopter wakes, it is necessary to initialise the simulation with a larger time-step to eliminate the transient flow in the wake of the ship.

- The helicopter and ship speeds were set to 10 $m.s^{-1}$. A non-dimensional time-step $dt = 2.0$ was used, and the rotors were kept fixed.
- The time step was then reduced to $dt = 0.1636$ and the rotors were set to rotate at their nominal speed.
- The residual loads were removed to avoid immediate drift from the prescribed trajectory.
- The simulation was then started with $dt = 0.1636$ and HFM was used to calculate the aircraft motion.

Results in figure 7.11 show the flowfield around the helicopter in isolated and shipborne conditions at the beginning of the manoeuvre. The Linear Integral Convolution method initially proposed by Cabral and Leedom [2] is used to visualise the flowfield in the moving frame of reference while the contours show the distribution of streamwise velocity. This flow visualisation method is described in more details in appendix B. The topology of the flow around the helicopter is similar and there is a separation between the ship and helicopter wakes, with the helicopter wake being distorted by the ship wake behind the hangar. This suggests a weak effect of the ship wake on the helicopter loading at the beginning of the manoeuvre. Contours of pressure coefficient are based on the main rotor tip velocity.

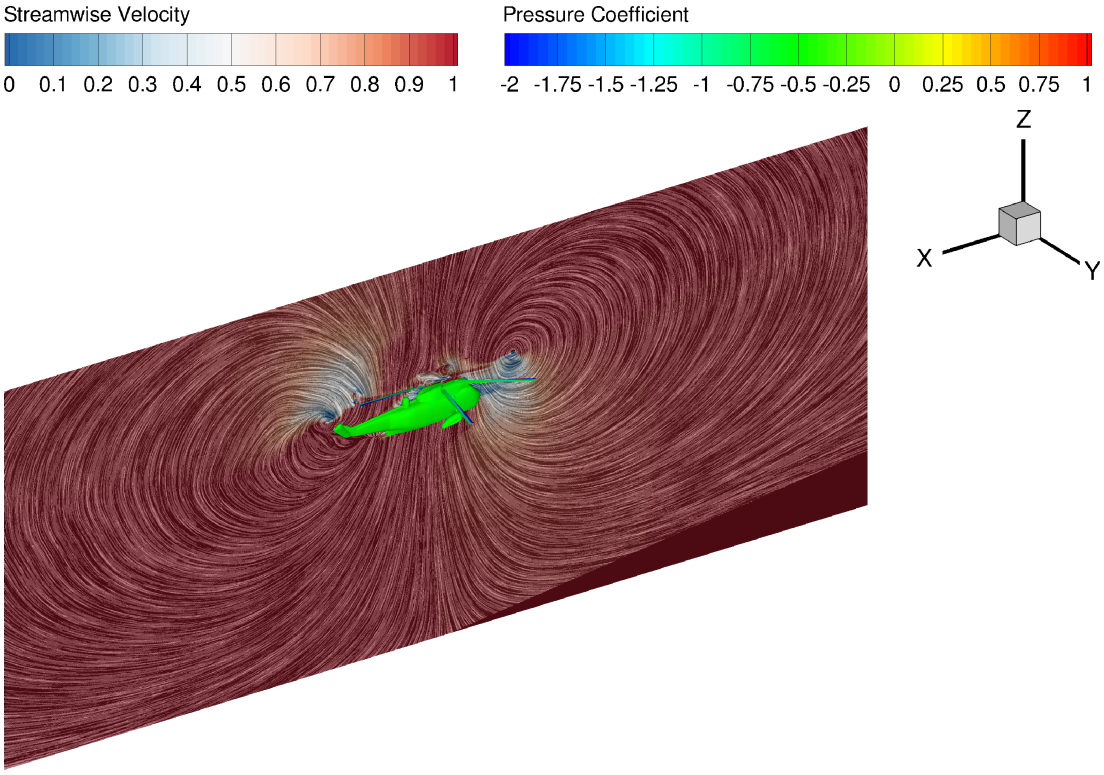

(a) Isolated helicopter, t = 0.5 seconds

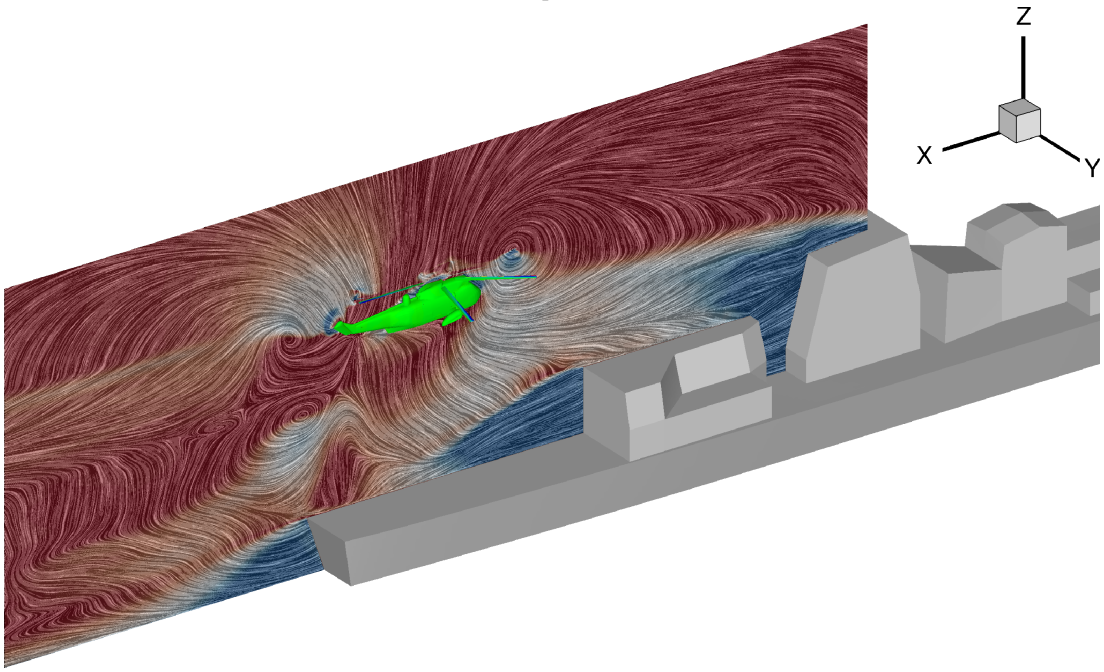

(b) Shipborne helicopter, t = 0.5 seconds

Figure 7.11: Flowfield and pressure on the helicopter at the beginning and the end of the manoeuvre, with and without ship wake. Contours of pressure coefficient based on free-stream velocity. Slice of flowfield topology computed using the LIC method in the moving frame of reference, colored with streamwise velocity.

7.5.2 Comparison Between Isolated and Coupled Responses

Results for the landing manoeuvre performed with and without the effect of the ship wake are compared directly to assess the effect of the ship wake. Figure 7.12 shows the two pilot responses and the subsequent trajectories. As predicted, results show little influence of the ship wake at the beginning of the manoeuvre, when the helicopter is located about 15 meters above the ship deck. The trajectory and pilot controls are similar until the 4th second (3 seconds through the manoeuvre). After 4 seconds, the helicopter rolling angle and lateral position show some discrepancies between the two cases.

Overall, the trajectory is followed accurately and the pilot activity is similar in both instances. The rolling angle is larger in the shipborne case and the longitudinal cyclic deviates further, suggesting an increased activity of the pilot. The main rotor collective is comparatively smaller in the shipborne case which contradicts the previous conclusions of section 6.2.5 that an increased collective is necessary to counteract the increased inflow behind the hangar. However, this can be partially explained as the main rotor plane is closer to the optimal horizontal (Φ closer to zero and Θ closer to the shaft angle of 7 degrees) and therefore provides more vertical lift. The rotor disc is higher above the hangar roof than in the calculations of section 6.2.5 and the effect on the rotor thrust is expected to be smaller. No calculation could be performed with the helicopter at touchdown altitude because of restrictions imposed by the Chimera method. Results in terms of forces and moments are shown in figure 7.13. Despite some differences in pitching moments, loads appear very similar throughout the manoeuvre.

Several surges are visible in the loads of figure 7.13, that appear when restarting the CFD computation. Future work will be carried out to ensure any restart is seamless.

Individual blade loads are shown in figure 7.14. The pitch angle of the first blade is shown with and without the harmonic content for both cases and the corresponding flapping and lead-lag aerodynamic moments at the hub are plotted. Results show similar values of loading at the beginning of the manoeuvre and discrepancies appear as the helicopter approaches the deck.

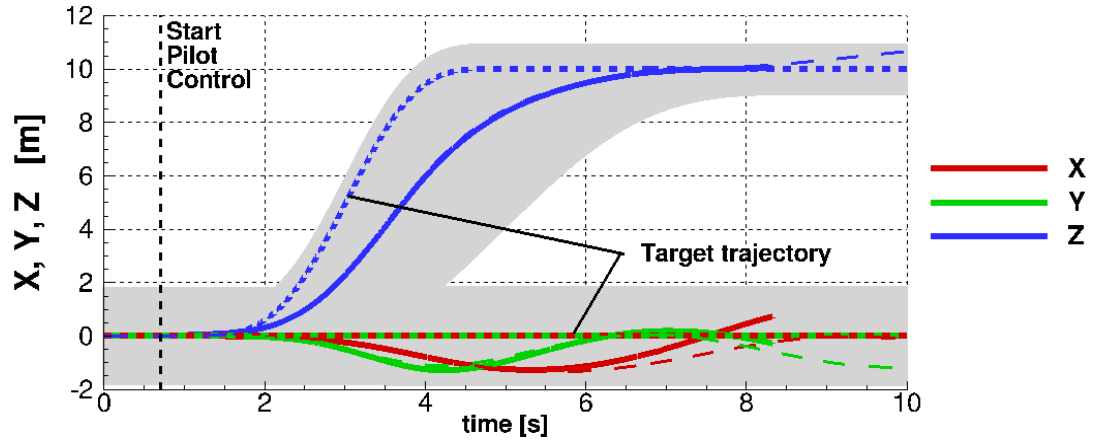

(a) Positions

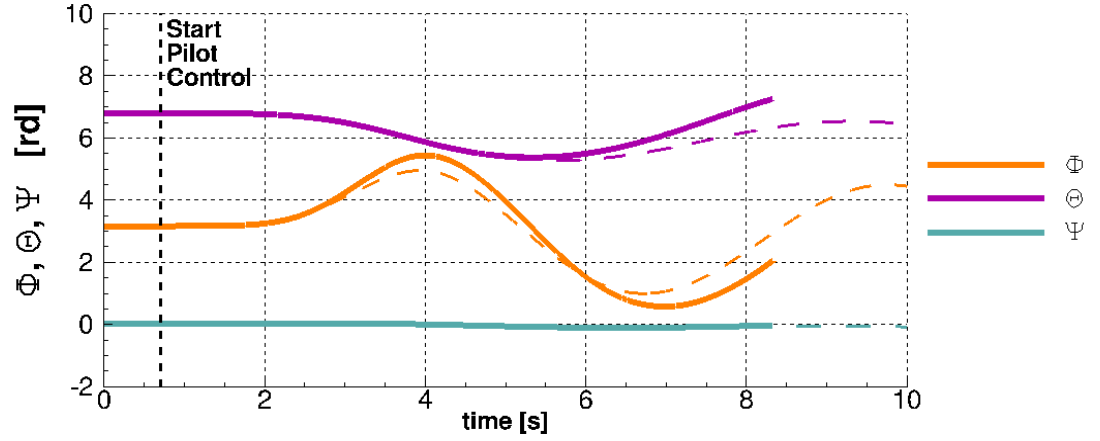

(b) Attitude Angles

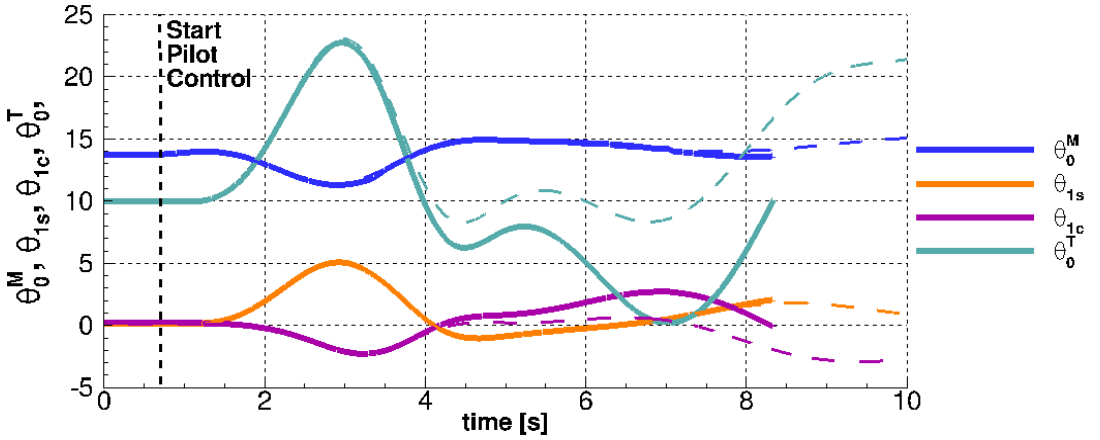

(c) Control Angles

Figure 7.12: Comparison of the pilot and aircraft response during the piloted landing manoeuvre with and without the effect of the ship wake. Dashed lines correspond to the isolated case. Solid lines correspond to the shipborne case.

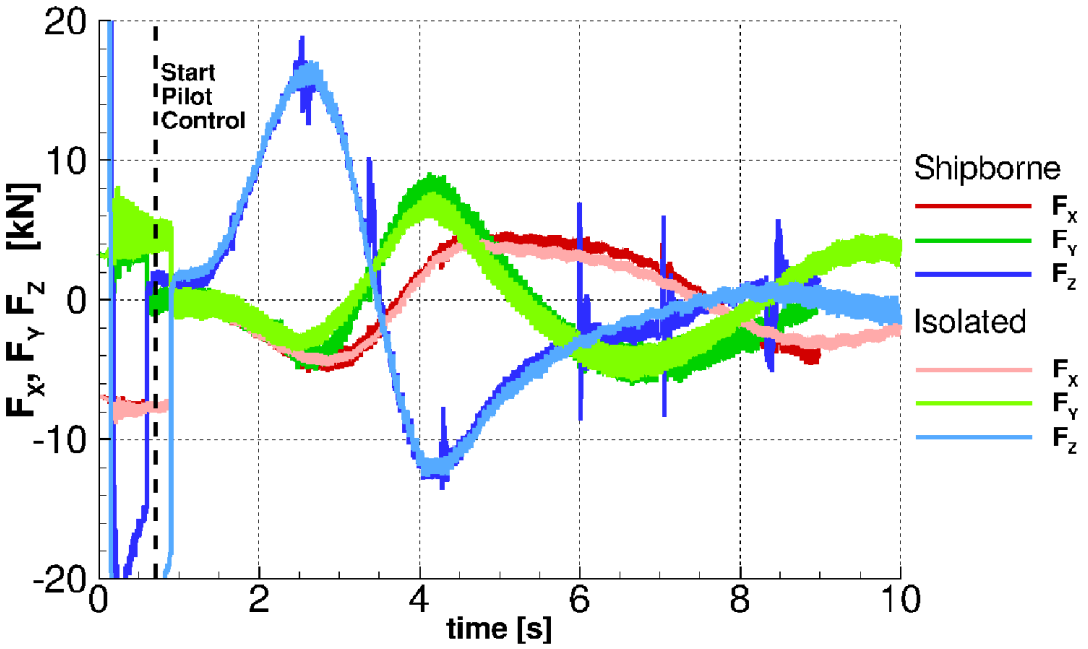

(a) Global forces

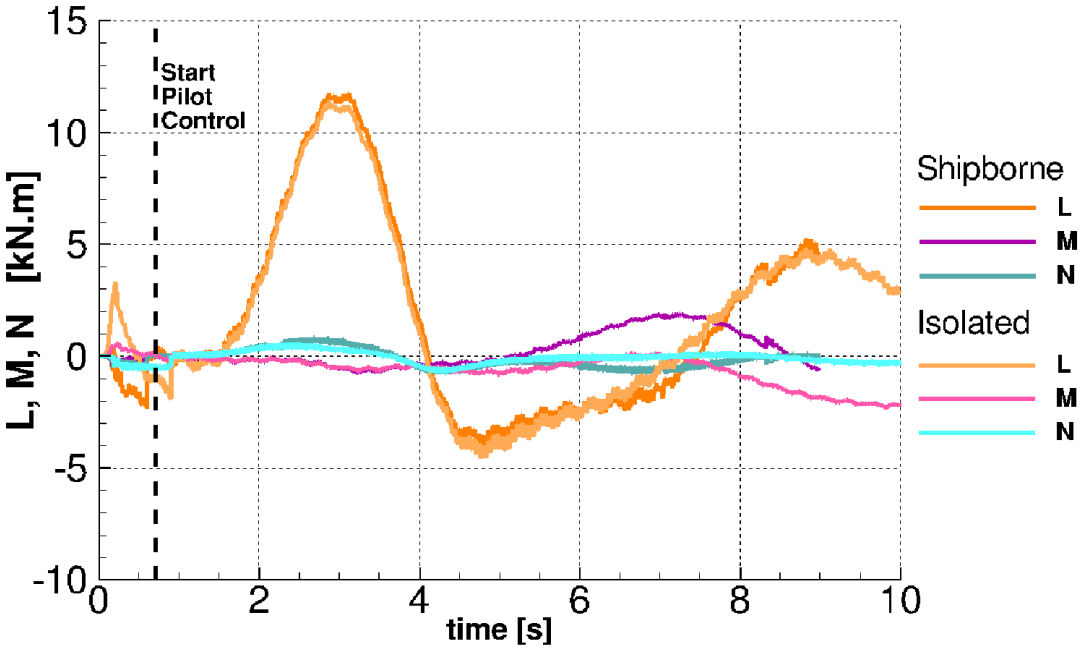

(b) Global moments

Figure 7.13: Comparison of the global forces and moments on the aircraft during the piloted landing manoeuvre with and without the effect of the ship wake.

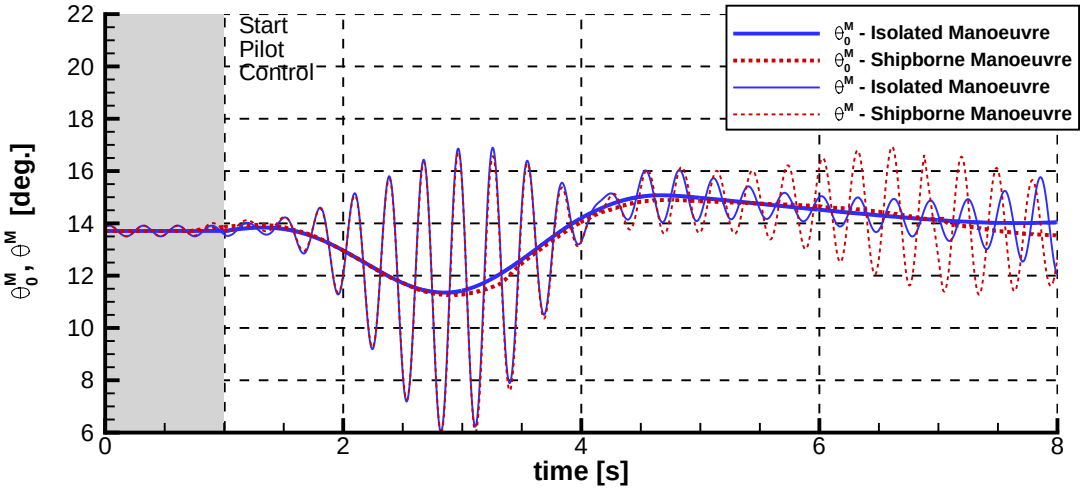

(a) Main rotor pitch angles

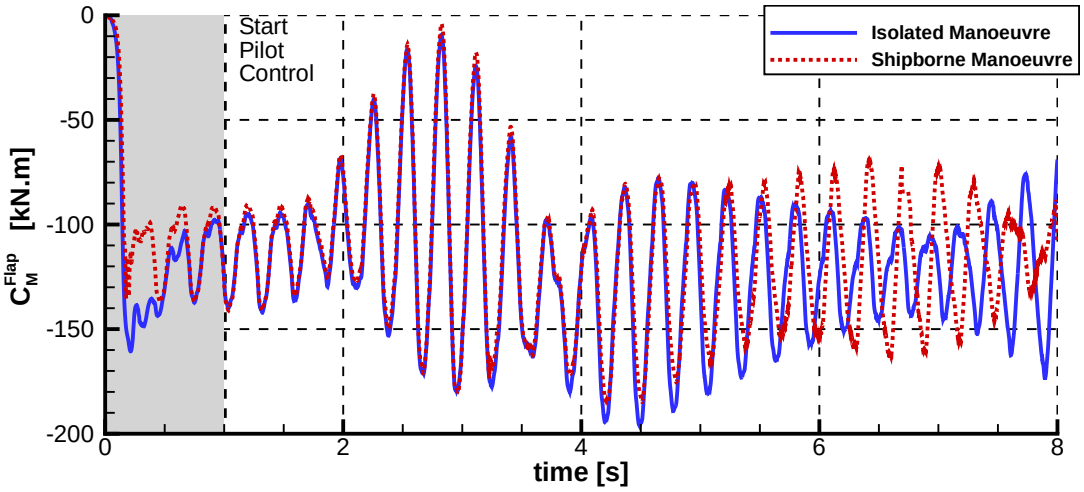

(b) Reference blade flapping moment

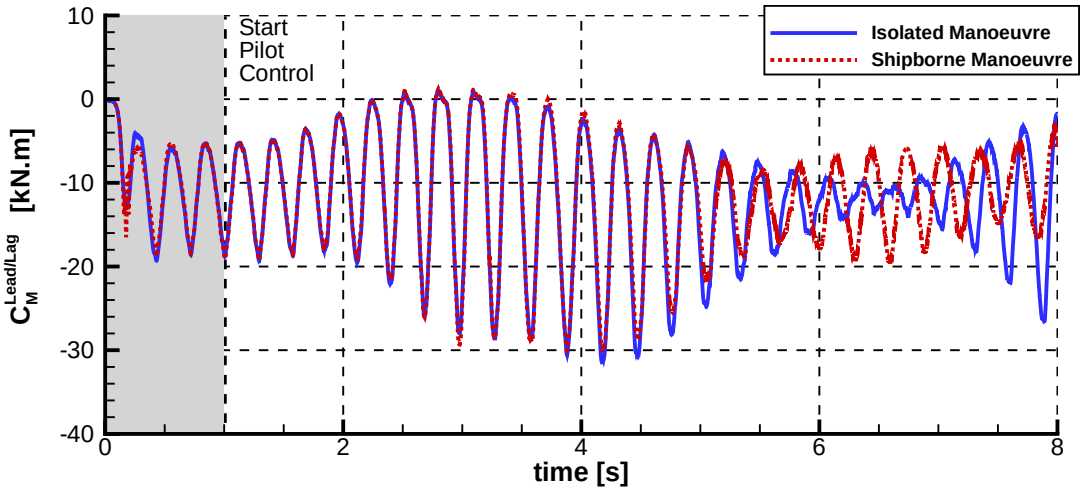

(c) Reference blade lead-lag moment

Figure 7.14: Comparison of the blade flapping and lead-lag moments during the piloted landing manoeuvre with and without the effect of the ship wake.

The flow visualisations presented previously in figure 7.11 for the beginning of the manoeuvre are reproduced in figure 7.15. They correspond to the 8 seconds time mark, with the helicopter close to the deck, and show more clearly an interaction between the two wakes. The development of the rotor wake is confined by the presence of the hangar door and the deck and extends downstream. Vortical structures that emanate from the ship superstructure are clearly visible, although they show signs of dissipation and do not seem to affect greatly the helicopter aerodynamics.

Figure 7.16 shows the distribution of non-dimensional w-velocity through the rotor disc at four instances during the manoeuvre. After 2 revolutions, the aircraft has just started descending and the isolated and shipborne cases show similar wake topologies. As the aircraft descends, it enters the ship wake and the topology of the global wake shows the presence of vortical structures that characterise the unsteadiness of the flow. The inflow velocity through the rotor disc is more important at 6 and 8 seconds in the shipborne case due to the downwash behind the hangar.

Contours of non-dimensional w-velocity are shown in figure 7.17 in the ship symmetry plane. Traces of the vortices created in the vicinity of the ship are clearly visible, as well as the fuselage wake below the helicopter. At the four-seconds mark, natural downwash combined with the rotor effect leads to an increased value of w-velocity through the rotor disc. At six and eight seconds, the apparent downwash reduces suggesting a partial ground effect caused by the deck. After eight seconds, the upwash velocity of the flow between the nose of the aircraft and the hangar increases as the rotor wake is confined between the helicopter and the deck.

Figure 7.18 shows the distribution of the pressure coefficient on the fuselage and ship deck, five seconds into the manoeuvre. The pressure coefficient is calculated based on the freestream velocity $C_P = \frac{P}{\frac{1}{2}\rho U_\infty^2}$. Levels of C_P show clearly the area where the helicopter wake impinges the deck. The downwash velocity is significantly higher than the freestream, leading to levels of pressure coefficient above one. The downwash over the fuselage constantly changes due to the blades passing in close proximity. Changes in pressure distribution on the fuselage are clearly visible, with high pressure levels on the boom and the roof of the cabin, and low values on the side of the aircraft where the flow accelerates.

7.6 Conclusions on Coupled Simulations

The discrepancies between the results in the calculations of section 7.2 suggests that the Sea King model in HFM that uses approximate aerodynamic models poorly represents the characteristics of the aircraft obtained using the CFD. Despite the

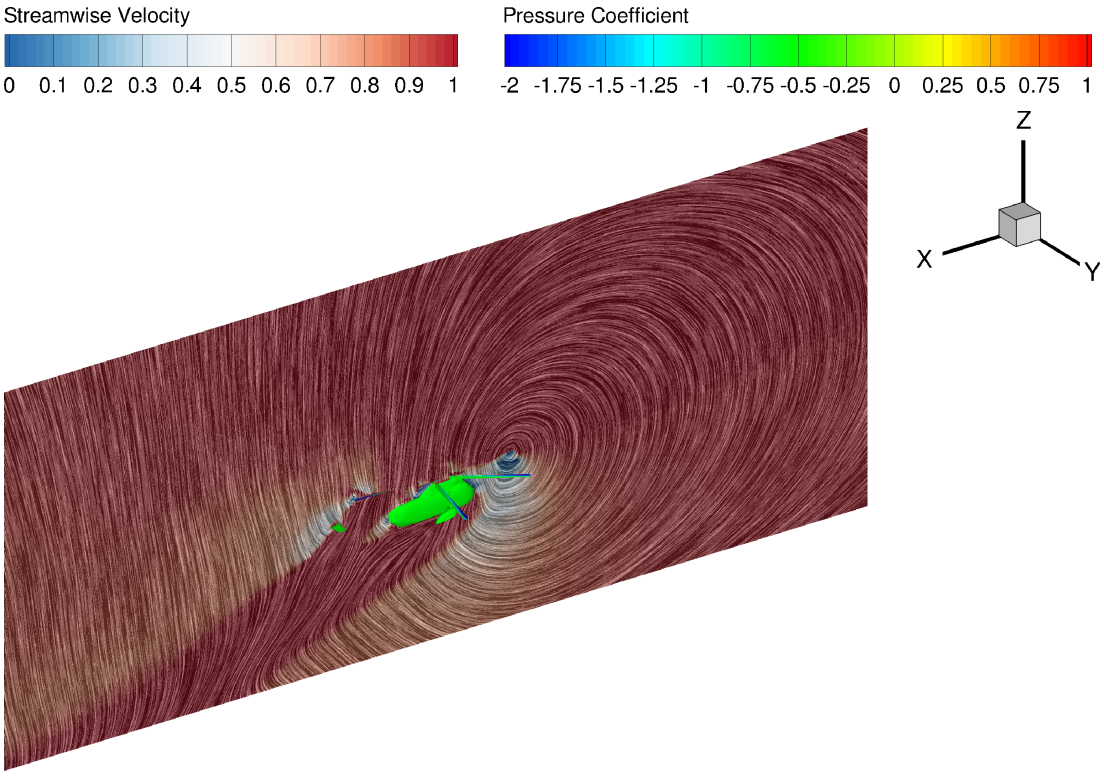

(a) Isolated helicopter, t = 8 seconds

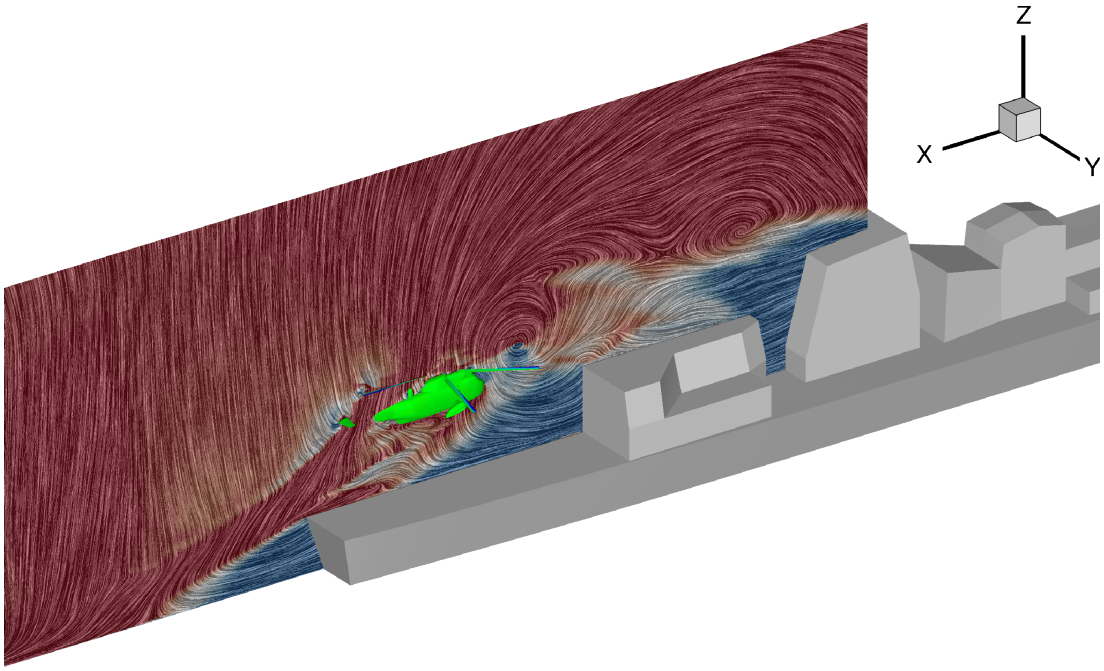

(b) Shipborne helicopter, t = 8 seconds

Figure 7.15: Flowfield and pressure on the helicopter at the end of the manoeuvre, with and without ship wake. Contours of pressure coefficient based on free-stream velocity. Slice of flowfield topology computed using the LIC method in the moving frame of reference, colored with streamwise velocity.

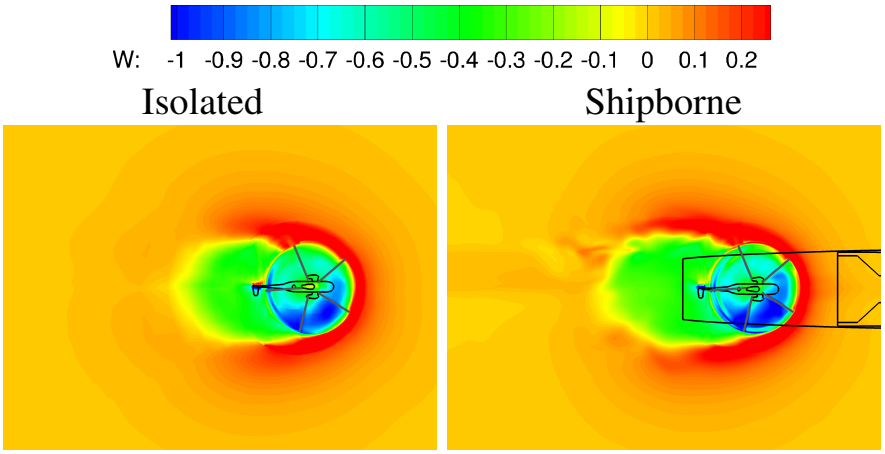

(a) Revolution 7 - t = 2 seconds

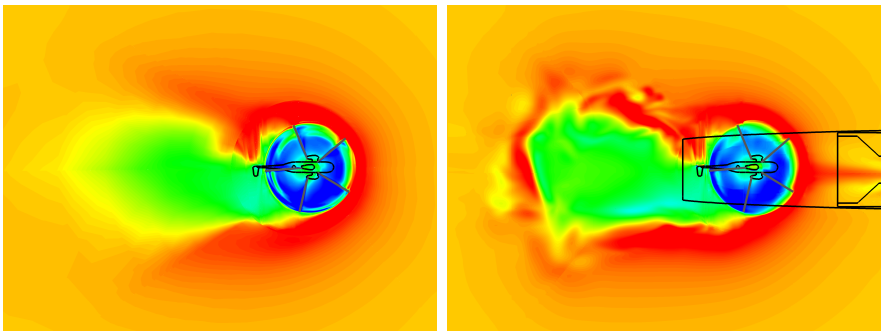

(b) Revolution 14 - t = 4 seconds

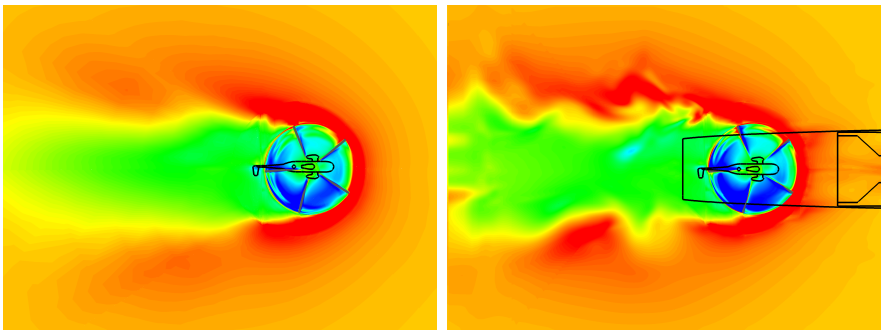

(c) Revolution 21 - t = 6 seconds

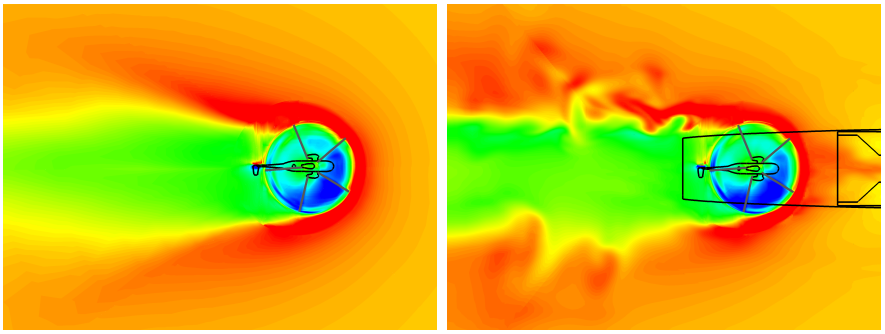

(d) Revolution 28 - t = 8 seconds

Figure 7.16: Distribution of inflow through the rotor plane during the (left) isolated manoeuvre and (right) shipborne manoeuvre.

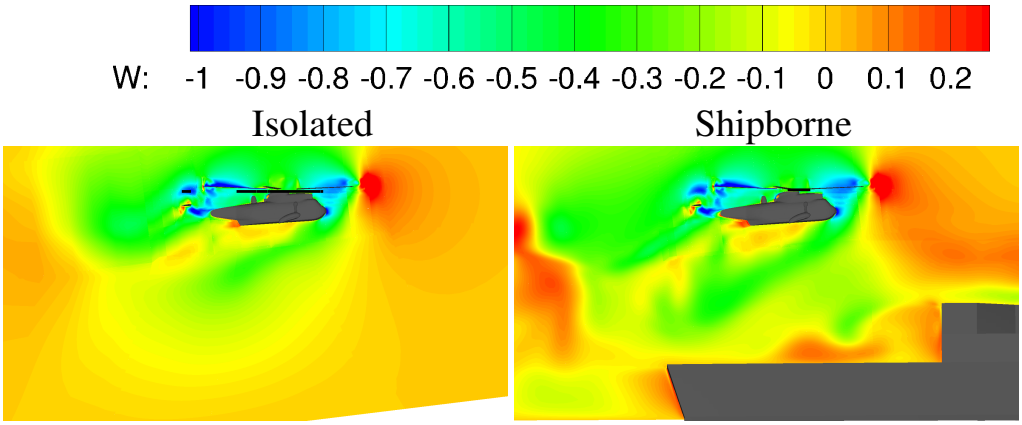

(a) Revolution 7 - t = 2 seconds

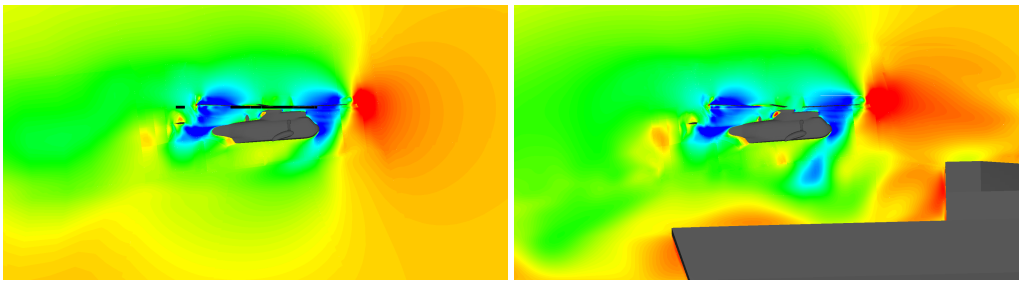

(b) Revolution 14 - t = 4 seconds

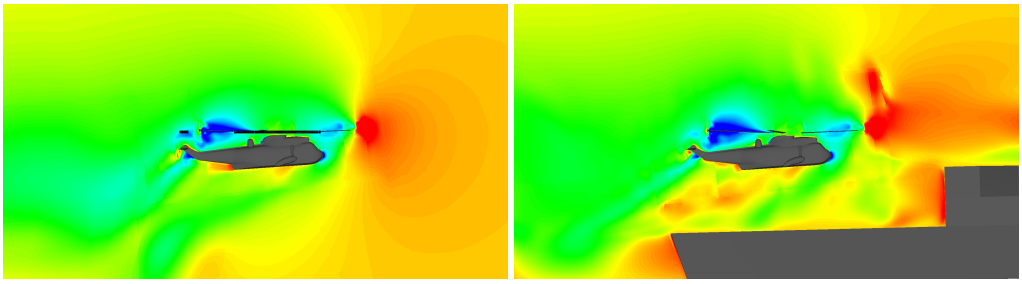

(c) Revolution 21 - t = 6 seconds

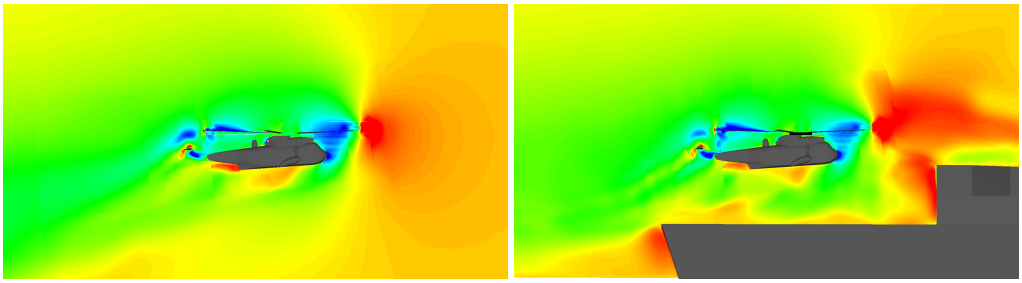

(d) Revolution 28 - t = 8 seconds

Figure 7.17: Distribution of inflow in the symmetry plane during the (left) isolated manoeuvre and (right) shipborne manoeuvre.

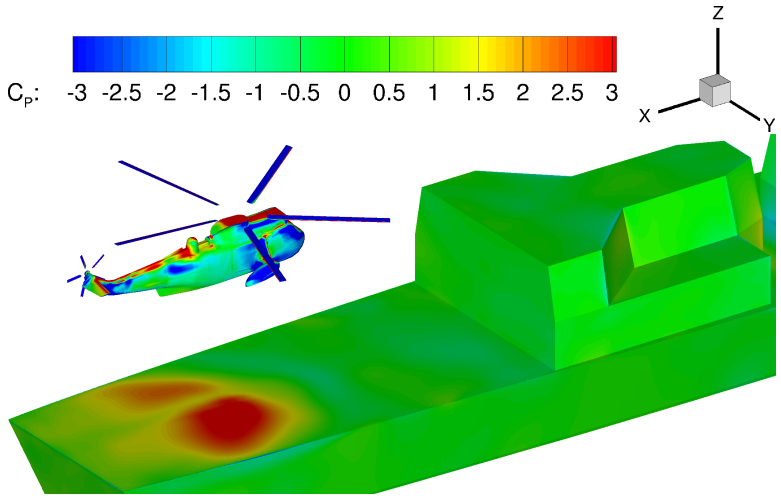

(a) Revolution 17 - Ψ^M = 0 degrees

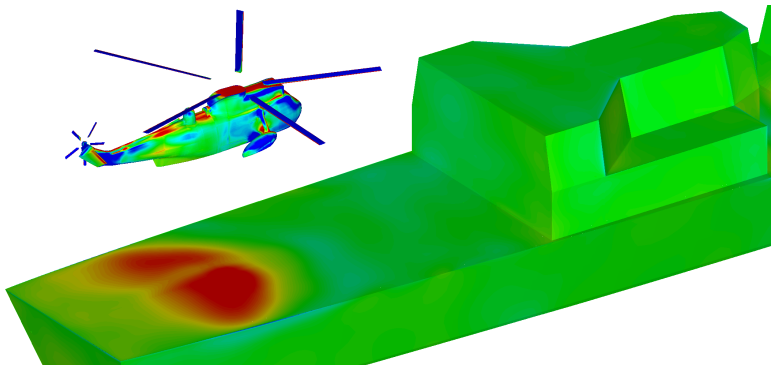

(b) Revolution 17 - Ψ^M = 18 degrees

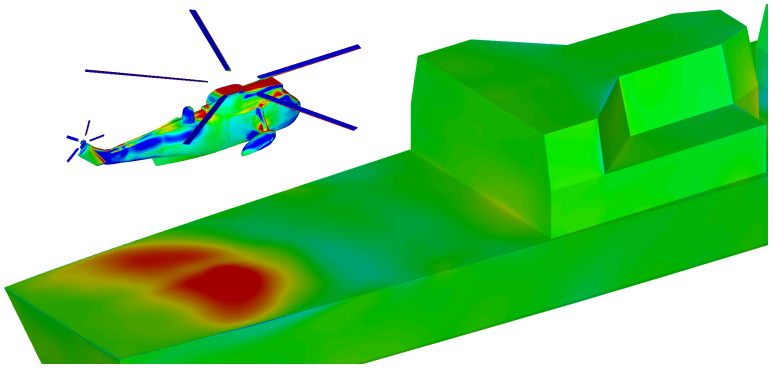

(c) Revolution 17 - Ψ^M = 36 degrees

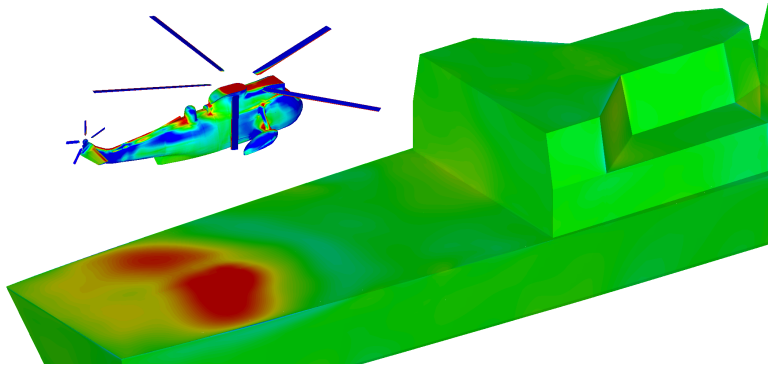

(d) Revolution 17 - Ψ^M = 54 degrees

Figure 7.18: Distribution of pressure coefficient on the fuselage and deck at 4 azimuthal angle of the main rotor. C_P scaled with the freestream velocity.

simplicity of the HFM model, it provided matrices for the linear models that proved accurate enough to provide good tracking performance even when using CFD.

A 10 $m.s^{-1}$ headwind case was chosen to ensure that the newly implemented method would not fail to maintain the helicopter position and attitude within a reasonable margin. More challenging flow conditions may require a more accurate linearised model, perhaps directly based on the CFD results. However, it demonstrates that the method is robust and suitable for such calculations.

Several aspects of the simulations carried out in this chapter could be improved. The grids used for the Sea King helicopter and ship were relatively coarse given the size of the computational domain and more realistic simulations may require a substantially higher number of grid cells.

The time-resolution requirement for rotor blades simulation is about one order of magnitude smaller than for ship wake simulations. It is necessary to choose the smaller time-step to ensure convergence of the solver and one-degree azimuthal steps of the main rotor were chosen to limit the computational time. As a consequence, the time-accuracy for the ship wake was largely exceeding the requirements $\delta t < \frac{\delta x}{U_\infty}$ for the grid density used δx. The region of the deck was meshed with a typical cell size of 0.3 m, giving 50 cells per ship beam. Five newton steps were used per time step to reduce the CPU time required.

The $k-\omega$ *SAS* turbulence model used for coupled calculation proved to maintain a more reasonable level of unsteadiness than the baseline $k-\omega$ model and is more stable than the DES model. However, it only preserved the largest structures over long distances and therefore the ship wake had a minimal impact on the helicopter aerodynamics. A finer, more homogeneous ship/background grid or a turbulence model that better preserves the vorticity may be required to add higher-frequency content to the simulation.

Chapter 8

Conclusions

Previous work on the simulation of ship/helicopter dynamic interface has been presented in the first chapter and shows that studies have been conducted with various levels of approximations depending on the simplified models used. CFD for manoeuvring aircraft has not yet been considered and this thesis represent steps towards this goal.

Experimental data generated for the Simple Frigate Shape 2 and the GOAHEAD full helicopter configuration was used to validate the block-structured parallel solver HMB2 developed at the university of Liverpool. Results show that the mean characteristics of the ship wake are well predicted and, given good quality grids, DES-SA [107] and $k-\omega$-SAS [115] turbulence models were also adequate to capture the unsteadiness of the flowfield. The SAS model was chosen to carry out the FM/CFD simulations due to the lower grid requirements and its numerical stability. The Test Case 2 of the GOAHEAD campaign was used to validate the predictions of HMB2 for helicopters at low advance ratio. Steady and unsteady loading on the fuselage were fairly predicted, as well as the rotor loading despite the use of an approximate trim state predicted using the HOST comprehensive rotor code [128]. These results give confidence in the ability of the HMB2 solver to simulate ship and helicopter wakes, and their interaction with fair accuracy.

To study the problem of the rotor/ship airwake interaction, the Canadian Patrol Frigate (CPF) geometry was chosen as a good compromise between geometrical realism and grid complexity. HMB2 was used for the study and the URANS $k-\omega$ model was chosen after demonstrating that the URANS and DES models resulted in similar mean flow characteristics for the ship wake.

The superposition method is used frequently to account for some of the rotor/airwake coupling effects without having to simulate the coupled problem. The

accuracy of the method was assessed by comparing isolated, superimposed and coupled rotor and ship wakes. Results show that, at the considered flow conditions, a coupled calculation is required.

A coarser grid was used to study the influence of the rotor position on the inflow velocity and compare it with the one obtained from an isolated actuator disc. Results show that the inflow velocity varies significantly depending on the position as well as wind direction due to various factors: deficit of velocity and downwash behind the hangar, upwash/downwash in the presence of a side-wind, partial ground effect.

The actuator disc method used to estimate the interaction of the rotor and ship wakes did not account for changes of the blade loading distribution due to the ship wake. A realistic dynamic interface simulation should include ship and rotorcraft in the CFD calculation. The previous actuator disc was replaced by a Sea King 5-bladed rotor with equivalent characteristics. A trimming method was applied to ensure that the rotor was performing under the same conditions. Results show that the collective required to maintain thrust increases by 20% when shipborne compared to isolated forward flight. The lateral cyclic varied by 7% to counteract the effect of the vortical structure of the wake at the considered 12 degrees wind angle. Resolving the blades allows accurate prediction of the loading across the rotor disc, albeit at a much greater cost compared to actuator disc simulations.

The Helicopter Flight Mechanics (HFM) multi-body dynamics solver was then tested as a standalone code and in coupled mode with HMB2. HFM builds a model of a helicopter based on first principles of rotorcraft flight and simple aerodynamics models. A linearisation method that computes Jacobian matrices via a second order finite difference method was implemented and used to build a trimming method. This was combined with a LQR pilot model. The helicopter was trimmed before each calculation and the linear pilot model was generated around the trimmed position. By providing a target trajectory to HFM, it was possible to simulate piloted manoeuvres, whether in standalone mode using simplified aerodynamics models, or in coupled mode using the CFD loads directly. Simulations of the last branch of the shipborne landing manoeuvre were performed using CFD, with and without the presence of the ship. Pilot activity and helicopter attitude show some differences, suggesting an influence of the ship wake on the aircraft.

The feasibility of simulating rotorcraft flight simulation directly using CFD was demonstrated using realistic ship and aircraft geometries, for the last part of a landing manoeuvre. The trajectory was tracked within the margins set for the descent manoeuvre of the ADS33 document, despite the pilot model relying on an approximate

linearised model of the aircraft. During coupled simulations of the landing, the aircraft follows the same trajectory at the beginning and some discrepancy appears as the helicopter enters the ship wake. The trajectory is followed closely suggesting that the ship wake only has a weak effect on the helicopter loads.

Considering that, given good quality meshes, the solver gave good prediction for both ship wake and helicopter loads. it is believed that more realistic simulations of the ship/helicopter interaction can be performed by increasing the spatial and temporal discretisation.

The method could be further improved by adding the effects of the atmospheric boundary layer and the ship motion. Different scenarios should be investigated for different wind speed and direction, and for longer manoeuvre, including the lateral reposition that precedes the landing. More accurate simplified models should be implemented into HFM in order to provide more accurate trimming method and pilot model. CFD-based linearised models may be generated via finite-differences or the computationally cheaper adjoint-method recently developed in Liverpool [136], in order to further improve the trimming and the pilot models.

References

[1] A.R.S. Bramwell, G.T.S. Done, and D. Balmford. *Bramwell's Helicopter Dynamics*. Butterworth-Heinemann, 2001.

[2] B. Cabral and L.C. Leedom. Imaging Vector Fields Using Line Integral Convolution. *20th Annual Conference and Exhibition on Computer Graphics and Interactive Techniques - Anaheim, CA, USA*, 1993.

[3] S.J. Zan. On Aerodynamic Modeling and Simulation of the Dynamic Interface. *Proceedings of the Institution of Mechanical Engineers, Part G: Journal of Aerospace Engineering*, 219(5):393–410, 2005.

[4] N.H. Wakefield, S.J. Newman, and P.A. Wilson. Helicopter Flight Around a Ship's Superstructure. *Proceedings of the Institution of Mechanical Engineers, Part G: Journal of Aerospace Engineering*, 216(1):13, 2002.

[5] Van Hoydonck W.R.M., Haverdings H., and Pavel M.D. A Review of Rotorcraft Wake Modeling Methods for Flight Dynamics Applications. 2009.

[6] S.A. Polsky. Progress Towards Modeling Ship/Aircraft Dynamic Interface. In *HPCMP Users Group Conference*, pages 163–168. IEEE, 2006.

[7] S.A. Polsky. Computational Analysis for Air/Ship Integration: 1st Year Report. In *High Performance Computing Modernization Program Users Group Conference (HPCMP-UGC)*, pages 109–114. IEEE, 2010.

[8] D.M. Roper, I. Owen, G.D. Padfield, and S.J. Hodge. Integrating CFD and Piloted Simulation to Quantify Ship-Helicopter Operating Limits. *Aeronautical Journal*, 110(1109):419–428, 2006.

[9] R.G. Lee and S.J. Zan. Unsteady Aerodynamic Loading on a Helicopter Fuselage in a Ship Airwake. *Journal of the American Helicopter Society*, 49:149, 2004.

[10] G.F. Syms. Numerical Simulation of Frigate Airwakes. *International Journal of Computational Fluid Dynamics*, 18(2):199–207, 2004.

[11] C.H. Kaaria, J.S. Forrest, I. Owen, and G.D. Padfield. Simulated Aerodynamic Loading of an SH-60B Helicopter in a Ship's Airwake. *European Rotorcraft Forum*, 2:1001–1013, 2009.

[12] C.H. Wilkinson, S.J. Zan, N.E. Gilbert, and J.D. Funk. Modelling and Simulation of Ship Air Wakes for Helicopter Operations: A Collaborative Venture. In *RTO Applied Vehicle Technology Panel Symposium*, pages 8–1, 1999.

[13] J.G. Leishman. *Principles of Helicopter Aerodynamics*. Cambridge Univ Pr, 2006.

[14] D.A. Griffiths and J.G. Leishman. A Study of Dual-Rotor Interference and Ground Effect Using A Free-Vortex Wake Model. *Circulation*, 2:1, 2002.

[15] C. Phillips, H.W. Kim, and R.E. Brown. The Flow Physics of Helicopter Brownout. In *66th American Helicopter Society Forum: Rising to New Heights in Vertical Lift Technology*, 2010.

[16] H.C. Curtiss Jr, M. Sun, W.F. Putman, and E.J. Hanker Jr. Rotor Aerodynamics in Ground Effect at Low Advance Ratios. *Journal of the American Helicopter Society*, 29:48, 1984.

[17] J. Light and T. Norman. Tip Vortex Geometry of a Hovering Helicopter Rotor in Ground Effect. *Journal of the American Helicopter Society*, 38(2):1611, 1989.

[18] A.J. Landgrebe. An Analytical and Experimental Investigation of Helicopter Rotor Hover Performance and Wake Geometry Characteristics. Technical report, DTIC Document, 1971.

[19] E.A. Fradenburgh. Aerodynamic Factors Influencing Overall Hover Performance. *Aerodynamics of Rotary Wings*, pages 7–1, 1972.

[20] J.S. Hayden. The Effect of the Ground on Helicopter Hovering Power Required. In *Annual Forum Proceedings of the American Helicopter Society*, pages 10–12, 1976.

[21] N. Iboshi, N. Itoga, J. Prasad, and L. Sankar. Ground Effect of a Rotor Hovering Above a Confined Area. *Annual Forum Proceedings of the American Helicopter Society*, 2:1249–1262, 2008.

[22] S.J. Hodge, S.J. Zan, D.M. Roper, G.D. Padfield, and I. Owen. Time-Accurate Ship Airwake and Unsteady Aerodynamic Loads Modeling for Maritime Helicopter Simulation. *Journal of the American Helicopter Society*, 54(2):0220051–02200516, 2009.

[23] N.H. Wakefield, S.J. Newman, and P.A. Wilson. CFD Predictions of the Influence of External Airflow on Helicopter Operations When Ooperating From Ship Flight Decks. In *RTO Applied Vehicle Technology Panel Symposium*, pages 2–1, 1999.

[24] E. Alpman, L.N. Long, D.O. Bridges, and J.F. Horn. Fully-Coupled Simulations of the Rotorcraft/Ship Dynamic Interface. In *Annual Forum Proceedings of the American Helicopter Society*, volume 63, page 1367. American Helicopter Society, inc.

[25] D.O. Bridges, J.F. Horn, E. Alpman, and L.N. Long. Coupled Flight Dynamics and CFD Analysis of Pilot Workload in Ship Airwakes. In *Collection of Technical Papers - 2007 AIAA Atmospheric Flight Mechanics Conference*, volume 1, pages 471–489, 2007.

[26] D.M. Roper, I. Owen, and G.D. Padfield. CFD Investigation of the Helicopter-Ship Dynamic Interface. *Annual Forum Proceedings of the American Helicopter Society*, 2:1985–2002, 2005.

[27] D. Lee and J.F. Horn. Simulation of Pilot Workload for a Helicopter Operating in a Turbulent Ship Airwake. *Proceedings of the Institution of Mechanical Engineers, Part G: Journal of Aerospace Engineering*, 219(5):445–458, 2005.

[28] D. Lee, N. Sezer-Uzol, J.F. Horn, and L.N. Long. Simulation of Helicopter Shipboard Launch and Recovery With Time-Accurate Airwakes. *Journal of Aircraft*, 42(2):448–461, 2003.

[29] S.J. Zan. Experimental Determination of Rotor Thrust in a Ship Airwake. *Journal of the American Helicopter Society*, 47, 2002.

[30] B.T. Cheney and S.J. Zan. CFD Code Validation Data and Flow Topology for TCCP AER-TP-2 Simple Frigate Shape. *Ottawa, Canada*, 1999.

[31] S.J. Zan. Surface Flow Topology for a Simple Frigate Shape. *Canadian Aeronautics and Space Journal*, 47(1):33–43, 2001.

[32] Y. Nacakli and D. Landman. Helicopter Downwash/Frigate Airwake Interaction Flowfield PIV Surveys in a Low Speed Wind Tunnel. *Annual Forum Proceedings of the American Helicopter Society*, 4:2988–2998, 2011.

[33] D. Stargel and D. Landman. A Wind Tunnel Investigation of Ship Airwake/Rotor Downwash Coupling Using Design of Experiments Methodologies. In *50th AIAA Aerospace Sciences Meeting including the New Horizons Forum and Aerospace Exposition, Nashville, Tennessee*, 2012.

[34] J.S. Forrest and I. Owen. An Investigation of Ship Airwakes Using Detached-Eddy Simulation. *Computers and Fluids*, 39(4):656 – 673, 2010.

[35] S.J. Zan, G.F. Syms, and B.T. Cheney. Analysis of Patrol Frigate Air Wakes. In *RTO Applied Vehicle Technology Panel Symposium*, pages 7–1, 1999.

[36] R.G. Lee and S.J. Zan. Wind Tunnel Testing of a Helicopter Fuselage and Rotor in a Ship Airwake. *Journal of the American Helicopter Society*, 50:326, 2005.

[37] M.J. Silva. Wind Tunnel Investigation of the Aerodynamic Interactions Between Helicopters and Tiltrotors in a Shipboard Environment. Technical report, DTIC Document, 2004.

[38] A.J. Wadcock. PIV Measurements of the Wake of a Tandem-Rotor Helicopter in Proximity to a Ship. Technical report, DTIC Document, 2004.

[39] G.K. Yamauchi, A.J. Wadcock, and M.R. Derby. Measured Aerodynamic Interaction of Two Tiltrotors. In *Annual Forum Proceedings of the American Helicopter Society*, volume 59, pages 1720–1731. American Helicopter Society, inc, 2003.

[40] M.R. Derby and G.K. Yamauchi. Design of 1/48th-Scale Models for Ship/Rotorcraft Interaction Studies. In *21st Applied Aerodynamics Conference*, volume 23, page 26, 2003.

[41] W. Johnson. Wind Tunnel Measurements and Calculations of Aerodynamic Interactions Between Tiltrotor Aircraft. Technical report, DTIC Document, 2003.

[42] G. Rajagopalan, S. Niazi, A.J. Wadcock, G.K. Yamauchi, and M.J. Silva. Experimental and Computational Study of the Interaction Between a Tandem-Rotor Helicopter and a Ship. In *Annual Forum Proceedings of the American Helicopter Society*, volume 61, page 729. American Helicopter Society, inc, 2005.

[43] G.F. Syms. Simulation of Simplified-Frigate Airwakes Using a Lattice-Boltzmann Method. *Journal of Wind Engineering and Industrial Aerodynamics*, 96(6):1197–1206, 2008.

[44] S.A. Polsky. A Computational Study of Unsteady Ship Airwake. Technical report, DTIC Document, 2003.

[45] J.W. Bunnell. An Integrated Time-Varying Airwake in a UH-60 Black-Hawk Shipboard Landing Simulation. In *AIAA Modeling and Simulation Technologies Conference and Exhibit, Montreal, Canada*, pages 6–9, 2001.

[46] S. Ananthan, J. Baeder, B. W. C. Sim, S. Hahn, and G. Iaccarino. Prediction and Validation of the Aerodynamics, Structural Dynamics, and Acoustics of the SMART Rotor Using a Loosely-Coupled CFD-CSD Analysis. *Proceedings of the American Helicopter Society*, 2010.

[47] S. Thomas, S. Ananthan, and J.D. Baeder. Wake-Coupling CFD-CSD Analysis of Helicopter Rotors in Steady and Maneuvering Flight Conditions. pages 758–777, 2010. cited By (since 1996)0.

[48] M.J. Bhagwat, R.A. Ormiston, H.A. Saberi, and H. Xin. Application of Computational Fluid Dynamics/Computational Structural Dynamics Coupling for Analysis of Rotorcraft Airloads and Blade Loads in Maneuvering Flight. *Journal of the American Helicopter Society*, 57(3), 2012.

[49] A. Abhishek, S. Ananthan, J. Baeder, and I. Chopra. Prediction and Fundamental Understanding of Stall Loads in UH-60A Pull-up Maneuver. *Proceedings of the American Helicopter Society*, 2010.

[50] P. Masarati, M. Morandini, and P. Mantegazza. An Efficient Formulation for General-Purpose Multibody/Multiphysics Analysis. *Journal of Computational and Nonlinear Dynamics*, 2014.

[51] K. Yu, D. A. Wachspress, H-A. Saberi, M. J. Hasbun, J. C. Ho, and H. Yeo. Helicopter Rotor Structural Load Predictions with a Comprehensive Rotorcraft Analysis. *Proceedings of the American Helicopter Society*, 2012.

[52] P. Beaumier, M. Costes, O. Rodriguez, M. Poinot, and B. Cantaloube. Weak and Strong Coupling Between the elsA CFD Solver and the HOST Helicopter Comprehensive Analysis. *ONERA: Tire a Part*, (186):1, 2005.

[53] G. Servera, P. Beaumier, and M. Costes. A Weak Coupling Method Between the Dynamics Code HOST and the 3D Unsteady Euler Code WAVES. *Journal of Aerospace Science and Technology*, 5(6):397–408, 2001.

[54] F. Dehaeze and G.N. Barakos. Hovering Rotor Computations Using an Aeroelastic Blade Model. *Royal Aeronautical Society*, 116(1180), 2012.

[55] Tang L., Dinu A., and Polsky S. Reduced-Order Modeling of Rotor-Ship Interaction. In *Aerospace Sciences Meeting of the American Institute of Aeronautics and Astronautics*, 2012.

[56] M. Jarkowski, M.A. Woodgate, G.N. Barakos, and J. Rokicki. Towards Consistent Hybrid Overset Mesh Methods For Rotorcraft CFD. *International Journal for Numerical Methods in Fluids*, 2011.

[57] I.C. Cheeseman and W.E. Bennett. The Effect of the Ground on a Helicopter Rotor in Forward Flight. *ARC R&M*, 3021:1–10, 1955.

[58] G.D. Padfield. *Helicopter flight dynamics*. John Wiley & Sons, 2008.

[59] D.A. Peters. How Dynamic Inflow Survives in the Competitive World of Rotorcraft Aerodynamics. *Journal of the American Helicopter Society*, 54(1):11001–11001, 2009.

[60] D.M. Pitt and D.A. Peters. Theoretical Prediction of Dynamic-Inflow Derivatives. *Vertica*, 5(1):21–34, 1981.

[61] A.M. Arney and N.E. Gilbert. A User's Manual for the ARL Mathematical Model of the Sea King Mk-50 Helicopter: Part 1. Basic Use. Technical report, DTIC Document, 1988.

[62] A.M. Arney and N.E. Gilbert. A User's Manual for the ARL Mathematical Model of the Sea King Mk-50 Helicopter: Part 2. Use with ARL Flight Data. Technical report, DTIC Document, 1988.

[63] R.A. Feik and R.H. Perrin. Identification of an Adequate Model for Collective Response Dynamics of a Sea King Helicopter in Hover. Technical report, DTIC Document, 1988.

[64] R.A. Hess. Simplified Approach for Modelling Pilot Pursuit Control Behaviour in Multi-Loop Flight Control Tasks. *Proceedings of the Institution of Mechanical Engineers, Part G: Journal of Aerospace Engineering*, 220(2):85–102, 2005.

[65] R. Bradley and G. Brindley. Progress in the Development of a Versatile Pilot Model for the Evaluation of Rotorcraft Performance, Control Strategy and Pilot Workload. *Aeronautical Journal*, 107(1078):731–738, 2003.

[66] D. Thomson and R. Bradley. Inverse Simulation as a Tool for Flight Dynamics Research - Principles and Applications. *Progress in Aerospace Sciences*, 42(3):174 – 210, 2006.

[67] H. Kwakernaak. *Linear optimal control systems*. Wiley Interscience, New York, 1972.

[68] R.A. Hess. *Unified Theory for Aircraft Handling Qualities and Adverse Aircraft - Pilot Coupling*. American Institute of Aeronautics and Astronautics, 1997.

[69] M. Mohammad and A.K. Cook. Review of Pilot Modelling Techniques. *48th AIAA Aerospace Sciences Meeting Including The New Horizons Forum and Aerospace Exposition*, 2010.

[70] D.L. Kleinman, S. Baron, and W.H. Levison. An Optimal Control Model of Human Response Part I: Theory and Validation. *Automatica*, 6(3):357–369, 1970.

[71] R.A. Hess. Simplified Technique for Modeling Piloted Rotorcraft Operations Near Ships. *Journal of Guidance, Control, and Dynamics*, 29(6):1339–1349, 2006.

[72] Aeronautical Design Standard. Handling Qualities Requirements for Military Rotorcraft (ADS-33E-PRF). *Redstone Arsenal, Alabama: US Army Aviation and Missile Command, Aviation Engineering Directorate*.

[73] R.A. Hess. Obtaining Multi-Loop Pursuit-Control Pilot Models From Computer Simulation. *Proceedings of the Institution of Mechanical Engineers, Part G: Journal of Aerospace Engineering*, 222(2):189–199, 2008.

[74] R.A. Hess and C. Gao. A Generalized Algorithm for Inverse Simulation Applied to Helicopter Maneuvering Flight. *Journal of the American Helicopter Society*, 38(4):3–15, 1993.

[75] J-J Philippe and J-J Chattot. Experimental and theoretical studies on helicopter blade tips at onera. 1980.

[76] George Barakos, R Steijl, K Badcock, and A Brocklehurst. Development of CFD capability for full helicopter engineering analysis. In *31st European Rotorcraft Forum, Florence, Italy, Sept*, 2005.

[77] Ph. Spalart. Strategies for Turbulence Modelling and Simulations. *International Journal of Heat and Fluid Flow*, 21(3):252–263, June 2000.

[78] O. Reynolds. On the Dynamical Theory of Incompressible Viscous Fluids and the Determination of the Criterion. *Philosophical Transactions of the Royal Society of London*, A(186):123–164, 1895.

[79] J. Boussinesq. *Théorie de l'Écoulement Tourbillonant et Tumultueux des Liquides dans des Lits Rectilignes à Grande Section, Tome I-II*. Gaulthier-Villars, Paris, France, first edition, 1897.

[80] A. Jameson. Time Dependent Calculations Using Multigrid, with Applications to Unsteady Flows Past Airfoils and Wings . In *10th Computational Fluid Dynamics Conference, Honolulu, HI*, 1991. AIAA-91-1596.

[81] S. Osher and S. Chakravarthy. Upwind Schemes and Boundary Conditions with Applications to Euler Equations in General Geometries. *Journal of Computational Physics*, 50:447–481, January–February 1983.

[82] P.L. Roe. Approximate Riemann Solvers, Parameter Vectors, and Difference Schemes. *Journal of Computational Physics*, 43(2):357–372, October 1981.

[83] B. van Leer. Flux-vector splitting for the euler equations. In *Eighth International Conference on Numerical Methods in Fluid Dynamics*, volume 170 of *Lecture Notes in Physics*, pages 507–512. Springer Berlin / Heidelberg, 1982.

[84] O. Axelsson. *Iterative Solution Methods*. Cambridge University Press, Cambridge, MA, edition, 1994.

[85] M. Woodgate, K. Badcock, B. Richards, and R. Gatiganti. A Parallel 3D Fully Implicit Unsteady Multiblock CFD Code Implemented on a Beowulf Cluster. In *Parallel CFD 1999, Williamsburg, VA, USA*, 1999.

[86] UK Research Councils. HECToR: UK National Supercomputing Service. http://www.hector.ac.uk/, 2007.

[87] Ph. Spalart and S.R. Allmaras. A One-Equation Turbulence Model for Aerodynamic Flows. *La Recherche Aérospatiale*, 1:5–21, 1994.

[88] D.C. Wilcox. Multiscale Model for Turbulent Flows. *AIAA Journal*, 26(11):1311–1320, November 1988.

[89] F.R. Menter. Two-Equation Eddy-Viscosity Turbulence Models for Engineering Applications. *AIAA Journal*, 32(8):1598–1605, August 1994.

[90] P. Chassaing. *Turbulence en Mécanique des Fluides*. Cépaduès-Éditions, Toulouse, France, first edition, 2000.

[91] M.V. Morkovin. Effects of Compressibility on Turbulent Flows. *Mécanique de la Turbulence*, 108:367–380, 2007. Coll. CNRS, CNRS, Paris.

[92] T. Cebeci and A. M. O. Smith. *Analysis of Turbulent Boundary Layers*. Number 15. Applied Mathematics and Mechanics. Academic Press, New York, NY, 1974.

[93] B. Baldwin and H. Lomax. Thin-layer Approximation and Algebraic Model for Separated Turbulent Flows. In *AIAA 16th Aerospace Sciences Meeting, Huntsville, AL.*, January 16–18 1978.

[94] B. S. Baldwin and T. J. Barth. A One-Equation Turbulence Transport Model for High Reynolds Number Wall-Bounded Flows. Technical Memorandum NASA-TM-102847, NASA, August 1990.

[95] W.P Jones and B.E Launder. The Prediction of Laminarization with a Two-Equation Model of Turbulence. *International Journal of Heat and Mass Transfer*, 15(2):301–314, 1972.

[96] S. Moir and A. Gould. VoTMATA — British Aerospace Default Model. Technical report, BAE SYSTEMS, 1998.

[97] K. Hanjalić and B. E. Launder. A Reynolds Stress Model of Turbulence and its Application to Thin Shear Flows. *Journal of Fluid Mechanics*, 52:609–638, 1972.

[98] P. A. Durbin. Near-Wall Turbulence Closure Modeling without Damping Functions. *Theoretical and Computational Fluid Dynamics*, 3(1):1–13, 1991.

[99] T.J. Craft, B.E. Launder, and K. Suga. Development and Application of a Cubic Eddy-Viscosity Model of Turbulence. *International Journal of Heat and Fluid Flow*, 17(2):108–115, 1996.

[100] T. P. Sommer, R. M. C. So, and H. S. Zhang. A Near-Wall Four-Equation Turbulence Model for Compressible Boundary Layers. Technical Report NASA-CR-4436, NASA, April 1992.

[101] P. Malecki. *Étude de Modèles de Turbulence pour les Couches Limites Tridimensionnelles*. PhD thesis, ENSAE, Toulouse, France, 1994.

[102] K. Hanjalic, B. E. Launder, and R. Schiestel. Multiple-Time-Scale Concepts in Turbulent Transport Modeling. In *Von Karman Institute for Fluid Dynamics Measurements and Predictions of Complex Turbulent Flows*, volume 1, 1980.

[103] S.-W. Kim. Numerical Investigation of Separated Transonic Turbulent Flows with a Multiple-Time-Scale Turbulence Model. Technical Memorandum NASA-TM-102499, NASA, January 1990.

[104] C.P. Chen. A Non-Isotropic Multiple-Scale Turbulence Model. Technical Report NASA-CR-184217, NASA, September 1990.

[105] S. Deck, Ph. Duveau, P. d'Espiney, and Ph. Guillen. Development and Application of Spalart-Allmaras One Equation Turbulence Model to Three-Dimensional Super sonic Complex Configurations. *Aerospace Science and Technology*, 6(3):171–183, March 2002.

[106] P. Spalart, W.H. Jou, M.Kh. Strelets, and S.R. Allmaras. Comments on the Feasibility of LES for Wings, and on a Hybrid RANS/LES Approach. In *First AFOSR International Conference on DNS/LES, Columbus, OH*, August 1997.

[107] P.R. Spalart and M. Shur. On the Sensitization of Turbulence Models to Rotation and Curvature. *Aerospace Science and Technology*, 1(5):297–302, July 2002.

[108] A.N. Kolmogorov. Equations of Turbulent Motion of an Incompressible Turbulent Fluid. *Izvestiya Akademii Nauk SSSR, Seriya Fizicheskaya*, 6(1–2):56–58, 1942.

[109] F. H. Harlow and P. I. Nakayama. Turbulence Transport Equations. *Journal of Fluid Mechanics*, 10(11):2323–2332, 1967.

[110] D.B. Spalding. The Prediction of Two-Dimensional, Steady Turbulent Flows. Technical Report Heat Transfer Section Report EF/TN/A/16, Imperial College, 1969.

[111] C.G. Speziale and P.S. Bernard. The Energy Decay in Self-Preseving Isotropic Turbulence Revisited. *Journal of Fluid Mechanics*, 241:645–667, 1992.

[112] D.A. Johnson and L.S. King. A Mathematically Simple Turbulence Closure Model for Attached and Separated Turbulent Boundary Layers. *AIAA Journal*, 23(11):1684–1692, November 1985.

[113] P. Nayyar and G. Barakos. A Summary of Turbulence Modelling Approaches in CFD. Aerospace Engineering Report 0206, University of Glasgow, September 2002.

[114] D.C. Wilcox. Simulation of Transition with a Two-Equation Turbulence Model. *AIAA Journal*, 32(2):247–255, February 1994.

[115] F. Menter and Y. Egorov. SAS Turbulence Modelling of Technical Flows. *Direct and Large-Eddy Simulation VI*, pages 687–694, 2006.

[116] Y. Egorov and F. Menter. Development and Application of SST-SAS Turbulence Model in the DESIDER Project. *Advances in Hybrid RANS-LES Modelling*, pages 261–270, 2008.

[117] F.R. Menter and Y. Egorov. The Scale-Adaptive Simulation Method for Unsteady Turbulent Flow Predictions. Part 1: Theory and Model Description. *Flow, Turbulence and Combustion*, 85(1):113–138, 2010.

[118] Y. Egorov, F.R. Menter, R. Lechner, and D. Cokljat. The Scale-Adaptive Simulation Method for Unsteady Turbulent Flow Predictions. Part 2: Application to Complex Flows. *Flow, Turbulence and Combustion*, 85(1):139–165, 2010.

[119] F. Menter, A. Garbaruk, P. Smirnov, D. Cokljat, and F. Mathey. Scale-Adaptive Simulation with Artificial Forcing. *Progress in Hybrid RANS-LES Modelling*, pages 235–246, 2010.

[120] M. Strelets. Detached Eddy Simulation of Massively Separated Flows. In *AIAA 39th Aerospace Sciences Meeting and Exhibit, Reno, NV*, January 8–11 2001. AIAA-2001-0879.

[121] J.S. Batten, U.C. Goldberg, and S.R. Chakravarthy. Sub-Grid Turbulence Modeling for Unsteady Flow with Acoustic Resonance. In *AIAA 38th Aerospace Sciences Meeting, Reno, NV*, January 10–13 2000. AIAA-00-0473.

[122] P. Spalart, S. Deck, M.L. Shur, K.D. Squires, M.Kh. Strelets, and A. Travin. A New Version of Detached-Eddy Simulation, Resistant to Ambiguous Grid Densities. *Theoretical and Computational Fluid Dynamics*, 20:181–195, 2006.

[123] G.A.M. Van Kuik. *On the Limitations of Froude's Actuator Disc Concept*. Thesis, 1991.

[124] H. Glauert. Airplane Propellers. In *Aerodynamic Theory*, pages 169–360. Springer, 1935.

[125] V.I. Shaidakov. Disk Vortex Theory of Main Rotor with Constant Loading on the Disk. *Helicopters Design Aerodynamics*, 381, 1976.

[126] N.C. Wells. *The Atmosphere and Ocean: A Physical Introduction*. Advancing Weather and Climate Science. John Wiley & Sons, 2012.

[127] A. Antoniadis, B. Zhong, and D. Drikakis. Generation of Advanced Helicopter Experimental Aerodynamic Database for CFD Code Validation. Technical report, GOAHEAD Partners European Commission, 2005.

[128] B. Benoit, K. Kampa, W. von Grunhagen, P-M Basset, and B. Gimonet. HOST, a General Helicopter Simulation Tool for Germany and France. In *Proceedings of the American Helicopter Society*, volume 56, pages 1110–1131. American Helicopter Society, Inc, 2000.

[129] O.J. et al. Boelens. Aerodynamic Simulation of a Complete Helicopter Configuration. Technical report, Nationaal Lucht- en Ruimtevaartlaboratorium, 2007.

[130] K.J. Schultz, W. Splettstoesser, B. Junker, W. Wagner, E. Schoell, G. Arnaud, E. Mercker, K. Pengel, and D. Fertis. A Parametric Wind Tunnel Test on Rotorcraft Aerodynamics and Aeroacoustics (HELISHAPE)-Test Documentation and Representative Results. In *22nd European Rotorcraft Forum, Brighton, UK*, 1996.

[131] E. W. Quon, P. A. Cross, Smith M. J., Rosenfeld N. C., and Whitehouse G. R. Investigation of Ship Airwakes Using a Hybrid Computational Methodology. In *Annual Forum Proceedings of the American Helicopter Society*, 2014.

[132] N. Rosenfeld, K. Kimmel, and A. J. Sydney. Investigation of Ship Topside Modeling Practices for Wind Tunnel Experiments. *Proceedings of the AIAA Science and Technology Forum*, 2015.

[133] S.J. Lawson, C. Crozon, F. Dehaeze, R. Steijl, and G.N. Barakos. Computational Fluid Dynamics Analyses of Ship Air Wakes Using Detached-Eddy Simulation. *European Rotorcraft Forum Proceedings*, 1:502–523, 2012.

[134] R. Steijl and G. Barakos. Sliding Mesh Algorithm for CFD Analysis of Helicopter Rotor-Fuselage Aerodynamics. *International Journal for Numerical Methods in Fluids*, 58(5):527–549, 2008.

[135] Ronald A Hess and Yoon C Jung. An Application of Generalized Predictive Control to Rotorcraft Terrain-Following Flight. *Systems, Man and Cybernetics, IEEE Transactions on*, 19(5):955–962, 1989.

[136] M. Biava, M. Woodgate, and G. Barakos. Discrete Adjoint Methods for the Computation of Rotorcraft Aerodynamic Derivatives. In *Proceedings of the 53rd AIAA Aerospace Sciences Meeting, AIAA Science and Technology Forum*. American Institute of Aeronautics and Astronautics, 2015.

[137] J.E. Bresenham. Algorithm for Computer Control of a Digital Plotter. *IBM System Journal*, 1965.

[138] Short LIC Source Code. *http://www.zhanpingliu.org/research/flowvis/lic/LIC_Source.htm*.

[139] L.K. Forssell and S.D. Cohen. Using Line Integral Convolution for Flow Visualisation: Curvilinear Grids, Variable-Speed Animation, and Unsteady Flows. *IEEE Transactions on Visualisation and Computer Graphics*, 1995.

[140] H.W. Shen and D.L. Kao. A New Line Integral Convolution Algorithm for Visualizing Time-Varying Flow Fields. *IEEE Transactions on Visualisation and Computer Graphics*, 1998.

Appendix A

Description of the Sea King Helicopter Model

Unless otherwise stated, the aircraft data used in this work is based on the Sea King MK50 Helicopter. Table A.1 compile informations found in DTIC reports [61–63].

The following figures can be found in Arney and Gilbert [61] and give information about the geometry of the aircraft. position of the equipment (Figure A.1), Variation of the CG position (Figure A.2) and aircraft moments of inertia as function of the weight (Figure A.3).

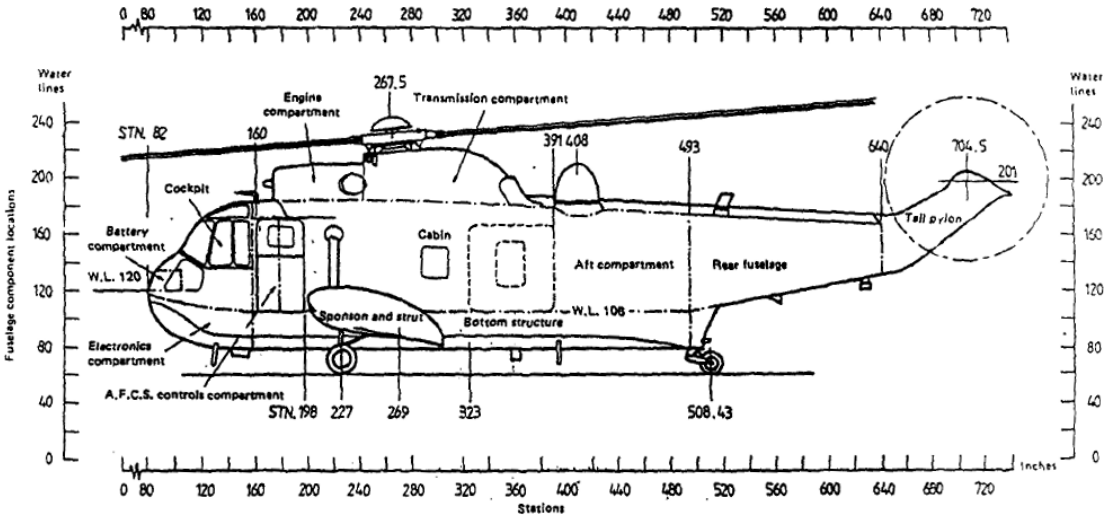

Figure A.1: View of the Sea King fuselage with waterline and datum reference. CG positions CGx and CGz are absolute, HR and XCH are the CG position with waterline 232 and fuselage station 267.4 (datum)

Variable	DTIC Value	SI value
All Up Weight (AUW)	18500 *lb*	8391.46 *kg*
Main rotor lock number	10.76	10.76
Tail rotor lock number	5.10	5.10
Roll 2nd moment of inertia	14275 $slugs.ft^2$	19354.3 $kg.m^2$
Pitch 2nd moment of inertia	48375 $slugs.ft^2$	65587.69 $kg.m^2$
Yaw 2nd moment of inertia	39150 $slugs.ft^2$	53080.27 $kg.m^2$
CGz*	145 *inches*	3.683 *m*
CGx*	-1.03 *inches*	-0.026 *m*
HR*	7.2 *ft*	2.19456 *m*
XCH*	0.09 *ft*	0.027 *m*
Rotor radius	31 *ft*	9.4488 *m*
Blade chord	1.52 *ft*	0.4633 *m*
Hinge offset	1.05 *ft*	0.32 *m*
Blade twist	-8.0 *degrees*	-8.0 *degrees*
Blade mass	181 *lb*	82.1 *kg*
Rotation speed Ω	21.89 $rd.s^{-1}$	21.89 $rd.s^{-1}$
Lock Number γ	11.51	11.51
Ratio rotor/blade inertia	6	6
Main rotor forward angle (from A.1)	4.2 *degrees*	4.2 *degrees*

Table A.1: Physical characteristics of the Sea King MK50 helicopter [61–63]

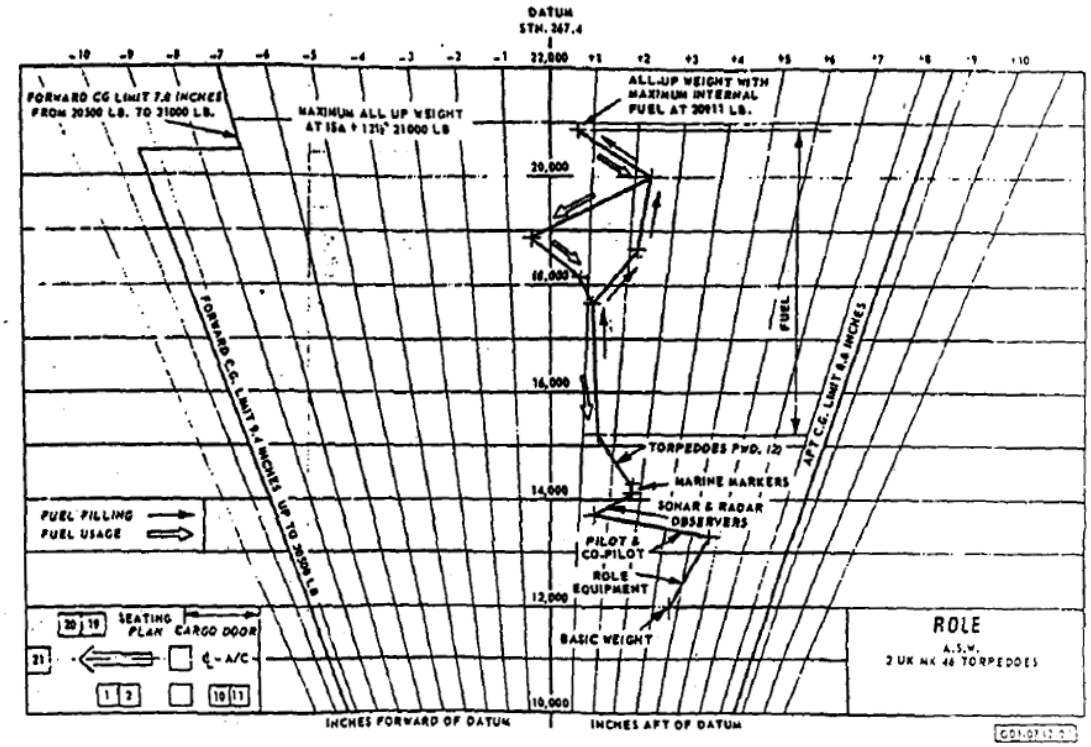

Figure A.2: Position of CG from the datum as function of the equipment and quantity of fuel on board.

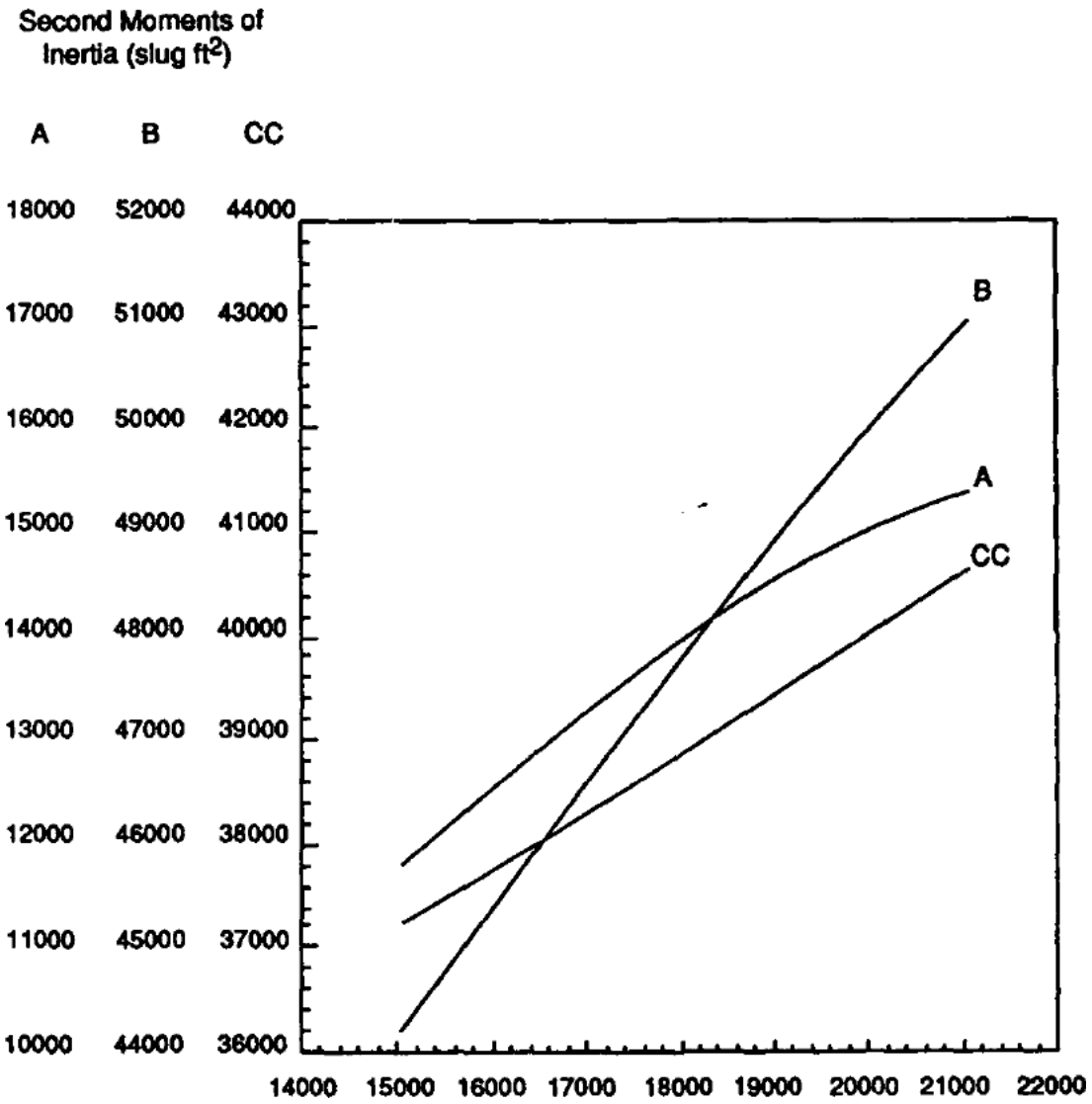

Figure A.3: Value of the Roll (A), pitch (B) and yaw (CC) 2nd moments of inertia as function of the aircraft weight.

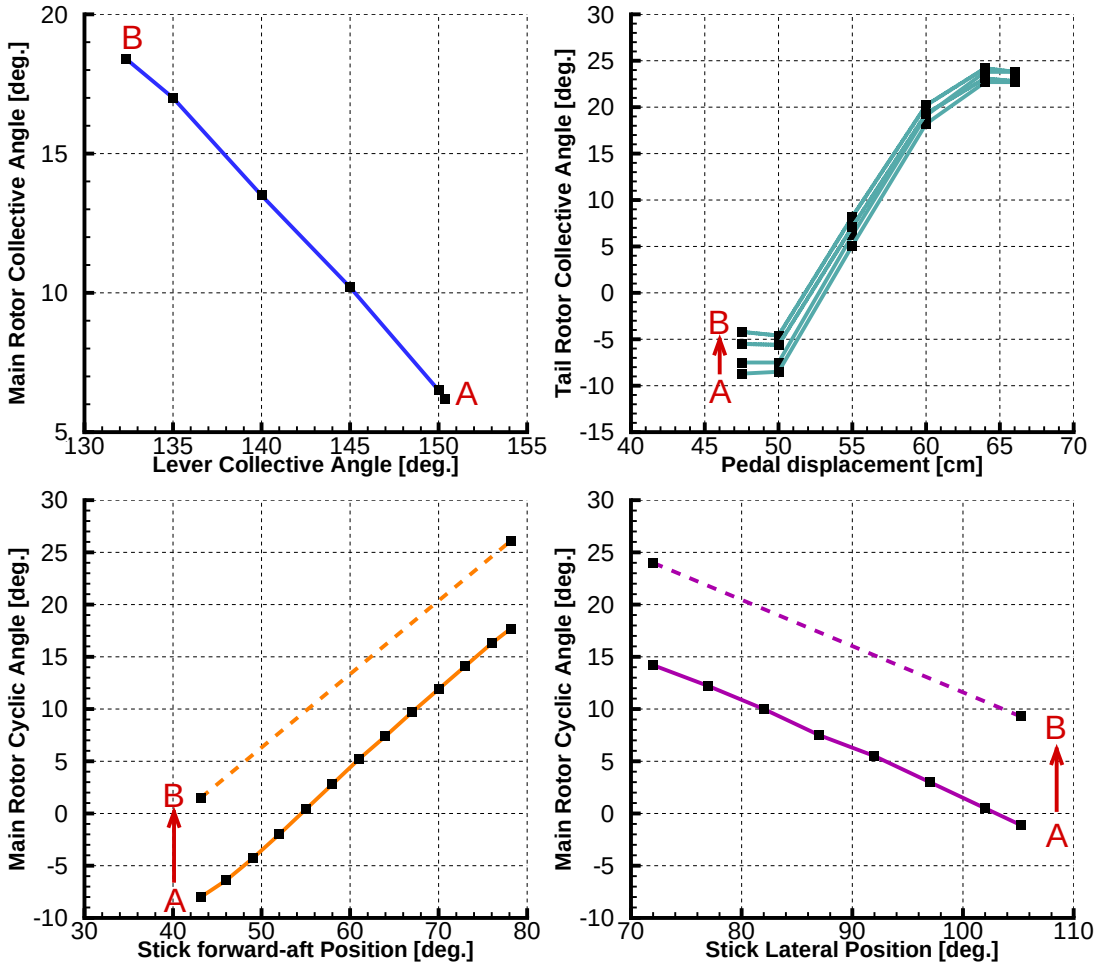

Figure A.4: Transfer functions between pedals and stick displacements and blade angles.

Appendix B

Linear Integral Convolution Method for Flow Visualisation

Streamlines and particle tracing methods are efficient and common tools for visualising flowfields. They give an intuitive description of the flowfield by showing the path that particles follow in the three dimensional environment. However, results often depend greatly on the number of seeding particles and their initial position, and may give an incomplete description of the flowfield by missing small, isolated features.

The Line Integral Convolution (LIC) method was proposed by Cabral and Leedom [2] to alleviate some of these problems, and is a generalisation of the DDA line drawing approach described by Bresenham [137]. The principle of the method can be described as the computation of small, local streamlines from a cloud of points randomly distributed inside the domain. It can process dense 2D or 3D vector fields and found applications in many domains from image processing to the representation of fluid flows.

The standard algorithm applicable to fluid mechanics starts from a "textured" image of the domain, which is usually a white noise (Figure B.1 (a)). The velocity vector field is used to calculate local streamlines which originate in the center of each pixel and moves in both the positive and negative directions (Figure B.1 (b)). The output image is the result of the one dimensional convolution of the random field and the kernel function filter, computed along the local streamlines. An exact integral of the convolution kernel is used to normalise the output of the convolution and avoid distortion in brightness and contrast due to the filter shape.

A short version of the code can be found in [138].

Figure B.2 shows the results of the previous DDA method and the LIC method

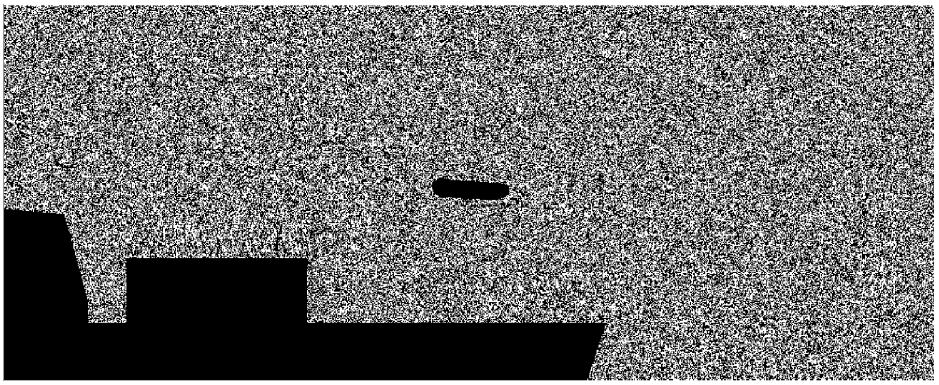

(a) Initial white noise field

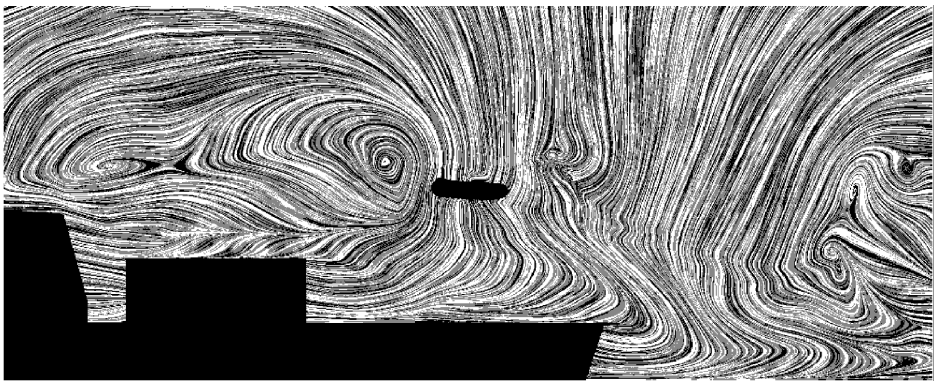

(b) white noise field after LIC processing

Figure B.1: White noise field (a) before and (b) after LIC processing.

applied to a turbulent flowfield using an initial white noise field.

An extension of the standard LIC algorithm to curvilinear grids and a method for the visualisation of the vector magnitude was presented by Forssell and Cohen [139]. In the same work a first methodology to use the LIC with unsteady flows is discussed: the idea is to change the convolution path from streamlines to pathlines. Shen and Kao [140], finally, proposed an Unsteady Flow LIC to overcome the lack of coherence intrinsic in the previous approach.

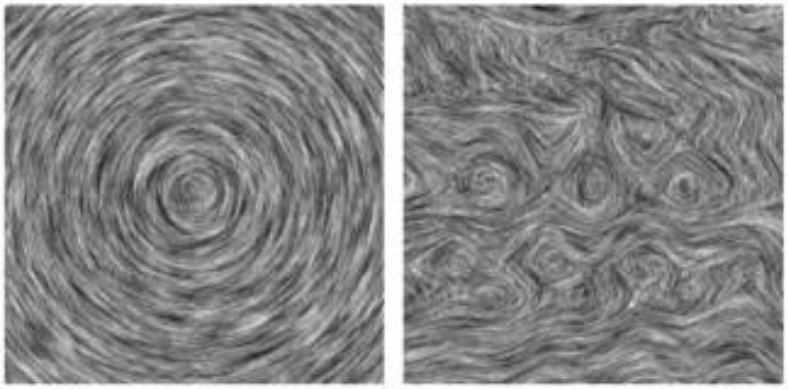

(a) DDA convolution over white noise.

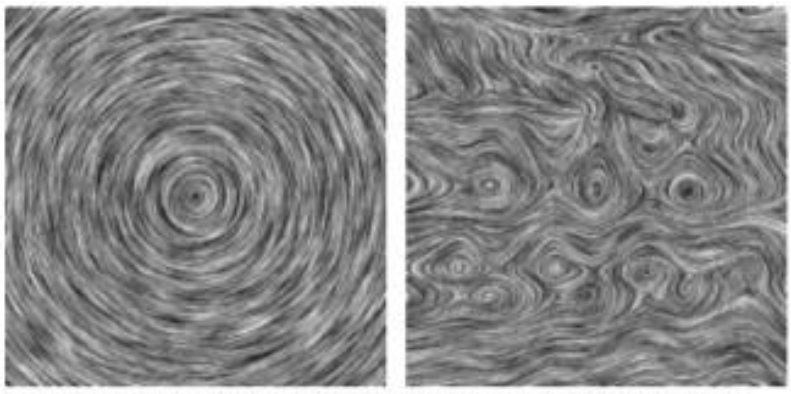

(b) LIC over white noise.

Figure B.2: Comparison between DDA and LIC visualisation techniques [2]: circular and turbulent fluid dynamics vector fields.